Decay Spectroscopy of Isomerically Pure Beams of ^{178}Au and its Daughters

Christopher Adam Abbott Page

PhD

University of York

Physics, Engineering, and Technology

February 2025

Declaration

I declare that this thesis is a presentation of original work and I am the sole author. This work has not previously been presented for a degree or other qualification at this University or elsewhere. All sources are acknowledged as references.

Abstract

In many regions of the nuclear landscape, competition between spherical and deformed configurations leads to the phenomenon of shape coexistence due to the delicate balance between shell and collective effects. The region around the $Z = 82$ proton-shell closure and the $N = 104$ neutron midshell contains some of the clearest examples of this phenomenon and has thus been the focus of intense theoretical and experimental study in recent decades.

The results presented in this thesis form a contribution to this long-term programme through an in-depth decay spectroscopy study of ^{178}Au (Z=79, N=99) and its daughters. In-source laser spectroscopy by Cubiss *et al.* [1] at the ISOLDE facility confirmed the existence of a previously predicted, strongly deformed isomer, ^{178}Au^m, coexisting with the more weakly deformed ground state, ^{178}Au^g. As part of Cubiss' study, highly selective resonant laser ionisation allowed separate α-decay studies of ^{178}Au^{g,m} to be performed. In the present work, the same technique was used to produce isomerically pure beams of each of these two states for a detailed decay spectroscopy study of the α- and EC/β^+-decay branches of ^{178}Au^{g,m}, and their daughters, at the ISOLDE Decay Station (IDS).

Separate fine-structure α-decay schemes for $^{178}_{79}$Au$^{g,m} \rightarrow ^{174}_{77}$Ir^{g,m} and $^{174}_{77}$Ir$^{g,m} \rightarrow ^{170}_{75}$Re were produced, expanding substantially on those from earlier works [1–3]. The first ever isomerically selective electron-capture (EC)/β^+ decay studies of ^{178}Au$^{g,m} \rightarrow ^{178}$Pt and ^{174}Ir$^{g,m} \rightarrow ^{174}$Os were also performed for this thesis. All together, these decay schemes include 70 new states, 11 new α decays and 119 new γ-ray transitions. The half lives of ^{178}Au^{g,m} were measured which gave values consistent with those determined by Cubiss but have smaller uncertainties. The multipolarities of γ-ray transitions observed following the α decay of ^{178}Au^{g,m} to ^{174}Ir were determined, as were reduced α-decay widths (δ^2_α) and hindrance factors, HF_α. The proportion of EC/β^+ decay feeding to each state in ^{178}Pt and ^{174}Os was calculated, allowing log ft values for these decays to be experimentally determined for the first time. These were used in conjunction with HF_α to propose spin-parity and configu-ration assignments for ^{178}Au^{g,m} and ^{174}Ir^{g,m} and infer information on the shape of ^{178}Pt. The E0-transition strengths for decays between the states in two strongly mixed rotational bands in ^{178}Pt were determined and used to calculate a lower limit for the difference in the mean-square charge radii of the bandheads. Using mass measurements reported by Cubiss and α-decay Q values deduced in this work, the excitation energy of the states fed by the α decay of ^{178}Au^{g,m} and ^{174}Ir^{g,m} were determined. While all α decays from ^{178}Au^g were assigned as feeding directly or indirectly to ^{174}Ir^g (and ^{178}Au^m to ^{174}Ir^m), it was found that ^{174}Ir^g feeds to a long-lived, low-spin state 47(17) keV more energetic than the high-spin state fed by ^{174}Ir^m. This indicates a possible inversion of state ordering in ^{170}Os relative to ^{174}Ir and ^{178}Au.

Acknowledgements

During my Ph.D., I have met many incredible people, both through work and as I have lived in two amazing cities, York and Geneva. There are a great many who have helped and supported me through this project, but a special few to whom I am especially grateful and would like to thank individually.

First and foremost, Andrei and James: thank you for your supervision throughout my studies. Andrei, you have always modelled the very best of the "work hard, play hard" mindset, encouraging me to achieve the best I can. To James, although I was your first student, your advice, insight, and knowledge of the field have been exceptional. I wish you all the best in Edinburgh, a great city which I absolutely loved.

I would also like to extend my heartfelt thanks to Razvan for the constant encouragement and guidance you have provided over the last few years. You were an excellent teacher during our period together at ISOLDE and gave me the confidence to take over many of your responsibilities at IDS. Thank you! Zixuan too, for putting up with me through some incredibly busy campaigns when we were both extremely sleep deprived!

To my parents, thank you for steadfastly and lovingly supporting me through not just this project but everything before it. To my brother, Matt, for always being there, despite juggling a full-time job and raising a beautiful young family. The frequent midnight calls as we were both on night shifts were a particular highlight!

In both Geneva and York, I have made some wonderful friends who have helped me feel at home in both places, despite long periods away. In particular, I'd like to thank Stephen, Rachel, Tom and Imi for helping me feel welcome when I first arrived in, and then later returned to, York.

Caleb and Christian, thank you for making me feel so welcome in Geneva - I wish you both all the best as you now start a new phase of life as parents. Jeán and Steph - thank you for all your encouragement and for being such great friends. Also to Jan - it was great to find a German with a sense of humour who was always up for heading to R1 on a Friday evening after a long week - Danke!

To the friends I made before I started who have been there for me since before I started, thank you for everything. To Adam, for the weekly wind-down and catch up, helping me to avoid working *all* of the time. Ally, Johnny, Immy, Liz, and Owen: it was great to have you all over to visit while I was in Geneva and a pleasure to show you around both the lab and city. And to anyone else who isn't named here - for your support, friendship, and encouragement,

Thank you! Chris

Contents

List of Tables

List of Figures

1 Introduction

The shape of a nucleus is a fundamental property that can have a significant influence on other aspects of nuclear structure, such as state energies, half lives and the available decay modes. While some of the key features of the nuclear landscape can be explained by assuming nuclei are spherical, most exhibit some degree of deformation in their own intrinsic frame of reference. Most commonly, this takes the form of quadrupole deformation, in which a nucleus may be thought to have been 'stretched' (like a rugby ball) or 'squashed' (like a discus) from an originally spherical shape. More exotic forms of deformation have also been found in recent years, such as in ^{224}Ra, which was found to be 'pear shaped' [4]. Spherical nuclei tend to have a proton number (Z) and neutron number (N) equal to one of the so-called magic numbers (2, 8, 20, 28…) which correspond to closed proton/neutron shells. Between these shell closures, however, nuclei tend to exhibit strong deformation. The degree of quadrupole deformation for nuclei across the chart is shown in Fig. 1.1.

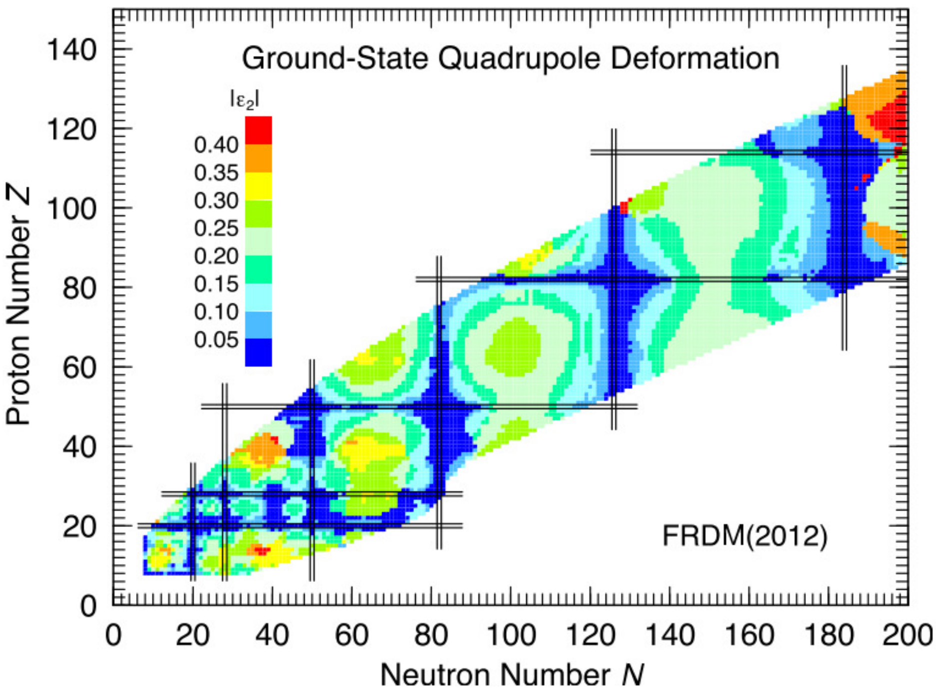

Figure 1.1: Segrè chart showing the calculated ground-state deformation of $N < 200$ nuclei. Neutron- and proton-shell closures are shown by horizontal/vertical black lines. Figure taken from Ref. [5].

Figure 1.1 shows the nuclear deformation for ground-state configurations only. However, nuclei can be excited to higher-energy states, possibly leading to a change of the overall nuclear shape. In some cases, these states lie within a relatively small energy range of each other, producing a phenomenon known as 'low-energy shape coexistence'. This was first observed by Morinaga *et al.* [6] when a rotational band was found within the doubly magic ^{16}O nucleus, as shown in Fig. 1.2.

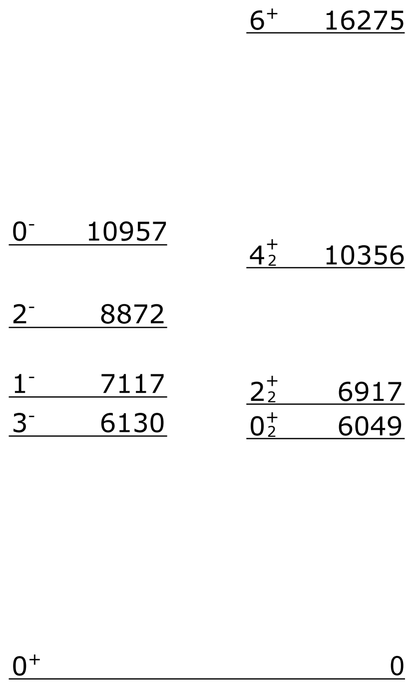

Figure 1.2: Part of the level scheme for ^{16}O. The states shown on the left-hand side are typical of 1p-1h excitation while those on right form a rotational band. Figure adapted from Ref. [7] using data from Ref. [8].

The surprising aspect of Fig. 1.2 is that the excitation energy of the deformed 0^+_2 state (6049 keV) is lower than that of the lowest-energy single-particle state of 6130 keV. Within quantum mechanics, a spherically symmetric rotational state is not possible, so a nucleus must be deformed for a rotational band to be built upon it. Typically, this can be achieved through a multi-nucleon excitation. The result that this requires less energy than a single-particle excitation is therefore somewhat counterintuitive. Similar results have since been found across the nuclear landscape, although modelling them remains a significant challenge for nuclear theory [9].

The work presented in this thesis forms part of a long-term investigation into the structure, nuclear deformation, and shape coexistence of neutron-deficient gold isotopes that has been performed using a combination of decay and laser spectroscopy, mass measurements, and in-beam techniques - see e.g. Refs. [1, 10, 11]. This region exhibits some of the strongest evidence of shape coexistence that is known across the nuclear chart. The analysis presented in Chapter 6 was performed using data gathered as part of the IS665 experiment performed at ISOLDE, CERN in August 2021 [12, 13]. During this experiment, beams of either the ground state of, or an isomer in, ^{178}Au were produced separately which were sent to the ISOLDE Decay Station for charged-particle and γ-ray spectroscopy.

2

Theories of Nuclear Structure

2.1 The Liquid Drop Model

The discipline of nuclear physics arguably began with α-particle scattering experiments reported in 1911 by Geiger and Marsden which were performed under the supervision of Ernest Rutherford [14]. Although most of the α particles traveling through the gold foils were deflected by only small angles, approximately one in 20,000 were deflected by an angle of at least 90°. From this, Rutherford concluded that the 'plum pudding' atomic model proposed by Thomson [15, 16] could not be correct and that atoms instead must have a large concentration of both mass and positive charge at their centre: the nucleus.

The obvious objection to this theory is that it confines many positively charged particles to a small volume, despite the large electrostatic repulsion that they should experience. By 1930, further α-particle scattering data showed some evidence of a strong, short-range, attractive force within the nucleus. This led Gamow to propose a model that assumed the nucleus behaves like a liquid drop, with this force being equivalent to the surface tension in droplets of water [17]. Although originally formulated assuming that α particles were the constituent part of the nucleus, instead of a combination of protons and neutrons (the neutron was discoverd two years later in 1932 [18]), this model correctly predicted the experimentally measured relationship between the nuclear radius and mass

$$R = r_0 A^{1/3}, \tag{2.1}$$

where r_0 is now known to be approximately 1.2 fm, equivalent to a nuclear density of ~ 0.15 fm^{-3}. In 1935, Weizsäcker proposed an expression to calculate the binding energy for a nuclear liquid drop [19]

$$E_B = a_V A - a_S A^{2/3} - a_C \frac{Z(Z-1)}{A^{1/3}} - a_A \frac{(N-Z)^2}{A} \pm \delta(N, Z). \tag{2.2}$$

Each of the terms in this equation represents a different physical aspect of the system:

- $a_V A$ - the 'volume' term describes the attractive force provided by all nucleons in the system through the strong nuclear force. Each additional nucleon is assumed to provide a constant increase in this attraction.

- $a_S A^{2/3}$ - the 'surface' term corrects for the lower force acting upon nucleons on the nuclear surface than on those towards the centre of the nucleus.

- $a_C \frac{Z(Z-1)}{A^{1/3}}$ - the Coulomb term accounts for the repulsive electrostatic force between the protons in the nucleus.

- $a_A \frac{(N-Z)^2}{A}$ - the 'asymetry' term reflects the observation that nuclei with $N \approx Z$ tend to be more stable than those with a significant proton-neutron imbalance.

- $\pm\delta(N, Z)$ - the pairing term is included to reproduce the increased stability observed in even-even nuclei.

Equation 2.2 explains much of the general trend in the binding energy per nucleon shown in Fig. 2.1. Notably, the peak in the binding energy per nucleon observed around ^{56}Fe gives an indication of the range of the strong nuclear force.

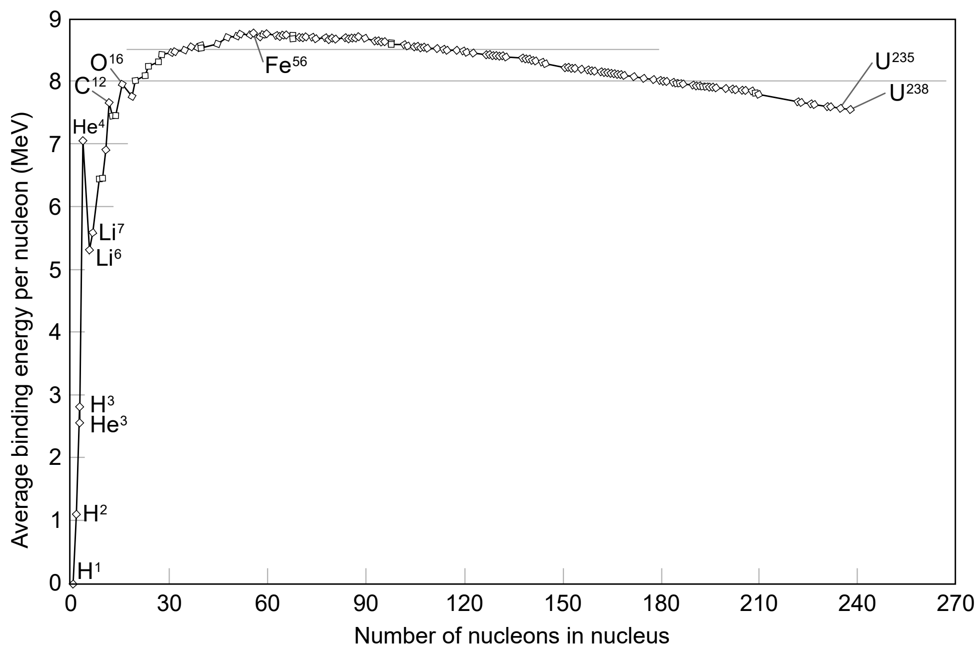

Figure 2.1: The binding energy per nucleon for stable isotopes as a function of mass number. Figure taken from Ref. [20]

2.2 The Spherical Shell Model

One particularly striking aspect of Fig. 2.1 that cannot be explained by the liquid drop model is the sudden increases in the binding energy per nucleon of some nuclides, most clearly ^{4}He or ^{16}O. Both of them have N and Z equal to a so-called magic number: 2, 8, 20, 28, 50, 82, or 126. These correspond to particularly tightly bound configurations with significantly larger nucleon separation energies than surrounding nuclei.

To describe this behaviour, Ivenenko and Gapon proposed a nuclear shell model in 1930 [21, 22], analogous to the one proposed for atoms by Bohr to descibe electron energy levels in 1913 [23]. At the core of the nuclear shell model (as for the atomic equivalent) is the Pauli exclusion principle which forbids more than one particle of a particular type from occupying identical quantum states. This means that, as nucleons are added to the nucleus, they must fill higher-energy states.

While Bohr used the Coulomb potential within the Schrödinger equation for the atom, the potential to use in the nuclear shell model is not immediately clear. The most simple option used is the spherically symmetric, three-dimensional harmonic oscillator (HO), which has the form

$$V_{HO}(r) = \frac{1}{2}m\omega^2 r^2, \tag{2.3}$$

where, typically, $\omega \approx 41A^{1/3}$ MeV/$\hbar$ [24]. Solving the Schrödinger equation for the harmonic oscillator potential in one dimension has the standard result of the eigenvalues

$$E = \left(n + \frac{1}{2}\right)\hbar\omega, \tag{2.4}$$

where $n = 0, 1, 2 \ldots$ For a spherically symmetric nucleus, this result can be generalised to three dimensions to give

$$E = \left(n_x + n_y + n_z + \frac{3}{2}\right)\hbar\omega, \tag{2.5}$$

where $n_{x,y,z} = 0, 1, 2 \ldots$ For $N \equiv n_x + n_y + n_z$, this model predicts the state degeneracy to be $(N + 1)(N + 2)/2$. In each of these states, there are two possible orientations for the nucleons' intrinsic spin which doubles the number of nucleons that can occupy each state. Therefore, the 3D harmonic oscillator predicts shell closures at 2, 8, 20, 40, 70, 112. Although the first three values match the experimentally determined magic numbers, the higher-N predictions fail to replicate the data, as shown in Fig. 2.2.

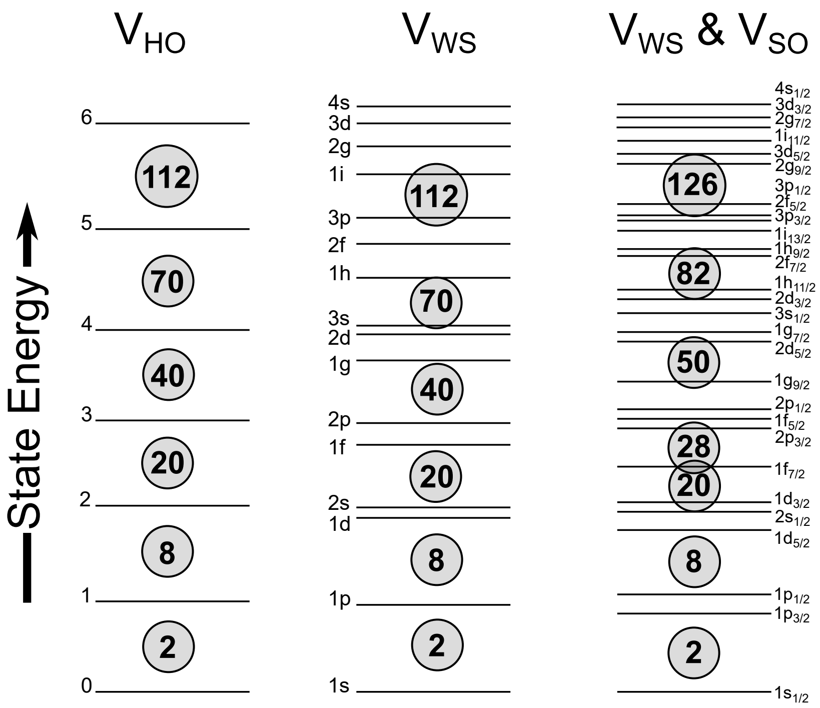

Figure 2.2: Plot of the number of nucleons that can fit into each shell assuming the 3D harmonic oscillator potential (left), the Woods-Saxon potential (centre) and the Woods-Saxon potential with the spin orbit interaction (right). The number of nucleons in a nucleus at each major shell closure is encircled for emphasis. Figure adapted from Ref. [25].

The 3D HO shell model predicts some key features of nuclei but is not without problems. For example, the potential given in Eq. 2.3 is unphysical because it tends to infinity, rather than 0, as r increases. Therefore, the Woods-Saxons potential, V_{WS}, is often used instead as it more realistically models a homogeneous field and nuclear density within the nucleus and the smooth change of the potential to 0, over some finite distance, a

$$V_{WS}(r) = \frac{-V_0}{1 + \exp\left[\frac{r-R}{a}\right]}, \tag{2.6}$$

where V_0 is the well depth. Changing the potential to Eq. 2.6 alone is not sufficient to reproduce the experimentally measured shell closures. To do so, a spin-orbit potential should be added which has the form [26, 27]

$$V_{SO}(r) = V_1 \frac{1}{r} \frac{\mathrm{d}V_{WS}}{\mathrm{d}r} \langle \mathbf{l} \cdot \mathbf{s} \rangle, \tag{2.7}$$

where $\mathbf{l}$ is the orbital angular momentum of the nucleon, $\mathbf{s}$ is the intrinsic spin ($|\mathbf{s}| = 1/2$) angular momentum and V_1 is an energy scaling factor. The coupling of the intrinsic spin and orbital angular momentum of the nucleon to give the total angular momentum, j, increases the state degeneracy. Without this coupling, there are $2l + 1$ substates but with it this becomes $2j + 1$. The energy splitting caused by this can be comparable to the difference in shell energies, and correctly predicts the major shell gaps, as illustrated in Fig. 2.2. The states produced by the Woods-Saxon potential with the spin-orbit interaction are labelled by three quantum numbers: the principle quantum number (equivalent to n in the harmonic oscillator), the orbital angular momentum, l, written in spectroscopic notation (s, p, d, f etc. for l = 0, 1, 2, 3), and the total angular momentum, $j = l \pm s = l \pm \frac{1}{2}$.

2.3 The Deformed Shell Model

The shell model developed in Sec. 2.2 assumes that nucleons move in a spherically symetric potential. This correctly predicts the experimentally determined major shell closures and key properties of magic and doubly magic nuclei but fails to describe the properties of other nuclei. One of the main reasons for this is that non-magic nuclei are often deformed, which invalidates one of the key assumptions of the spherical shell model. In 1955, Nilsson and Mottelson [28, 29] expanded upon earlier work by Mayer [27] to include the impact of quadrupole deformation into a deformed shell model. Such a system can be described using an anisotropic HO Hamiltonian

$$H = H_0 + C\mathbf{l} \cdot \mathbf{s} + D\mathbf{l}^2, \tag{2.8}$$

where C and D are scaling factors and

$$H_0 = -\frac{\hbar^2}{2M}\nabla^2 + \frac{M}{2}\left(\omega_x^2 x'^2 + \omega_y^2 y'^2 + \omega_z^2 z'^2\right). \tag{2.9}$$

Quadrupole deformation can be modelled by the parameter β_2, which describes the relative length of one axis of the nucleus compared to the other two

$$\beta_2 = \frac{4}{3}\sqrt{\frac{\pi}{5}}\frac{\Delta R}{r_{\mathrm{sph}}}, \tag{2.10}$$

where ΔR is the difference between the semi-major and semi-minor axes of the spheroid.

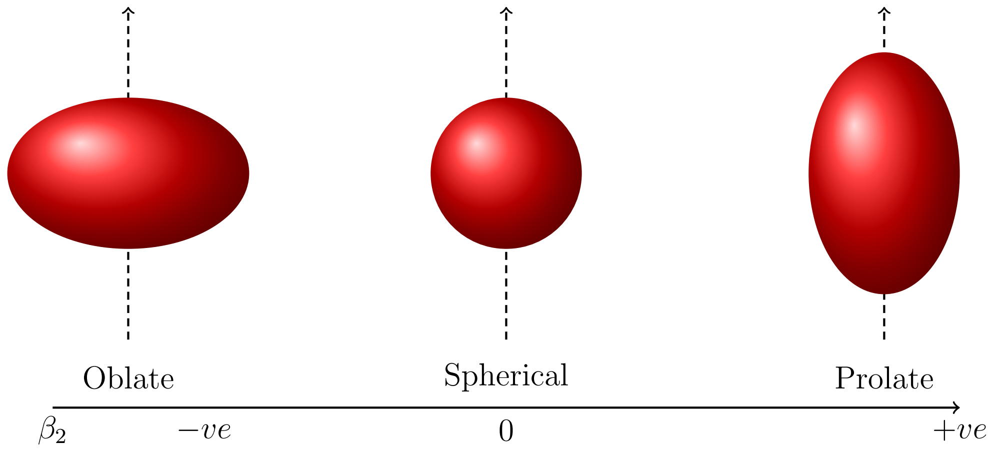

Figure 2.3: Representation of oblate, spherical, and prolate nuclear shapes. The parameter β_2 indicates the quadrupole deformation, with negative values representing oblate ('squashed') deformation, $\beta_2 = 0$ corresponding to a sphere, and positive values indicating prolate ('stretched') deformation. Dashed, black lines show the axis of symmetry for each spheroid

For both prolate and oblate deformation, the symmetry of the potential that led to the $2j + 1$ degeneracy for the spherical case is broken, with only two nucleons being able to occupy each state in this adapted model. Therefore, new quantum numbers are used to describe the states produced by the Nilsson model: the projection of the total angular momentum on the symmetry axis (Ω), the oscillator shell number, N, the number of oscillators aligned in the z direction, n_z, and the projection of the orbital angular momentum along the symmetry axis, Λ. These are usually written together, with the parity of the nucleus, π, in the format $\Omega^\pi[\mathrm{N}n_z\Lambda]$. When included on a Nilsson diagram, the parity is often dropped as this is indicated by the line style. These values are illustrated in Fig. 2.4 for a prolate nucleus.

The energy of a particular state determined using the Nilsson model depends on the magnitude, and relative orientation, to the nuclear deformation. The calculated energies for proton and neutron states are shown in Figs. 2.5 and 2.6, respectively, as a function of ϵ_2 which is related to β_2 through the relationship [20]

$$\epsilon_2 \approx 0.946\beta_2(1 - 0.1126\beta_2). \tag{2.11}$$

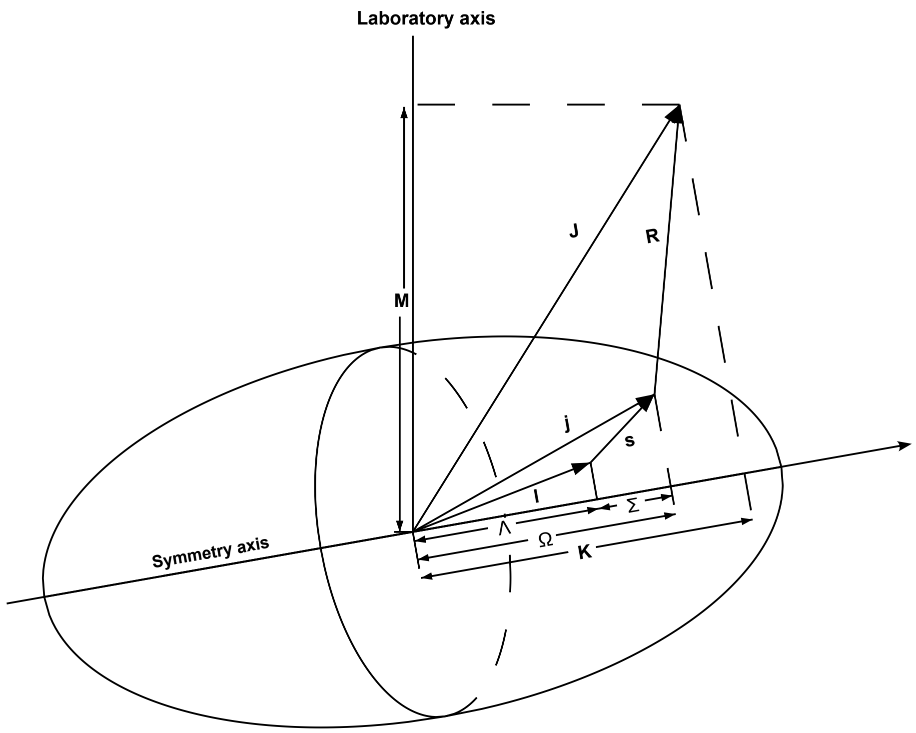

Figure 2.4: Plot illustrating the quantum numbers used in the Nilsson model of the nucleus. Figure adapted from Ref. [20].

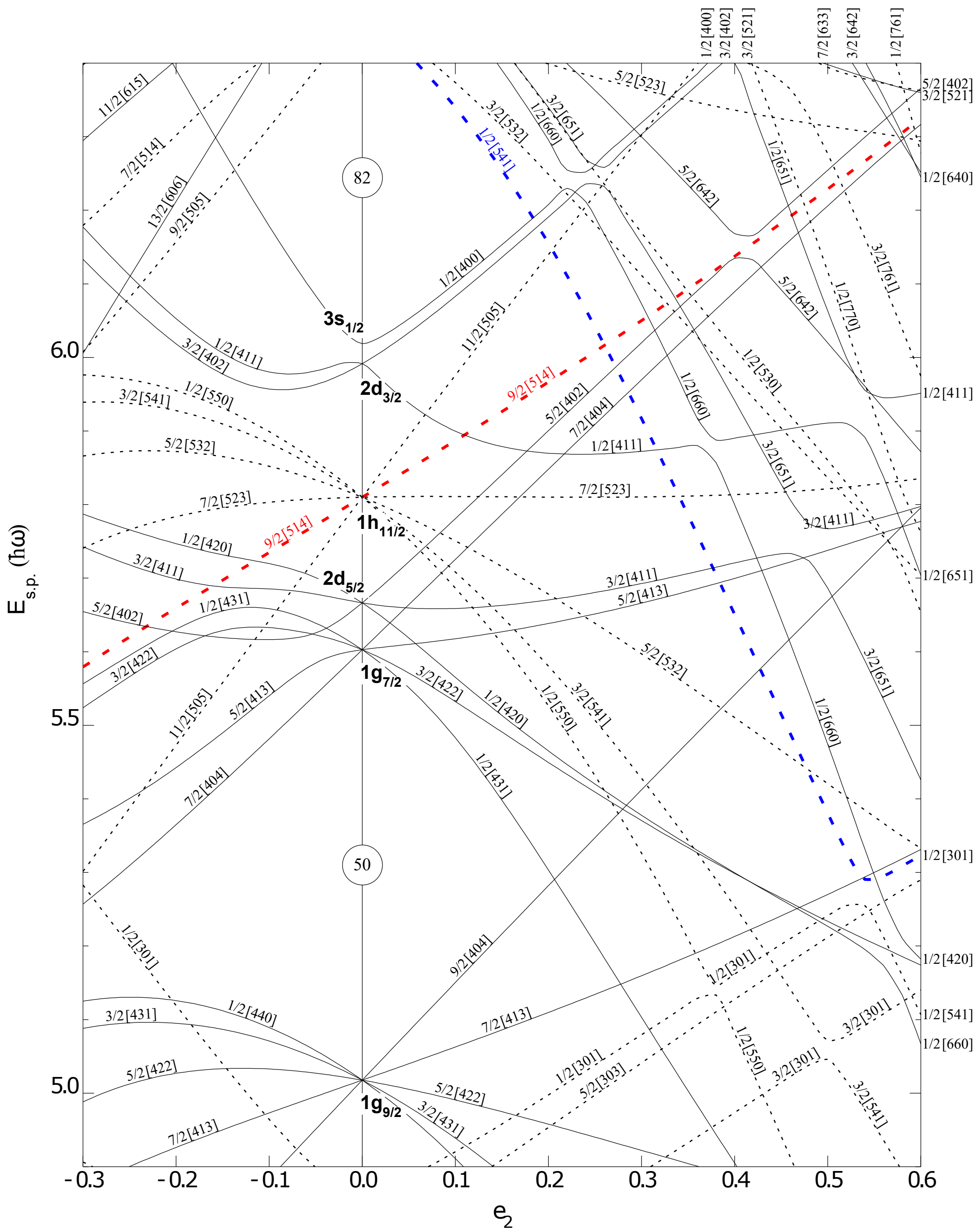

Figure 2.5: Example Nilsson diagram for protons with 50$\leq$ Z $\leq$82. Dashed lines are used to illustrate negative-parity states while solid lines are used for positive-parity states. The assignments proposed by Cubiss *et al.* in Ref. [1] for ^{178}Au^{g,m} are shown in blue and red, respectively. Note that the same colour coding is used throughout this thesis when properties of ^{178}Au^{g,m} are plotted together. Magneta is used instead to indicate equally applicability to each state, as in Fig. 2.6. Figure adapted from Ref. [20].

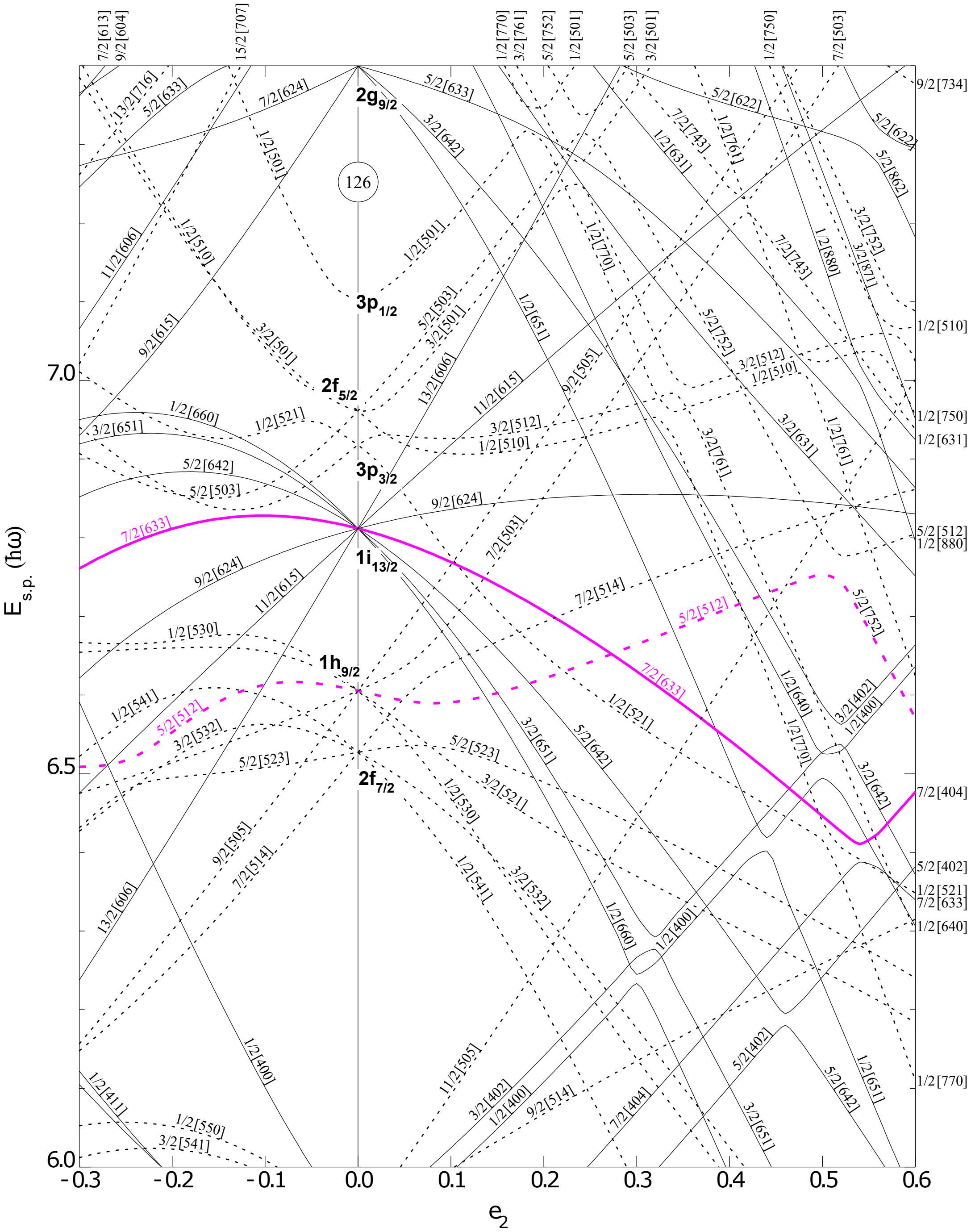

Figure 2.6: Example Nilsson diagram for neutrons with 82$\leq N \leq$126. Dashed lines are used to illustrate negative-parity states while solid lines are used for positive-parity states. The assignments proposed by Cubiss *et al.* in Ref. [1] for ^{178}Au^{g,m} are shown in magenta. Figure adapted from Ref. [20].

2.4 Excited nuclear states

There are several mechanisms by which a nucleus may be excited from its lowest-energy (ground) state to a more-energetic configuration. The most obvious of these, within the context of the spherical-shell and Nilsson models already discussed, is by exciting nucleons into higher-energy states. For even-even nuclei, the pairing interaction ensures that the ground state always has a total angular momentum and spin of $J^{\pi} = 0^{+}$. The properties of the ground and excited states in odd-mass nuclei, such as the spin and parity, are determined by the unpaired nucleon. For even-A nuclei, however, the total angular momentum is determined by the quantum angular momentum addition rule

$$|J_1 - J_2| \leq J \leq J_1 + J_2, \tag{2.12}$$

where, for odd-odd nuclei, the subscripts 1 and 2 represent the single-particle proton and neutron states and for even-even nuclei they correspond to the unpaired nucleons. In general, Eq. 2.12 has multiple solutions. The lowest-energy configuration is usually given by the one in which the intrinsic spin vectors are parallel, according to the Blatt-Biedenharn rule [30]. The total parity of a nucleus is given by the product of each of the individual nucleons' parities. The energies of excited states in even-even nuclei are typically significantly higher than in odd-odd cases because a relatively large amount of energy is required to overcome the pairing potential.

2.4.1 Rotational States

Another way to excite a nucleus is to introduce a collective rotation. This is only possible if the nucleus is deformed. The existence of such states was first proposed in Ref. [31] and developed further in Ref. [32] to explain the higher-than-expected E2-transition rates, compared to the Weisskopf estimates - see Sec. 3.3. Classically, the rotational energy of a rigid object with a moment of inertia $\mathcal{I}$ is $E = \frac{1}{2}\mathcal{I}\omega^2$, where ω is the angular velocity. The quantum mechanical equivalent of this can be calculated using the angular momentum operator

$$E = \frac{\hbar^2}{2\mathcal{I}} J(J+1), \tag{2.13}$$

where J ($\mathbf{J} = \mathbf{L} + \mathbf{S}$) is the quantised total angular momentum of the system. If the object in question is a uniform ellipsoid, the moment of inertia is given by

$$\mathcal{I}_{\mathcal{RR}} = \frac{2}{5} M R^2 (1 + 0.31\beta_2). \tag{2.14}$$

The evaluated [33] excitation energies of the rotational states in ^{164}Er are given in Table 2.1, along with the predicted values based on this rigid-rotor model.

Table 2.1: Comparison of the experimentally measured excitation energy for rotational states within ^{164}Er, E_{exp}, [33] with those determined with the rigid rotor model, E_{rr} . The absolute value of the difference between these energies, $|\Delta E|$, is also given. The moment of inertia was calculated based on the energy difference between the 0^+ and 2^+ states.

J	J(J+1)	E_{exp} [keV]	E_{rr} [keV]	$\|\Delta E\|$ [keV]
0	0	0	0	-
2	6	91.38	91.38	-
4	20	299.43	304.6	5.17
6	42	641.39	639.66	1.73
8	72	1024.62	1096.56	71.94
10	110	1518.08	1675.3	157.22

This rigid-rotor model gives remarkably good predictions for the excitation energy of the various states given in Table 2.1, given its simplicity. As J increases, however, the difference between the predicted state energies and those measured becomes increasingly large, primarily due to nucleus being somewhat fluid and not perfectly rigid. For an incompressible fluid within a rotating vessel, the moment of inertia is instead given by [25]

$$\mathcal{I}_{Fl} = \frac{9}{8\pi} M R^2 \beta. \tag{2.15}$$

The moment of inertia given in Eq. 2.15 is typically a significant underestimation with the true moment of inertia normally lying between it and the value predicted by Eq. 2.14, reflecting the nucleus' behaviour as being somewhere between the extremes of perfectly rigid and fluid.

2.5 Low-energy Shape Coexistence

It is well known that different arrangements of atoms within molecules often can lead to significantly different macroscopic properties. A clear example of this is to consider two of the distinct structures of pure carbon: graphite and diamond. While diamonds are extremely hard, transparent, and electrically insulating, graphite is made up of many layers of single-atom-thick graphene that are only weakly bound together and are good conductors of electricity. Similarly, nucleons may arrange themselves in multiple different configurations, with the respective energy minima competing to provide the ground-state configuration [9, 34, 35].

As shown in Fig. 2.7, this phenomenon, know as *low-energy shape coexistence*, has since been found in many different regions across the Segrè chart. It was first reported for the doubly magic ^{16}O, in which a rotational band built on a 6.06-MeV 0^+ state was found to coexist with the typical spherical-like structure built upon the ground state [6]. Quantum mechanics does not allow a sphere to rotate, leading Morinaga to conclude that this excited state must be deformed. This idea was explored further by Brown [36–38] who performed two-particle two-hole (2p-2h) and 4p-4h calculations that were able to explain the observed structure.

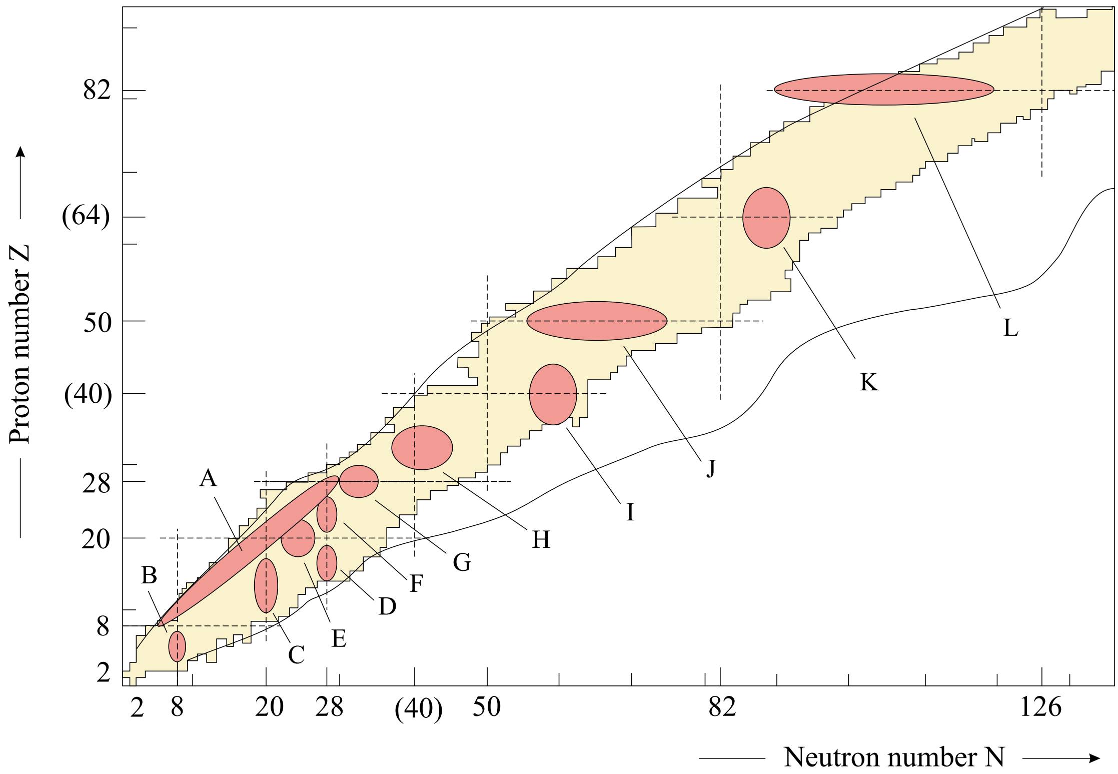

Figure 2.7: Chart of nuclides showing the regions in which shape coexistence has been found. Figure taken from Ref. [9].

This concept was later extended to other regions of the nuclear chart, including to the neutron-deficient isotopes near to the $Z = 82$ shell closure that are the subject of this thesis [39, 40]. A recent example of this is the case of ^{186}Pb, in which both prolate and oblate states have been observed within ≈650 keV of the spherical ground state [41, 42]. The excitation energy of a 2p-2h *intruder* state can be estimated by initially taking the difference in spherical-shell-model separation energies and applying three correction terms [9],

$$E_{\text{int}} = 2(\epsilon_{j_\pi} - \epsilon_{j'_\pi}) - \Delta E_{pair} + \Delta E_M + \Delta E_Q, \tag{2.16}$$

where ϵ_{j_π} is the proton-separation energy for state j^π, ΔE_{pair} is the pairing correction and $\Delta E_{M,Q}$ are the monopole and quadrupole interaction terms, respectively. The value of E_{int} is shown as a function of N in Fig. 2.8. The pairing potential is a result of the attractive force between nucleons in the same shell to form a 0^+ state. The gain in binding energy from this is independent of the neutron number, N, for a given element and reduces the excitation energy of such a state by ≈2 MeV in the vicinity of the $Z = 82$ shell closure. The monopole interaction term models the interaction between the protons and the partially filled neutron shell. It has been shown [39], that the strength of the quadrupole interaction can be modelled as

$$\Delta E_Q \simeq 4K_0\sqrt{\Omega_\pi - N_\pi}\sqrt{\Omega_\nu - N_\nu}N_\nu N_\pi, \tag{2.17}$$

where N_ρ and Ω_ρ are the valence nucleon number and degeneracy for $\rho = \pi, \nu$, respectively. The 2p-2h energy predicted by Eq. 2.16 is shown in Fig. 2.8, which demonstrates the dominance of the monopole and quadrupole terms in the region around N=104.

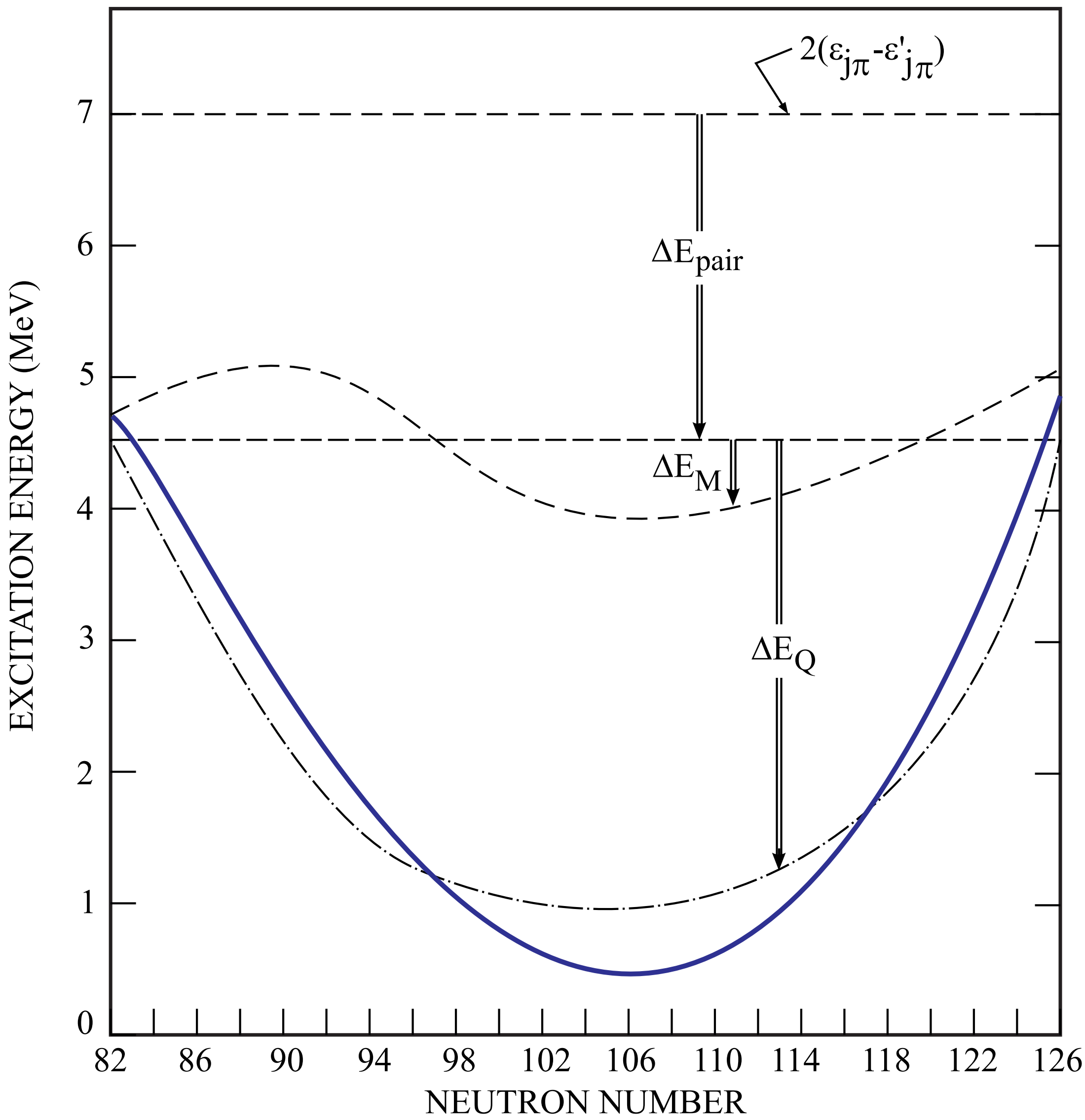

Figure 2.8: The contribution of the four energy terms given in Eq. 2.16 for a 2p-2h 0^+ intruder state. The total state energy is shown by the solid blue line. Figure taken from Ref. [9].

3 Theories of Radioactive Decay

Of the more than 3000 nuclides that have been experimentally identified, less than 10% are stable with the rest undergoing some form(s) of radioactive decay. The half lives, energies, and decay-modes available can vary significantly and provide a wealth of information on the underlying nuclear structure. A wide variety of different decay modes have been observed, as shown in Fig. 3.1. This chapter will explore the types of decay that were investigated in this thesis.

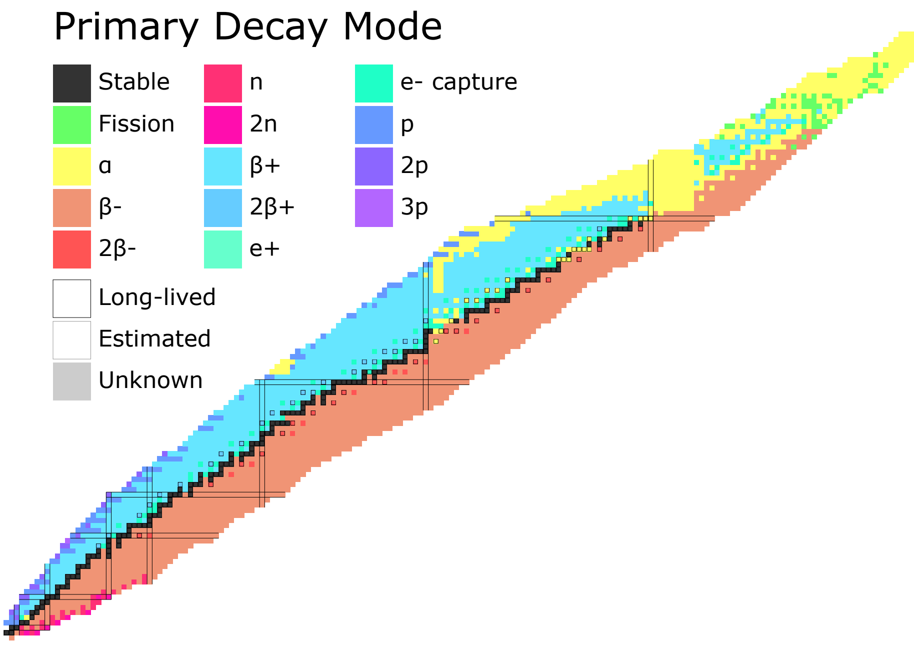

Figure 3.1: The Segrè chart with each nuclide colour coded by the primary decay mechanism. Black horizontal and vertical lines indicate major shell closures. Figure adapted from Ref. [43].

3.1 α decay

The competition between the attractive, short-range strong and the long-range electromagnetic forces can lead to the spontaneous emission of charged particles from sufficiently heavy nuclei. As Z increases, the Coulomb repulsion grows approximately with Z^2, while the strong nuclear force only grows with the number of nucleons, $A \underset{\sim}{\propto} Z$ [25]. Due to the double-magicity of the ^{4}He nucleus, it has a relatively large binding energy of

28.3 MeV [44]. This makes its emission energetically favourable for many nuclides over similar processes, such as proton emission (see, e.g. Refs. [45–47]) or spontaneous fission (see e.g. Refs. [48, 49]). The emission of a ^{4}He nucleus is called α decay with the α particles typically being ejected with between 5 and 10 MeV of kinetic energy.

Shortly after α decay was first discovered, the strong relationship shown in Fig. 3.2 [25] between the total energy available in an α decay, Q_α, and the lifetime of the parent was noted by Geiger and Nuttall.

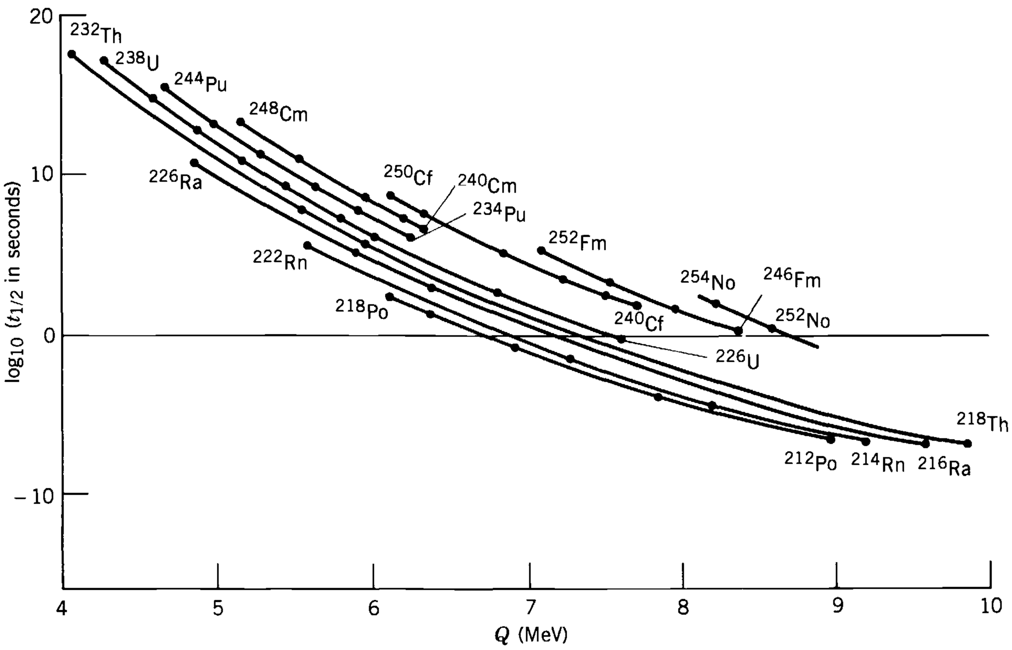

Figure 3.2: Geiger-Nuttall plot of the parent half life as a function of the total energy available for α decay for a selection of even-even nuclei. Figure taken from Ref. [25].

Geiger and Nuttall formulated a simple, empirical relationship between the α-particle energy, E_α, and the half life of the parent nucleus [50, 51]

$$\log(T_{1/2}) = \frac{A(Z)}{\sqrt{E_\alpha}} + B(Z), \tag{3.1}$$

where $A(Z)$ and $B(Z)$ are constants that depend on the atomic number of the parent nucleus, and the α-particle energy, E_α, is related to Q_α as

$$Q_\alpha = \left(1 + \frac{m_\alpha}{m_d}\right) E_\alpha, \tag{3.2}$$

where m_α and m_d are the masses of the α particle and daughter nucleus, respectively. The factor of m_α/m_d is necessary to account for the kinetic energy of the recoiling daughter nucleus.

The relationship given in Eq. 3.1 was successfully described, independently, by Gamow, and Gurney and Condon in 1928 [25]. In their model, the α particle is assumed to be pre-formed within a heavier nucleus and repeatedly colliding with a large potential barrier. Crucially, crossing this barrier is classically forbidden, meaning the α particle can only escape through quantum tunneling. Beyond a certain distance from the nuclear core (r >a) the potential is modelled solely by the repulsive Coulomb term, as shown in Fig. 3.3.

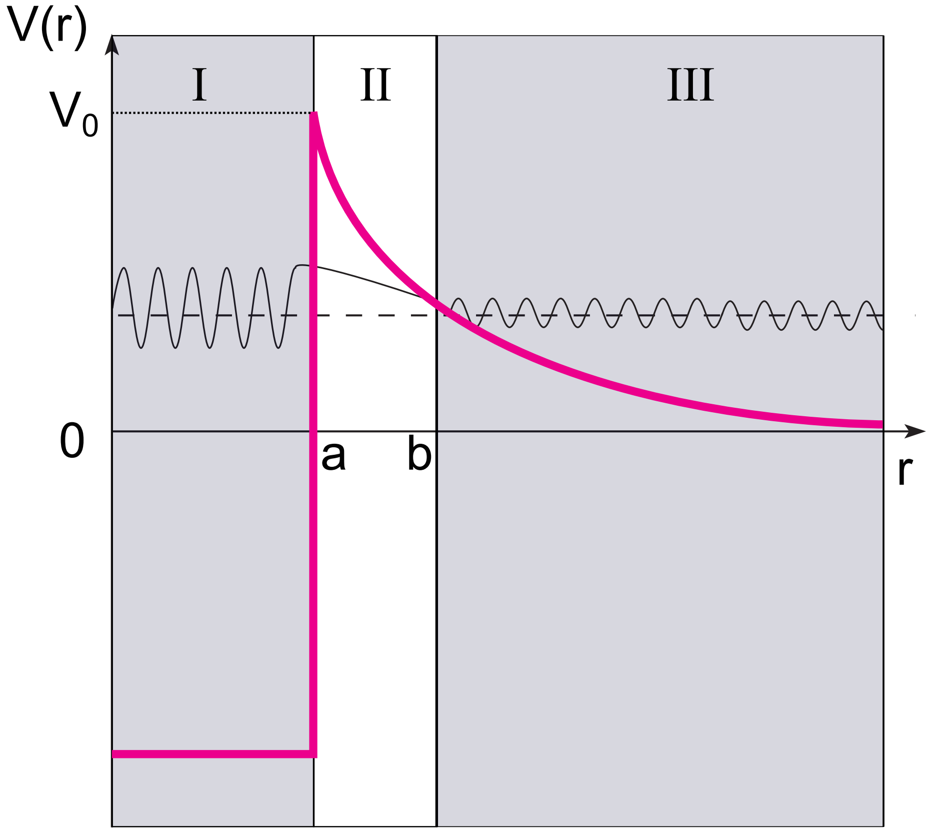

Figure 3.3: Sketch of the nuclear potential (magenta) and the resultant wavefunction of an α particle. Figure modified from Fig. 12.8(b) of Ref. [52].

The potential shown in Fig. 3.3 has three distinct regions: $r \leq$ a, a $< r \leq$ b, and $r >$ b. In regions I and III, the α particle has the sinusoidal, free-particle wavefunctions shown in Fig. 3.3. By modelling region II as a series of finite-height, rectangular square wells with the infinitesimal width dr, it can be shown that the probability of penetrating the full barrier is [25, 53],

$$P = \exp\left[-2\frac{zZ'e^2}{4\pi\epsilon_0}\sqrt{\frac{2m}{\hbar^2 Q}}\ \arccos\sqrt{x} - \sqrt{x(1-x)}\right], \tag{3.3}$$

where $x = a/b$, z and Z' are the proton numbers of the α particle and daughter nucleus, respectively, e is the elementary charge, m is the reduced mass, and ϵ_0 is the permittivity of free space. The probability given by Eq. 3.3 is the chance of the pre-formed α particle tunneling through the barrier into region III each time it reaches r=a. To determine the probability per unit time, this needs to be mulitplied by the number of barrier collisions per unit time. This can be estimated using the empirical nuclear radius formula given in Eq. 2.1 and the kinetic energy (and thus, the speed) of the α particle to predict the half life [25, 53]

$$t_{1/2} = \ln(2)\ \frac{a}{c}\sqrt{\frac{mc^2}{2(V_0+Q)}}\exp\left\{\frac{zZ'e^2}{2\pi\epsilon_0}\sqrt{\frac{2mc^2}{(\hbar c)^2 Q}}\left(\frac{\pi}{2} - 2\sqrt{x}\right)\right\}. \tag{3.4}$$

The half-life estimate given by Eq. 3.4 is known as the Gamow law and reproduces the experimentally observed trend in the measured half lives. Since this result was first published, many variations of this idea have been put forward, such as the one discussed in Sec. 6.2.1.

While the Gamow law for α decay is a good starting point for understanding the decay process, it does not take into account the impact of several key factors, such as a change of angular momentum or nuclear parity. To account for this, an additional *centrifugal barrier* term can be added to the potential. Since the α particle is a ^{4}He nucleus that is generally in its ground state, any difference in angular momentum between the parent and daughter nuclei must be compensated for by imparting orbital angular momentum, l_α on the α particle. This increases the height of the potential barrier through which the α particle has to tunnel by $l_\alpha(l_\alpha+1)\hbar^2/(2mr^2)$. Since the parity change during α decay depends only on the value of l_α $[\Delta\pi = (-1)^{l_\alpha}]$, conservation of parity can restrict the possible values of l_α.

Another aspect of this model that is perhaps unrealistic is the assumption that the α particle and daughter nucleus are preformed and remain distinct from one another until the α decay has occured. If the parent and daughter nuclei have significantly different structures, this assumption becomes particularly unrealistic. To account for this, the reduced α-decay width, δ_α^2 (also known as the *spectroscopic factor*), is used, which is defined as the overlap of the initial and final wavefunctions

$$\delta_\alpha^2 = |\langle\psi_p|\psi_d\cdot\varphi_\alpha\rangle|^2, \tag{3.5}$$

where the wavefunctions for the parent, daughter and α particle are ψ_p, ψ_d, and φ_α, respectively. Rasmussen introduced an experimental way to calculate the value of δ_α^2 [54, 55]

$$\delta_\alpha^2 = \frac{\lambda h}{P}, \tag{3.6}$$

where λ is the decay constant. It is often useful to compare experimentally determined δ_α^2 values for different decay paths (which have reduced α-decay widths of $\delta_{\alpha,i}^2$ for path i) which can give a direct insight into the difference between the parent and daughter wavefunctions. This can be done through the calculation of the α-decay hindrance factor, HF_α which is simply the ratio of each $\delta_{\alpha,i}^2$ value to that of an unhindered decay, $\delta_{\alpha,U}^2$.

$$HF_{\alpha,i} = \frac{\delta_{\alpha,U}^2}{\delta_{\alpha,i}^2}. \tag{3.7}$$

The larger the value of $HF_{\alpha,i}$, the greater the difference in structure or angular momentum between the parent and daughter states.

3.2 β decay

The term β decay can refer to three distinct but similar processes: β^+, β^- and electron-capture (EC) decay. In β^+ decay, a positron (e^+) is emitted by the nucleus as a proton is converted to a neutron while during β^- decay an electron (e^-) is emitted as a neutron is converted to a proton. The EC-decay process competes with β^+ decay in atoms; instead of emitting a positron, the nucleus 'captures' an atomic electron which combines with a proton to form a neutron and a neutrino. Unlike for α decay, the $e^\pm$ energy spectra for $\beta^\pm$ decay are continuous without distinct peaks corresponding to transitions to particular states.

This continuous distribution led Pauli to propose the existence of a new particle in 1931 that is also emitted in β decay, the neutrino (ν) [56]. This idea was formalised by Fermi in 1933 [57] although the neutrino was not discovered until 1956 [58], two years after Fermi's death. Therefore, the three equations defining the different types of β decay are:

$$\begin{aligned}
\beta^- :&\quad {}^A_Z X_N \rightarrow {}^A_{Z+1} Y_{N-1} + e^- + \bar{\nu}_e, \\
\beta^+ :&\quad {}^A_Z X_N \rightarrow {}^A_{Z-1} Y_{N+1} + e^+ + \nu_e, \\
\mathrm{EC} :&\quad {}^A_Z X_N + e^- \rightarrow {}^A_{Z-1} Y_{N+1} + \nu_e.
\end{aligned}$$

Because the electron and neutrino both have an intrinsic spin of 1/2, the total spin of the $e^\pm$ and ν can add up to 0 or 1. Such cases are called 'Fermi' and 'Gamow-Teller' β decay, respectively. If the difference in angular momentum between parent and daughter state is greater than 1, or they have different parities, the decay must proceed through a 'forbidden' transition. This term is something of a misnomer as it implies that such decays cannot occur. In reality, they can, although at a reduced rate compared to the $l = 0$ 'allowed' decays. Forbidden decays can be broken up into a number of different categories, as summarised in Table 3.1

Table 3.1: Summary of the change in total and orbital angular momentum and typical log ft values from different β-decay types [25].

Transition Type		l	s_β+s_ν	$\Delta\pi$	Typical log ft value
Allowed	Fermi	0	0	no	5.5±1.5
	Gamow-Teller	0	±1	no	
First-forbidden	Fermi	1	0	yes	7.5±1.5
	Gamow-Teller	1	±1	yes	
Second-forbidden	Fermi	2	0	no	~ 12
	Gamow-Teller	2	±1	no	
Third-forbidden	Fermi	3	0	yes	~ 16
	Gamow-Teller	3	±1	yes	

To understand the observed β-particle energy distribution, Fermi began by considering his golden rule for any quantum-mechanical transition rate, λ

$$\lambda = \frac{|V_{fi}|^2 \rho(E_f)}{h}, \tag{3.8}$$

where $\rho(E_f)$ is the density of final state and V_{fi} models the interaction potential between the initial and final states

$$V_{fi} \propto \int (\psi_f^* \varphi_e^* \varphi_\nu^*) O \psi_i dv, \tag{3.9}$$

where $\varphi_{e,\nu}$ and $\psi_{i,f}$ are the wavefunctions of the $e^\pm$, neutrino, and initial (parent) and final (daughter) nucleus, respectively. In the so-called 'allowed' approximation, the $e^\pm$ are given the wavefunctions of free particles which allows Eq. 3.8 to be expressed as

$$\lambda = \frac{g^2 |M_{fi}|^2}{2\pi^3 \hbar^7 c^3} \int_0^{p_{\max}} F(Z', p) p^2 (Q_\beta - T_e)^2 dp, \tag{3.10}$$

where $F(Z', p)$ is known as the Fermi function which models the Coulomb interaction, g is the weak-interaction coupling constant, Q_β is the β-decay Q value, and T_e is the kinetic energy of the electron/positron. This integral is usually replaced in Eq. 3.10 with the variable

$$f(Z', E_0) = \frac{1}{(m_e c)^3 (m_e c^2)^2} \int_0^{p_{\max}} F(Z', p) p^2 (E_0 - E_e)^2 dp. \tag{3.11}$$

Substituing this into Eq. 3.10 and converting the decay width, λ, to the half life, $t_{1/2}$, gives

$$f t_{1/2} = \frac{2\pi^3 \hbar^7 \ln(2)}{g^2 m_e^5 c^4 |M_{fi}|^2} \propto \frac{1}{|M_{fi}|^2}. \tag{3.12}$$

The values of $ft_{1/2}$ can vary by several orders of magnitude so it is typical for the base-10 logarithm to be taken. Since the value of log ft is dependent only on constants and the nuclear matrix element, $|M_{fi}|^2$, log ft values give a direct probe of the similarity of the parent and daughter nuclear structures. This is, in some ways, equivalent to the δ_α^2 values discussed in Sec. 3.1.

One significant difference between α and β decay is the sensitivity to the Q value. Since α particles must tunnel through a potential barrier, the decay rate to a particular state in the daughter nucleus depends exponentially on the α-particle energy. Conversely, β decay has a much lower dependence on the Q value (so long as the decay is energetic enough to produce the β particle in the first place), meaning that it can lead to significant population of high-energy states. This can complicate experimental investigations of β decay, since these states may depopulate through high-energy γ rays that are not efficiently detected by most detectors. This is known as 'Pandemonium' [59] and can mean that β-decay feeding is incorrectly assigned to a particular state.

3.3 γ decay

So far, two processes through which one nuclide can decay to another have been explored. Following either α or β decay, the daughter nucleus is not necessarily produced in its ground state. If this is the case, it is possible for the nucleus to de-excite through one of four processes: single or double γ-ray emission, internal conversion (IC), or internal pair production. Pair production is only energetically allowed for transition energies above $2m_ec^2 \approx$1.022 MeV. Double γ-ray emission is generally exceptionally rare so is also not relevant to this work [60, 61].

In single γ-ray emission, one photon is emitted during the de-excitation of the nucleus with energy

$$E_\gamma = E_i - (E_f + T), \tag{3.13}$$

where $E_{i,f}$ are the excitation energies of the initial and final states, respectively and T is the recoil energy. The value of T is generally neglible so this term is often dropped. Not only does γ decay reduce the energy of the nucleus but it can also cause a change in angular momentum, both from the photon's single unit of intrinsic spin and as orbital angular momentum, l. All γ rays can, in general, be classified as either electric or magnetic depending on if l is even or odd and if there is a change in the parity of the nucleus [25]

$$\text{Electric :}\Delta\pi = (-1)^l,$$
$$\text{Magnetic :}\Delta\pi = (-1)^{l+1}.$$

The value of l for a γ ray depends on the angular momenta of the initial (J_i) and final (J_f) states through the quantum mechanical angular momentum addition rules.

$$|J_i - J_f| \leq l \leq J_i + J_f \tag{3.14}$$

It is possible for multiple integer values to l to satisfy these selection rules; for example, a $3^+ \rightarrow 2^+$ transition can, in principle, proceed through a combination of M1, E2, M3, E4, M5 components. In reality, such a large number of components for γ decay is seldom considered as lower-l transitions tend to dominate over higher-l ones. Estimates for the lifetimes of states that can γ decay can be estimated using Fermi's Golden rule. The formulae obtained are known as Weisskopf estimates, which are given in Table 3.2.

In general, Weisskopf estimates do not predict lifetimes that reflect the experimentally measured values accurately. For E1 transitions, for example, the actual half lives are typically $\sim$10,000 times longer than predicted by Weisskopf estimates This is partly because they are built on the often unreasonable assumption of only a single particle change between the initial and final states which is rarely the case. It is also common for E2 transition rates to be enhanced relative to Weisskopf estimates, particularly when they correspond to the transitions between the various states in rotational bands.

3.4 Internal Conversion

In γ decay, a nucleus de-excites through the emission of a photon. For internal conversion (IC) decay, however, the nucleus interacts electromagnetically with atomic electrons. In doing so, the electron is given sufficient energy to escape the atom. Assuming the atomic recoil is small, the energy of a conversion electron (CE) emitted is

$$E_{CE} = E_\gamma - b_e(K, L, M \ldots), \tag{3.15}$$

Table 3.2: Table summarising the Weisskopf half-life estimate formulae for various multipolarity γ rays where the energy, E_γ, is given in keV [25].

	Multipolarity		Weisskopf Estimate formula	
ΔL	$\Delta\pi$ = yes	$\Delta\pi$ = no	$t_{1/2}(\mathrm{E})$ $[s]$	$t_{1/2}(\mathrm{M})$ $[s]$
1	E1	M1	$\frac{6.76 \times 10^{-6}}{E_\gamma^3 A^{2/3}}$	$\frac{2.20 \times 10^{-5}}{E_\gamma^3}$
2	M2	E2	$\frac{9.52 \times 10^{6}}{E_\gamma^5 A^{4/3}}$	$\frac{3.10 \times 10^{7}}{E_\gamma^5 A^{2/3}}$
3	E3	M3	$\frac{2.04 \times 10^{19}}{E_\gamma^7 A^{2}}$	$\frac{6.66 \times 10^{19}}{E_\gamma^7 A^{4/3}}$
4	M4	E4	$\frac{6.50 \times 10^{31}}{E_\gamma^9 A^{8/3}}$	$\frac{2.12 \times 10^{32}}{E_\gamma^9 A^{2}}$

where $b_e(K, L, M \ldots)$ is the binding energy of the electron in the K, L, M... orbital. The value of b_e depends on Z and the electronic state from which the CE is being removed; as E_γ increases, IC of more tightly bound electrons becomes possible. Since γ-ray emission and IC are generally in competition, it is useful to define the internal conversion coefficient (ICC)

$$\alpha_{tot/K/L/M} = \frac{N_{ICtot/K/L/M}}{N_\gamma}. \tag{3.16}$$

The value of α depends strongly on Z, the electron shell involved, the transition energy and multipolarity, as shown in Fig. 3.4.

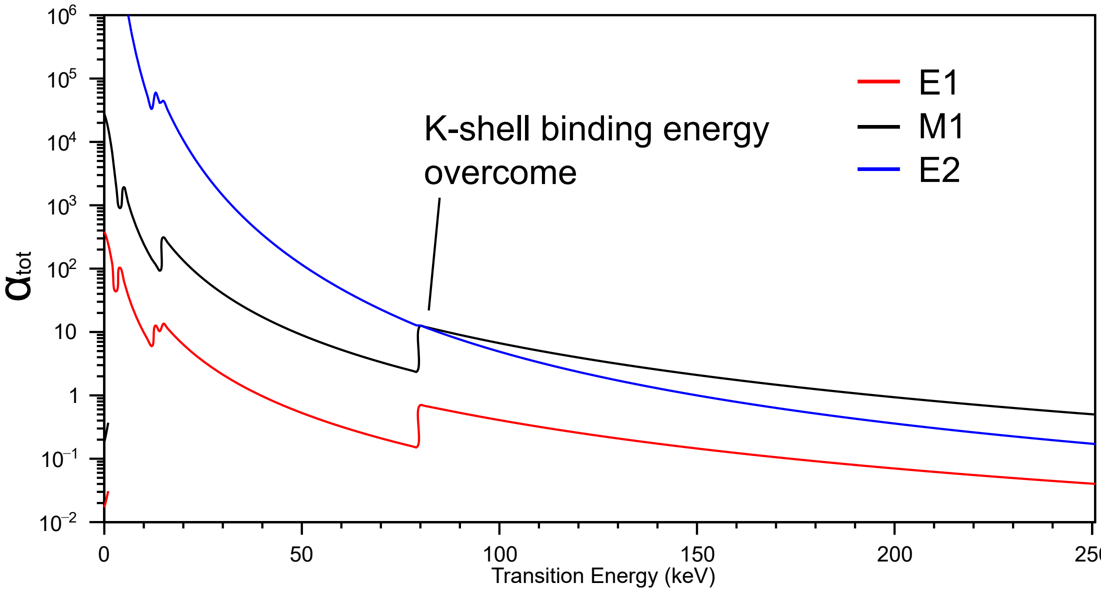

Figure 3.4: Plots of the total conversion coefficient as a function of the transition energy for platinum for E1 (red), M1 (black) and E2 (blue) transitions. The values of α_{tot} were calculated at 1-keV intervals using BrIcc [62].

Table 3.3: Summary of the electron Siegbahn notation for characteristic x-ray transitions and the corresponding electron energy levels. Adapted from Ref. [20].

Classical designation (Siegbahn notation)	Associated initial - final shell vacancies
K_{α_1}	K - L_3
K_{α_2}	K - L_2
K_{α_3}	K - L_1
K_{β_1}	K - M_3
K_{β_2}	K - N_2N_3
K_{β_3}	K - M_2
K_{β_4}	K - N_4N_5
K_{β_5}	K - M_4M_5
$KO_{2,3}$	K - O_2O_3
$KP_{2,3}$	K - P_2P_3
L_{α_1}	L_3 - M_5
L_{α_2}	L_3 - M_4
L_{β_1}	L_2 - M_4
$L_{\beta_{2,15}}$	L_3 - N_4N_5
L_{β}	L_1 - M_3

After an IC transition occurs, the vacant electron state is quickly filled by a higher-energy electron causing the emission of a characteristic x ray. Since the energy of these x rays is determined by Z, the measurement of them (particularly K x rays) provides a powerful tool in decay spectroscopy to determine the element in which an IC transition occured - see Fig. 3.5. The specific atomic transitions corresponding to each x ray are often presented in terms of Siegbahn notation which is summarised in Table. 3.3.

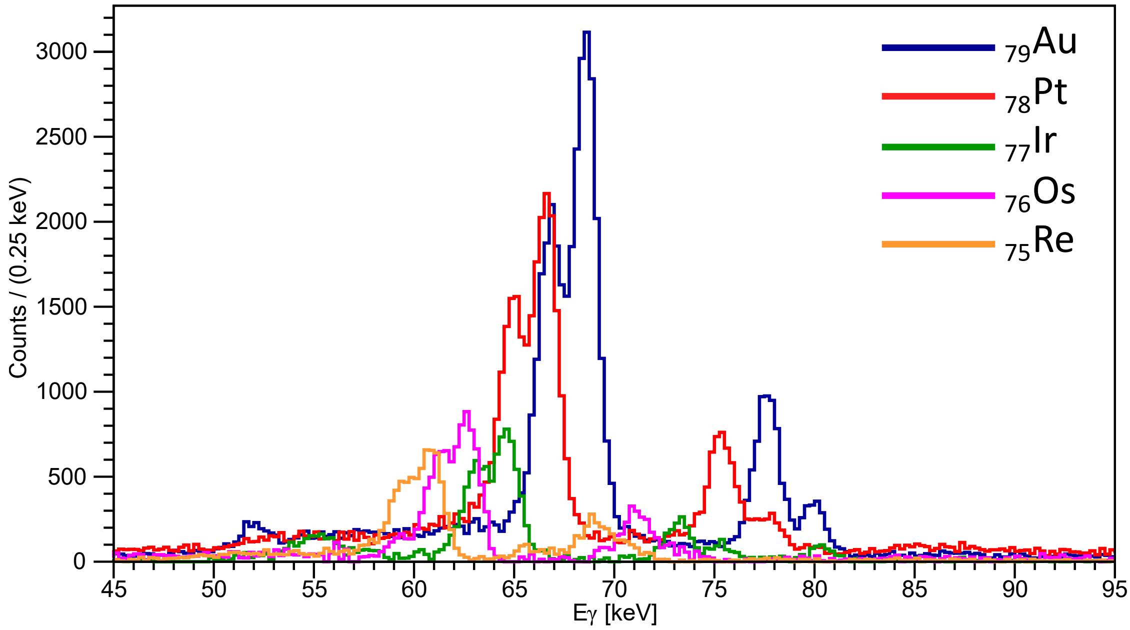

Figure 3.5: The K x-ray energy spectra produced by gating on γ-ray tranistions within each of the elements from gold to rhenium. Each individual spectrum is a background subtracted projection of the prompt γ-γ coincidence matrix gated on a well-known γ ray in the appropriate element. These spectra were produced as part of the analysis presented in Chapter 6.

Because the photon has an intrinsic angular momentum of $1\hbar$, γ-ray emission cannot facilitate transitions between two $J = 0$ states [63]. For such transitions, IC (in addition to double γ-ray emission and internal pair production) can still occur without violatng the conservation of angular momentum. Low-energy E0 transitions between 0^+ states have become of particular interest recently as they correspond directly to a change in the nuclear shape [9, 63, 64]. A strong E0-transition strength is considered to be a clear indication of nuclear shape coexistence.

In general, the largest E0 components occur in strongly mixed configurations of states with significantly different mean-square charge radii. Assuming the mixing of two configurations with amplitudes of α and $\beta = \sqrt{1-\alpha^2}$, it can be shown that the E0-transition strength, $\rho^2(E0)$ is [63]

$$\rho^2 = \frac{Z^2}{R^4}\alpha^2\beta^2(\Delta\langle r^2\rangle)^2. \tag{3.17}$$

Thus, the E0-transition strength can provide a direct way to calculate the difference in mean square charge radius, $\Delta\langle r^2\rangle$.

4 Experimental Method

4.1 Radiation Detection

Since radioactivity was first discoverd by Wilhelm Röntgen in 1895 [65], many new techniques and technologies have been developed to measure its properties. The first radiation detectors used were photographic plates that could be used to detect x rays. The needs of both the research and industrial communities since then have led to the development of many categories of detectors.

As discussed in Chapter 3, the energy released in radioactive decay can offer key insights into nuclear structure, especially when combined with other information such as lifetimes or branching ratios. To measure these characteristics of radiation, the one of the most popular types of detector employ semiconductor crystals, which are described below.

4.1.1 Semiconductor Detectors

The lattice structures of large crystals produce energy bands for the electrons within the solid. In general, these bands can be classified as either 'conduction' or 'valence', depending on whether the electrons are bound to a specific lattice site or not. For an insulator, the energy difference between these bands (or, 'band gap') is typically E_g >5 eV while, for conductors, these two bands can overlap. Semiconductors, however, have a bandgap that is typically $\approx$ 1 eV. When an electron is excited across the bandgap, it is said to leave a 'hole' behind that can be filled by another conduction-band electron. Both electrons and holes can move through the crystal, either via diffusion or under the influence of an electric field. Holes can move through the crystal like a positively charged particle because, when an electron fills a hole at one lattice site, it does so by producing a new one in a neighbouring position.

As radiation passes through a semiconductor crystal, some of the energy deposited produces electron-hole pairs. The number of electron-hole pairs produced is proportional to the energy lost in the crystal up to some limit, typically tens of MeV. Given the average energy required to produce an electron-hole pairs in semiconductors is $\approx$3 eV per pair, ionising radiation will produce $\approx$100,000 electron-hole pairs for every 300 keV deposited in the crystal. Creating a large number of electron-hole pairs is useful as the statistical limit of the final energy resolution of a detector is proportional to the square root of the number of charge carriers.

If a voltage is applied across the semiconductor crystal, the liberated charge can be efficiently transported to electrodes connected to external circuitry. The amount of charge collected can be used to determine the amount of energy deposited in the active volume of the detector. For an intrinsic semiconductor, a sufficiently high voltage would lead to a leakage current far too large to measure the relatively small number of electron-hole pairs created by incident radiation.

The usual solution to this problem is to form the semiconductor into a diode. The most common semiconductors used in radiation detectors, germanium and silicon, are both tetravalent, group IV elements that can be doped by adding small quantities of the group III and group V elements either side of them in the periodic table (aluminium and phosphorus, for silicon; gallium and arsenic for germanium). When a small amount of the corresponding group V element is added to a monatomic crystal, it forms four covalent bonds with the surrounding atoms in the crystal but has one valent electron that is 'left over'. This electron can easily be excited into the conduction band and move through the crystal, forming an 'n-type semiconductor', since it donates a net of negative charge carriers to the conduction band. Conversely, adding a small amount of a group III element adds atoms to lattice sites that require an additional electron from the conduction band to make four bonds so effectively contributes an extra 'hole' to the lattice. Since the hole behaves in many ways like a positive particle, such a crystal is known as a 'p-type semiconductor'.

When placed together, the excess free charge in n- and p-type semiconductors will diffuse across the boundary. As they do so, the net charge imbalance produces a potential difference that opposes the diffusion, until an equilibrium is reached. This device is known as a PN junction diode but other forms, such as a PIN, with a region of intrinsic semiconductor between the p-doped and n-doped regions are also commonly used. A PIN-type detector typically has relatively small p- and n-doped regions compared to the intrinsic semiconductor region. Dopant atoms act as recombination sites which increase the variation in the number of charge carriers collected. Therefore, removing the dopant atoms from most of the detector crystal reduces the number of recombination sites and improves the energy resolution of the detector.

If a small voltage is applied to the diode in the 'forward direction', a relatively large current can flow through the diode. If, however, the diode is 'reverse' biased, it will instead increase the size of the depletion layer, until the depletion region is nearly the size of the entire crystal. This is ideal because the depletion region forms the active part of the detector crystal. At higher reverse-bias voltages, the crystal will 'break down' and a large current will flow, as illustrated in Fig. 4.1.

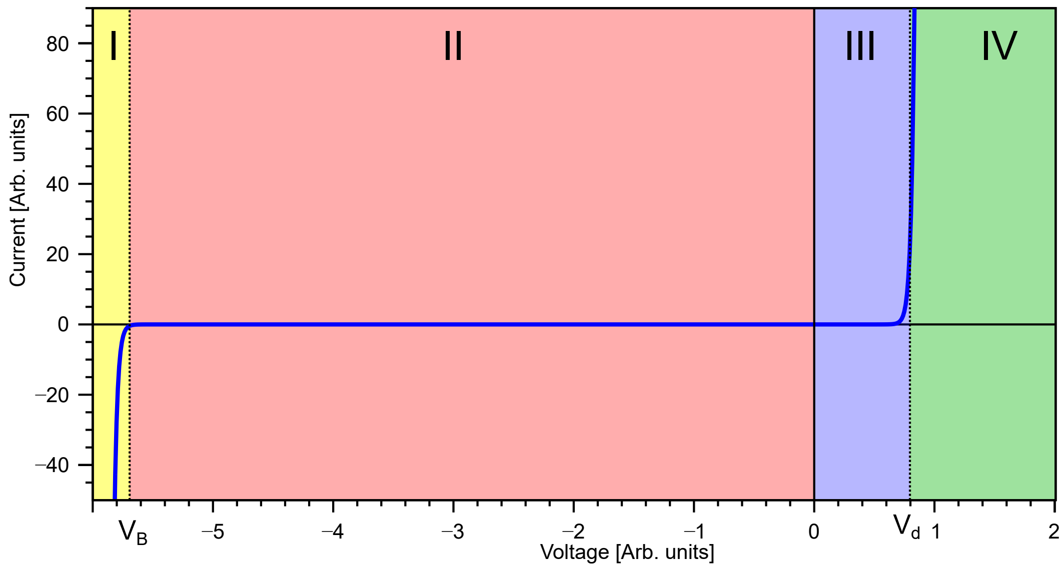

Figure 4.1: Sketch of the voltage versus current curve for a typical diode. The four regions correspond to: I - Below the breakdown voltage, V_B, a large current may flow 'backwards'. II: Reverse bias region - in this region, the bias voltage may be increased significantly without much current flowing. III: for small forward biases below the saturation voltage, V_d, only a very small current will flow. IV: above the saturation voltage, V_d, a large current may flow through the diode in the 'forward' direction.

This is because, during the reverse biasing, charge is removed which cannot easily be replenished due to the diode's resistance to electrical charge carriers flowing back into the detector. Therefore, a diode can be reverse biased to a very high voltage, providing the strong electric field throughout the crystal required to collect induced charges efficiently without producing a high leakage current. For a typical germanium crystal used in a radiation detector, several kV of bias may be applied producing a leakage current of less than 1 nA.

A key performance characteristic of a detector is its energy resolution. If it is assumed that the probability for a particular charge carrier being produced and collected follows a Poissonian distribution, the uncertainty in the recorded energy ΔE will follow:

$$\Delta E \propto \sqrt{N}, \tag{4.1}$$

where N is the number of charge carriers collected. In reality, the Poissonian assumption does not hold and the measured resolution of detectors is generally better than this. Fundamentally, this is because electron excitations are not independent of one another as assumed for a Poissonian distribution. To account for this, the Fano factor, F, is introduced [66]:

$$F = \frac{\sigma^2_{Q\ meas}}{\sigma^2_{Q\ stat}}. \tag{4.2}$$

From this, it can be shown that the crystal used places a lower limit on the final uncertainty in the energy measured, $\sigma_{E\ meas}$ is

$$\sigma_{E\ meas} \geq \sqrt{F(X)\mathcal{E}(X)E}, \tag{4.3}$$

where X is a material, $\mathcal{E}$ is the average energy required to produce an electron-hole pair and E is the energy deposited in the detector. It is usual to express the resolution as a Full Width at Half Maximum (FWHM), rather than as a standard deviation. This conversion is trivial for Gaussian limit of the Poisson distribution:

$$\Delta E \geq 2\sqrt{2\ \ln(2)}\sqrt{F(X)\mathcal{E}(X)E}. \tag{4.4}$$

It is clear from Eq. 4.4 that the choice of material for a semiconductor detector is crucial for obtaining the best possible energy resolution. Ideally, the product of the Fano factor and the energy required to produce an electron-hole pair would be minimal.

High Purity Germanium detectors

One of the most common choices for a detector that is in widespread use is High Purity Germanium (HPGe) detectors. The term 'high purity' is something of an understatement as the purity of the crystals produced is the highest of any macroscopic subtance commercially produced [67]. Impurities in these detectors are typically of the order 1 part per 10^{12} [68], several orders of magnitude below what is typical for the semiconductors used in computer chips. Reducing the impurities to such low levels is crucial for optimum performance, as impurities can act as recombination sites for electron-hole pairs. One of the main advantages of HPGe is that it has a small bandgap so many electron-hole pairs can be produced per unit of energy deposited. The small band gap does, however, mean that enough electron-hole pairs will be created by thermal excitation to dominate the signal produced by incident radiation at normal ambient temperatures. The probability per unit time of thermal excitation of an electron from the valence to the conduction band is [67]

$$p_x(T) \propto T^{3/2} \exp\left(- \frac{E_g}{2k_B T}\right), \tag{4.5}$$

where T is the absolute temperature and k_B is Boltzman's constant. From Eq. 4.5, it is clear that a reduction in the number of thermally excited electrons can be reduced significantly through a reduction of the absolute temperature of the crystal. Therefore, HPGe detectors are cooled with liquid nitrogen from an ambient temperature of $\approx$300 K to $\approx$100 K. Doing so reduces the number of thermally excited electron-hole pairs by $\approx$13 orders of magnitude.

The cryogenic equipment takes up space within the detector volume near to the germanium crystals, especially the cold finger which keeps the detector cold. To reduce the impact of this, four HPGe crystals can be placed around a single cold finger to form a HPGe 'clover' detector, so called because it has a cross-section similar to a four-leaf clover [69]. To keep the crystals cold, the inside of the detector is kept under a high vacuum during operation of $\sim 10^{-6}$ mBarr. This has the added benefit of keeping the crystals free of contamination from the atmosphere.

The casing that maintains this vacuum will absorb heavy charged particles (α particles typically have a range in aluminium of $\lesssim$100 μm), and low-energy x rays and γ rays. Sometimes, HPGe detector casings have a front face made of a thin carbon or beryllium foil to reduce the attenuation of these low-energy photons.

Silicon Detectors

It has already been shown how sensitive p_x is to small changes in the ratio $E_g/(2\ k_BT)$. The bandgap for silicon is slightly larger than for germanium E_g(Si) = 1.16 eV vs E_g(Ge) = 0.72 eV, at 77K [66, 70], but this is sufficient for most silicon detectors not to require cryogenic cooling to produce usable signals. They, therefore, can be placed directly inside a vacuum chamber without anything that would block heavy charged particle from a source or implantation spot, making them ideal for α-particle spectroscopy. Since the γ-ray absorption probability scales approximately with $Z^{4.5}$, silicon ($Z = 14$) has a substantially lower probability of detecting γ rays than germanium ($Z = 32$). Given the relatively short range of α particles in silicon (typically tens of μm), silicon detectors used for α-particle spectroscopy are typically up to a few hundred μm thick which also substantially lowers the probability of γ-ray absorption.

Regardless of the type of semiconductor detector used, the output signal from it is in the form of a small charge pulse that is then processed with electronics, such as a preamplifier, which is described in Sec. 4.1.2. Often, preamplifier modules are built in to the casing of HPGe detectors but not for the much smaller silicon detectors commonly used, which usually operate under vacuum. The final signal produced by such a preamplifier for HPGe clover detectors is shown in Fig. 4.2.

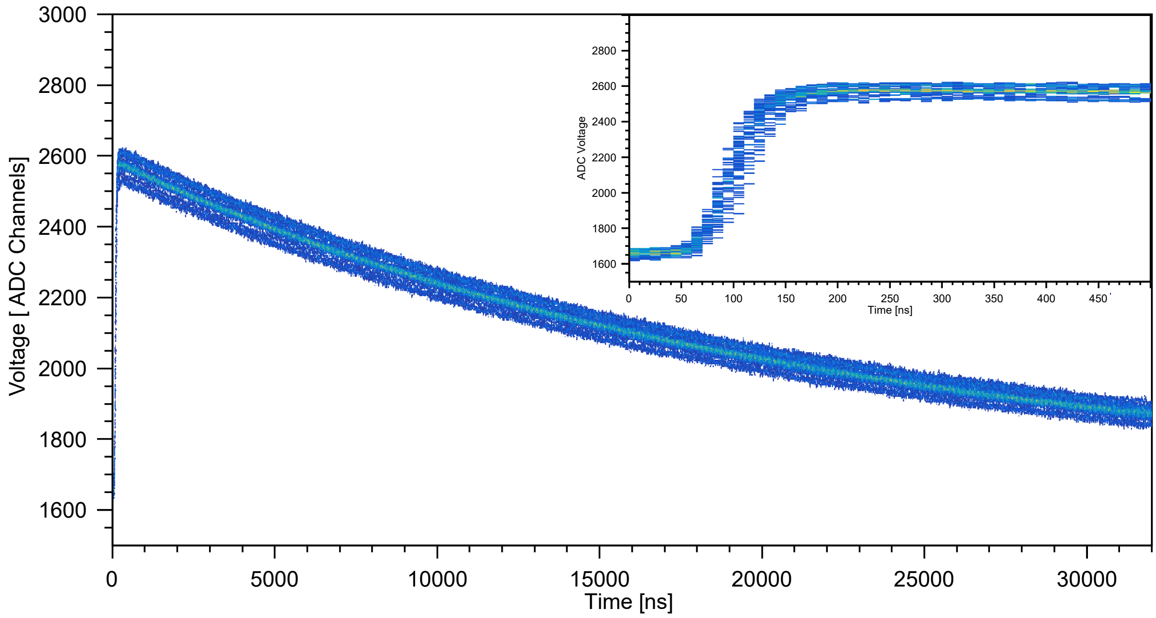

Figure 4.2: Plot of the traces gathered from ambient background corresponding to the 511-keV annihilation peak collected using two HPGe clover detectors. The voltage was sampled at 100 MHz and stored as a series of 14-bit unsigned integers. The inset shows the first 500 ns to illustrate the rise of the signal.

4.1.2 Signal Amplification

So far, the operating principles for two categories of detectors have been discussed. In both cases, the output from the detector is a small charge pulse that is collected, either directly from the active portion of the crystal or from a PMT/SiPM. The role of preamplifiers has already been alluded to, in particular in converting a short pulse to the signal shapes shown in Fig. 4.2.

The size of the signals produced by these detectors is typically far too small to be practically measurable in either digital or analogue electronics[1]. It is therefore necessary to amplify the signal further. This is usually done with a charge-sensitive preamplifier, which also shapes the signal to a form that can be processed with trapezoidal and CFD filters, as described in Secs. 4.1.3 and 4.1.4.

A simplified circuit diagram for the charge-sensitive preamplifier is shown in Fig. 4.3. The capacitor C_b acts to block the large bias voltage for the detector passing through the preamplifier as charge will quickly build up on this capacitor until it provides a voltage that is equal and opposite to that of the bias supply.

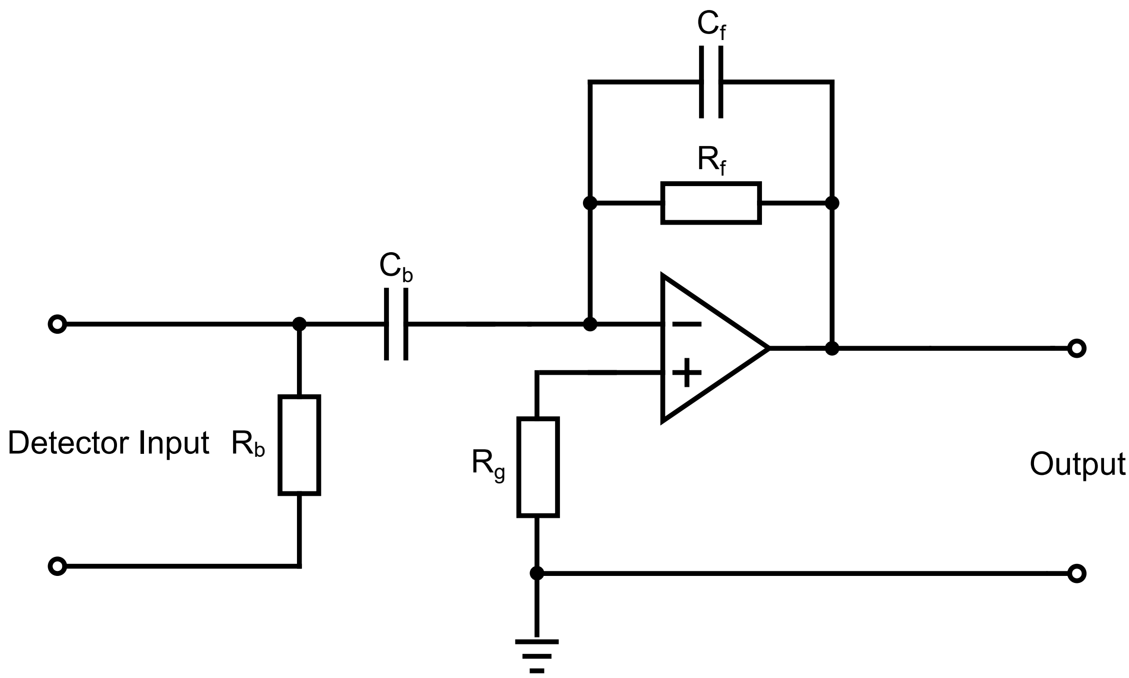

Figure 4.3: Circuit diagram of a charge-sensitive preamplifier of the type common in nuclear spectroscopy detectors.

The amplification in the preamplifier shown in Fig. 4.3 is performed by the operational amplifier (OP AMP), represented in the circuit diagram by the triangle with two inputs. An OP AMP is a very common electronic component designed to prevent any current flowing between the two terminals, even if an external voltage is applied. To do this, the OP AMP is configured to provide an output voltage that counters the input. The input

[1]For a 300-keV γ ray being absorbed in a HPGe detector, the 100,000 electrons that would ideally be collected at the anode have a total charge of $|Q|$=16 fC. If collected over 50 ns, the average current would be 0.3 μA.

impedance of the two pins is configured to be very large compared to any of the resistors in the circuit, so current can only flow through the resistor R_f, and not through the OP AMP itself. By considering the voltage drop across the resistors R_f and R_g, it can be shown that the output voltage of the operational amplifier must be

$$V_{out} = V_{in} \cdot \left(1 + \frac{R_f}{R_g}\right) \equiv A \cdot V_{in} \tag{4.6}$$

to prevent a current flowing between the pins, where A is the amplification factor. In the case of the circuit shown in Fig. 4.3, the value of V_{in} is not constant with time. When radiation deposits energy in a detector, the liberated charge will be deposited onto C_b. This will draw an equal amount of charge from the capacitor C_f which will then discharge through the resistor R_f. Therefore, the voltage output over time is given by the RC-circuit equation

$$V(t) = V_0 \exp\left(-\frac{t}{R_f C_f}\right). \tag{4.7}$$

It is the RC circuit within the preamp that is responsible for the exponential decay of the voltage in the traces shown in Fig. 4.2. The exponential rise of the signal output is a consequence of the finite time taken to collect the total amount of charge onto the capacitor C_f. Once this signal is obtained, it can be amplified further or, if it is large enough, sent directly to a Data AcQuisition system (DAQ). Two of the key types of process performed on the preamplified signal are described in Secs. 4.1.3 and 4.1.4.

4.1.3 Trapezoidal Filter

The preamplified signals from a semiconductor or scintillator detector have a rapid increase in the voltage as charge is collected followed by an exponential drop back to the baseline. The 'height' of this signal is proportional to the energy deposited in the system but determining this directly is not trivial. One potential method would be to use the difference between the voltage sampled just before the radiation is detected (to find a baseline) and the peak voltage measured. This method has several main flaws: it assumes instantaneous collection of all charge, it requires a very high sample rate to be implemented digitally, and is susceptible to electric noise and pileup.

All of these problems can be resolved using a filter, most commonly a trapezoidal filter. In general, an unweighted trapezoid filter can be used for any kind of 'step-like' function and has the form [67, 71]

$$S(n) = \sum_{i=n-k}^{n} V_i - \sum_{i=n-l-k}^{n-l} V_i, \tag{4.8}$$

where V_i are the digitised voltages, k integration window and l is a delay[2]. The filter output from Eq. 4.8 is proportional to the difference of the average signal voltage measured before and after the radiation was detected. This eliminates much of the uncertainty caused by the presense of electrical noise, which typically follows a symmetric Gaussian distribution, and removes much of the impact of the finite charge collection time.

[2]The form of the trapezoidal filter given in Eq. 4.8 is a discretised form. A continuous version used in analogue electronics is also available but was not used in this work and follows the same pricniples as ths discrete version.

The exponential decay of the voltage through the RC circuit remains an issue for this filter, but this can easily be rectified if the decay time of the signal is known. Applying this correction and Eq. 4.8 to the average of the traces[3] shown in Fig. 4.2 gives the trapezoid filter shown in Fig. 4.4.

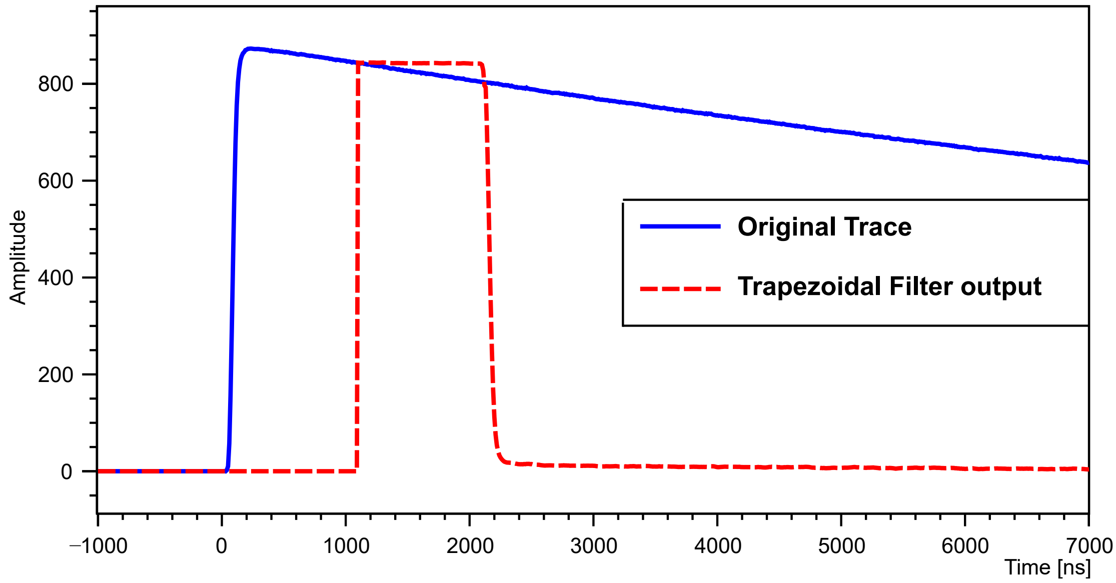

Figure 4.4: The average of the traces shown in Fig. 4.2 before (blue) and after (red) a trapezoidal filter is applied. The exponential decay of the signal from the RC circuit in the preamplifier is corrected for in the green curve to give a trapezoid shape.

A key consideration when using a trapezoidal filter is the number of samples to use (the value of k in Eq. 4.8). A larger value will reduce the impact of electrical noise on the result but is more susceptible to pielup events, where multiple events combine and artificially increase the measured energy. For this reason, the Pixie-16 DAQ used to collect the data presented in Chapter 6 employs two such filters. One filter uses a smaller range to detect pileup while the second uses a larger range to determine the energies more reliably.

The trapezoidal filter is implemented digitally in Field Programmable Gate Arrays (FPGAs) in the Pixie-16 DAQ [71]. Therefore, converting the filtered trapezoid to obtain an energy value can be done trivially. In Pixie-16 systems, the uncalibrated energy is taken as a single digitised value of the trapezoid at a time after the trigger. This time is determined using the user-given rise- and decay-times of the signal in such a way that guarantees the sample is taken during the flattop of the trapezoid. Different types of Pixie-16 modules will write this energy as a 12-, 14-, or 16-bit number to disk - see Ref. [71] for more information.

[3]This average was calculated by taking the average voltage value measured at each time value for all traces recorded.

4.1.4 Constant Fraction Discrimination

Along with the energy and particle type, a reliable measurement of ‘when’ radiation was detected provides crucial information. The analysis presented in Chapter 6 relies heavily on coincidences which require an accurate determination of the relative times of detection of radiation. The signals produced by the detectors have, in general, the shapes shown in Fig. 4.2.

The most obvious way to determine the time of an event is to record the time at which the voltage measured crosses some threshold value. While simple to implement, this method is not without its drawbacks, most notably the introduction of a ‘timewalk’. If two signals arrive simultaneously, but one is substantially larger in amplitude than the other, the exponential growth in voltage over time will result in the smaller signal being detected later.

One way reduce this problem is by using the Constant Fraction Discrimination (CFD) algorithm. As the name suggests, instead of waiting for the trace to reach a fixed threshold, CFD takes the time of arrival by determining when a constant fraction of the peak is reached. The signal is split into two and one part is delayed, inverted, and scaled relative to the other. Therefore, the voltage at sample i, V_i is

$$V_i = V_i - s \cdot V_{i-d}, \tag{4.9}$$

where s is the scale factor and d is the delay in samples. This is illustrated for the averaged trace shown in Fig. 4.2 in Fig. 4.5

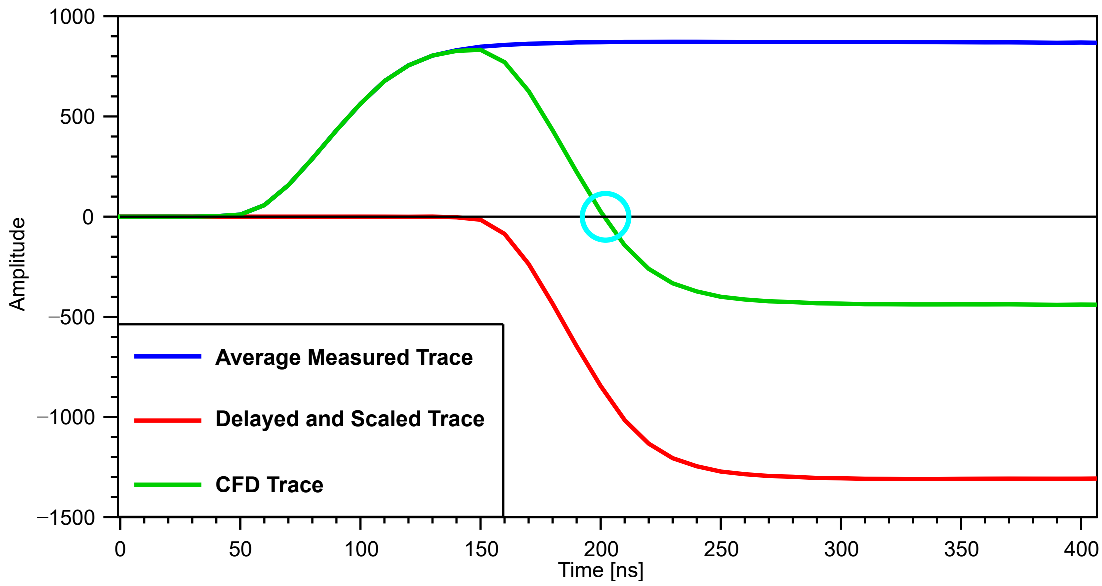

Figure 4.5: The average of the traces collected using HPGe two clover detector shown in Fig. 4.2 (blue), the delayed and scaled signal (red; delay = 100 ns, scale = 1.5), and the produced CFD (green). The zero-crossing point of the CFD is encircled in cyan.

In pricniple, the CFD is a continuous function but when implemented in digital electronics, it is sampled at some discrete frequency. For the data presented in Chapter 6, this sampling frequency was 250 MHz. The zero-crossing time is determined through a linear interpolation of the points either side of the CFD going from positive to negative. Tests using $LaBr_3(Ce)$ detectors show that with the 250-MHz Pixie-16 DAQ, the limit of timing resolution is ≈540 ps (FWHM), nearly an order of magnitude better than the sampling frequency. The main contribution to this resolution is from the sampling speed as a 500-MHz Pixie-16 module using the same parameters and detectors can achieve a resolution of 320 ps. Regardless of the module frequency used, the CFD eliminates almost all of the time walk allowing a single time gate to be used across the full energy range.

4.2 The ISOLDE Facility

The data analysed for this thesis were obtained during experiments performed at the **I**sotope **S**eparator **O**n-**L**ine **DE**vice (ISOLDE) facility at CERN - see Fig. 4.6. ISOLDE is the longest-running experiment at CERN, having begun operation in 1967. Major upgrades to the facility took place in 1974 and 1992 which have allowed it to produce more than 1300 isotopes of 73 elements [72–75].

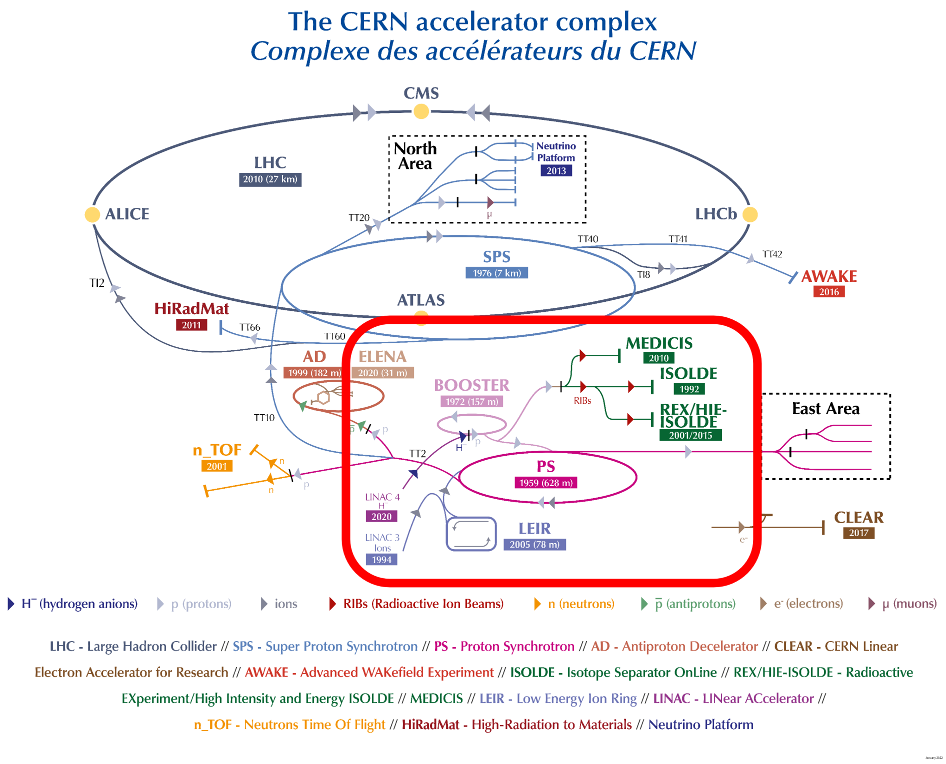

Figure 4.6: Diagram of the CERN accelerator complex, taken from [76]. The ISOLDE facility is shown in dark green. The part of the complex relevant for experiments at ISOLDE is emphasised with a red box.

4.2.1 Radioactive Ion Beam Production at ISOLDE

Production of Radioactive Ion Beams (RIBs) at ISOLDE starts with impinging a proton beam with a current of up to 2.1 μA and an energy of 1.4 GeV onto a target. The proton beam used at CERN is organised into a series of typically 20-50 pulses arranged into a regular, repeating 'supercycle'. Subsequent pulses within the supercycle are sent at 1.2-s intervals with approximately half of the total beam current being allocated to ISOLDE. As the proton request changes, the supercycle may be modified which typically happens every few hours.

The proton beam is directed to the target station for one of ISOLDE's two separators: the General Purpose Separator (GPS) and the High Resolution Separator (HRS). Over twenty different target materials have been used, including uranium carbide, UC_x, molten lead, and silicon carbide. The target material and design are key decisions when designing an experiment. The proton beam induces three main types of reaction in the target [77], which are illustrated in Fig. 4.7:

- **Spallation** - high-energy protons hit nuclei within the target and excite individual nucleons to high-energy states. Deexcitation of the parent nucleus happens through a combination of γ-ray emission or through nucleon evaporation. Typically, this leads to the release of tens of nucleons per proton impact, some of which may induce further reactions.
- **Fission** - incident protons are absorbed into the target nucleus, exciting it to a high-energy state from which it can fission. This can produce neutron-rich nuclei up to A≈150.
- **Fragmentation** - a high-energy proton hits nuclei in the target, causing it to split into two or more frgaments that can differ in mass greatly and allows for the production of some of the lightest isotopes produced at ISOLDE.

Once the desired nuclei are produced, they must be extracted from the target as quickly, efficiently, and selectively as possible. The targets used at ISOLDE are electrically heated to ≈2000 °C with a current of $\sim$ 650 A. Some of the energy of the proton beam and induced nuclear reactions will cause further heating. The high target temperature increases the rate of extraction of reaction products into the ion source. The target material is made into a powder comprising nanoscopic grains which are pressed into disks to produce a porous stucture which increases the rate of diffusion of the reaction products through the target. After escaping from the target material, reaction products move into a transfer line which leads to an ion source.

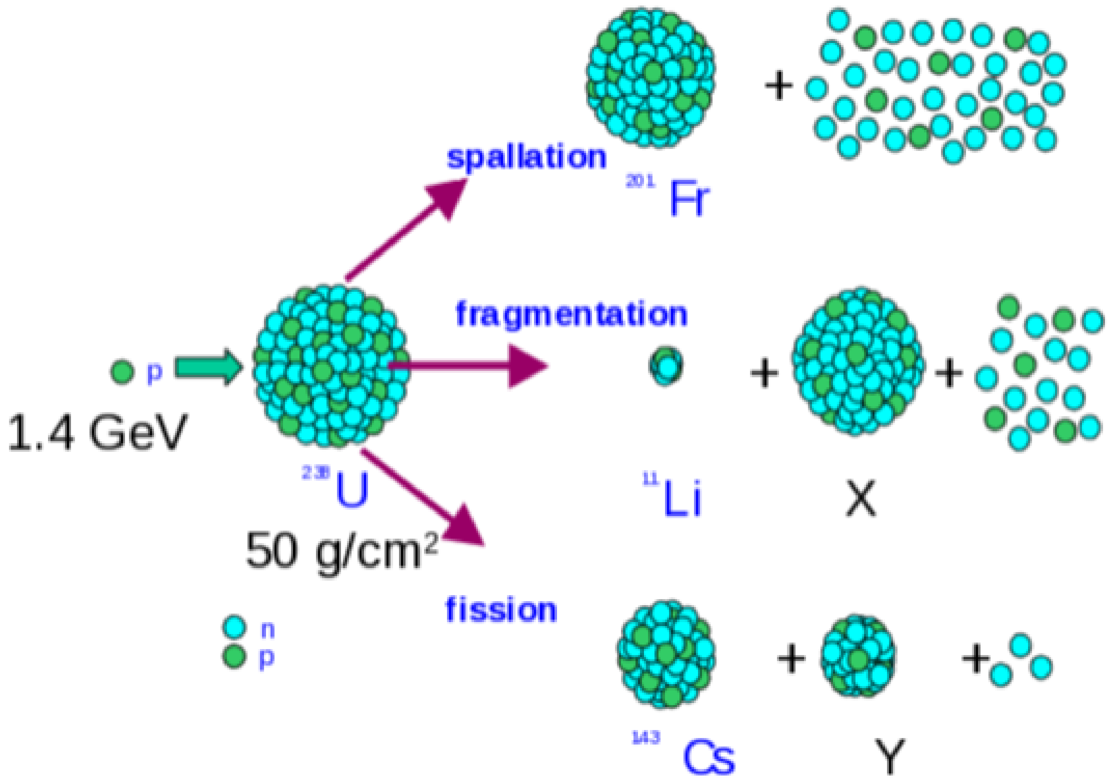

Figure 4.7: Illustration of the three main reaction mechanisms used to produce radioactive ion beams at ISOLDE: spallation, fission, and fragmentation [73, 78].

4.2.2 Ionisation of Radioactive Atoms

Upon leaving the target, the reaction products are all in an ionic or atomic form due to the high temperature. Several different ionisation methods have been developed at ISOLDE since it first started operating to produce produce ions. These include

- **Surface-ionisation source** - elements with low first-ionisation energies (particularly in group I of the periodic table, such as francium) can easily lose their valence electron in collisions with the walls of the ion source. Surface ionisation will happen to some degree with all types of ion source. This can lead to a significant amount of isobaric contamination in the beams produced, especially in cases where an isobar of the element being studied is strongly produced and easily ionised.

- **Resonance Ionisation Laser Ion Source (RILIS)** - lasers are tuned to the atomic energy-level spacings for the element of choice. Typically, two or three transitions will be used to excite an electron through the atomic energy levels until ions are formed.

- **Plasma-ionisation source** - for elements whose valence electrons are too tightly bound for either surface ionisation or laser ionisation to be used. The products from the target are injected into an ion source filled with plasma. This plasma, typically made from argon or xenon, reacts with atoms from the target and strips off an electron to become neutral. This ion source is the least selective and can lead to significant quantities of isobaric contamination but can be used in cases where RILIS is unsuitable.

RILIS

Of the ion sources that have been used at ISOLDE, the most common is RILIS which was used to ionise the $^{178}\mathrm{Au}^{g,m}$ studied for this thesis [78–82]. RILIS provides a highly selective and efficient ionisation mechanism for many elements. Lasers are used to excite electrons through the atomic structure until an ion is formed. The two most common laser types used by RILIS are titanium-doped sapphire (Ti:Sa) lasers and broadband dye lasers (BBDLs). Both types of laser produce a broad spectrum of frequencies which is sent through a series of Fabry-Pérot etalons and diffraction gratings to produce a final beam with a well-resolved frequency corresponding to the desired atomic transition.

Two or three laser beams are typically produced in this way, each of which produces one step within a multi-step laser-ionisation scheme. Using several steps together is preferable to a single, high frequency laser as it prevents the beam accidentally ionising other elements. Producing high-energy lasers in the ultraviolet part of the spectrum ($\approx$10 eV/photon) with the required intensity is also technically challenging. Such a laser would damage most optical elements that are commercially available. These lasers are sent through optical fibres to the ion source, through a transparent window.

The high velocities of atoms in the ion source cause the frequencies of the laser light in the reference frame of the atoms to be shifted due to the Doppler effect. Since the speeds and directions of travel of the atoms are random, the Doppler shift experienced varies, effectively reducing the laser resolution. This is a more signficant problem for lower-mass atoms than heavier ones, because the speeds are higher, at the same temperatures.

In some cases, such as ^{178}Au, the hyperfine splitting is sufficiently broad that it can be well resolved in the ion source cavity, despite the impact of Doppler broadening. The

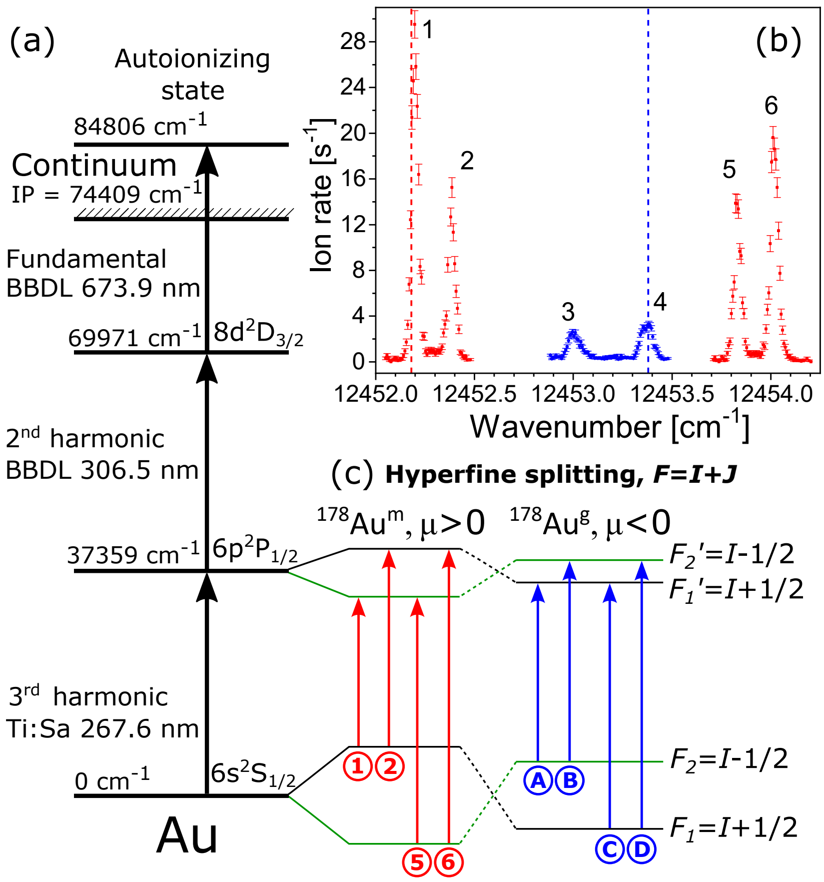

Figure 4.8: (a,c) Diagram illustrating the laser ionisation scheme used to produce isomerically pure beams of ^{178g,m}Au. (b) hyperfine spectrum measured for ^{178g,m}Au. Data for the ground state are shown in blue while for the isomer are shown in red. N.B that this colour coding is used in many cases throughout this thesis, with magenta being in cases that apply to both ^{178}Au^{g} and ^{178}Au^{m} Figure taken from [1]

HFS of ^{178}Au was measured by Cubiss *et al.* in Ref. [1] and is shown in Fig. 4.8(b). To produce isomerically selective beams for this thesis, the first-step laser wavenumbers of 12453.4(2) cm^{-1} and 12452.2(2) cm^{-1} were chosen for ^{178}Au^{g,m}, respectively. The errors given on these wavenumbers include the uncertainty on the laser produced combined with the effective impact of Doppler broadening.

4.2.3 Mass Separation

Ions are extracted from the ion source by an electrostatic potential of 30 kV$\leq V \leq$50 kV and are sent through a uniform magnetic field $\mathbf{B}$ for mass separation. The ions will move in such a field along a circular path with radius

$$r = \sqrt{\frac{m}{q}} \cdot \frac{\sqrt{2V}}{|\mathbf{B}|}, \tag{4.10}$$

where $|\mathbf{B}|$ can be tuned by chaging the current flowing through the solenoid. Therefore, for a given extraction voltage and magnet strength, all ions with the same m/q ratio will travel in a circle of the same radius. The ions are then separated by their mass-to-charge ratio, m/q, by passing through a narrow slit in the magnet.

The accelerating voltage is usually determined by the requirements of the experiment being performed and the current passing through the electromagnet's coil is set to produce the required value of r. At ISOLDE, there are two separators that can be used: the General Purpose Separator (GPS) or the High Resolution Separator (HRS). GPS utilises a single quadrupolar electromagnet to bend the beam in an arc of radius 1.5m with a bending angle of 70° giving it a resolving power of $M/\Delta M \approx 2400$. HRS uses two quadrupolar electromagnets which bend the beam around arcs with radii 1m and bending angles of 90° and 60° giving a total resolving power of $M/\Delta M \approx 5000$.

4.3 ISOLDE Decay Station

Decay spectroscopy measurements of ^{178}Au^{g,m} were made at the ISOLDE Decay Station (IDS) [12, 72, 83–85]. IDS is a highly-versatile experimental setup that can be used for performing several different types of decay measurement including γ-ray spectroscopy, charged-particle spectroscopy, fast timing, β-delayed neutron time of flight spectroscopy and, combined with RILIS, decay-tagged in-source laser spectroscopy. Although the setup is optimised in each experiment for the particular measurement, there are some key parts that are common between all configurations. These include a Pixie-16 Data Acquisition System (DAQ), a tape station and, after a recent upgrade, up to 15 HPGe clover detectors.

IDS Tape Station

During most experiments at IDS, the beam is implanted into a 50-μm-thick aluminised Mylar foil up to 5 km in length. This tape is fed between two wheels, as shown in Fig. 4.9 which can be moved manually or automatically after a given number of proton pulses, supercycles, or a particular time period. The time between tape movement is normally chosen by considering the half-life of the isotope(s) of interest compared to those of contamination as well as their relative production rates to prevent detector saturation.

For the measurements of $^{178}\mathrm{Au}^{g,m}$, the tape was typically moved every hour between subsequent runs.

Once the tape is moved away from the implantation spot, it can be transported to a secondary decay position or stored around the spools seen in Fig. 4.9. Lead bricks are placed on top of the box to shield the detectors around the implantation point from radiation emitted inside the tapestation.

Figure 4.9: A photograph of the IDS tape station with the front cover removed. The two large wheels in the middle of the photograph are the spools around which the tape is wound and transferred between in operation. The tape is fed between the smaller wheels nearer to the top and centre of the photograph before going upwards into the vacuum chamber being used for a particular experiment.

Digital Signal Processing

All amplified detector signals and logic pulses were recorded using a Xia Pixie-16 [71] Data Acquisition System (DAQ) with four 16-channel, 16-bit, 250-MHz modules. Logic pulses for the opening/closing of the beamgate, impact time of protons, tape movement, and the start of the supercycle were also recorded. Each module performed real-time signal processing on FPGAs to determine the energy and time of arrival of each signal. The energy was determined using an on-board trapezoidal filter while the time of arrival of an event was determined using an on-board CFD algorithm with linear interpolation to determine the zero-crossing time. The data were written to disk in a list mode ".ldf" file in an "event-by-event" style. Each event comprises 128 bits, broken up into four 32-bit words, as illustrated in Table 4.1

Table 4.1: Table showing the information stored in the header of events stored in list-mode data files produced by a Xia Pixie-16 DAQ with revision F firmware. Taken from [71].

<table>
<tr><th>Index</th><th colspan="6">Data</th></tr>
<tr><td rowspan="2">0</td><td>[31]</td><td>[30:17]</td><td>[16:12]</td><td>[11:8]</td><td>[7:4]</td><td>[3:0]</td></tr>
<tr><td>Finish Code</td><td>Event Length</td><td>Header Length</td><td>CrateID</td><td>SlotID</td><td>Chan#</td></tr>
<tr><td rowspan="2">1</td><td colspan="6">[31:0]</td></tr>
<tr><td colspan="6">EVTTIME_LO[31:0]</td></tr>
<tr><td rowspan="2">2</td><td>[31]</td><td>[30]</td><td>[29:16]</td><td colspan="3">[15:0]</td></tr>
<tr><td>CFD forced trigger bit</td><td>CFD trigger source bit</td><td>CFD Fractional Time[13:0] × 16384</td><td colspan="3">EVTTIME_HI[15:0]</td></tr>
<tr><td rowspan="2">3</td><td>[31]</td><td colspan="2">[30:16]</td><td colspan="3">[15:0]</td></tr>
<tr><td>Trace Out-of-Range Flag</td><td colspan="2">Trace Length</td><td colspan="3">Event Energy</td></tr>
</table>

4.4 Experimental Setup

The ^{178}Au^{g,m} decay data were taken during the IS665 experiment [13] which studied the α and EC/β^+ decay, and fission of a series of neutron-deficient gold isotopes using the setup shown in Fig. 4.10.

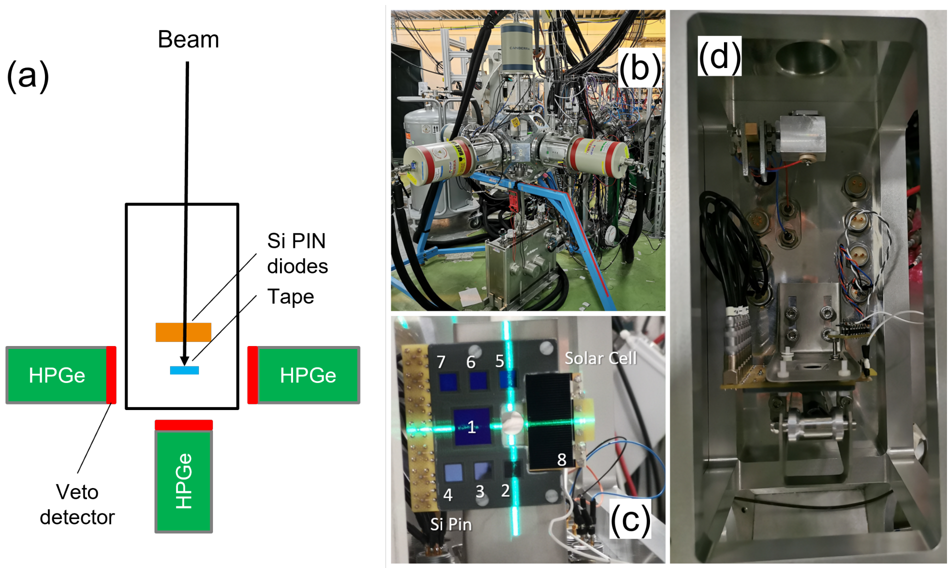

Figure 4.10: Experimental setup used to collect the decay data from ^{178}Au^{g,m}. (a): a simplified block diagram showing a 2-dimensional cross-section of the detectors used and showing the direction of the beam into the chamber, through the hole in the array of Si PIN diodes to be implanted into the aluminised Mylar tape. (b): a wide view of IDS, taken just before the experiment; (c): the array of Si PIN diodes and the hole through which the beam passed. The solar cell labelled was used to measure fission fragments from other isotopes studied in the same experimental campaign - no fission fragments were detected from ^{178}Au^{g,m}; (d) a top-down view of the inside of the vacuum chamber.

Upon entering the IDS chamber, the beam passed through a 10-mm-diameter hole in a board containing an array of seven Si PIN diode detectors before being implanted into the IDS tape. The Si detectors faced the implantation point, and were used to measure α particles and conversion electrons.

The implantation spot was surrounded by four HPGe clover detectors arranged around the faces of the cuboidal vacuum chamber. To reduce the attenuation of x rays and low-energy γ rays as much as possible, the chamber walls were made of 0.5-mm-thick aluminium. The front face of two of the clovers was made of a polymer foil, typically ~ 0.3 mm [68] (instead of aluminium, like the rest of the casing), to reduce the absorption of low-energy photons further. Preamplifier circuitry was built into the casing of the HPGe clover detectors, between the active area of the crystals and the liquid nitrogen dewars. The preamplifier output signals from the HPGe clover detectors were sent directly into the DAQ. The signals from the silicon detectors were sent to an external preamplifier module a few cm from the chamber before being sent to the DAQ.

Calibration of Germanium Detectors

The energy-calibration function and efficiency curve for the HPGe detectors were produced by fitting γ-ray peaks from the decay of ^{152}Eu, ^{137}Cs, and ^{60}Co [33]. Additionally, the well-know 2615-keV γ ray from ^{208}Tl, and the 1764- and 2204-keV peaks from ^{214}Bi were used to provide higher-energy calibration [33]. The function fitted to the efficiency data has the form [86]

$$\mathcal{E}(E_\gamma) = \frac{P_1 + P_2 \ln(E_\gamma) + P_3 \ln(E_\gamma)^2 + P_4 \ln(E_\gamma)^3 + P_5 \ln(E_\gamma)^4}{E_\gamma}, \tag{4.11}$$

where P_i $(i = 1, 2, 3, 4, 5)$ were determined from a fit to the data. The fitted, uncalibrated spectra for a single crystal are shown in Fig. 4.11 (a-c). The fit centroids (in ADC channels) are plotted against energy in Fig. 4.11(d). This fit gives a rapid variation in the expected efficiency around its maximum at $E_\gamma \approx 50$ keV. As will be shown in Chapter 6, having a well-characterised efficiency curve in this region is important to determine the number of K x rays emitted from the various nuclei studied. To verify the efficiency curve in this energy region, the relative intensities of the osmium $K_{\alpha,\beta}$ peaks gated on the 5921-keV α decay from ^{178}Pt which feeds the 2^+ yrast state in ^{174}Os were used. The only source of osmium K x rays coincident with this α decay is from the internal conversion of the well-known 158-keV pure E2 transition to the ground state of ^{174}Os. The K conversion coefficient for this transition was determined using BrIcc, providing a verification of the efficiency curve in this region. The expected values from the standard-source data shown in Fig. 4.11(d) are compared to the values determined from the ^{174}Os K x rays in Table 4.2. These values are in good agreement, with the main contribution to the uncertainty for the ^{174}Os values being the efficiency normalisation for the 158-keV γ ray which used the standard-source data. Therefore, although the rapidly change in efficiency around the maximum could lead the to large uncertainties in the γ-ray intensities discussed in Chapter 6, this region is well constrained by the number of points used to fit the efficiency curve. The largest contributions to the uncertainties in the γ-ray intensities are from the source activity uncertainties and the statistics available.

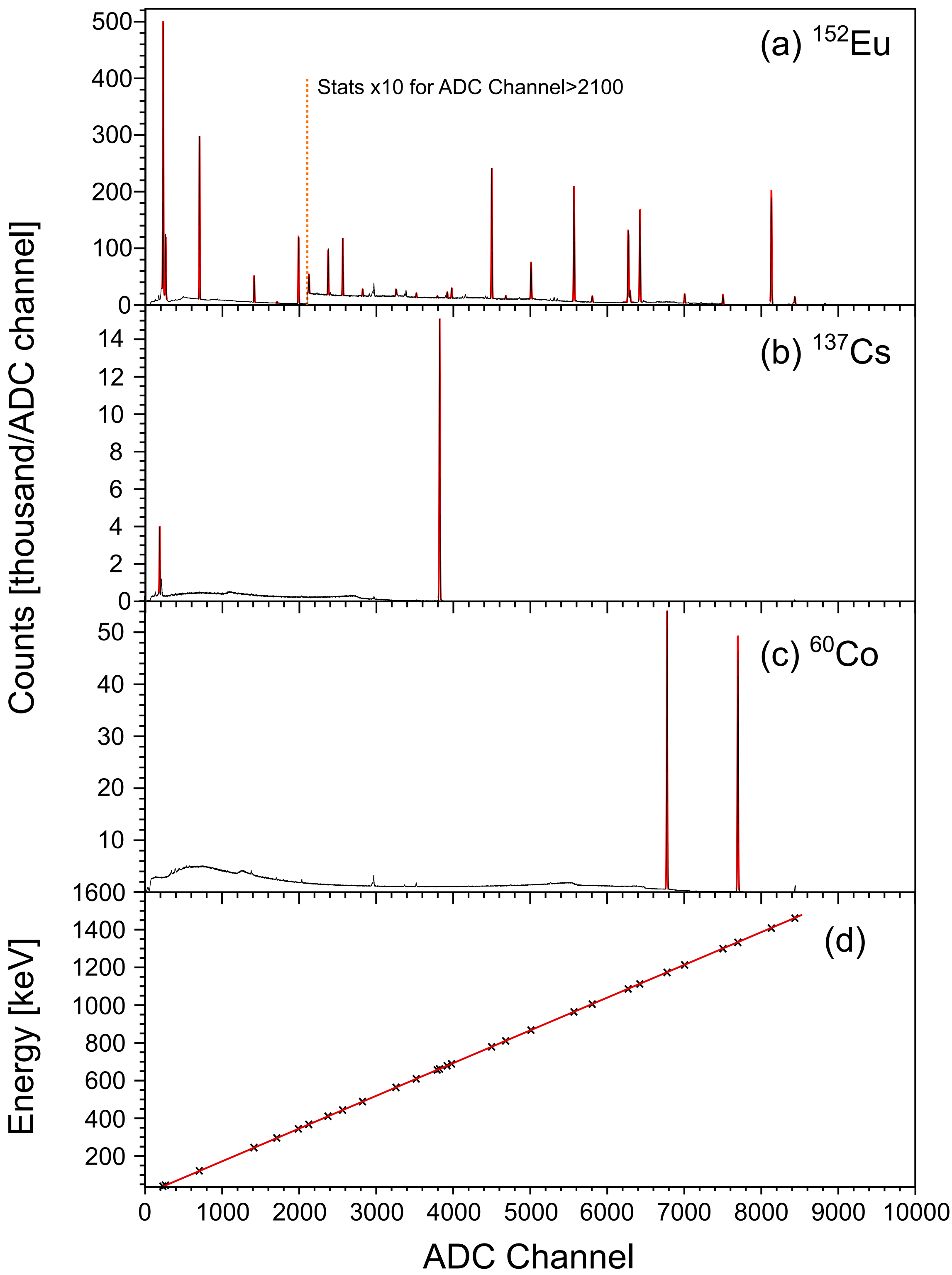

Figure 4.11: (a-c) plots of the uncalibrated ^{152}Eu, ^{137}Cs, and ^{60}Co γ-ray spectra, respectively, recorded in one clover crystal. Panel (d) shows the calibration function with a linear fit to these. Error bars are too small to be seen on this scale but are shown in the residual plot given in Fig. 4.12(a).

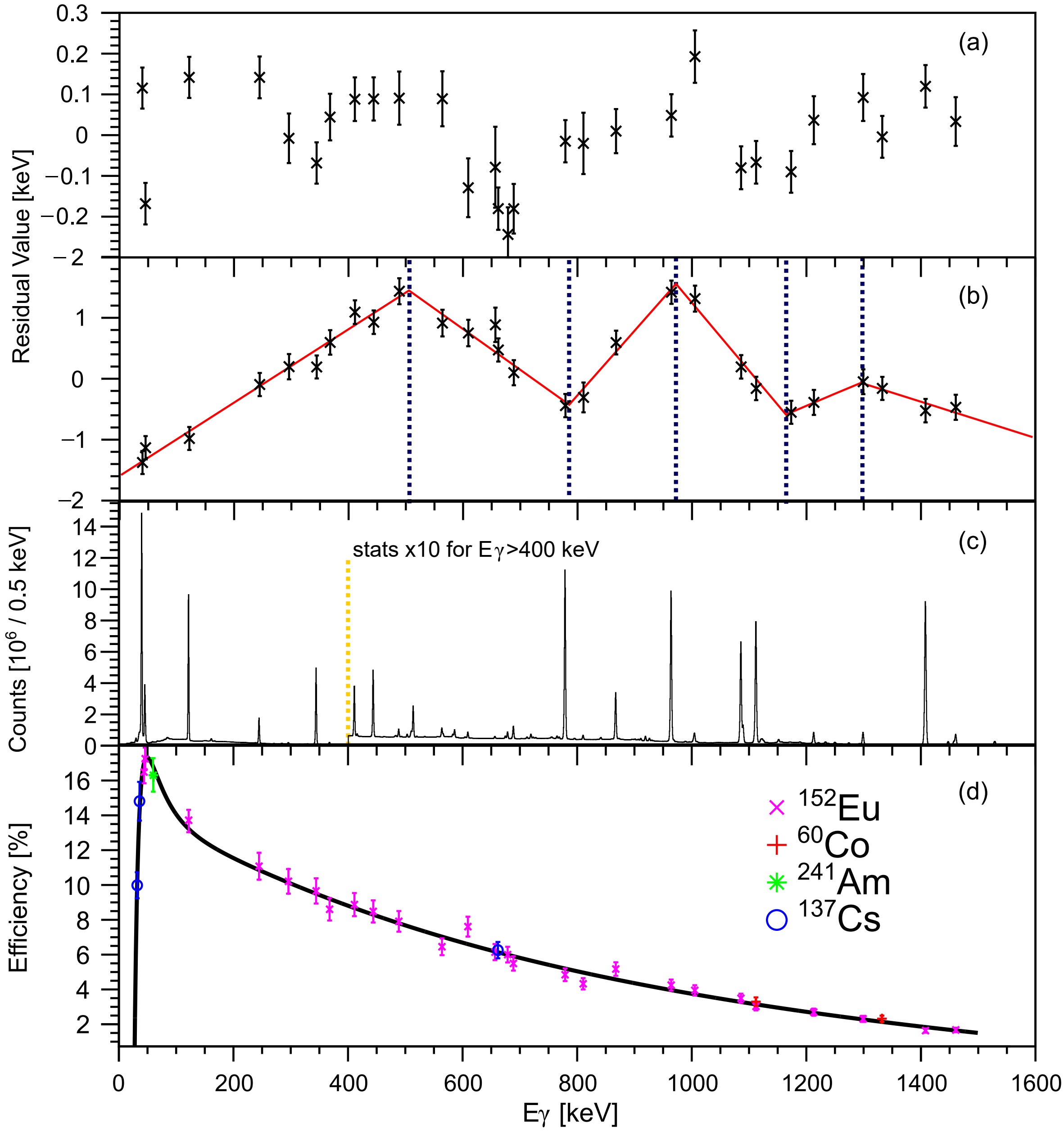

Figure 4.12: Calibration procedure performed using ^{152}Eu, ^{60}Co, and ^{137}Cs radioactive sources. (a): the residuals for a 'good' channel unaffected by the linearity problem. (b): the residuals for a 'bad' channel along with fits for a sawtooth correction term to the calibration. The intereception between the straightlines fit to each tooth are shown with dashed lines for emphasis. (c): the total singles spectrum take for ^{152}Eu after the full calibration was performed. (d): the total efficiency curve for all 16 crystals with addback enabled, along with the fitted efficiency curve shown in black.

Table 4.2: Comparison of the expected γ-ray detection efficiency from the standard-source data shown in Fig. 4.11(d) to the values determined from the osmium K x rays coincident with the 5291-keV α decay of ^{178}Pt.

K x ray		Efficiency [%]	
Label	E [keV]	Sources	^{174}Os α-γ
$K_{\alpha,1}$	63.000	16.8(6)	17.0(7)
$K_{\alpha,2}$	61.486	16.9(6)	17.1(7)
$K_{\beta,1}$	71.414	16.3(5)	16.7(6)
$K_{\beta,2}$	73.363	16.2(5)	16.0(6)

There is a well-known issue with the implementation of the trapezoidal filter algorithm in the FPGAs used in 250- and 500-MHz Pixie-16 modules [87]. This sometimes, but not always, causes the residuals from an energy calibration curve to form a "sawtooth" pattern, as illustrated in the difference between Figs. 4.12(a,b). These teeth were fitted with a series of straight lines, as shown in Fig. 4.12(b) which were used to correct for this non-linear behaviour.

It was found that this was a problem for eight of the sixteen channels used for the HPGe Clover detectors leading to residual energies of up to $\approx$2 keV when a linear calibration function was used. This problem was not resolved by polynomial calibration functions up to a quintic. The fact that eight channels are affected is consistent with the known cause of the issue. The FPGAs that perform the trapezoidal filter serve four channels each (see Fig. 5-1 of Ref. [71]), indicating that two of the four FPGAs used suffer from this probelm. The energies at which the 'teeth' occur are not the same for all detectors, likely due to the inconsistent gain applied to each signal. As a result, a single γ-ray could be made to look like several distinct transitions. Therefore, separate linear calibration functions were produced for each region of the saw tooth. Initially, a linear function was fit to the full set of calibration points and the residuals were calculated. A series of straight lines was fit to each 'tooth', as shown in Fig. 4.12(b), making this calibration equivalent to a series of individual linear calibrations. The interception points between these lines were calcualted and used to ensure that the overall calibration function was continuous. To ensure that the linearity issue did not produce any artificial peaks, γ-ray energy spectra produced using the two unaffected FPGAs were compared to the spectra produced with all four FPGAs.

Calibration of Silicon Detectors

Four sets of energy calibrations were performed for the Si PIN diode detectors: for α particles and CE in each of two separate gain modes. While for HPGe detectors, standard radioactive sources are sufficient to produce a good energy calibration, α particles lose a signficant and angle-dependent amount of energy while escaping from the tape into which the parent nuclei were implanted during the experiment.

To calibrate the detectors for α particles, the α-decay peaks given in Table 4.3 were fit with Crystalball functions - see Eq. 6.3 [88]. The isotopes used for the calibration were (with the exception of ^{178}Pt) produced for other measurements during the same experiment. Runs were only used for calibration if performed no more than one hour before (or after) the beginning (or end) of the collection of ^{178}Au^{g,m} decay data, due to the noticeable gain shift over time. The small gain shift between calibration runs was corrected for using the ^{178}Pt α-decay peaks at 5291(4) and 5446(3) keV. Therefore, each silicon detector had a separate calibration function for each run.

Table 4.3: Summary of the α-decay energies used in the calibration of the silicon detectors. The rows have been split between two pairs of lines for the sake of space. Note that ^{178}Pt was not produced directly but it followed the EC/β^+ decay of ^{178}Au. The α-decay energies were taken from Refs. [11, 89–95]

Parent nucleus	^{177}Au	^{179}Au	^{178}Pt	^{211}Bi
E_α [keV]	6161(7)	5848(5)	5291(4), 5446(3)	6622.9(6), 6278.2(7)
Parent nucleus	^{198}At	^{215}At	^{202}Fr	^{219}Fr
E_α [keV]	6750(4), 6852(4)	8026(4)	7238(5)	7312.3(18)

The α-particle detection efficiency was determined using well-characterised ^{148}Gd, ^{239}Pu, ^{241}Am, and ^{244}Cm sources to be 3.8(4)%. It was verified by comparing the intensity of the 5291-158.7 keV α-γ coincidence group from the decay of ^{178}Pt to ^{174}Os in singles to α-γ coincidence, corrected for the internal conversion coefficient of the 158.7-keV transition.

To produce the CE calibration, prompt CE-γ coincidence matrices were produced for each silicon detector. The CE energies were uncalibrated while the γ-ray energy calibrations discussed above were used. Projections of this matrix, gated on the strongest γ rays between states in the yrast bands in ^{178}Pt, ^{174}Os, and ^{178}Os were used to identify the CE peaks in the spectra - see Fig. 4.13. Once each peak was identified, the energy of the corresponding transition was calculated using BrIcc [62].

Prompt Timing Gates

Even relatively broad coincidence gates require timing precision of a few tens of ns per detector to prevent the breadth of the overall timing distribution being dominated by different processing speeds and cable lengths. To correct for this, the time difference between the detection of the 1173- and 1332-keV γ rays following the decay of ^{60}Co was calculated for each detector, relative to one HPGe clover crystal. The time-difference histograms are shown in Fig. 4.14.

The mean values from the Gaussian distributions shown in Fig. 4.14 were subtracted from all timestamps for the appropriate detector to align the measurement times for production of the various coincidence matrices. These plots were then remade and refit to ensure they all had a centre at $\Delta t_{\gamma\gamma} = 0$. An equivalent process was then performed to synchronise the times of the silicon detectors with the HPGe clovers by looking at the time difference betwen the 5291-keV α decay to the 2_1^+ state in ^{174}Os and the prompt 158-keV $2_1^+ \rightarrow 0_1^+$ γ ray.

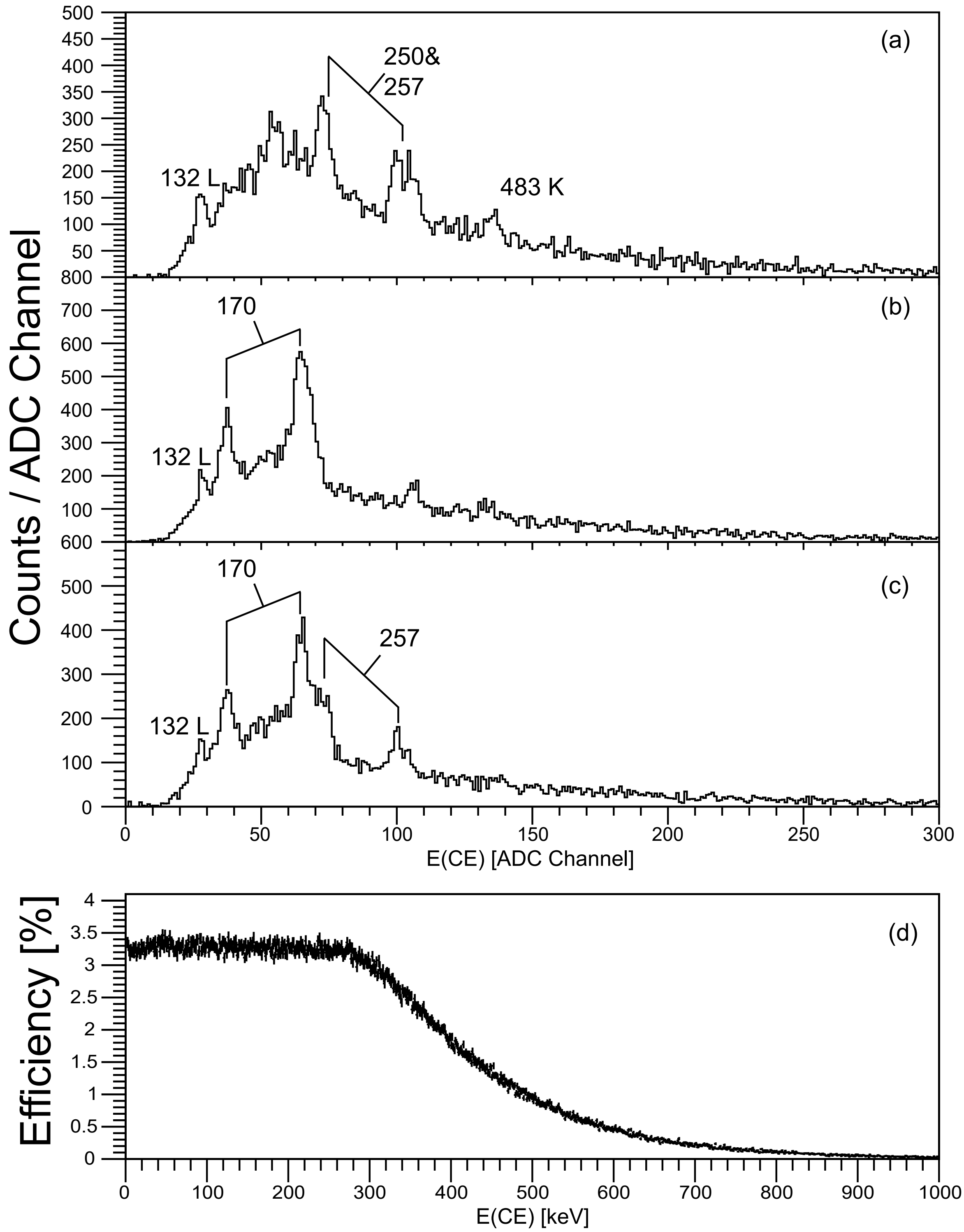

Figure 4.13: Uncalibrated, background-subtracted projections of a prompt conversion-electron-γ matrix, gated on the (a) 170-keV, (b) 257-keV, and (c) 337-keV γ rays between the yrast states in ^{178}Pt. The strongest conversion electron peaks are identified and labelled. The simulated CE detection efficiency is shown in (d), as a function of the energy.

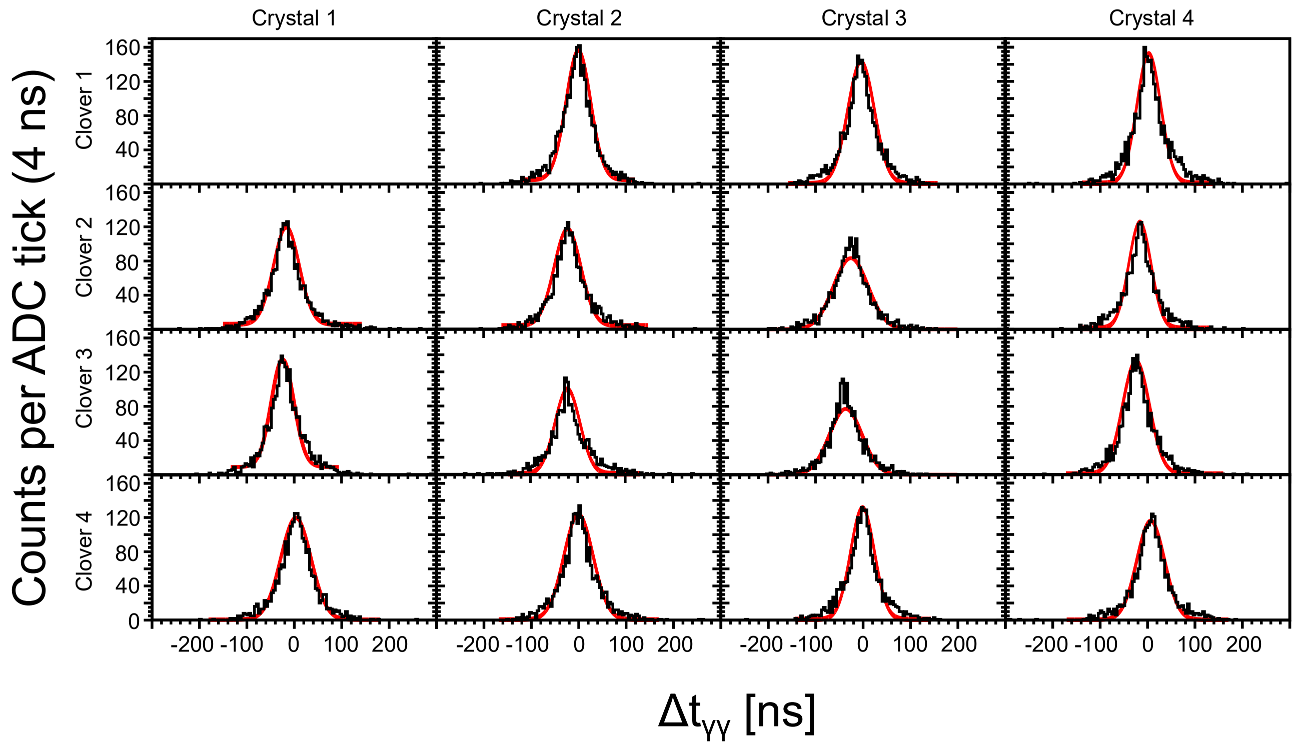

Figure 4.14: Plot of the difference in detection times of the 1173- and 1332-keV γ rays in clover 1, crystal 1 with each other crystal. Each distribution is fitted with a Gaussian function, the mean of which is used to align the times within the sort code. Since clover 1, crystal 1 is used as the reference, this histogram is empty. All histograms have the same horizontal- and vertical-axis scales for easier comparison.

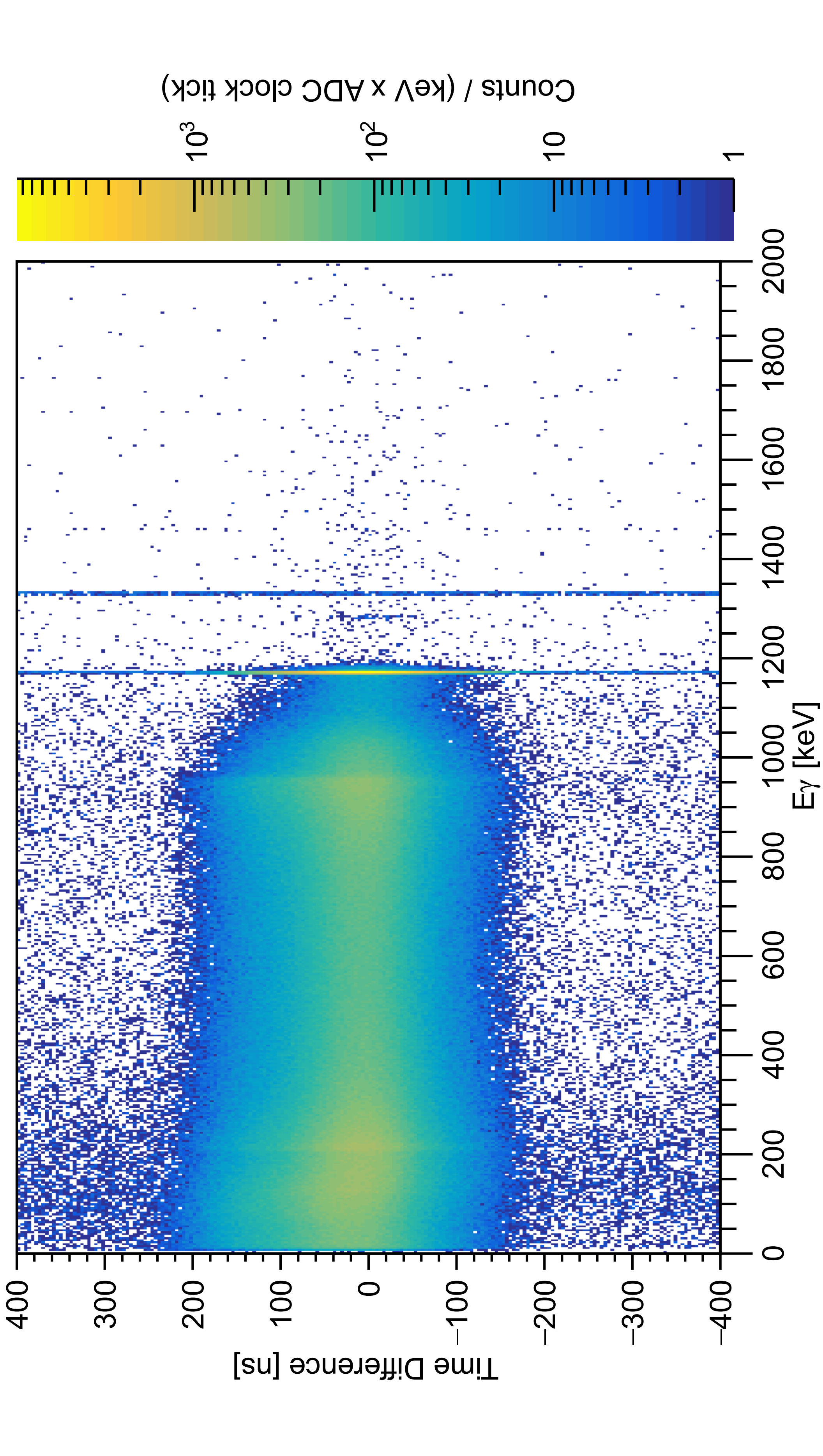

Figure 4.15: Time walk matrix showing the energy and time difference of γ rays coincident with ther 1332-keV γ ray. The bins are 1-keV wide on the horizontal axis and 4-ns wide on the vertical, which corresponds to one ADC clock tick.

5

Previous Studies of ^{178}Au and its Daughters

5.1 Previous α-decay Study of ^{178}Au$\rightarrow^{174}$Ir

The first α-decay study of ^{178}Au was reported by Siivola in 1968 [92] in which a 5920-keV α decay from a $t_{1/2}$ =2.6(5)-s state was identified. A later study using the velocity filter SHIP by Keller *et al.* [96] confirmed this 5920-keV decay and proposed two additional α decays from ^{178}Au at E_α =5980 and 5850 keV. A fourth α-decay transition was reported by Page *et al.* [97] at E_α =5886(9) keV.

In 2015, a combined mass-, laser-, and decay-spectroscopy study of ^{178}Au was performed at ISOLDE [1, 98]. The laser-spectroscopy component of this experiment isolated two states in ^{178}Au: the weakly deformed ground state (^{178}Au^g) and a strongly deformed, long-lived isomer (^{178}Au^m) - see Fig. 4.8(b). The existence of two such states was first proposed by Davidson *et al.* in Ref. [99], as discussed below.

By exploiting the hyperfine structure, isomerically pure beams of ^{178}Au^{g,m} were sent to ISOLTRAP [100] for mass measurements and the Windmill for decay spectroscopy measurements. The ISOLTRAP mass measurements showed that the excitation energy of ^{178}Au^m is 189(14) keV. The Windmill setup was optimised for α-particle detection efficiency and was used to produce separate fine-structure α-decay schemes for ^{178}Au^{g,m}, which are shown in Fig. 5.1.

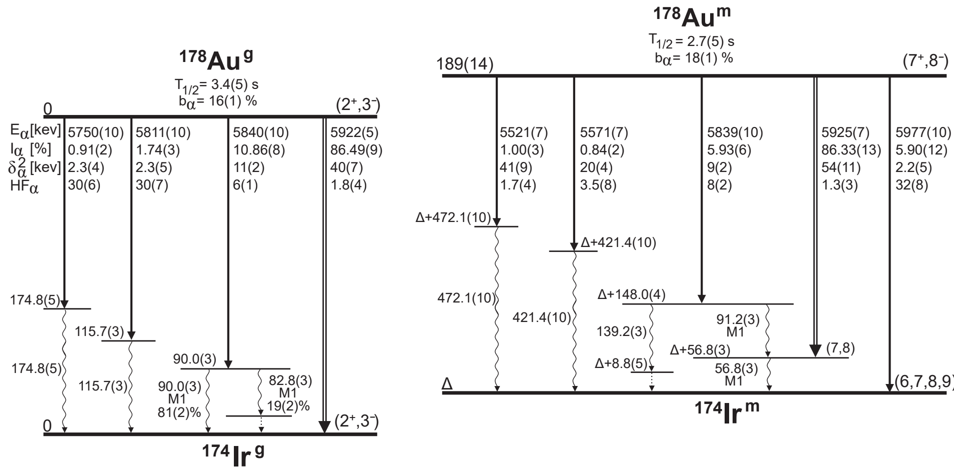

Figure 5.1: The α-decay schemes obtained for ^{178}Au^{g,m} $\rightarrow^{174}$Ir from Ref. [1].

The α-particle and γ-ray energies shown in Fig. 5.1, combined with the mass measurements performed at ISOLTRAP reported in the same study, showed that the isomerism observed in ^{178}Au persisted into ^{174}Ir. These mass measurements were used as an additional way to check the level of contamination in the beam, which was found to be negligibly low. Because γ-γ coincidence analysis could not be performed with the data collected using the Windmill system, only very limited spectroscopic information for the β-decay branch to ^{178}Pt was reported in Ref. [1] - see Fig. 5.2. Nevertheless, a similar EC/β^+ feeding pattern to ^{178}Pt was observed as by Davidson *et al*, as discussed below.

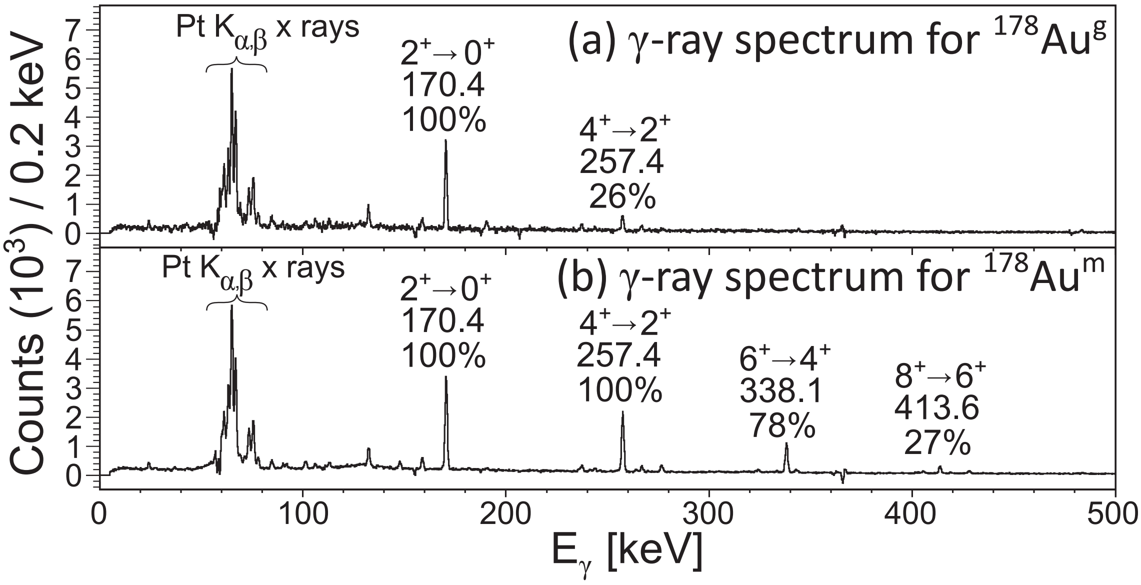

Figure 5.2: The singles γ-ray spectra for (a):^{178}Au^g and (b): ^{178}Au^m from Ref. [1] showing the difference in feeding to the yrast band states from each parent state.

The measured HFS of ^{178}Au was used to determine the magnetic moments of ^{178}Au^{g,m}. Spin, parity, and configuration assignments found to be consistent with these measurements and are summarised in Table 5.1.

Table 5.1: Magnetic dipole moments and Nilsson configurations of ^{178}Au states that were determined in Ref. [1], from which this table is reproduced. The values of $a(n,l)$ give the hyperfine coupling constants for atomic levels with quantum numbers n, and l, and $^{197}\Delta^{178}$ is the hyperfine anomaly between ^{197}Au and ^{178}Au. The values of the magnetic dipole moment, $\mu_{exp}(\mu_{N1,2})$,were calculated in two different ways - see the original publication for further detail.

State	I^π	$a(6s)$ (MHz)	$a(6p)/a(6s)$	$^{197}\Delta^{178}$ (%)	$\mu_{\rm exp}$ ($\mu_{N,1}$)	$\mu_{\rm exp}$ ($\mu_{N,1}$)	$\mu_{\rm add}$ ($\mu_{N,2}$)	Nilsson configuration
^{178}Au$^{\rm g}$	2^+	−12 760(300)	0.1122(60)	8.7(79)	−0.880(56)	−0.884(68)	−0.73(20)	$\pi 1/2^-[541]_{h9/2} \otimes \nu 5/2^-[512]_{h9/2}$
	3^-	−9 100(300)	0.1136(60)	10.6(80)	−0.941(69)	−0.962(77)	−0.74(21)	$\pi 1/2^-[541]_{h9/2} \otimes \nu 7/2^+[633]_{i13/2}$
^{178}Au$^{\rm m}$	7^+	19 602(40)	0.1137(13)	10.7(19)	4.74(20)	4.84(8)	4.67(34)	$\pi 9/2^-[514]_{h11/2} \otimes \nu 5/2^-[512]_{h9/2}$
	8^-	17 297(40)	0.1137(13)	10.6(18)	4.78(20)	4.89(8)	4.84(33)	$\pi 9/2^-[514]_{h11/2} \otimes \nu 7/2^+[633]_{i13/2}$
	8^+	17 297(40)	0.1137(13)	10.6(18)	4.78(20)	4.89(8)	5.61(34)	$\pi 11/2^-[505]_{h11/2} \otimes \nu 5/2^-[512]_{h9/2}$

5.2 Structure of ^{178}Pt

Two rotational bands are known to exist in the even-mass platinum isotopes: one built on a strongly deformed configuration and the other on a weakly deformed configuration - see Fig. 5.3. For platinum isotopes near stability, the weakly deformed states form the yrast band, while the strongly deformed states appear as an excited band [101]. However, in $^{178-186}$Pt$_{100-108}$ (which lie close to the $N = 104$ midshell), the proton-neutron quadrupole interaction lowers the energies of the strongly deformed states sufficiently for them to form the yrast band, with the strongly deformed 0^+ state providing the ground-state configuration. This reordering of states causes a sudden increase in ground-state deformation of $^{178-186}$Pt - see Fig. 6.27. For even-even platinum nuclei with $A \leq 176$, the weakening of the proton-neutron quadrupole interaction causes the strongly deformed configurations to rise in energy relative to the weakly deformed states, resulting in the latter once again providing ground-state configurations.

This unusual pattern led to significant interest in the structures of platinum isotopes around $N = 104$, in the 1980s and 1990s. Two studies of particular relevance to this thesis were by Davidson *et al.* [99] and Kondev *et al.* [102].

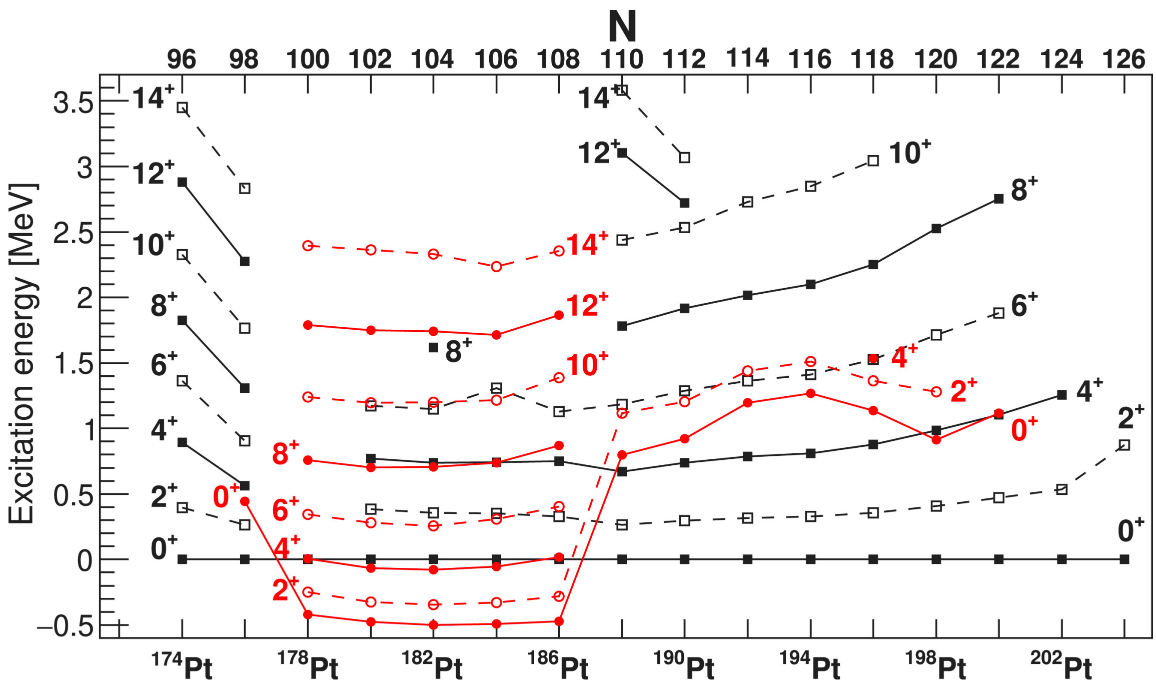

Figure 5.3: Plot of the energy systematics of neutron-deficient even-even platinum isotopes, relative to the 0^+ normal-order state. Intruder states are shown with red circles and normal-order state with black squares. Figure taken from Ref. [103].

In Davidson's work, ^{178}Au nuclei were produced through the ^{37}Cl(^{144}Sm, 3n)^{178}Au fusion-evaporation reaction using the 14UD Pelletron at the Australian National University. The EC/β^+ decay was studied through γ-ray and CE spectroscopy to produce the decay scheme shown in Fig. 5.4. The two rotational bands within ^{178}Pt that had previously been identified were found to be strongly mixed, particularly at low energies - see Table 10 of Ref. [99]. Significant feeding to 2^+, 4^+, and 8^+ states in ^{178}Pt was observed but there was relatively little direct feeding to the 6^+ state. This led Davidson to suggest that they had a mixed source of two β-decaying states in ^{178}Au, one with a spin of ∼3 and one with a spin of ∼7. Davidson's study was the first to identify a state at 2345.2 keV in ^{178}Pt which was determined to have $E_x = 2344.4$ keV in the present work. As will be shown in Chapter 7, this state is highly significant for the EC/β^+ decay of ^{178}Au^m.

Kondev explored the higher-energy states within ^{178}Pt using the ^{103}Rh(^{78}Kr,3p) reaction at the Argonne Tandem Linear Accelerator (ATLAS) facility in the USA [104, 105]. The beam provided by ATLAS had an energy of 350 MeV, allowing the high-spin states within two further bands to be populated. These bands were built on the 1573- and 1810-keV states first observed by Davidson, which were given $I^\pi = 5^-$ and (6^-) assignments, respectively. The prompt de-excitation by γ-ray emission was measured using the Gammasphere array coupled to the Fragment Mass Analyzer (FMA) [106] to produce level scheme shown in Fig. 5.5.

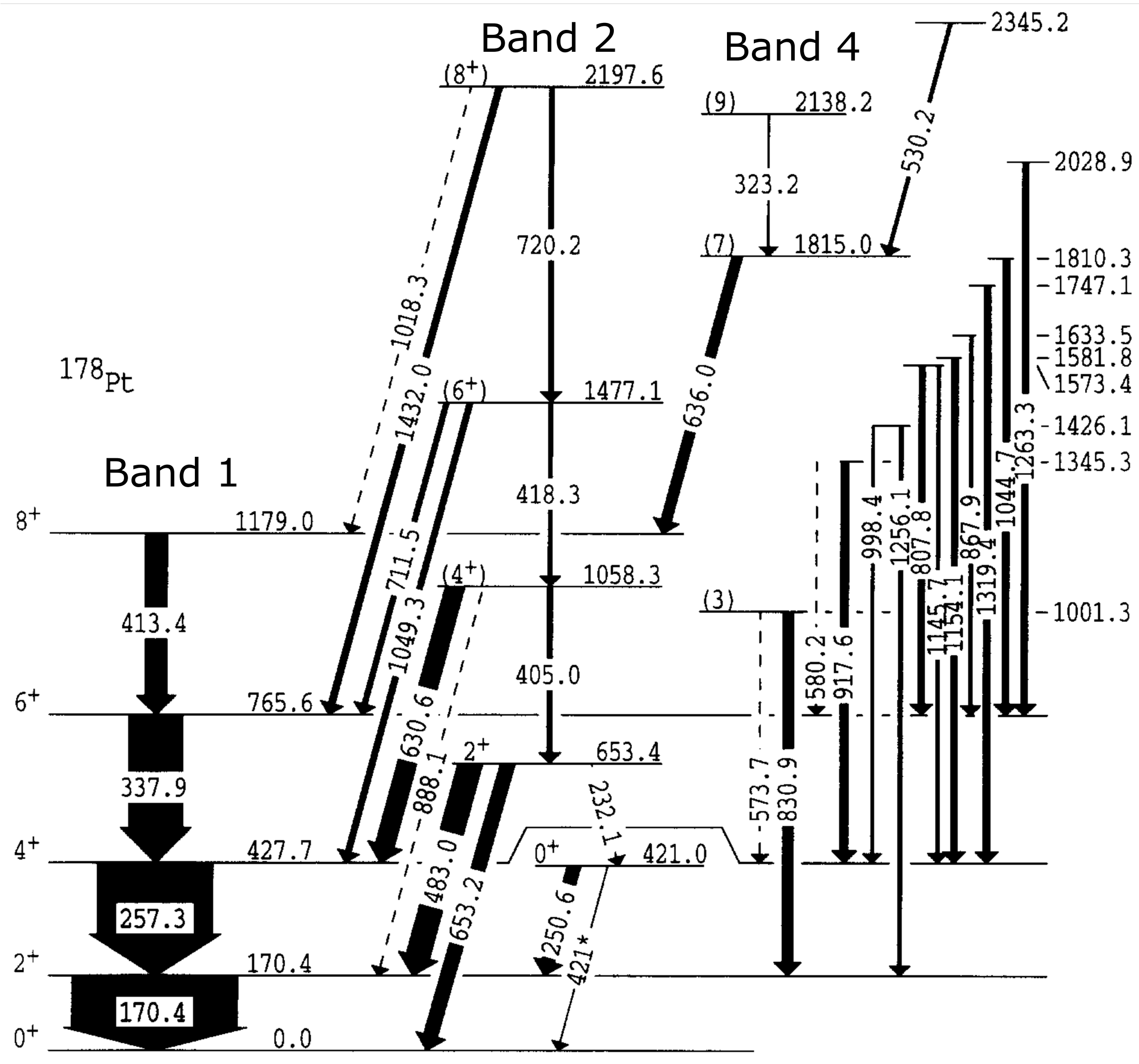

Figure 5.4: The EC/β^+ decay scheme produced by Davidson *et al.* in Ref. [99]. The band numbers given have been changed from those in the original study to be consistent with Fig. 5.5 and the new decay schemes produced for this thesis.

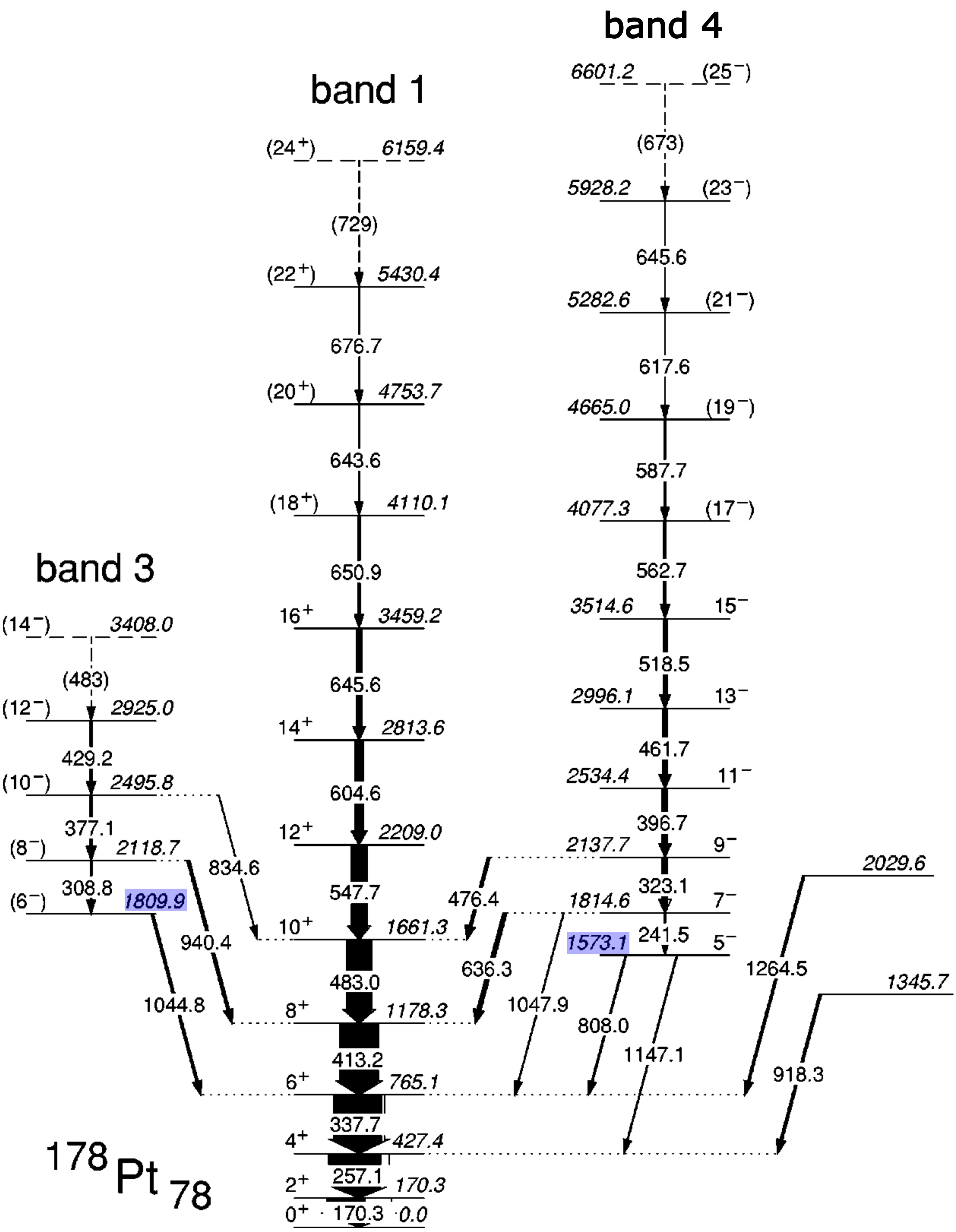

Figure 5.5: The level scheme produced by Kondev *et al.* in Ref. [102]. The band numbers given have been changed from those in the original study to be consistent with Fig. 5.4 and the new decay schemes produced for this thesis. The highlighted 1573.1- and 1809.9-keV states were originally discovered by Davidson *et al.* in Ref. [99] and found by Kondev to be bandheads for two rotational bands.

5.3 Recent In-beam study of ^{178}Au

In 2015, an in-beam γ-ray spectroscopy experiment was performed by the University of York group at the Accelerator Laboratory of the University of Jyväskylä (JYFL) [10, 107]. A 381-MeV ^{88}Sr beam with an average current of 6 pnA was impinged onto a 98%-enriched, 600-μgcm^{-2} ^{92}Mo target to produce ^{178}Au through a fusion-evaporation reaction. The target was surrounded by the JUROGAM II array [108], comprising 24 clover and 15 coaxial HPGe detectors fitted with a bismuth germanate (BGO) shields. The reaction products produced inside the target passed through the RITU separator [109] and into the GREAT spectrometer [110]. This allowed for the 373-ns isomer, and rotational bands shown in Fig. 5.6, to be identified within ^{178}Au. By comparison with well-known bands in ^{176}Ir, Nilsson orbital assignments for these two bands were made, as illustrated by the dashed red lines in Fig. 5.6.

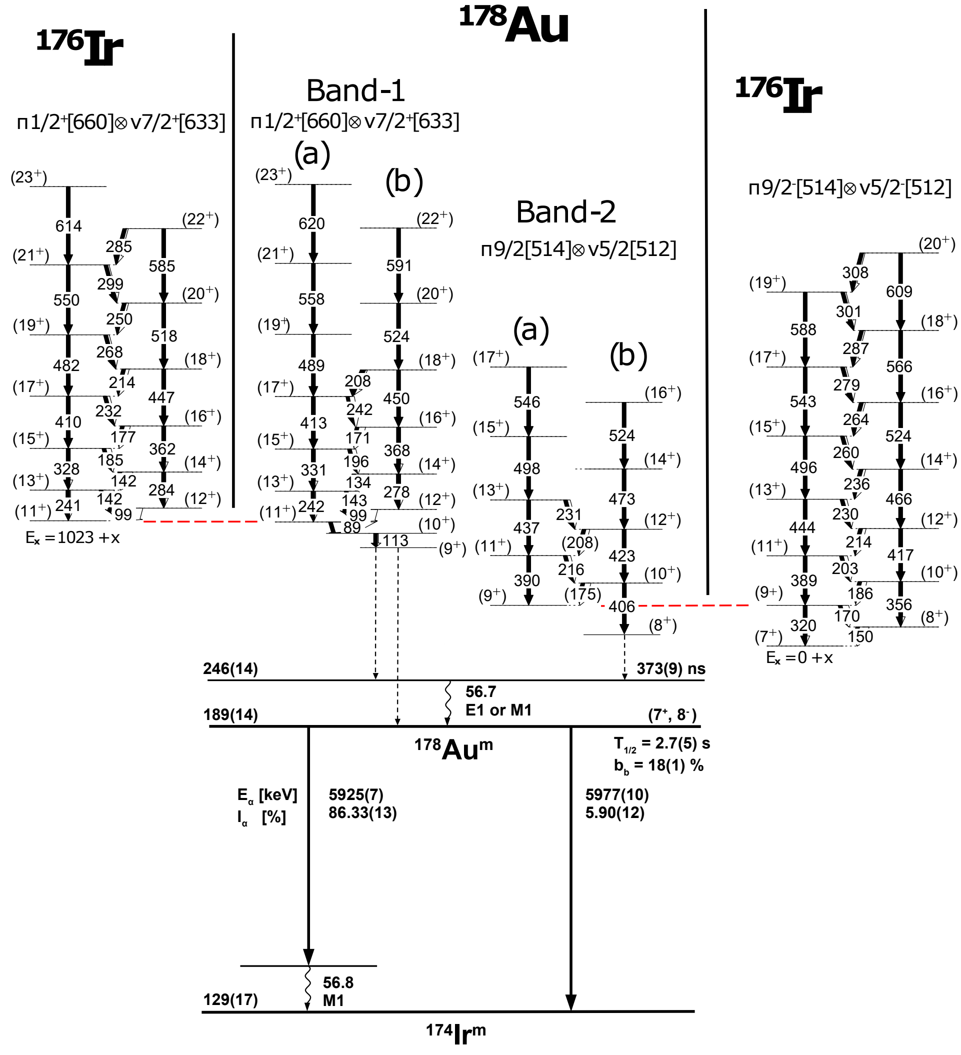

Figure 5.6: The level scheme determined from in-beam γ-ray spectroscopy of ^{178}Au. Figure taken from Ref. [10].

6
Results

In total, ^{178}Au^{g} was measured at IDS for 19 hours and 40 minutes. Because of a higher production rate, ^{178}Au^{m} data were collected for just 5 hours and 36 minutes. In their study [99], Davidson *et al.* observed approximately 5000 events in the 257-keV γ-ray ($4_1^+ \rightarrow 2_1^+$) peak when gated on the 170-keV γ ray ($2_1^+ \rightarrow 0_1^+$)[1]. In the present study, by comparison, about 400,000 170-257 keV coincidence events were recorded with each of the ^{178}Au^{g,m} beams. In Cubiss' study [1], the 170-keV peak in the γ-ray singles spectrum contained ≈400,000 for each of ^{178}Au^{g,m}, compared to 33 million and 7.2 million, respectively, in the present work[2]. The significantly higher statistics available in the present work allowed many new transitions to be added to the various decay schemes presented in this Chapter.

While the decay measurements of ^{178}Au^{g,m} were being made, the tape was typically moved approximately once per hour. This interval is significantly longer than the half lives of ^{178}Au^{g,m} [3.81(12) and 2.82(4) s, respectively - see Sec. 6.2] and their daughters. Therefore, in addition to studying the α and β decay of ^{178}Au^{g,m}, the daughters' decays were also investigated. These different decay paths are shown in Fig. 6.1 and discussed in this Chapter.

6.1 ^{178}Au α decay to ^{174}Ir

The α-decay singles spectra recorded at IDS for ^{178}Au^{g,m} are shown in Figs. 6.2(a,b), respectively. The corresponding prompt α-γ coincidence matrices (produced with the condition that $|\Delta t_{\alpha\gamma}| \leq$150 ns) are shown in Figs. 6.2(c,d). Projections of these matrices onto the E_γ axis for the regions inside the red dashed lines drawn on these α-γ matrices are shown in Figs. 6.2(e,f). The shapes of these were chosen to minimise the amount of background or grand-daughter decays included in the spectra. The description of the analysis of the α decay of ^{178}Au^{g,m} is split by parent state between Secs. 6.1.1 and 6.1.2.

[1] No singles spectrum is given in Ref. [99], which is why the number of events in the 170-257-keV γ-γ coincidence peak are compared to those available in the present work.

[2] A γ-γ coincidence matrix could not be constructed in Ref. [1] as the experimental setup used was optimised for α-particle detection efficiency. Hence, that study's statistics were compared to those available in the present work using singles spectra.

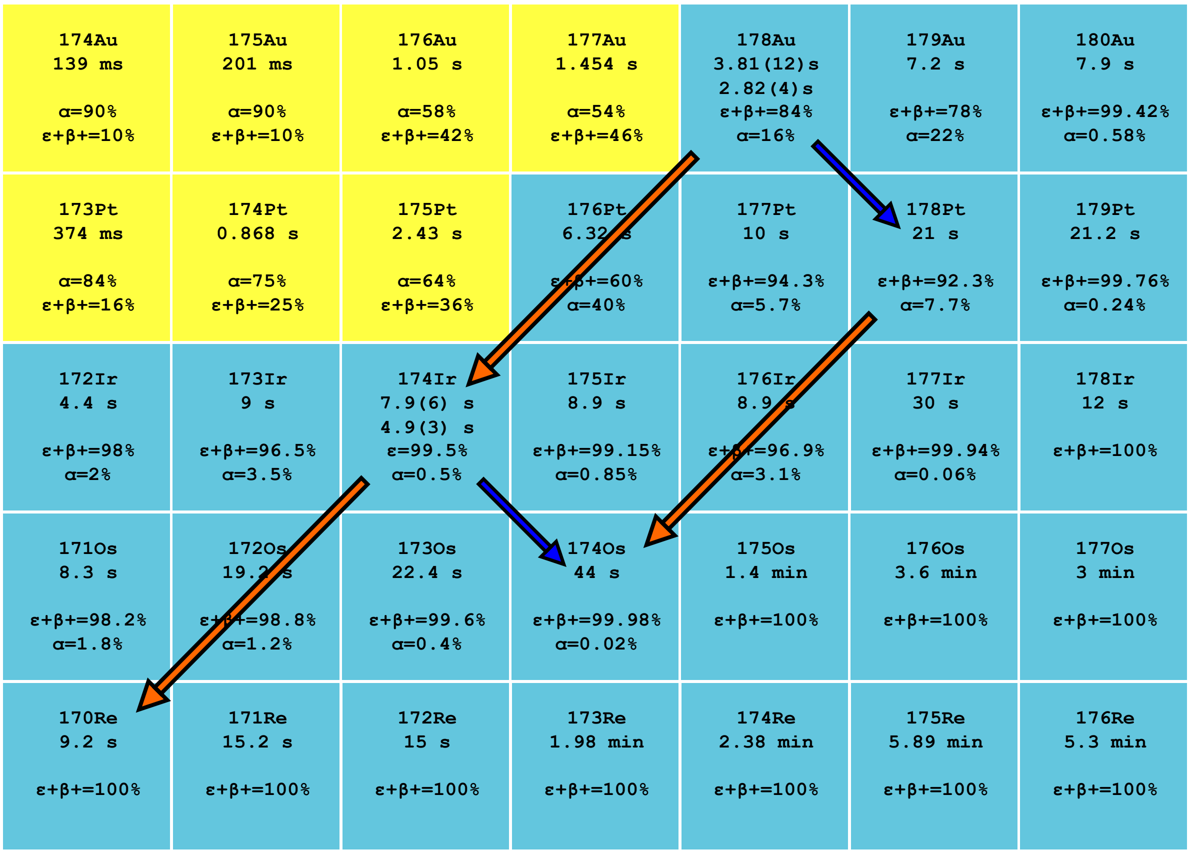

Figure 6.1: Part of the chart of nuclides [33] with the decays from ^{178}Au and its daughters shown with colour-coded arrows (orange arrows: α decay, blue arrows: EC/β^{+} decay). The half lives and branching ratios for the nuclides studied are taken from Refs. [2, 33, 99, 102, 111–116].

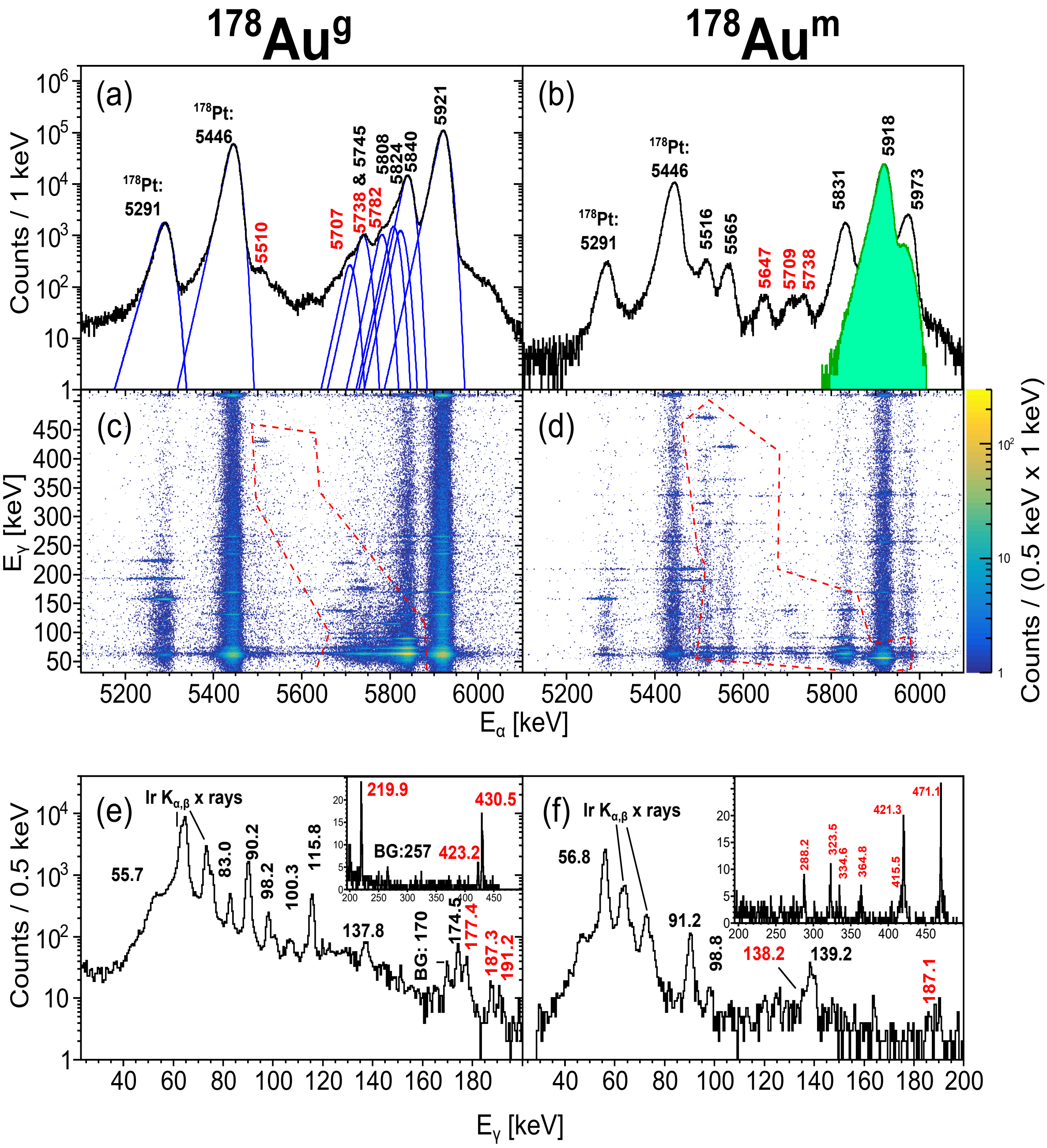

Figure 6.2: (a,b): the α-decay singles spectra for ^{178}Au^g and ^{178}Au^m, respectively. Some of the individual components of the sum of Crystalball fits [88] are shown in (a) to illustrate the overlap between many peaks in the region 5600 keV $\lesssim E_\alpha \lesssim$ 5850 keV. The peaks shown in green in (b) are the result of a Monte-Carlo simulation of the α-CE summing peak that artificially increases the apparent size of the 5973 keV α-decay peak in green. (c,d) - Prompt α-γ matrices for ^{178}Au^g and ^{178}Au^m, respectively. The polygons drawn on (c,d) with dashed red lines indicate the gates used to produce the γ-ray energy spectra shown in (e,f), respectively. Insets in (e,f) show higher energy regions of each spectrum. The energy labels for α- and γ-decay peaks seen in Ref. [1] are shown in black while new ones are shown in red.

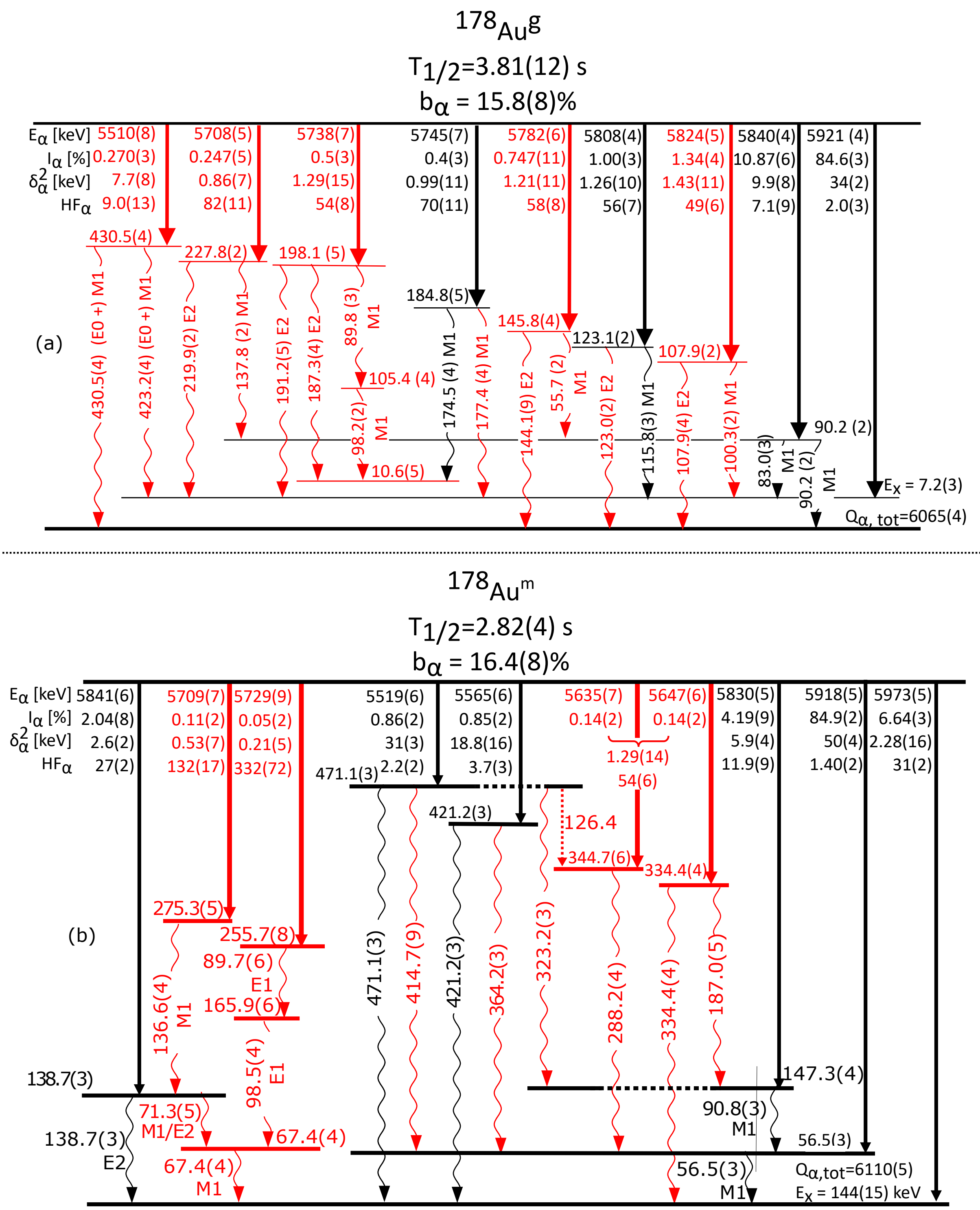

Figure 6.3: The α-decay schemes deduced in this study for (a) ^{178}Au^{g} and (b) ^{178}Au^{m}. Transition energies are given in keV. States and decays reported in Ref. [1] are shown in black while newly identified ones are shown in red.

6.1.1 α decay of ^{178}Au^{g} $\rightarrow^{174}$Ir^{g}

The most prominent peaks in the α-decay singles spectrum of ^{178}Au^{g} are at 5921(4) and 5840(4) keV. At lower energies, there are many peaks that overlap significantly with one another - see the constituent Crystalball functions of a fit to the spectrum shown in Fig. 6.2(a). The singles spectrum was used in conjunction with projections of the α-γ coincidence matrix shown in Fig. 6.2(c). The most important projections onto the E_α axis are shown in Fig. 6.4. All coincidences identified are summarised in Table 6.1.

Table 6.1: Summary of the α-decay paths for ^{178}Au^{g} giving the energies E_α, relative intensities, I_α, coincident γ-ray energies (E_γ), relative intensities (I_γ) and multipolarities, and their respective $Q_{\alpha,tot}$ values. For decay paths also reported in Ref. [1], the α-decay- and γ-ray energies are given together in the format E_α-E_γ.

E_α [keV]	E_γ [keV]	I_γ	Multipolarity	$Q_{\alpha,tot}$ [keV]	E_α-E_γ [1] [keV]
5921(4)	-	-	-	6058(4)	5922(5)
5840(4)	90.2(2)	100	M1	6065(4)	5840(10)-90.0(3)
	83.0(3)	32.1(9)	M1	6057(4)	5840(10)-82.8(3)
5824(5)	107.9(4)	8.0(7)	E2	6066(5)	
	100.3(2)	2.5(4)	M1	6058(5)	
5808(4)	123.0(3)	0.44(14)	E2	6065(4)	
	115.8(3)	9.1(8)	M1	6057(5)	5811(10)-115.7(3)
5782(6)	144.1(9)	1.8(3)	E2	6061(6)	
	55.7(2) + 90.2(2)	3.8(2)	M1	6064(6)	
	55.7(2) + 83.0(3)	3.8(2)	M1	6056(6)	
5745(7)	177.4(3)	2.2(4)	M1	6055(7)	
	174.5(4)	2.4(4)	M1	6052(7)	5750(15)-174.8(5)
5738(7)	191.2(4)	1.3(2)	E2	6062(8)	
	187.3(4)	1.4(2)	E2	6057(8)	
	89.8(3) , 98.2(2)	2.5(3) , 4.0(5)	M1, M1	6058(8)	
5708(5)	219.9(7)	1.4(3)	E2	6059(5)	
	137.8(4) + 90.2(2)	1.7(2)	M1	6067(5)	
	137.8(4) + 83.0(3)		M1	6060(5)	
5510(8)	430.5(4)	2.7(5)	E0+M1	6067(8)	
	423.2(4)	0.6(2)	E0+M1	6060(8)	

In Ref. [1], a 5922(5)-keV α decay was assigned as feeding of the ground state of ^{174}Ir directly and as accounting for 86.49(9)% of the α decays from ^{178}Au^{g}. This corresponds to the 5921(4)-keV α decay seen in the present work, which was not coincident with any γ rays, except through time-random coincidences, and gives Q_α=6058(4) keV.

The α decay at 5840(4) keV (corresponding to the 5840(10)-keV decay reported in Ref. [1]) is coincident with two γ rays at 83.0(3) and 90.2(2) keV - see Figs. 6.4(a,b). These decay paths give $Q_{\alpha,tot}$ values of 6057(4) and 6065(4) keV, respectively.

Three other α-decay peaks [5824(5), 5808(4), and 5510(8)] were found to be coincident with a pair of γ rays that differ in energy by $\approx$7 keV and give $Q_{\alpha,tot}$ values consistent with those of the 5840-83.0/90.2-keV groups - see Table 6.1. Therefore, the 90.2-keV γ ray was assigned as a transition directly to the ground state of ^{174}Ir. The 83.0-keV γ ray was assigned as feeding a 7.2(3)-keV state which is also directly fed by the 5921-keV α decay. The 5840-90.2-keV coincidence group was used to define the total energy available for this decay, $Q_{\alpha,ref}$=6065(4) keV. The 5922-keV α decay no longer being assigned as feeding of the ground state of ^{174}Ir causes a change in the calculated excitation energy of the isomer, ^{174}Ir^{m} - see Sec. 6.1.3.

The α decay at 5708 keV is coincident with two new γ rays at E_γ =219.9(7) keV and 137.8(4) keV [see Figs. 6.4(d,e)], as well as the already established 90.2- and 83.0-keV transitions - see Figs. 6.4(a,b). Based on their $Q_{\alpha,tot}$ values and energy difference, these new γ rays are assigned as feeding the 7.2- and 90.2 keV states, respectively.

The 5782-keV α decay is coincident with the 90.2, and 83.0 keV γ rays and a newly observed transition at 55.7(2) keV [see Fig. 6.4(c)], in addition to the 144.1-keV γ ray that feeds the ground state directly. The 55.7-keV γ ray was found to be in prompt γ-γ coincidence ($|\Delta t_{\gamma\gamma}| \leq$ 100 ns) with the 90.2-, and 83.0-keV transitions which therefore form cascades parallel to the 144.1-keV transition. Due to the low statistics for the 144.1(9)-keV γ ray, the excitation energy of the state populated by the 5782 keV α decay was determined to be 145.8(4) keV using the 55.7-90.2 keV cascade, rather than the direct decay.

The γ-ray energy spectrum produced by gating on the E_α ≈5740 keV region is shown in Fig. 6.5 (a). When separate gates are placed on each of the labelled γ rays, two distinct α-decay peaks are revealed at 5745(7) and 5738(7) keV - see Fig. 6.6. The 5745-keV α decay is coincident with the 177.4(3)- and 174.5(4)-keV γ rays, while the 5738-keV decay is coincident with the γ rays at 191.2(2), 187.3(3), 89.8(3), and 98.2(2) keV. The $Q_{\alpha,tot}$ values for the 5745-177.4-, and 5738-187.3-keV groups are consistent with that of the 5840-83.0-keV group, so are assigned as feeding the 7.2-keV state.

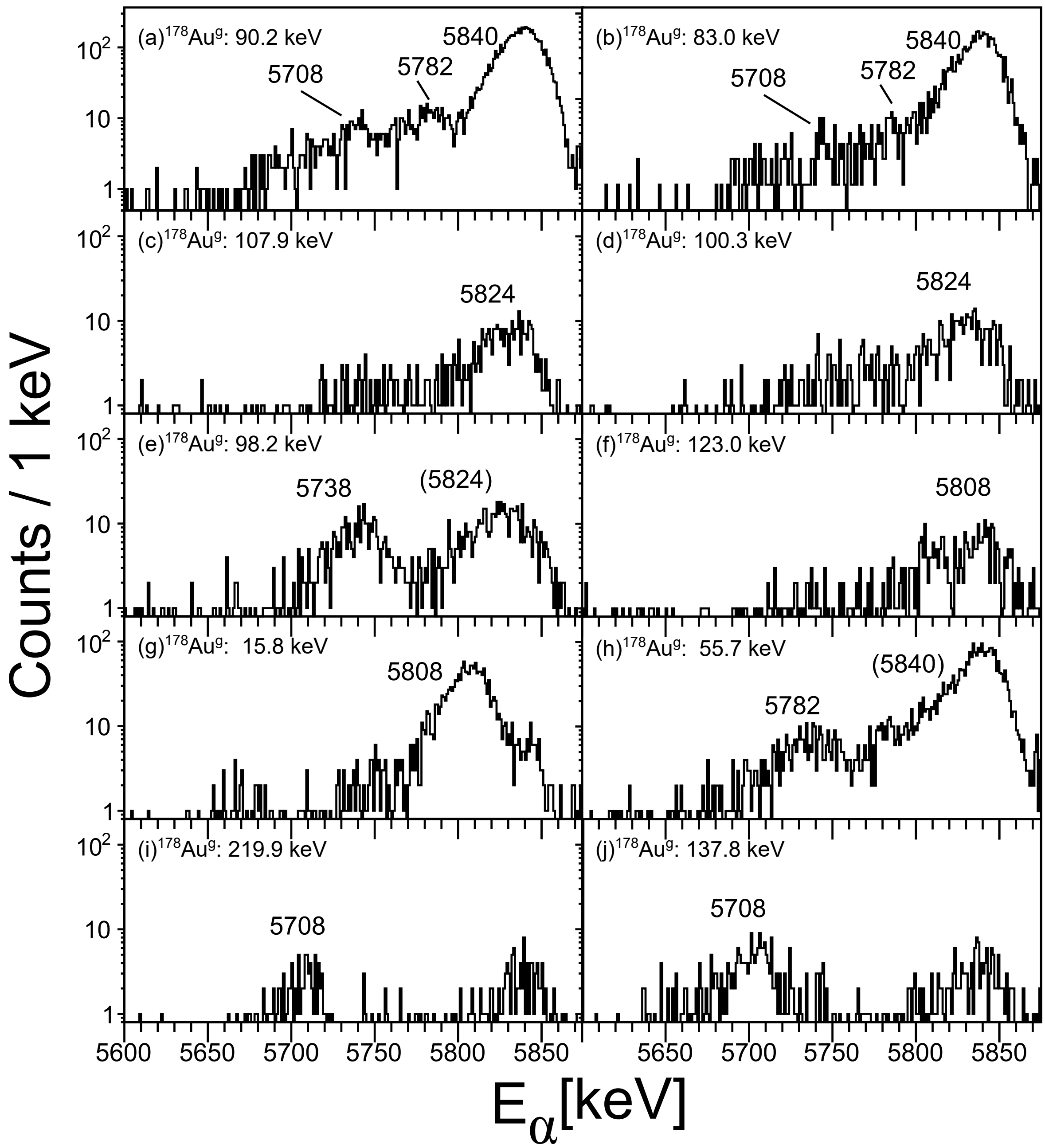

Figure 6.4: Projections of the α-γ coincidence matrix in Fig. 6.2(c) on the γ-ray energies shown on each panel. No background subtraction for these projections has been performed. The 5824-keV α-decay peak is present in (e) because of a strong overlap with the gate used and the 100.3-keV γ-ray peak. The 5782-keV α decay is present in (h) for a similar reason, as the gate on the 55.7-keV transition overlaps significantly with the K x-ray peaks.

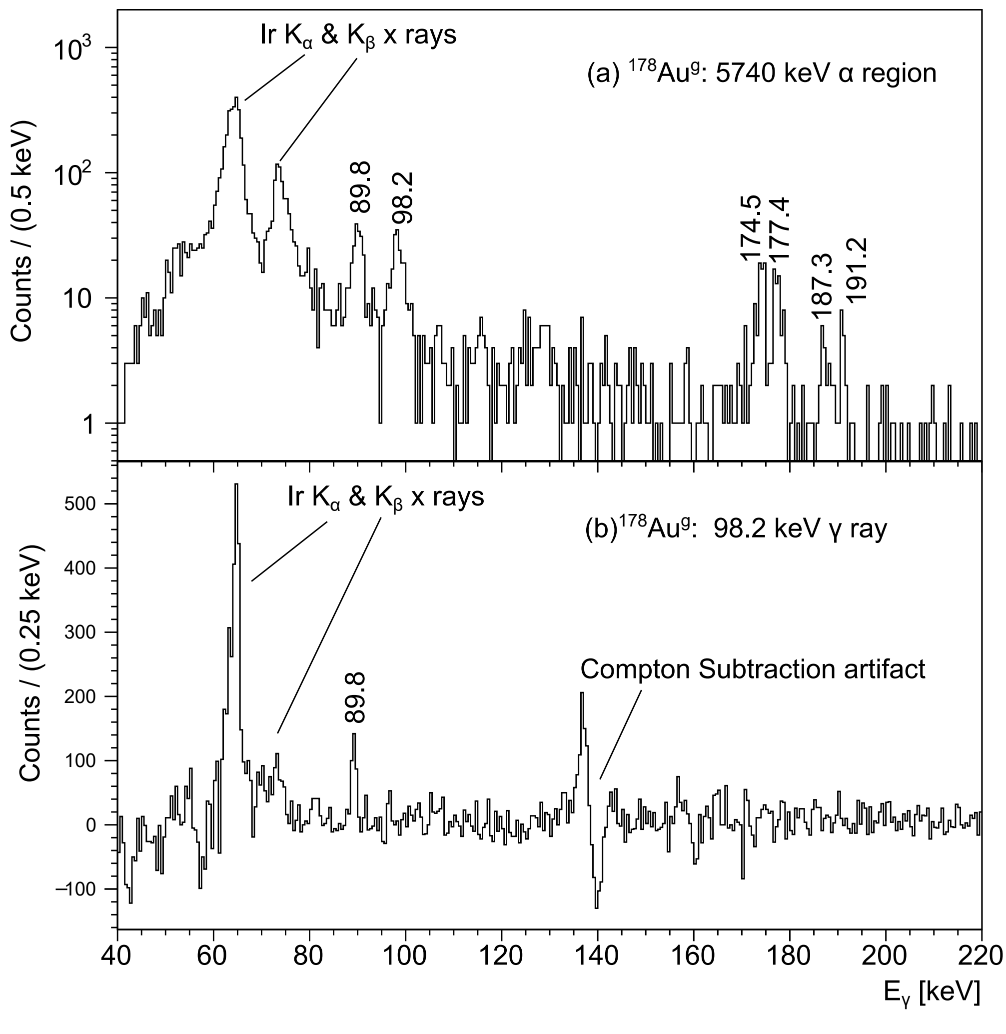

Figure 6.5: (a) Projection of the α-γ matrix shown in figure 6.2(c) on the peak at $E_\alpha \approx$5740 keV. (b) Background-subtracted projection of the γ-γ matrix gated on the 98.2 keV γ ray, confirming the coincidence with the 89.8-keV transition. The background-subtraction method is explained in Sec. 6.3 and illustrated in Fig. 6.17.

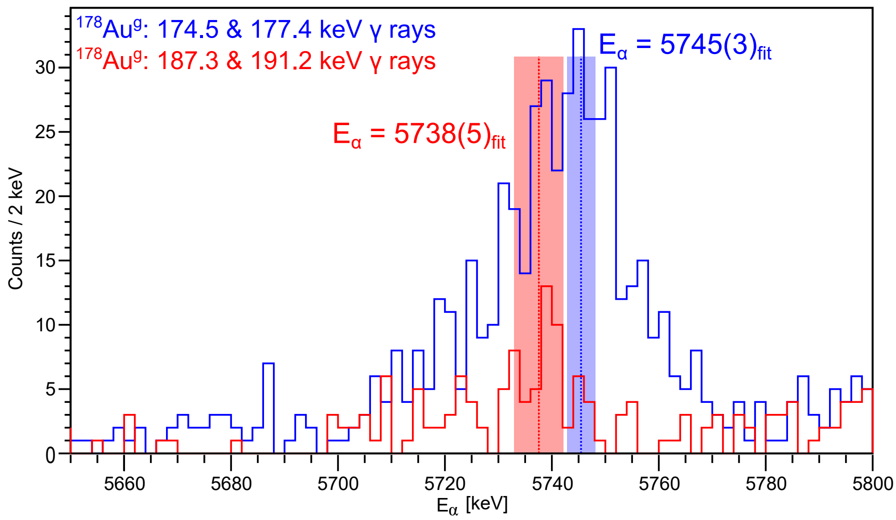

Figure 6.6: Projections of the α-γ matrix gating on the 174.5- and 177.4-keV γ rays (blue) and the 187.3- and 191.2-keV γ rays (red). The dotted lines indicate the mean values obtained from fitting each histogram with a Crystalball function. The shaded regions show the 1-σ statistical uncertainty region of these fit values.

The 89.8-, and 98.2-keV γ rays are in coincidence with each other [see Fig. 6.5 (b)] so form a cascade parallel to the 187.3-keV transition, feeding of a 10.6-keV state also populated by the 5745-174.5-keV decay path. The 5738-191.2- and 5745-177.4-keV groups are assigned as feeding of the ground state of ^{174}Ir. The 89.8-keV γ ray must be distinct from the 90.2-keV transition because there is no peak at 83.0 keV in Fig. 6.5(a).

Two γ rays at 423.2(4) and 430.5(4) keV are coincident with the 5510-keV α decay which is in coioncidence with a surprisingly large number of Ir K x rays - see Fig. 6.7. The shape of the K x-ray spectrum is also unusual; the efficiency-corrected relative intensities of the $K_{\alpha,\beta}$ x-ray peaks is $I(K_\beta)/I(K_\alpha) = 0.20(7)$, compared to a literature value of 0.345 [20]. Therefore, it is possible that this discrepancy in the intensity of the $K_{\alpha,\beta}$ x rays in Fig. 6.7 is partly due to contamination by some other γ ray(s) although to explain the number of 5510-keV α decays seen, at least one of the 430.5- or 423.2-keV transitions must have a significant E0 component.

Determination of γ-ray Multipolarities

Once the decay scheme was established, the multipolarity of each γ ray was investigated using two intensity-balance techniques. The total number of α decays feeding a short-lived state must equal the total number of γ-ray and CE transitions depopulating it. Therefore,

$$N_\alpha = \sum_i \frac{N_{\gamma,i}(\alpha_{tot,i} + 1)}{\mathcal{E}(E_{\gamma,i})}, \tag{6.1}$$

which can be rearranged to define the ratio R_{tot}

$$R_{tot} \equiv \frac{100}{N_\alpha} \sum_i \frac{N_{\gamma,i}\ (\alpha_{tot,i} + 1)}{\mathcal{E}(E_{\gamma,i})} = 100, \tag{6.2}$$

where N_α is the number of α decays feeding a particular state observed in the singles spectrum, $N_{\gamma,i}$ is the measured intensity of γ ray i depopulating that state, $\mathcal{E}(E_{\gamma,i})$

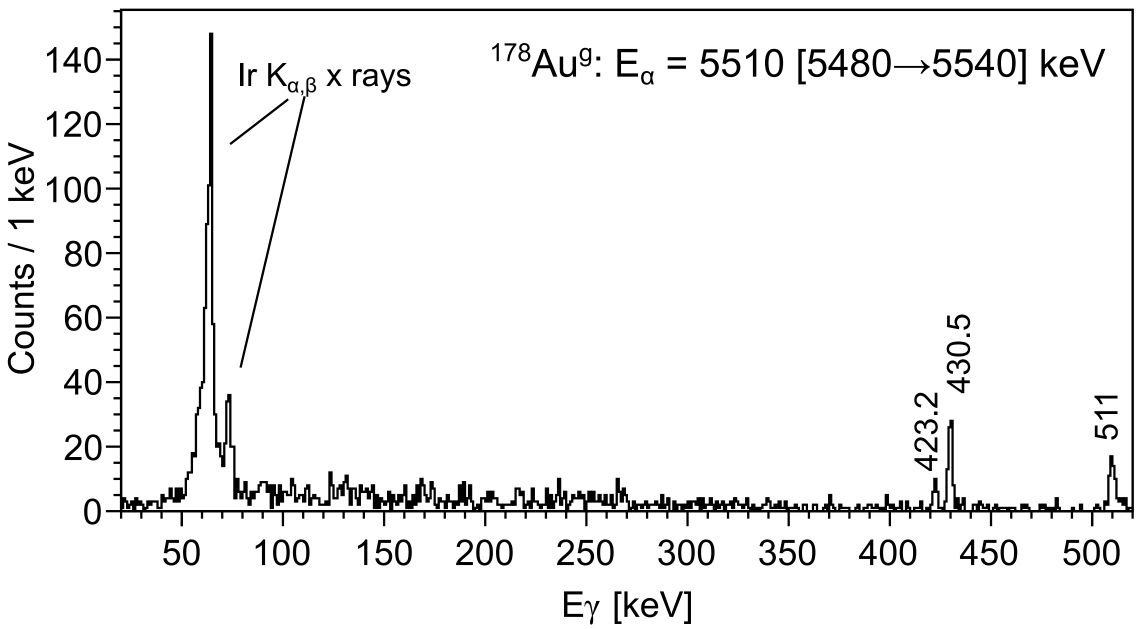

Figure 6.7: Projections of the α-γ matrix on the 5510-keV α decay.

is the absolute γ-ray detection efficiency, and $\alpha_{tot,i}$ is the total conversion coefficient. The quantity R_{tot} represents the ratio of the total number of transitions populating and depopulating a state, for a particular combination of multipolarities. The values $N_{\gamma,i}$ were determined by fitting Gaussian functions to the γ-ray peaks in α-gated spectra. The α-decay intensities were determined by fitting a series of Crystalball functions summed together to the α-decay singles spectrum. A single Crystalball function has the form [88]

$$f(x;A,B,n,\mu,\sigma) = \begin{cases} A\exp\left(-\frac{(x-\mu)^2}{2\sigma^2}\right) & \text{for } \frac{x-\mu}{\sigma} > -B, \\ A\left(\frac{n}{|B|}\right)^n \exp\left(-\frac{|B|^2}{2}\right)\left(\frac{n}{|B|}-|B|-\frac{x-\mu}{\sigma}\right)^{-n} & \text{for } \frac{x-\mu}{\sigma} \leq -B, \end{cases} \tag{6.3}$$

where A is the intensity, μ and σ define the high-energy Gaussian-like side of the function, and B and n define the shape of the low-energy tail of the distribution. This low-energy tail is required because α particles entering the silicon detectors at different angles will experience different effective dead-layer and tape thicknesses so will lose different amounts of energy before reaching the active part of the detector. All Crystalball functions included in the singles fit had the same shaping parameters (α, n, and σ) which were determined by fitting the γ-gated 5291-keV α-decay peak from ^{178}Pt to the 2_1^+ state in ^{174}Os. The individual Crystalball fits used for determination of the γ-ray multipolarities for ^{178}Au^g are shown in Fig. 6.2(a).

An alternative way to determine transition multipolarities is to compare the relative intensities of the K x rays and γ rays in coincidence with each α decay. Starting from the definition of the K conversion coefficient for transition i, $\alpha_{K,i}$, a ratio similar to R_{tot} can be defined for as

$$R_K \equiv \frac{100\cdot\mathcal{E}(E_{Kx})}{N_{Kx}}\cdot\sum_i \frac{N_{\gamma,i}\cdot\alpha_{K,i}(X)}{\mathcal{E}(E_{\gamma,i})} = 100, \tag{6.4}$$

where N_{Kx} is the number of K x rays observed in coincidence with the α decay populating a state and $\mathcal{E}(E_{Kx})$ is the absolute detection efficiency of the K x rays. The value of R_K is therefore equivalent to the ratio of expected K conversion for a particular set of transitions, compared to what was measured.

The condition that a transition is prompt limits its multipolarity to E0, E1, M1, or E2. Both R_{tot} and R_K strongly depend on the energy of a transition and its multipolarity. For a state depopulated by a single transition, Eqs. 6.2 and 6.4 can be solved exactly using the experimentally determined intensities to calculate the conversion coefficient. However, most states populated by the α decay of ^{178}Au were observed to depopulate by two or three parallel transitions. Therefore, R_K and R_{tot} are useful because they provide a way to compare different combinations of multipolarities. These different combinations are shown for the 5840-83.0/90.2-keV groups in Table 6.2.

Table 6.2: Tables showing the ratios (a) R_{tot} and (b) R_K, as defined in Eqs. 6.2 and 6.4, respectively. A value of 100 in both parts is expected for a pure combination of the transition multipolarities indicated by the row and column. Values within 1σ of 100 are shown with bold text.

(a)	R_{tot} values for each combination of multipolarities 90.2 keV γ				
		α_{tot}	E1	M1	E2
	α_{tot}	-	0.518	8.229	7.085
83.0 keV γ ray	E1	0.6373	32.4(11)	90(3)	81.0(14)
	M1	10.43	42.4(11)	**100(6)**	91.0(14)
	E2	10.09	41.7(12)	**97(6)**	90.2(14)
(b)	R_K values for each combination of multipolarities 90.2 keV γ				
		α_K	E1	M1	E2
	α_K	-	0.4162	6.776	0.825
83.0 keV γ ray	E1	0.5095	6(3)	76(8)	22(4)
	M1	8.583	35(4)	**104(8)**	49(5)
	E2	0.8199	11(3)	80(7)	26(3)

There are two combinations of multipolarities that produce R_{tot} values consistent with 100: M1-M1 and M1-E2 for the 90.2- and 83.0-keV transitions, respectively. These are the only combinations of multipolarities that can explain the relative intensity of the 5840-keV α decay and the two γ rays coincident with it. There are 25% more K x rays coincident with the 5840-keV α decay than would be expected for an M1-E2 assignemnt whereas an M1-M1 assignment correctly predicts the number of K x rays.

An equivalent process was performed using tables similar to Table 6.2 for each α decay from ^{178}Au^g except for those at E_α =5738 and 5745 keV. In these cases, the small energy difference between the two α decays meant that they could not be fitted individually in the α-decay singles spectrum. Also, six γ rays were observed in coincidence with these two α decays, which made checking every combination impractical.

The background-subtracted, prompt $\gamma-\gamma$ coincidence projection gated on the 98.2-keV γ ray [shown in Fig. 6.5(b)] was used to determine that $\alpha_{K,exp}$(89.2 keV)=7.2(6). This is in good agreement with the value expected for a pure M1 transition and an order of magnitude larger than for an E1 or E2 transition - see Table 6.3. Because the 98.2- and 89.2-keV transitions are in cascade, their total intensities must be equal when the correction for internal conversion is made. From this, it was determined that

α_{tot}(98.2 keV)=6.3(2). Thus, the 98.2-keV transition was also assigned as an M1 transition - see Table 6.3. It should be noted that, unless there is a strong E0 transition following either of these α decays, the 89.8- and 98.2-keV transitions both being M1 is the only way to explain the large number of K x rays seen in Fig. 6.5(b).

There is no parity change from the pair of M1 transitions comprising the 89.8-98.2-keV cascade, meaning that the parallel 187.3-keV transition cannot be E1. Also, since the two remaining γ rays coincident with each of these two α decays (174.5 and 177.4 keV, and 187.3 and 191.2 keV) are at similar energies and have almost identical intensities, it is highly likely that they have the same multipolarity as one another. Under these assumptions and correcting for the 89.8- and 98.2-keV transitions, it was determined that the 187.3- and 191.2-keV transitions are both pure E2 and the 174.5- and 177.4-keV transitions are both M1. This was done by comparing the total intensity of the combined α-decay peaks and the total number of K x-rays coincident with it with the total intensity of the six γ rays. No other combination of multipolarities for these six transitions yields a consistent intensity balance for both the total number of transitions and the total number K x rays coincident with these α decays.

Table 6.3: Summary of the total and K conversion coefficients for the γ rays coincident with the 5738- or 5745-keV α decays calculated using BrIcc [62]

	α_{tot}			α_K		
E_γ [keV]	E1	M1	E2	E1	M1	E2
89.8	0.524	8.33	7.22	0.4208	6.862	0.8265
98.2	0.418	6.45	4.97	0.3373	5.316	0.7713
174.5	9.70E-02	1.27	0.559	7.906E-02	1.257	0.5534
177.4	9.29E-02	1.21	0.526	7.59E-02	0.9906	0.2302
187.3	8.08E-02	1.04	0.435	6.19E-02	0.8509	0.2007
191.2	7.66E-02	0.976	0.404	6.29E-02	0.8033	0.1905

The 5510-keV α decay is coincident with a two γ rays at 423.2- and 430.5-keV. Given the relatively high energy of these transitions, there must be an E0 transition to explain the large number of K x rays coincident with the 5510-keV α decay.

6.1.2 α decay of ^{178}Au^m $\rightarrow^{174}$Ir^m

A similar analysis procedure was followed to produce the α-decay scheme shown in Fig. 6.3(b) for ^{178}Au^m $\rightarrow^{174}$Ir^m. The highest energy α-decay peak in Fig. 6.2(b) is at 5973(5) keV (reported as 5977(10) keV in Ref. [1]), giving $Q_{\alpha,ref} \equiv 6110(5)$ keV. The most intense α decay observed in the ^{178}Au^m data is at 5918(5) keV and is coincident with a single γ ray at E_γ =56.5(3) keV- see Fig. 6.8(a). The $Q_{\alpha,tot}$ value for this decay is 6111(5) keV, which is consistent with $Q_{\alpha,ref}$, suggesting both feed the same state in ^{174}Ir. The 5918-keV α decay was therefore used to establish a state at 56.5 keV. Four other α-γ coincidence groups were observed that give $Q_{\alpha,tot}$ values consistent with $Q_{\alpha,ref}$ at 5841-138.7(3), 5647-334.4(4), 5565-421.2(3), and 5519-471.1(3) keV [see Table 6.4 and Figs. 6.2(d,f), 6.9, and 6.12].

Table 6.4: Summary of the α-decay paths for ^{178}Au^m with the energies E_α, relative intensities, I_α, the coincident γ-rays' energies, E_γ, their relative intensities, I_γ, and their respective $Q_{\alpha,tot}$ values given. For decay paths also reported in Ref. [1], the α-decay- and γ-ray energies are given in the format E_α–E_γ. The observed but unplaced 5567-140.6-keV $\alpha - \gamma$ coincidence is included in bold for emphasis.

E_α [keV]	E_γ [keV]	I_γ	Multipolarity	$Q_{\alpha,tot}$ [keV]	E_α–E_γ [1] [keV]
5973(5)	-	-	-	6110(5)	5977(10)
5918(5)	56.5(3)	1000	M1	6111(5)	5925(7)-56.5(3)
5841(6)	138.7(3)		E2	6114(6)	5839(10)-139.2(3)
	71.9(6) + 67.4(4)		(M1/E2) + M1	6114(6)	
5830(5)	90.8(3)+56.5(3)	59(13)	M1	6113(6)	5839(10)-91.2(3)
5729(9)	98.5(4) + 89.7(6) + 67.4	1.6(2)	E1 + E1	6117(7)	
5709(6)	136.6(4)+138.7	4.5(7)	M1	6115(7)	
	136.6(4)+71.9(6)+67.4(4)		M1	6108(7)	
5647(6)	334.4(4)	4.9(10)	-	6111(6)	
	187.0(5)+90.8+56.5	2.3(6)	-	6111(6)	
5635(7)	288.2(5)+56.5		-	6109(7)	
5565(6)	421.3(3)	30(2)	-	6114(6)	5571(7)-421.4(10)
	364.8(3)+56.5(3)	4.5(9)	-	6115(6)	
5567(7)	**140.6(4)**		-	**5836(7)**	
5519(6)	471.1(3)	2.5(3)	-	6114(6)	5521(7)-472.1(10)
	415.5(7)+56.5(3)	0.9(4)	-	6115(6)	
	404.1(6) + 67.4	0.9(4)	-	6117(6)	
	323.5(5)+90.8(3)+56.5(3)	9.1(13)	-	6114(6)	
	288.2		-	5939(8)	

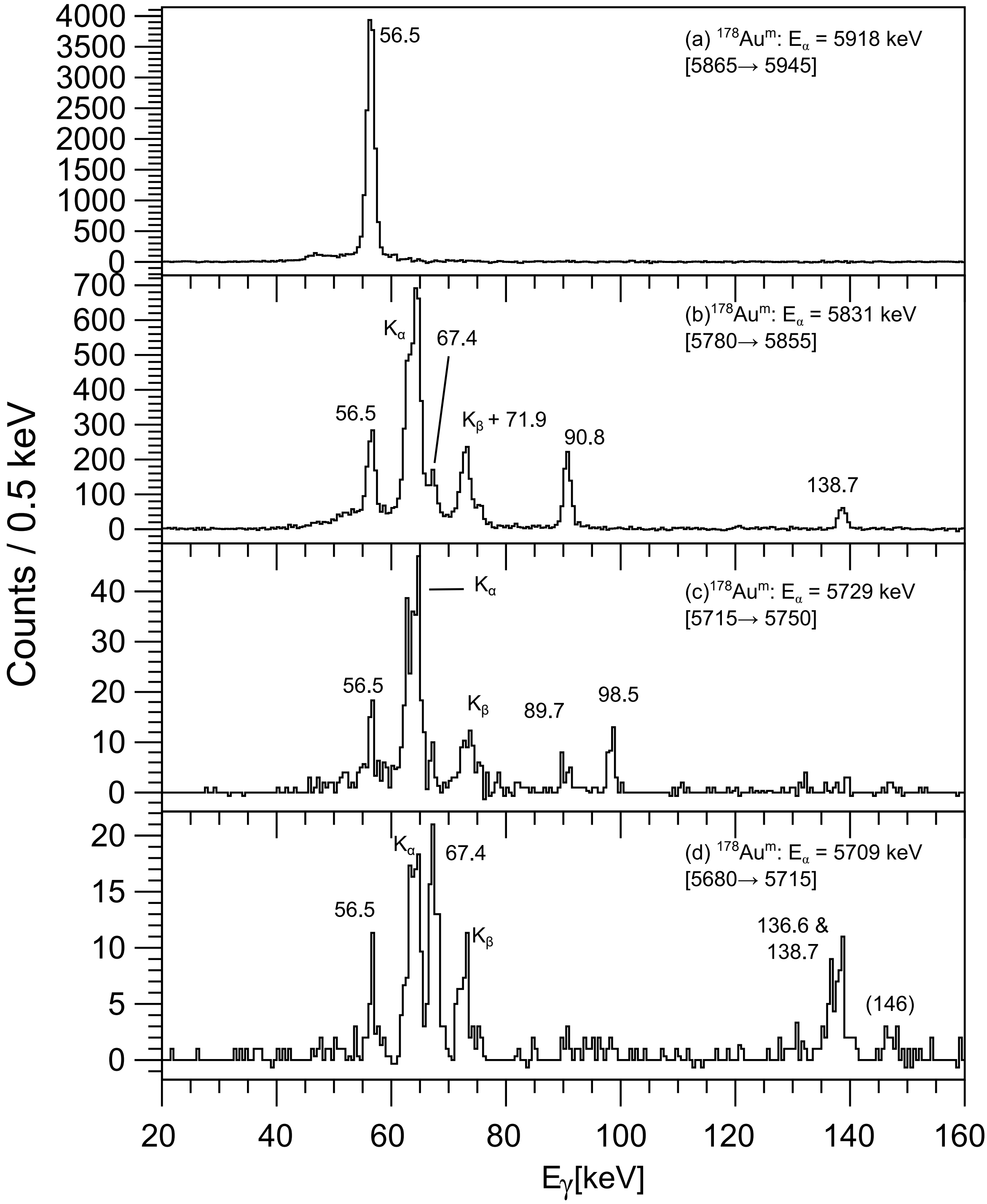

Figure 6.8: Projections of the α-γ matrix in figure 6.2(d) produced using the indicated gates. The peak in (d) at $\sim$146 keV was not placed in the decay and is quite likely a statistical fluctuation in background.

The projection of the 5831-keV α-decay peak, contains four well-defined transitions at E_γ =56.5(3), 67.4(4), 90.8(3), and 138.7(3) keV - see Figs. 6.8(b) and 6.9. The α-particle energy spectra produced by placing the inverse gates on the three strongest of these γ rays show a shift in the centre of the peaks (see Fig. 6.10), suggesting that there are two separate α decays at 5830(5) and 5841(6) keV. The 5830-keV α decay is assigned as feeding of a 147.3(4) keV state which decays by a 90.8(3) keV γ ray to the 56.5-keV state. The E_α=5841-keV decay is assigned as feeding of a 138.7(3) keV state which decays to $^{174}Ir^m$ directly, or through a 67.4-71.3-keV cascade. The 71.3-keV peak is partially obscured by the iridium $K_{\beta 1}$ x-ray peak (E = 73.560 keV [20]). However, when this is plotted alongside a clean K x-ray spectrum collected with the ground-state data, this γ-ray peak becomes clearly visible, as shown in Fig. 6.9.

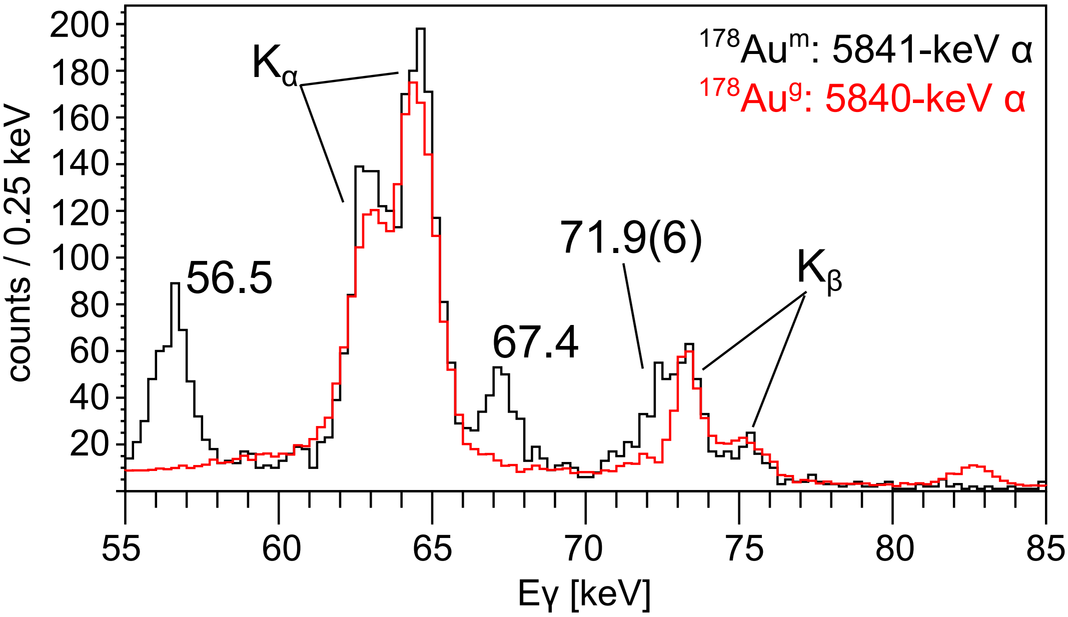

Figure 6.9: The γ spectra obtained using a narrow gate on the 5841 keV α decay from $^{178}Au^m$ (black) with the scaled x-ray spectrum gated on the 5840 keV α decay from $^{178}Au^g$ overlaid (red) to demonstrate the extra shoulder on the K_β x-ray peak from a γ-ray at 71.9(6) keV.

There is an α-decay peak at 5738 keV in coincidence with γ rays at 67.4, 89.7(6), and 98.5(4) keV - see Fig. 6.8(c). When gates are placed on these γ-rays, the resulting α-decay peak is shifted compared to the singles spectrum with a mean at 5729(9) keV, possibly indicating an α-decay doublet or significant α-electron summing. Based on the $Q_{\alpha,tot}$ value (determined using the γ-gated α-decay energy) this α decay is assigned as populating a 255.7(8)-keV state, which then decays to the 67.4 keV state through an 89.7-98.5 keV cascade. Additionally, there is a small peak at 56.5 keV which could indicate additional, unseen transition(s) that populate(s) the 56.5-keV state, shown on the decay scheme with a dashed line to indicate tentative status.

The $^{178}Au^g$ data containing an α decay at 5738 keV (coincident with a pair of γ rays at 98.2 and 89.8 keV) could indicate there is some contamination leading to the same decay being observed in both data sets. To check this, the full γ spectra obtained by placing the same α-decay energy gate for each dataset are given together in Fig. 6.11.

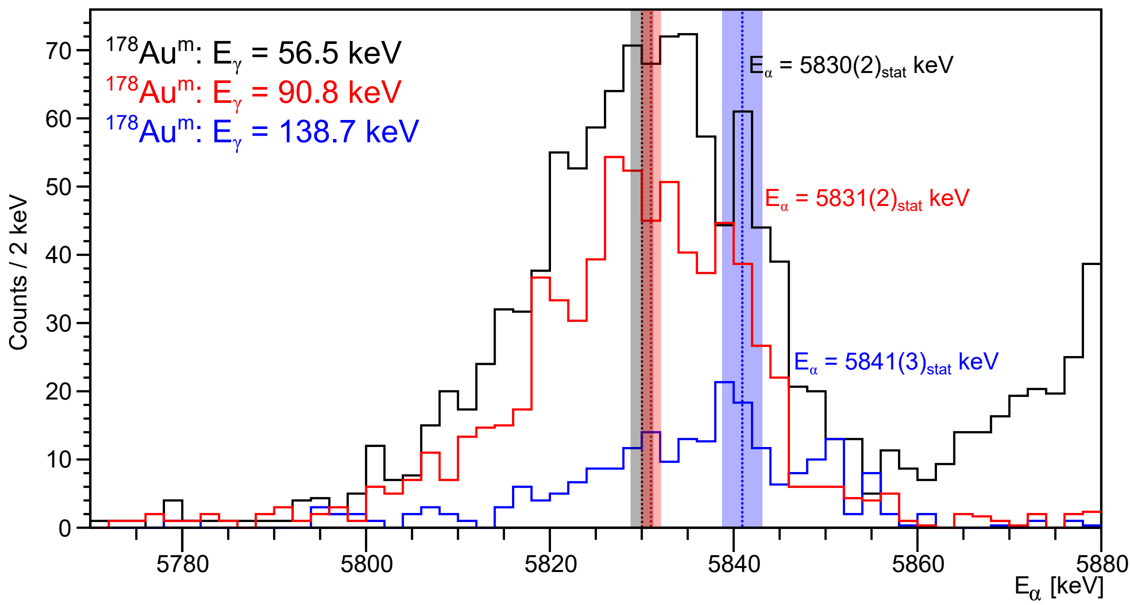

Figure 6.10: Projections of the α-γ matrix shown in figure 6.2(d) using the indicated gates on γ-ray energies. Dashed lines are shown in the appropriate colour at the mean energy from a Crystalball fit, with the shaded areas showing the $\pm 1\sigma$ regions. Gates on the 67.4- and 71.9 keV γ rays are not shown as these overlap significantly with various K x-ray peaks, making these spectra unhelpful.

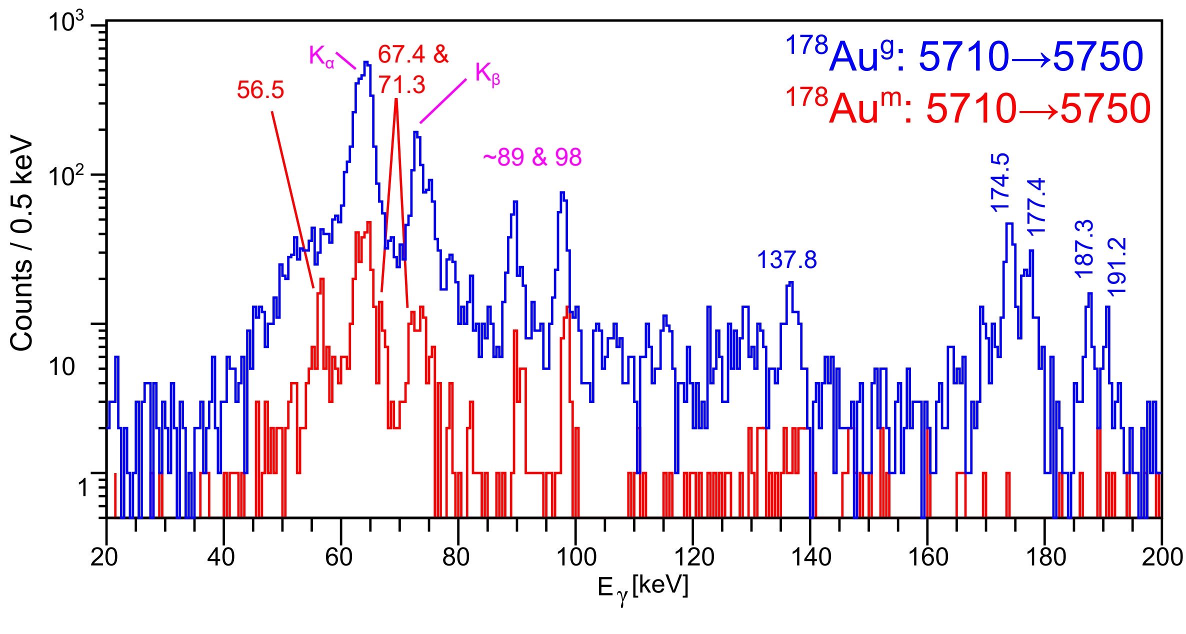

Figure 6.11: Projections of the α-γ matrices for ^{178}Au^{g} (blue) and ^{178}Au^{m} (red) using the same α-energy gate on the 5738/5729-keV region [5710→5750 keV].

Both spectra shown in Fig. 6.11 include the expected γ rays at 89 and 98 keV, in addition to the Ir $K_{\alpha,\beta}$ x-ray peaks. The similarities between these spectra end there, however, as they share no other γ-ray peaks in common. This suggests that the similarity in γ-ray energies for the transitions coincident with the 5738- and 5729-keV α decays from $^{178}Au^{g,m}$ is entirely coincidental.

The 5709-keV α decay is coincident with a γ-ray doublet comprising peaks at 136.6(4) and 138.7 keV as well as the 67.4-keV γ ray - see Fig. 6.8(d). The statistics are too low to determine if the K_β x-ray peak broadening from the 71.3-keV transition is also present in the spectrum gated on $E_\alpha = 5709$ keV. The 136.6-keV γ ray is assigned as feeding of the 138.7-keV state from a 275.3(5)-keV state populated directly by the 5709-keV α decay.

Three new γ rays are coincident with the 5647-keV α decay E_γ=187.0(5), 288.2(5), and 334.4 keV, in addition to the 56.5- and 90.8-keV transitions - see Fig. 6.12(a). Based on $Q_{\alpha,tot}$, the 334.4-keV γ ray was assigned to feed directly to $^{174}Ir^m$ while the 187.0 keV transition was assigned as feeding of the 147.3-keV state. The 288.2-keV transition cannot be confidently placed in the decay scheme.

The 5565(6)-keV α decay is coincident with four γ rays at 56.5, 140.6(4), 364.2(3) and 421.2 keV, as shown in Fig. 6.12(b). The 421.2- and 364.2-keV γ rays are assigned as feeding of $^{174}Ir^m$ and the 56.5 keV state, respectively, while the 140.6-keV γ ray cannot be confidently placed in the decay scheme.

In addition to the 471.1-keV γ ray reported in Ref. [1] and the previously discussed 56.5-, 67.4-, and 90.8-keV γ rays, the 5519-keV α decay is coincident with two new γ rays at 323.2(3), and 414.7(9) keV - see Fig. 6.12(c). Based on their respective $Q_{\alpha,tot}$ values these are assigned as feeding of the 147.3-, and 56.5-keV states, respectively. There is some overlap between the gate on the 5519-keV peak and the 5478-keV α decay from ^{174}Ir to ^{170}Re, leading to the 190.2- and 210.3 keV γ rays observed in e.g. Ref. [2] being seen in Fig. 6.12 (c). These are discussed further in Sec. 6.5 in which the full analysis of the α decay of ^{174}Ir is presented.

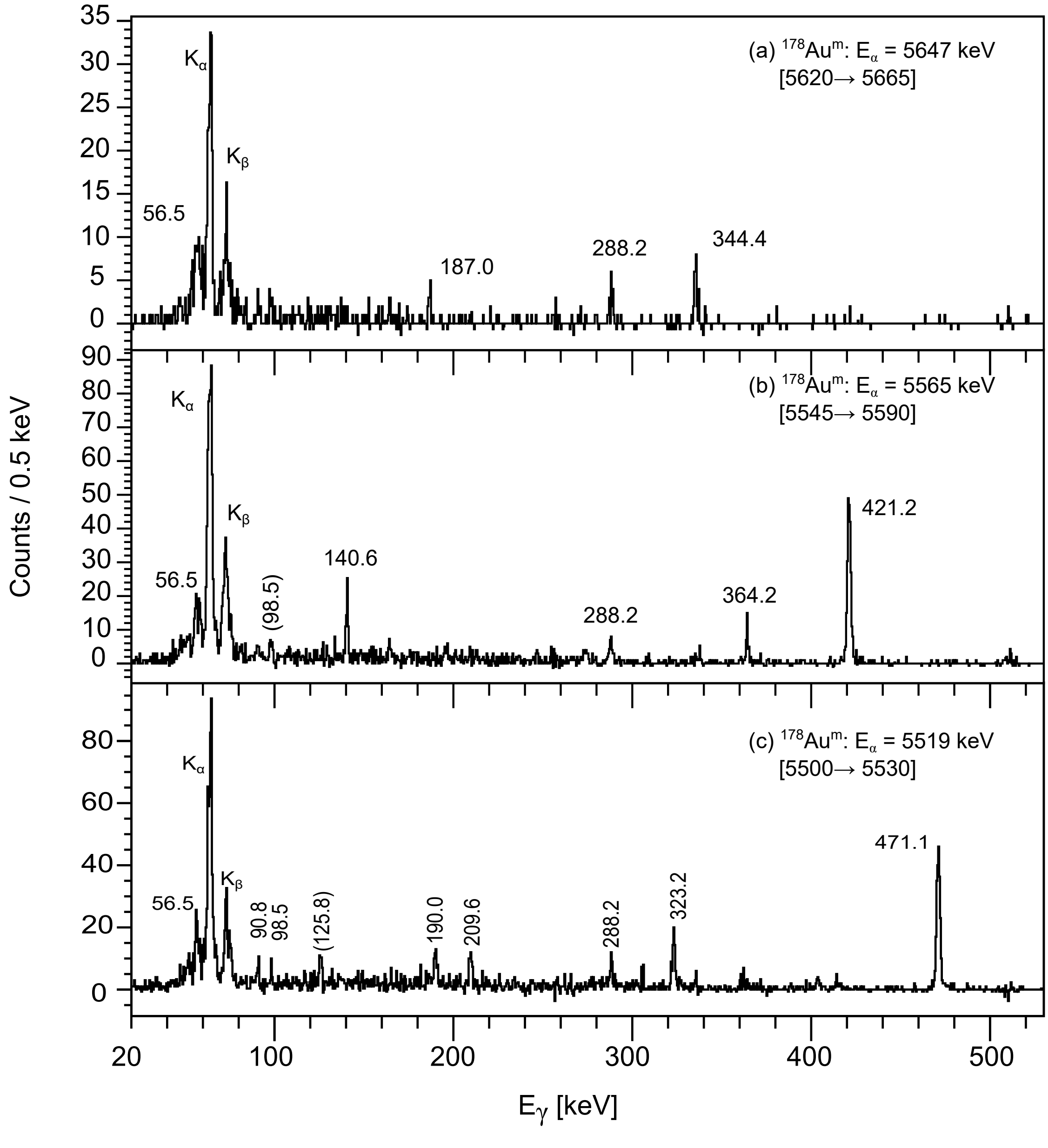

Figure 6.12: Projections of the α-γ matrix in Fig. 6.2(d) using the indicated gates on α-decay energies.

The multipolarities of the various γ rays observed following the α decay of ^{178}Au^m were investigated using the same methods as outlined in Sec. 6.1.1. Unlike ^{178}Au^g, the α decay of ^{178}Au^m populated several states that de-excited through more than just two transitions. This, and the relatively low conversion coefficients for some of these γ rays meant multipolarity assignments could not be made for all transitions.

6.1.3 Excitation Energy of the ^{174}Ir^m

Mass measurements of ^{178}Au^{g,m} performed at the ISOLTRAP MR-ToF [100] were reported in Ref. [1]. The excitation energy of ^{178}Au^m was determined to be 189(14) keV, based on the difference in the measured masses. Using this and the difference in the $Q_{\alpha,tot}$ values determined for ^{178}Au^{g,m}, the excitation energy of the isomer ^{174}Ir^m was determined to be 144(15) keV. Most of the difference between this and the value of 129(17) keV given in Ref. [1] is due to the difference in the $Q_{\alpha,tot}$ value for the decay of ^{178}Au^g as the 5921-keV α decay is not assigned as feeding directly to the ground state of ^{174}Ir in the present work.

6.1.4 Determination of the α-decay Branching Ratios

The α- and EC/β^+-decay branching ratios were calculated by comparing the number of α decays from ^{178}Au^{g,m} $\rightarrow$^{174}Ir to the number for ^{178}Pt$\rightarrow$^{174}Os. Correction was made for the α-decay branching ratio of ^{178}Pt, $b_\alpha(^{178}\mathrm{Pt})$=7.7(3)% [117]:

$$b_\alpha(^{178}\mathrm{Au}^g) = \frac{N_\alpha(^{178}\mathrm{Au}^g)}{N_\alpha(^{178}\mathrm{Au}^g) + N_\beta(^{178}\mathrm{Au}^g)} = \frac{N_\alpha(^{178}\mathrm{Au}^g)}{N_\alpha(^{178}\mathrm{Au}^g) + \frac{N_\alpha(^{178}\mathrm{Pt})}{b_\alpha(^{178}\mathrm{Pt})}}, \tag{6.5}$$

$$b_{\beta+/EC}(^{178}\mathrm{Au}^{g,m}) = 1 - b_\alpha(^{178}\mathrm{Au}^{g,m}). \tag{6.6}$$

Equations 6.5 and 6.6 are valid if there is a negligible amount of isobaric contamination of ^{178}Pt, or production of some other species that can decay to ^{178}Pt. Measurements were made during which the first step in the laser-ionisation scheme was disabled. The α and γ spectra collected during such runs was indistinguishable from background, meaning the ^{178}Au^{g,m} beams were clean.

The most likely candidate to escape the target before decaying to ^{178}Pt is ^{182}Hg. This α-decay path was previously studied (see e.g. Refs. [118–120]) which established a dominant 5867-keV α decay to the ground state of ^{178}Pt and a much less-intense 5700-keV α decay to the 170-keV state. In neither the main runs, nor measurements during which the first step of the laser was turned off, were either of these α decays observed. There is also no evidence of EC/β^+ decay to ^{182}Pt (from ^{182}Au) that would be expected if a significant amount of ^{182}Hg was being produced [99].

The b_α values determined for ^{178}Au^{g,m} were found to be similar to one another at $b_\alpha(^{178}\mathrm{Au}^g)$=15.8(8)% and $b_\alpha(^{178}\mathrm{Au}^m)$=16.4(8)%. Both of these values are consistent with those reported in Ref. [1], but have a higher precision.

6.2 Determination of the Half Lives of ^{178}Au^{g,m}

The half lives of ^{178}Au^{g,m} were determined using dedicated measurements in which implantation was stopped but the tape was not moved and the DAQ continued recording for at least 1 minute. Decay curves for ^{178}Au^{g,m} are shown in Figs. 6.13(a,b), respectively. As $b_\beta \approx 5b_\alpha$ and the γ-ray detection efficiency was generally much higher than that for α particles, prompt γ ray transitions from ^{178}Pt were used in addition to all α decays in the range 5600 keV$\leq E_\alpha \leq$ 6000 keV to produce these decay curves. For ^{178}Au^g, the prompt 170.1-, 257.3-, and 337.9-keV E2 transitions between the yrast states were used in addition to the 483.0-keV $2^+ \rightarrow 2^+$ γ ray. For ^{178}Au^m, the 413.1-keV γ ray between the 8^+ and 6^+ yrast states and the 630.8-keV $4^+ \rightarrow 4^+$ γ rays were also used. Background subtraction was performed by gating on nearby Compton scattered γ rays to produce decay curves that were fitted with exponential functions by minimizing the χ^2 value. The half-lives obtained were 3.81(12) s and 2.82(4) s for ^{178}Au^{g,m}, respectively, in good agreement with the values of 3.4(5) s and 2.7(5) s from Ref. [1], but with significantly higher precision.

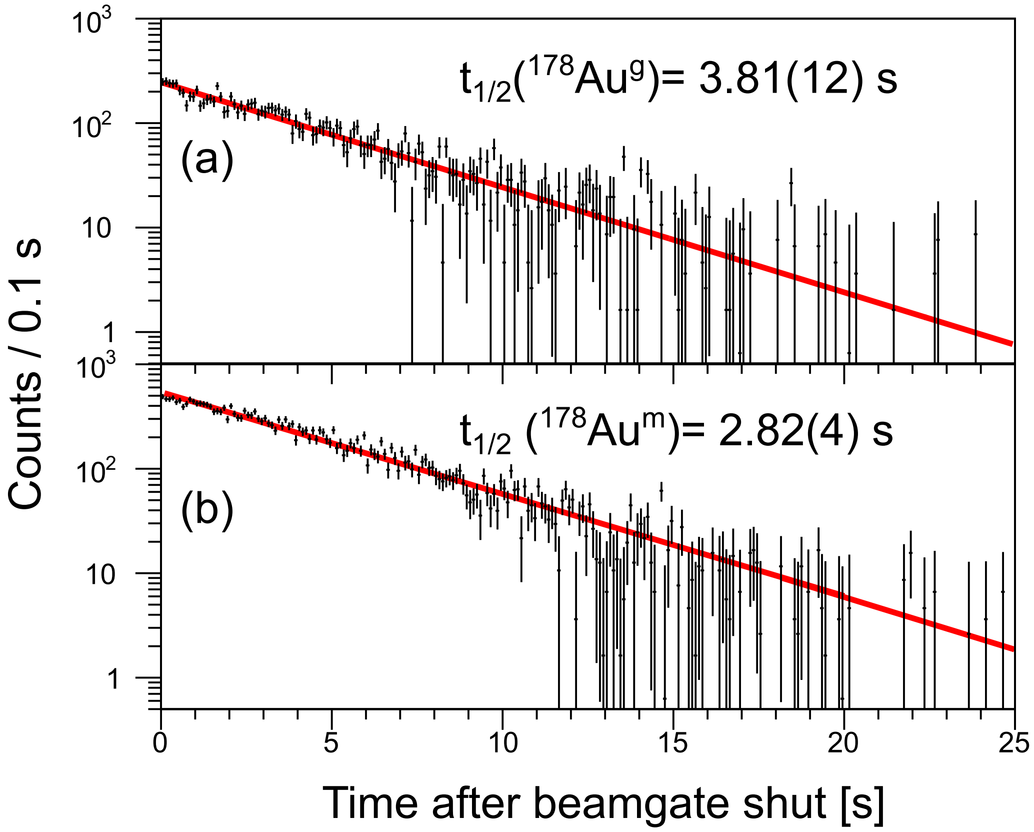

Figure 6.13: The decay curves obtained for (a) ^{178}Au^g and (b) ^{178}Au^m which are fitted with exponential functions to determine the half-life of each state.

6.2.1 Determination of Reduced α-decay widths

Reduced α-decay widths for the $^{178}\mathrm{Au}^{g,m} \rightarrow {}^{174}\mathrm{Ir}^{g,m}$ were calculated using the Rasmussen approach [54]. This involved calculating the pentration factor P using the equation

$$P = \exp\left\{ -2\int_{R_i}^{R_0} \frac{(2M)^{1/2}}{\hbar}\left[V(r) + \frac{2Ze^2}{r} + \frac{\hbar^2 l(l+1)}{2mr^2} - E_\alpha\right]^{1/2} \mathrm{d}r \right\}, \tag{6.7}$$

where M is the reduced mass of the α particle which has energy E_α, Z is the daughter nucleus' atomic number and l is the orbital angular momentum. The potential used was the empirical Igo potential [121], $V_I(r)$, rather than the simpler form used by Gamow to deduce Eq. 3.3

$$V_I(r) = -1100\ \exp\left[-\frac{r - 1.17A^{1/3}}{0.574}\right]\mathrm{MeV}. \tag{6.8}$$

The reduced α-decay widths, δ^2_α, were then calculated using the equation

$$\delta^2_\alpha = \frac{\lambda h}{P}. \tag{6.9}$$

A simplified form of Eq. 6.7 under the assumption that $l = 0$ was used to produce the δ^2_α values shown in Fig. 6.3. Hindrance factors were calculated by comparing the deduced values of δ^2_α to the average of the unhindered decays from ^{179}Au ($1/2^+ \rightarrow 1/2^+$, δ^2_α = 58(4) keV [11]) and ^{177}Au ($11/2^- \rightarrow 11/2^-$, δ^2_α = 82(14) keV [93]). This was the same method as that used in Ref. [1] and produced values that were consistent with what was reported in that study. The values of δ^2_α and HF_α are shown for each α decay in Fig. 6.3.

6.3 ^{178}Au EC/β^+ decay to ^{178}Pt

Prompt γ-γ coincidence analysis with the timing condition $|\Delta t_{\gamma\gamma}| \leq 100$ ns was used to construct separate EC/β^+ decay schemes for $^{178}\mathrm{Au}^{g,m}$. The γ-γ coincidence matrices are shown in Fig. 6.14 and the decay schemes produced are shown in Figs. 6.15 and 6.16. The width of the prompt time gate reflects the timing resolution for the HPGe detectors used (note the width of the distributions shown in Fig. 4.14) and ensures that almost all real prompt coincidence events were included in the gate while minimising the impact of time-random background events. Many of the transitions and states included in these decay schemes were previously seen by Davidson and/or Kondev in Refs. [99, 102] which are black in Figs. 5.4 and 5.5.

The raw projections of the γ-γ coincidence matrices included a significant number of background events. These events can be broadly split into two categories: time-random coincidences and coincidences with Compton-scattered photons. To estimate the background included in each projection of the prompt γ-γ matrix, an energy gate was placed on the Compton continuum near the peak of interest in an anti-prompt (400 ns$\leq$ $|\Delta t_{\gamma\gamma}| \leq$ 1000 ns) coincidence matrix. The background spectrum was scaled for the widths of the time and energy gates used before being subtracted 'bin-by-bin' from the raw energy spectrum to produce a background-subtracted projection, as illustrated in Fig. 6.17. An equivalent process was used to produce background-subtracted, γ-gated CE coincidence spectra.

All transitions from offband states reported by Davidson *et al.* in Ref. [99] were observed in either the $^{178}\mathrm{Au}^g$ or $^{178}\mathrm{Au}^m$ data. The non-yrast states reported by Kondev *et al.* in Ref. [102] were populated up to $E = 2137.7$ keV state (this study $E = 2137.5$ keV). Most of the new transitions are assigned as being from offband states to the rotational bands previously identified by Davidson. These are shown in red in the decay schemes shown in Figs. 6.15 and 6.16.

The energies and relative intensities of the K x rays coincident with each γ ray included in the decay schemes were compared to the literature values for platinum [20]. The time-difference distribution for each pair of coincident γ rays was also checked to see if any state is sufficiently long lived for its lifetime to be measured. The timing resolution available with the HPGe detectors was too poor for any such lifetime measurements to be made.

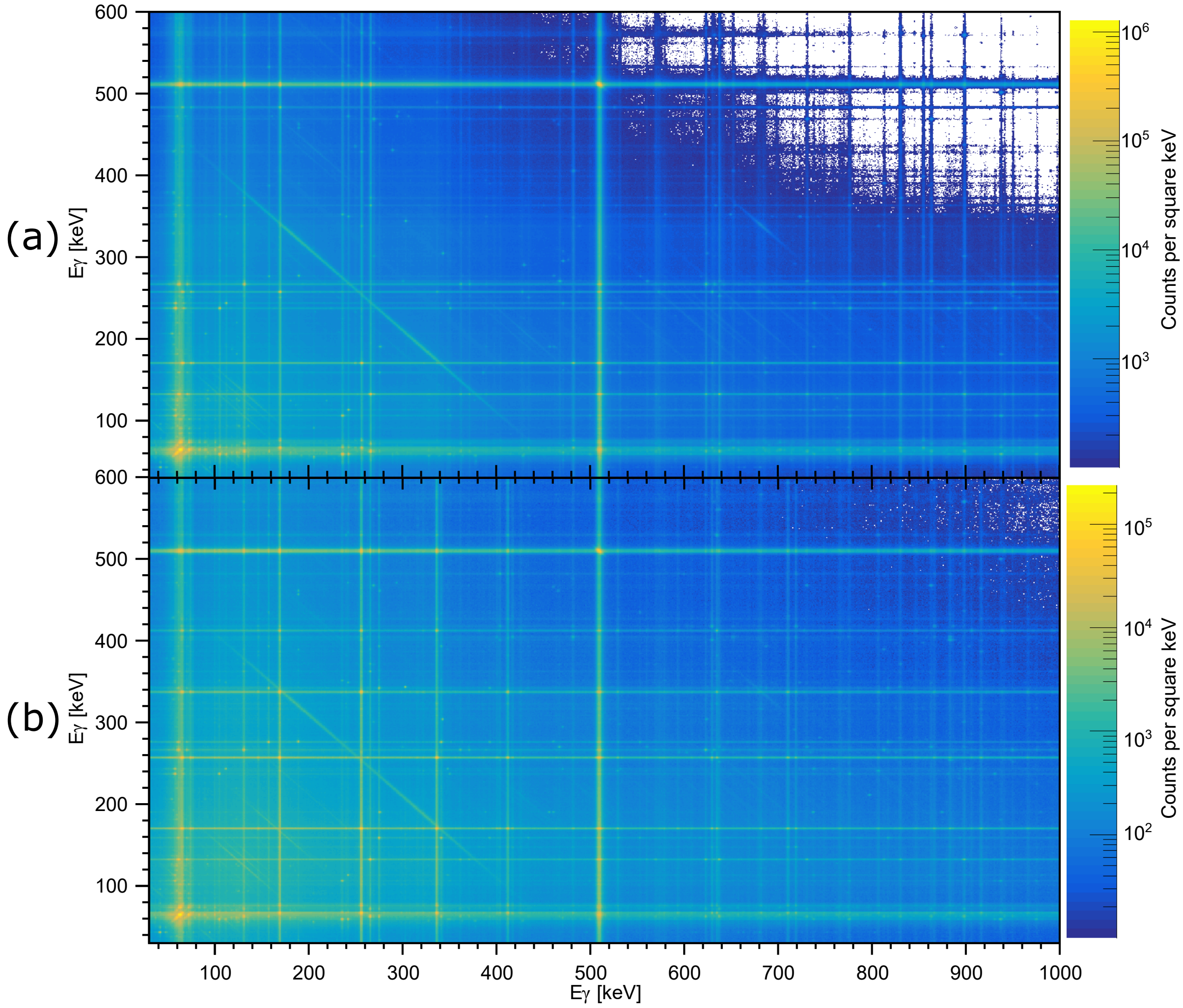

Figure 6.14: Part of the prompt γ-γ coincidence matrices produced using the ^{178}Au^g (a) and ^{178}Au^m (b) data. The full matrices used went up to E_γ=10 MeV but are zoomed in to the low-energy region to allow an easier visual comparison of the intensities of various γ rays. Note, in particular, the relative intensities of the 337- and 413-keV transitions within the yrast band of ^{178}Pt between (a) and (b) which are seen strongly from the high-spin isomer, ^{178}Au^m in (b) but not from the low-spin ground state, ^{178}Au^g in (a).

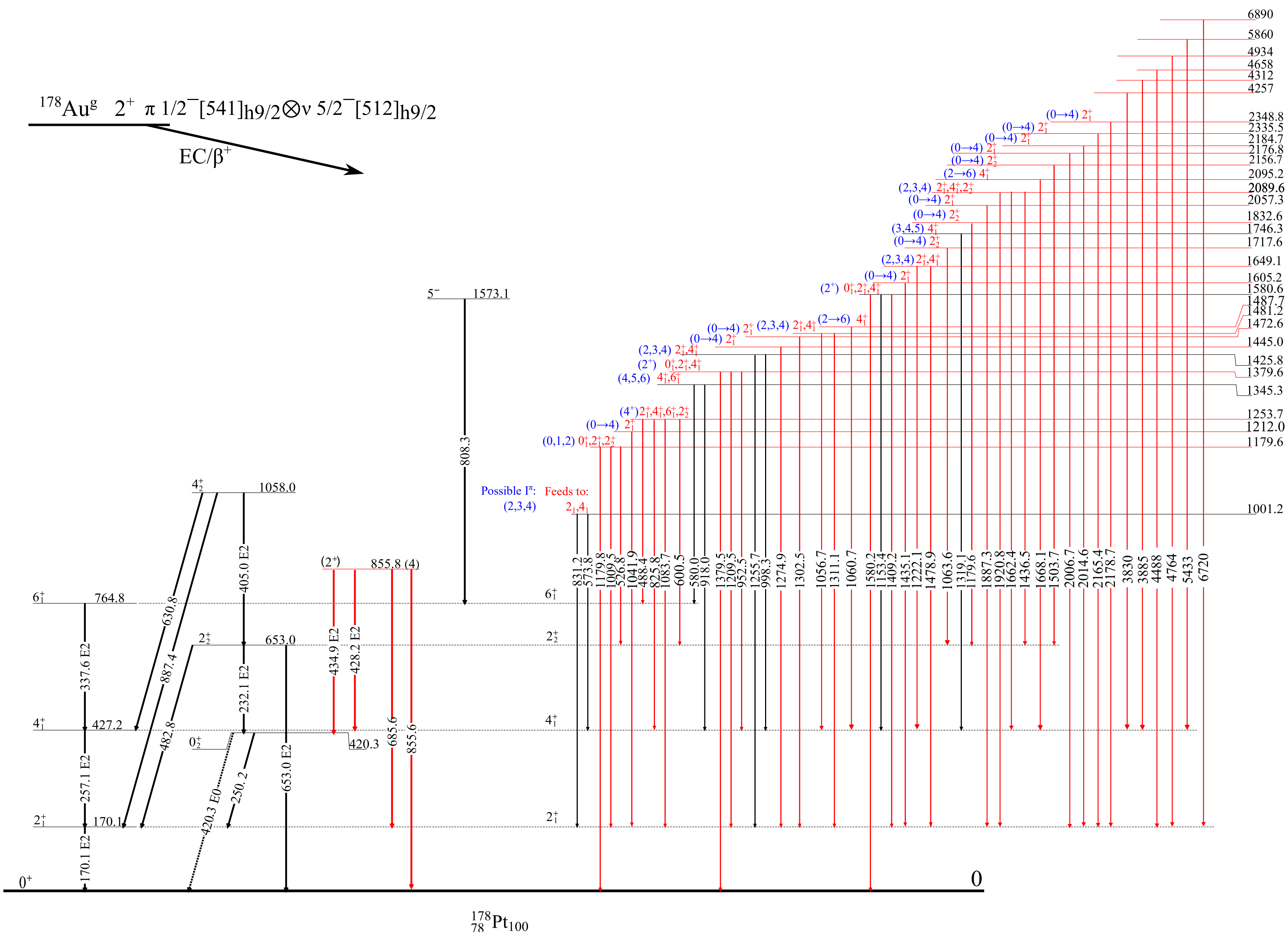

Figure 6.15: Decay scheme for the EC/β^+ decay of ^{178}Au^g. Newly discovered transitions and states are shown in red. Transition line thicknesses are all the same and do not correspond to the relative intensities observed for each transition.

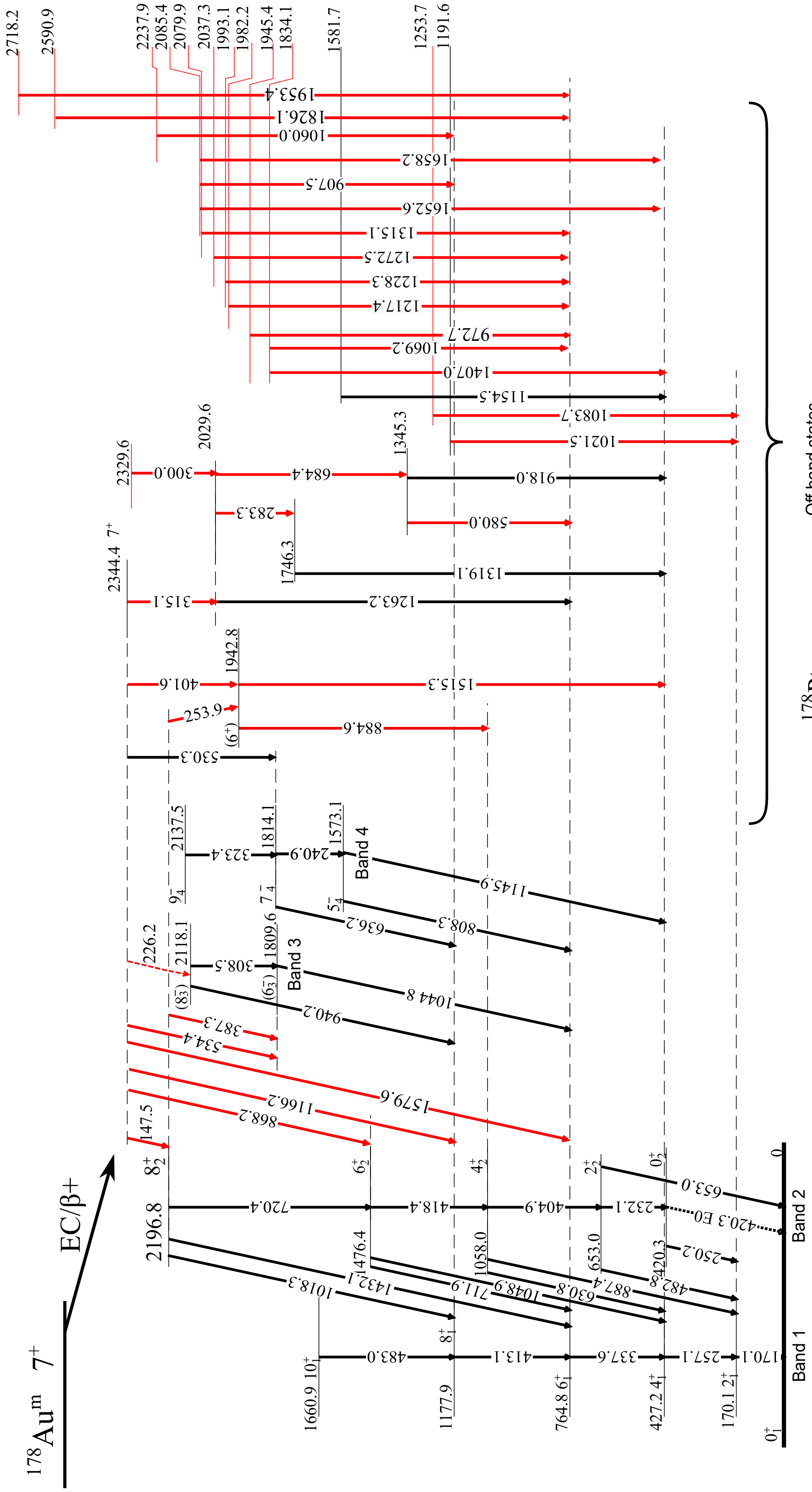

Figure 6.16: Decay scheme for the EC/β^+ decay of $^{178}Au^m$. Newly discovered transitions and states are shown in red. Transition line thicknesses are all the same and do not correspond to the relative intensities observed for each transition.

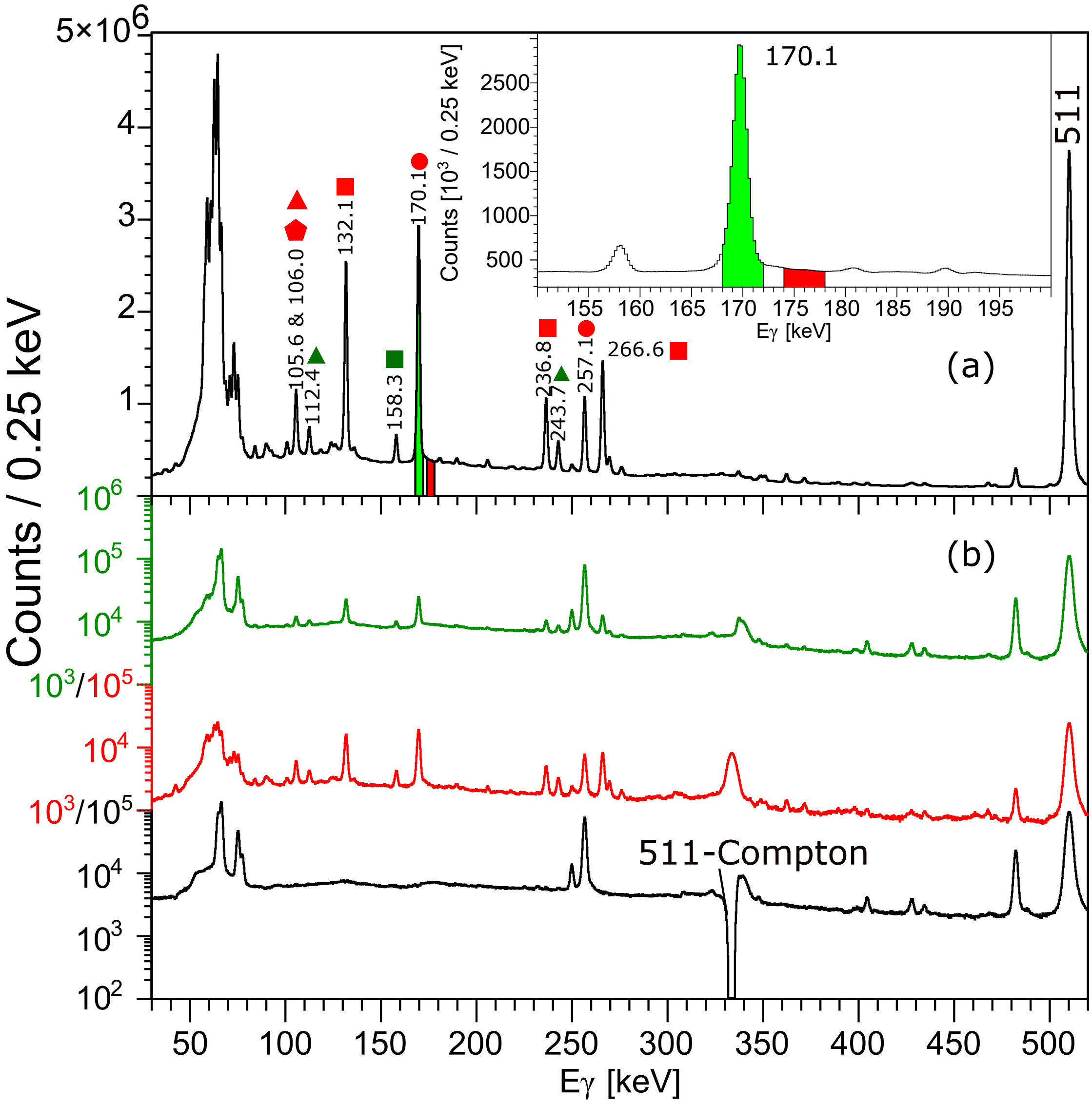

Figure 6.17: Demonstration of the background-subtraction performed throughout the analysis. (a) the total projection of the prompt γ-γ coincidence matrix with the raw spectrum and background spectrum gate conditions shown in green and red, respectively. The inset shows the same spectrum, zoomed in around these gates. The strongest peak energies are given with a symbol whose colour gives the emitting nucleus' A (red = 178, green = 174) and shape gives the element (circle = Pt, square = Os, pentagon = Re, triangle = W). (b) the raw projection on the prompt γ-γ matrix (green), the background spectrum from the anti-prompt γ-γ matrix (red) and the background subtracted spectrum (black). For ease of visual comparison the spectra in the bottom panel are offset from one another. The background subtraction effectively removed the strong peaks from known granddaughters of ^{178}Au and leaves a clean spectrum containing only peaks from ^{178}Pt.

6.3.1 EC/β^+ decay of ^{178}Au$^g \rightarrow^{178}$Pt

The well-established 170-, and 257-keV γ rays in ^{178}Pt ($2_1^+ \rightarrow 0_1^+$ and $4_1^+ \rightarrow 2_1^+$, respectively) are among the strongest transitions seen in Fig. 6.18(a). Projections of the prompt γ-γ matrix gated on these two γ rays are shown in Figs. 6.18(b,c).

The 337-keV $6_1^+ \rightarrow 4_1^+$ transition is also seen in Figs. 6.18(b,c) although it is much less intense than the 170- or 257-keV transitions, when corrections are made for detection efficiency and internal conversion. Population of this state is most likely due to the Pandemonium effect [59]. This would be consistent with the $I^\pi(^{178}\mathrm{Au}^g) = (2^+, 3^-)$ proposed by Cubiss *et al.* in Ref. [1].

All three γ-ray transitions identified by Davidson *et al.* in Ref. [99] as feeding the 2_1^+ state from band 2 are present in Fig. 6.18(b) at 250.2(2), 482.8(2), and 887.4(4) keV. Similarly, a γ ray at 630.8 keV corresponding to the $4_2^+ \rightarrow 4_1^+$ transition is present in both Figs. 6.18(b,c).

Additionally, all γ rays included in Davidson's decay scheme that feed from offband states to the 2_1^+ or 4_1^+ states, were found in the ^{178}Au^g data. All offband states reported by Davidson but not in the present work's ground-state data were observed when the isomer was instead sent to IDS - see Sec. 6.3.2. The transitions observed include a 573.8-keV γ ray from the 1001-keV state that was tentatively placed in Davidson's decay scheme - see Figs. 6.18(b,c).

In total, forty three new γ-ray transitions are assigned as feeding the 2_1^+, 4_1^+, 6_1^+, and 2_2^+ states from offband states. In many cases, these states were found to feed two or more lower-lying states, allowing tentative spin-parity restrictions to be placed. These are shown in blue on the left-hand side of each state in Fig. 6.15. Direct transitions from each of these off-band states to the ground state were searched for by gating on the corresponding energy region of the γ-γ matrix. If there were a peak in the γ-ray singles spectrum at the correct energy which was only coincident with 511-keV annihilation radiation and platinum K x-rays from K-electron capture, the transition to the ground state was included in the decay scheme. Six γ rays with $E_\gamma > 2.6$ MeV are included in the decay scheme. Their energies were determined by linear extrapolation, as there were no peaks in this range with well-known energies that could be used as calibration points. It is notable, however, that the detectors used unaffected by the linearity issue discussed in Sec. 4.4 linear responses consistent with one another up to at least 8 MeV.

Table 6.5: Summary of the γ-ray transitions observed from the EC/β^+ decay of ^{178}Au^g. The γ-ray energy, E_γ is given with the energy and J^π of the initial and final states indicated by the subscripts i and f, respectively. The relative transition intensity is also given.

E_γ [keV]	E_i [keV]	J_i^π	E_f [keV]	J_f^π	Intensity
170.1	170.1	2^+	0	0^+	1000
232.1	653.0	2^+	420.3	0^+	9.5(4)
250.2	420.3	0^+	170.1	2^+	44.3(4)
257.1	427.2	4^+	170.1	2^+	420(8)
337.6	764.8	6^+	427.2	4^+	17.1(3)
405.0	1058.0	4^+	653	2^+	8.6(9)
428.2	855.8	(2^+)	427.2	4^+	12.1(3)
434.9	855.8	(2^+)	420.3	0^+	2.3(4)
482.8	653	2^+	170.1	2^+	174(5)
488.4	1253.7		764.8	6^+	0.94(4)
526.8	1179.6		653.0	2^+	1.7(2)
573.8	1001.2		427.2	4^+	14.2(3)
580.0	1345.3		764.8	6^+	0.45(4)
600.5	1253.7		653.0	2^+	1.1(2)
630.8	1058.0		427.2	4^+	45.8(6)
653.0	653.0	2^+	0	0^+	25.2(18)
685.6	855.8	(2^+)	170.1	2^+	32.2(4)
808.3	1573.1		764.8	6^+	1.44(4)
825.8	1253.7		427.2	4^+	3.0(2)
831.2	1001.2	(2^+)	170.1	2^+	111(8)
855.6	855.6	(2^+)	0	0^+	60(4)
887.4	1058.0	4^+	170.1	2^+	13.3(5)
918.0	1345.3		427.2	4^+	7.8(3)
952.5	1379.6		427.2	4^+	9.2(5)
998.3	1425.8		427.2	4^+	18.2(4)
1009.5	1179.6		170.1	2^+	56.6(7)
1041.9	1212.0		170.1	2^+	9.4(6)
1056.7	1481.2		427.2	4^+	2.9(2)
1060.7	1487.7		427.2	4^+	16(3)
1063.6	1717.6		653.0	2^+	12(3)
1083.7	1253.7		170.1	2^+	16(4)
1153.4	1580.6		427.2	4^+	51.8(8)
1179.6	1832.6		653.0	2^+	6.3(4)
1209.5	1379.6		170.1	2^+	10.9(7)
1222.1	1649.1		427.2	4^+	23.4(17)
1255.7	1425.8		170.1	2^+	50.5(9)
1274.9	1445.0		170.1	2^+	30.2(9)
1302.5	1472.6		170.1	2^+	89(5)
1311.1	1481.2		170.1	2^+	3.0(8)
1319.1	1746.3		427.2	4^+	19.7(7)
1379.5	1379.5		0	0^+	19(3)
1409.2	1580.6		170.1	2^+	34.2(13)

E_γ [keV]	E_i [keV]	J_i^π	E_f [keV]	J_f^π	Intensity
1435.1	1605.2		170.1	2^+	47.7(13)
1436.5	2089.6		653.0	2^+	1.55(18)
1478.9	1649.1		170.1	2^+	5.0(3)
1503.7	2156.7		653.0	2^+	8.7(6)
1580.6	1580.6		0	0^+	8.7(9)
1662.4	2089.6		427.2	4^+	2.5(3)
1668.1	2095.2		427.2	4^+	23(2)
1887.3	2057.3		170.1	2^+	22(4)
1920.8	2089.6		170.1	2^+	11.9(9)
2006.7	2176.8		170.1	2^+	1.4(2)
2014.6	2184.7		170.1	2^+	2.0(3)
2165.4	2335.5		170.1	2^+	2.1(16)
2178.7	2348.8		170.1	2^+	4.2(7)
3830	4257		427.2	4^+	2.2(7)
3885	4312		427.2	4^+	7(3)
4488	4658		170.1	2^+	0.14(4)
4764	4934		170.1	2^+	0.11(4)
5433	5860		427.2	4^+	0.06(4)
6720	6890		170.1	2^+	<0.01

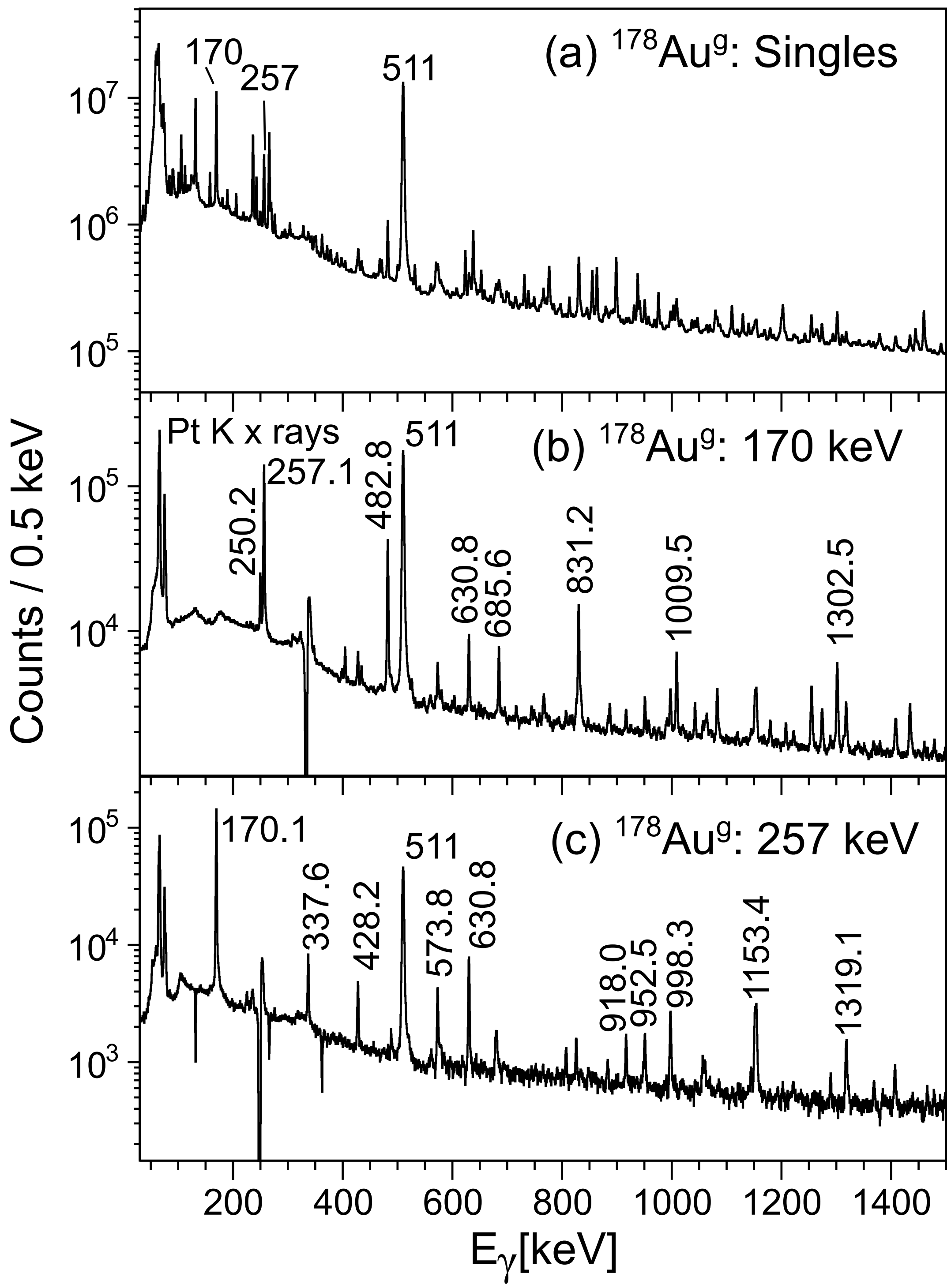

Figure 6.18: The γ-ray spectra produced by the ^{178}Au^{g} beam: (a) singles spectrum, (b,c) background-subtracted projections of the prompt $\gamma - \gamma$ matrix gated on the 170.1- and 257.1-keV γ rays, respectively.

6.3.2 EC/β^+ decay of ^{178}Au^m $\rightarrow^{178}$Pt

It was found that $\sim 39\%$ of the EC/β^+ decay of ^{178}Au^m populated the $6^+_{1,2}$ and $8^+_{1,2}$ states in ^{178}Pt - see Table 6.9. A small amount of feeding that can probably be attributed to Pandemonium [59] is observed to the 10^+_1 state but there was no direct feeding of the $2^+_{1,2}$, or $4^+_{1,2}$ states. This feeding pattern is consistent with the assignments for ^{178}Au^m proposed by Cubiss *et al.* in Ref. [1] of $(7^+, 8^-)$ - see Chapter 7. The interband $J \rightarrow J$ and $J \rightarrow (J-2)$ transitions between these two rotational bands are seen from the $J^\pi = 2^+$ state up to the $J^\pi = 8^+$, confirming the 1018.3-keV $8^+_2 \rightarrow 8^+_1$ transition tentatively proposed in Ref. [99]. This is discussed further in Sec. 6.3.3.

There are 27 new transitions added to the decay scheme for ^{178}Au^m, shown in red in Fig. 6.16. These include two transitions that feed from states reported in Ref. [99] to the 1814.6 keV 7^- state (this study, E = 1814.1 keV). Twelve of these are assigned as feeding of the yrast rotational band from offband states. These are grouped together on the right-hand side of Fig 6.32.

A new state at 1942.8 keV is fed by 253.9- and 401.6 keV γ rays from 2196.8-keV 8^+_1 and 2344.4-keV states seen earlier by Davidson, respectively. These two γ rays are both coincident with 884.6- and 1515.3-keV transitions that are assigned as feeding of the 4^+_1 and 4^+_2 states, respectively. Based on this feeding, a tentative 6^+ spin-parity assignment for the 1942.8-keV state is suggested.

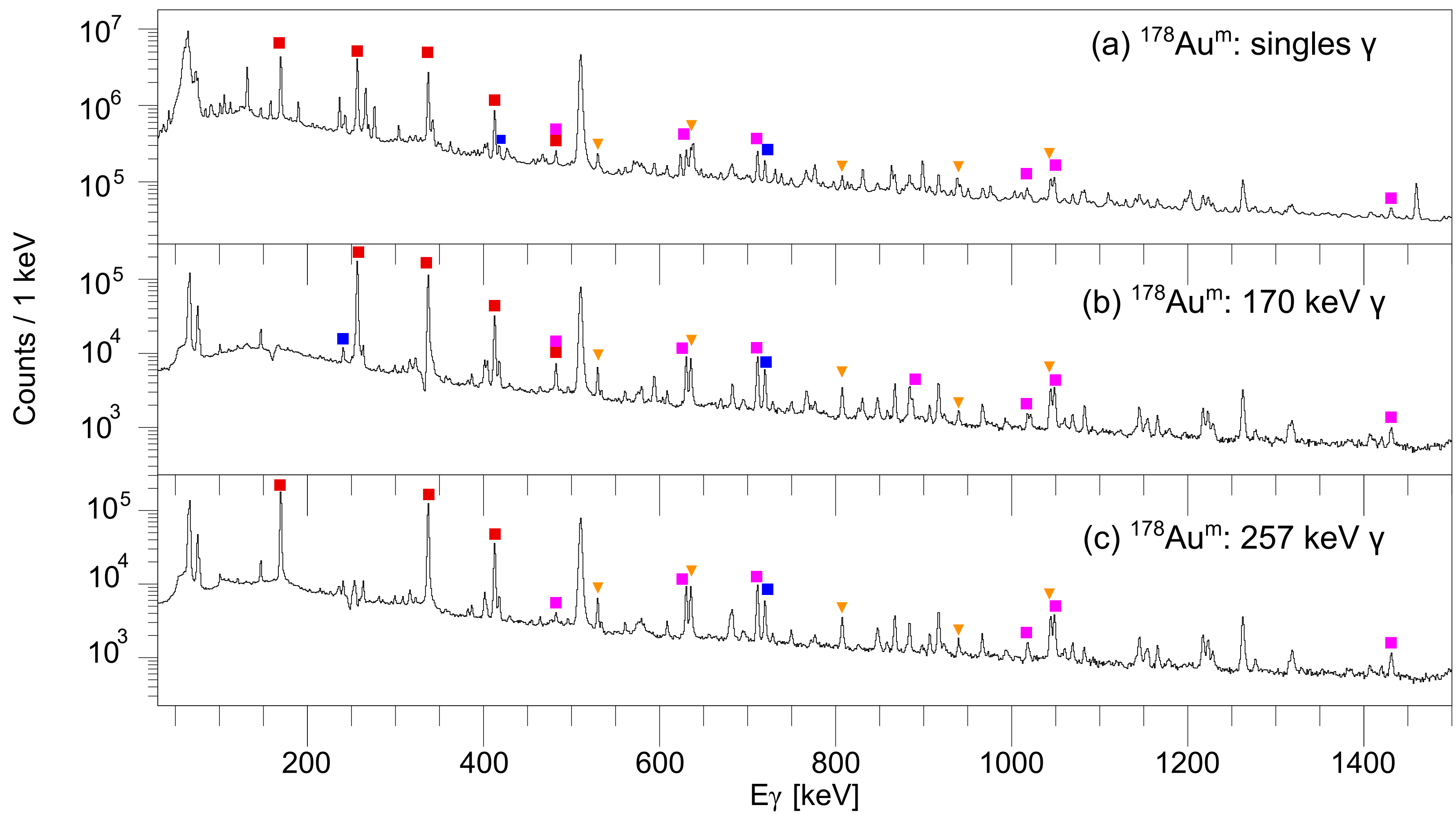

Figure 6.19: The γ-ray energy spectra collected with the ^{178}Au^{m} data with the gating conditions: (a) singles, (b) gate on the 170-keV γ ray, (c) gate on the 257-keV γ ray. The markers indicate: red square (■) - transitions within the yrast band, blue square (■) - transitions within the second rotational band, magenta square (■) - transitions between the yrast and second rotational bands, and orange triangle (▼) See also Fig. 6.20.

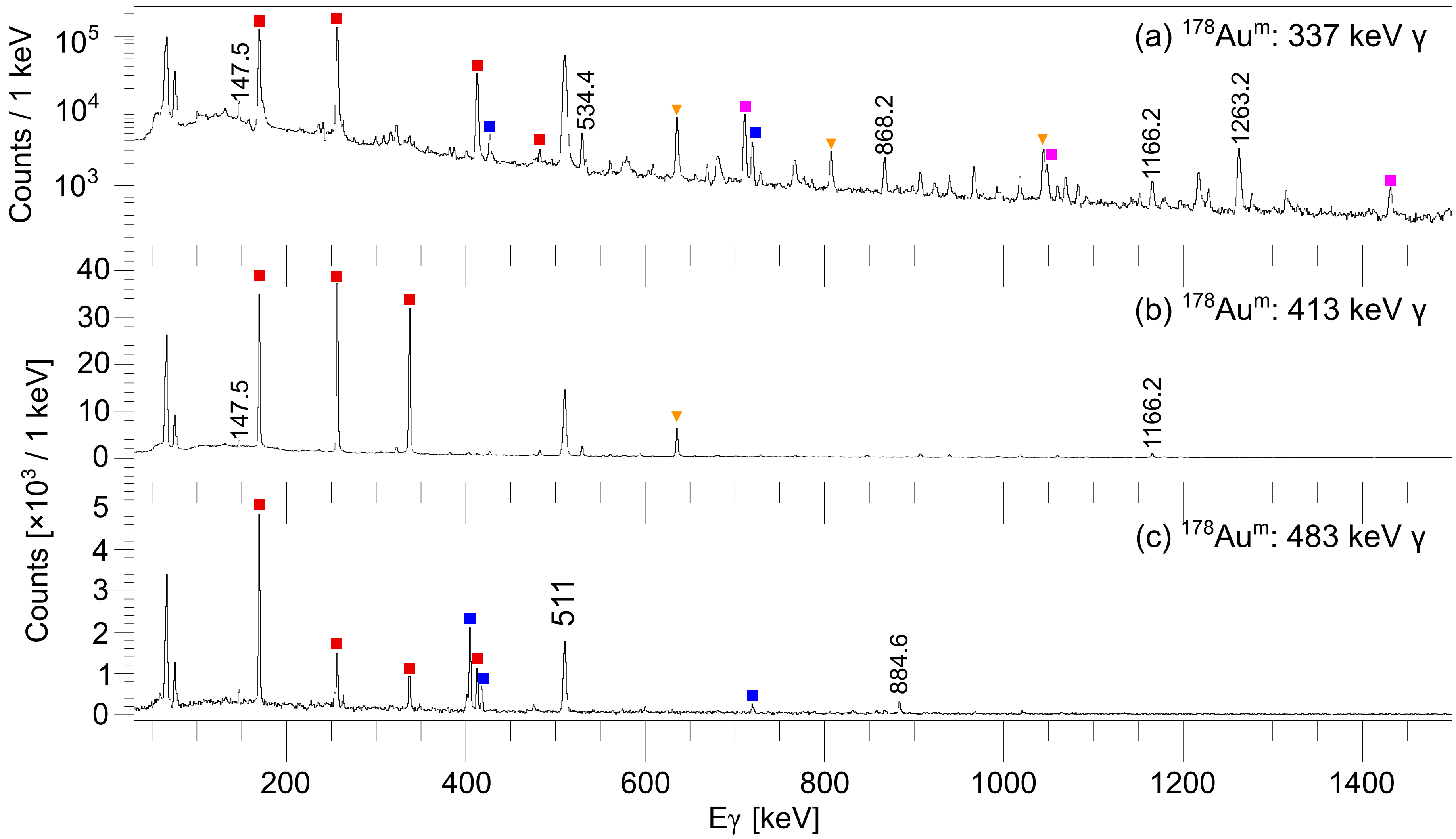

Figure 6.20: The γ-ray energy spectra collected with the ^{178}Au^{m} data gated on the (a) 337-, (b) 413-, and (c) 483-keV γ rays. The markers indicate: red square (■) - transitions within the yrast band, blue square (■) - transitions within the second rotational band, magenta square (■) - transitions between the yrast and second rotational bands, and orange triangle (▼). N.B. the gate on the 483-keV region contains both the $2_2^+ \rightarrow 2_1^+$ and $10_1^+ \rightarrow 8_1^+$ transitions. See also Fig. 6.19.

2344-keV State

In their study [99], Davidson *et al.* reported a 2345-keV state feeding the 1815-keV 7_4^- state through a 530.2-keV γ ray. Both states, and the connecting transition, are seen in the ^{178}Au^m data collected at IDS, at 2344.4, 1814.1, and 530.3 keV, respectively. As will be shown in Chapter 7, this state is important for the EC/β^+ decay of ^{178}Au^m as it receives ∼24% of EC/β^+-decay feeding. Therefore, background-subtracted projections of the γ-γ matrix gated on all eight transitions depopulating it are shown in Figs. 6.21 and 6.22. The highly fragmented depopulation of this state shows no clear preference for feeding any particular lower-energy state, which is indicative of a quasiparticle configuration in the parent state. If it were an excited state within a band, there would be a dominant transition to a lower-energy member of the band.

The γ rays that depopulate the 2344-keV state can be used to investigate its spin and parity. The values $\alpha_{K,L}$ for the 147-keV transition feeding the 8_2^+ state were calculated using the CE and γ-ray spectra produced by gating on the 720-keV $8_2^+ \rightarrow 6_2^+$ transition - see Fig. 6.23. While the uncertainty on the L-conversion coefficient for the 147-keV transition is too large to distinguish between it being M1 or E2, the experimentally determined α_K value given in Table 6.6 is consistent with an M1/E2 mixing ratio of 0.59(13). Therefore, the 2344-keV state must have a positive parity, and $I = 7, 8, 9$ based on the well-known $I^\pi = 8^+$ assignment of the daughter state. To verify this method, the values of $\alpha_{K,L}$ for the well-known 170-keV $2_1^+ \rightarrow 0_1^+$ E2 transition were also determined using the same spectra. The determined values are only consistent with the theoretical E2 ICCs, calculated using BrIcc - see Table 6.6. This provides extra confidence in the corresponding ICCs deduced for the 147-keV transtion.

Table 6.6: Theoretically calculated and experimentally determined K- and L-conversion coefficients for the 147- and 170-keV transitions, deduced using the spectra shown in Fig. 6.23 (a,b). The 170-keV transition is well known to be a pure E2 decay and was used to verify the method.

E_γ [keV]	α_K				α_L			
	E1	M1	E2	Exp	E1	M1	E2	Exp
147	0.1245	**1.8270**	**0.3571**	1.4(3)	0.0217	0.3021	0.5413	0.4(2)
170	0.0864	1.2120	**0.2539**	0.30(7)	0.0148	0.2000	0.2857	0.21(9)

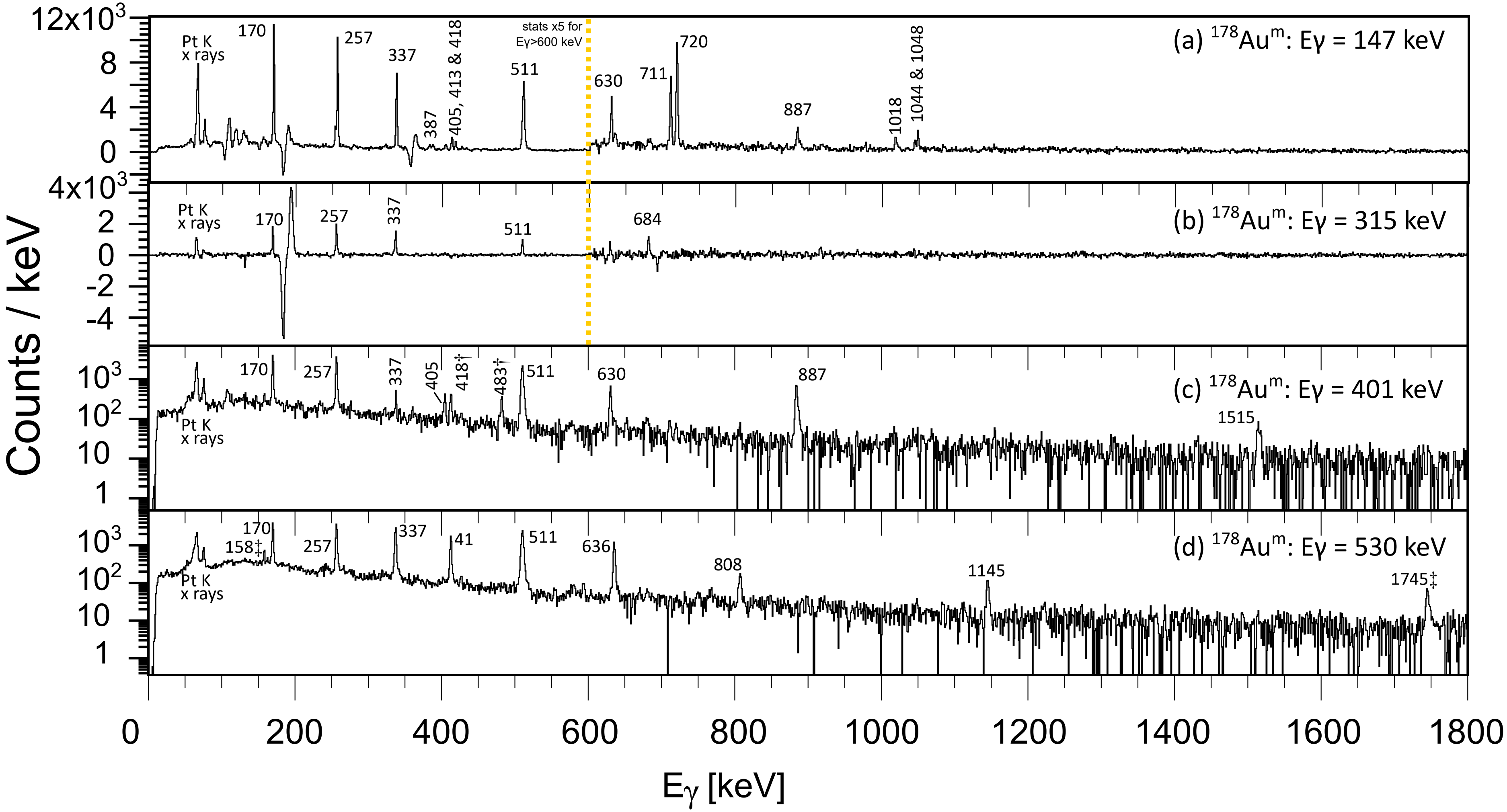

Figure 6.21: Projection of the ^{178}Au^{m} γ-γ coincidence matrix, gated on the (a) 147.5-, (b) 315.1-, (c) 401.6-, and (d) 530.3-keV γ rays depopulating the 2344.4-keV state. Transitions marked with an obelus (†) in (c,d) are present due to an overlaps of the gate used with the 405-keV $4_2^+ \rightarrow 2_2^+$ and 532-keV $2_2^+ \rightarrow 2_1^+$ γ rays in ^{178}Pt and ^{174}Os, respectively.

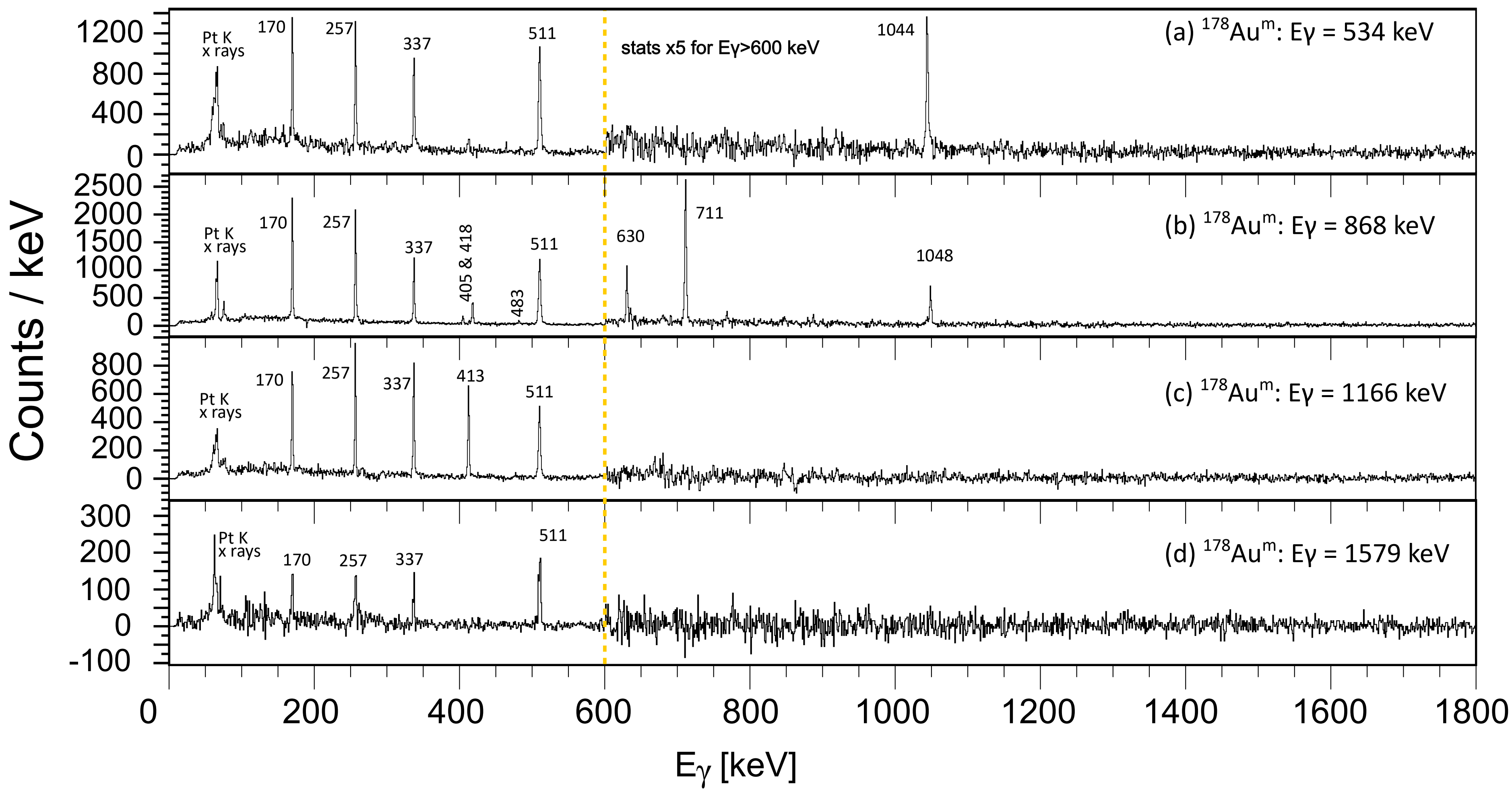

Figure 6.22: Projection of the ^{178}Au^m γ-γ coincidence matrix, gated on the (a) 534.4-, (b) 868.2-, (c) 1166.2-, and (d) 1579.6-keV γ rays depopulating the 2344.4-keV state.

Prompt γ rays from the 2344-keV state feed several $I = 6, 7, 8$ states. For these transitions to be prompt, they must be E1, M1, or E2, which restricts the spin of the 2344-keV state to $I = 6, 7, 8$. However, the $I = 6$ assignment can be ruled out due to the M1 component of the 147-keV transition to the 8_2^+ state.

The absence of γ rays directly feeding lower-lying 4^+ states further confirms the exclusion of the $I^\pi(2344\ \mathrm{keV}) = 6^+$ assignment. Were the 2344-keV state to have $I^\pi = 6^+$, it should decay to the $4_{1,2}^+$ through prompt E2 transitions. While γ rays from the 2344-keV state feeding the $6_{1,2}^+$(at E_γ = 1579.6 and 868.2 keV) and the $8_{1,2}^+$ (at E_γ = 1166.2 and 147.5 keV) are present in Figs. 6.20 and 6.24, there is no evidence for a 1917.2- or 1286-keV transition. Therefore, $I^\pi(2344\ \mathrm{keV}) = 7^+$ or 8^+.

The two remaining spin-parity options for the 2344-keV state can be distinguished between by analysing the decay to negative-parity states. If the 2344-keV state had $I^\pi = 8^+$, it should decay to the 7_4^-, 8_3^-, and 9_4^- states through fast E1 transitions. However, if $I^\pi(2344\ \mathrm{keV}) = 7^+$, E1 transitions would feed the 6_3^-, 7_4^-, and 8_3^- states but not the 9_4^- state, which would instead only be fed by a much slower M2 transition. Clear peaks at E_γ =530 and 534 keV are present in Figs. 6.24(b,c), which correspond to feeding from the 2344-keV state to the 7_4^- and 6_3^- states, respectively. There is a small peak at 226.3 keV in Fig. 6.24(c), which is designated as the '2344 keV $\rightarrow 8_3^-$' transition. There is no equivalent peak corresponding to feeding the 9_4^- state at 206 keV in Fig. 6.24(b). If $I^\pi(2344\ \mathrm{keV}) = 8^+$, the 206-keV transition would be much stronger compared to the 530-keV γ ray than the 226-keV γ ray relative to the 534-keV transition. This is clearly not the case so the feeding pattern from the 2344-keV state uniquely supports an $I^\pi = 7^+$ assignment.

Any transitions feeding the 2344-keV state should be present in all eight spectra shown in Figs. 6.21 and 6.22, although no such γ rays are observed. Therefore, the feeding of this state is entirely attributed to direct EC/β^+ decay from $^{178}\mathrm{Au}^m$. Using the method outlined in Sec 6.3.5, it was found that almost a quarter of the EC/β^+ decay from $^{178}\mathrm{Au}^m$ directly feeds this state. This corresponds to log ft=4.93(18), clearly indicating this is an allowed transition - see Table 6.9.

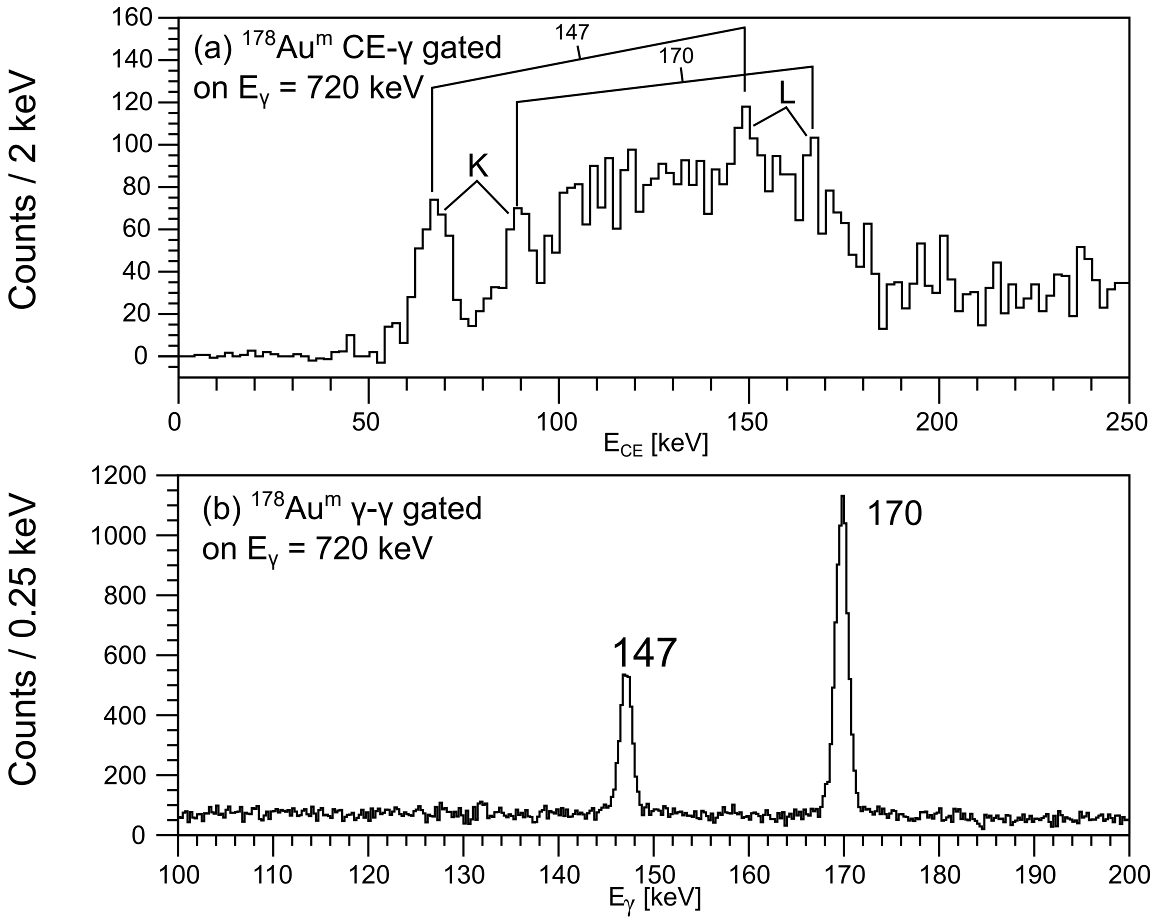

Figure 6.23: Projections gated on the 720-keV $8_2^+ \rightarrow 6_2^+$ transition of the ^{178}Au^m (a): CE-γ and (b): γ-γ coincidence matrices. By comparing the spectra shown in (a) and (b), it was determined that $\alpha_K(147 \text{ keV}) = 1.4(3)$ and $\alpha_L(147 \text{ keV}) = 0.4(2)$, consistent with a well-mixed M1/E2 transition. The 170-keV $2_1^+ \rightarrow 0_1^+$ transition is well-known to be purely E2 and was used to verify this method - see Table 6.6.

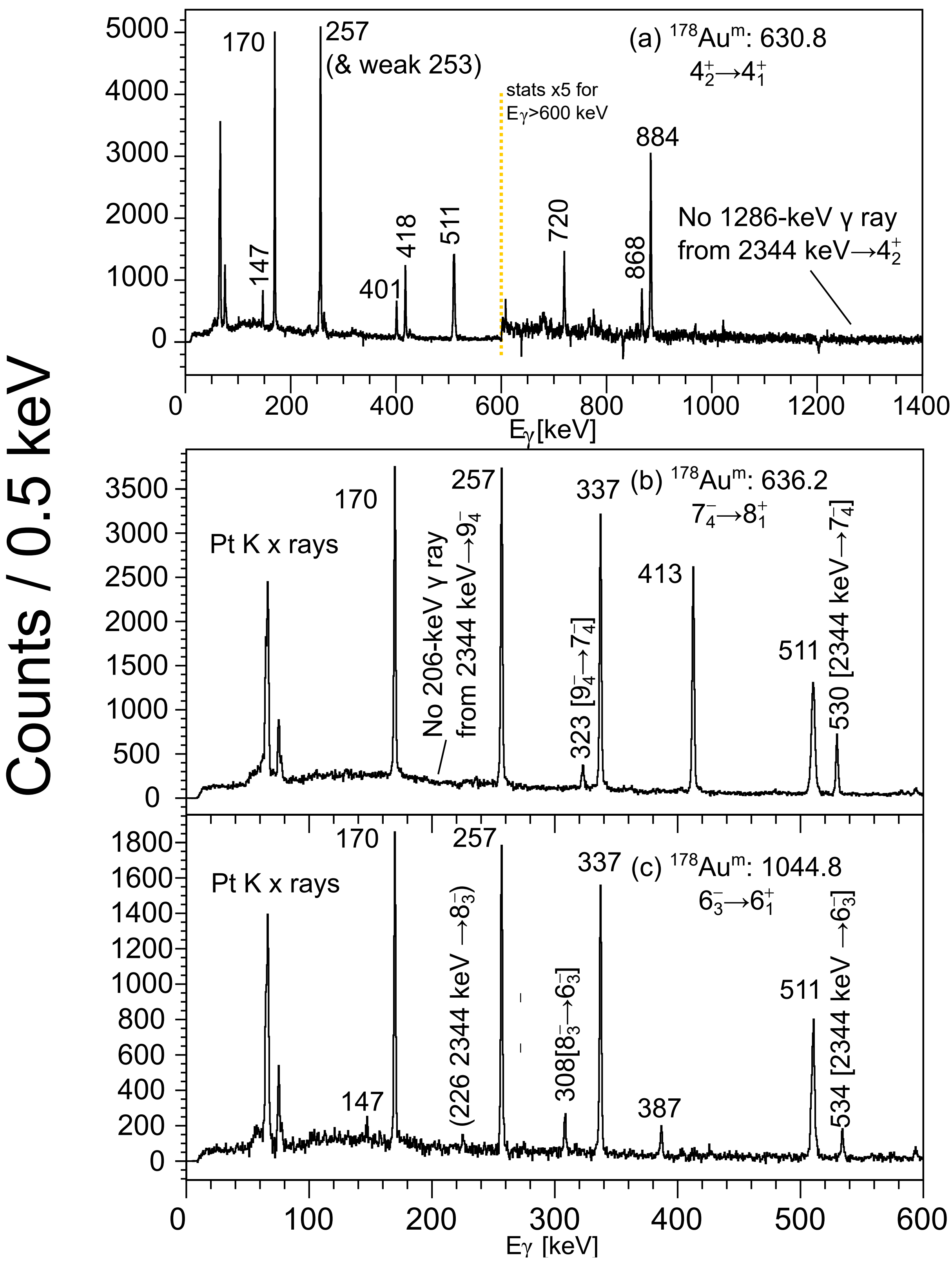

Figure 6.24: Projection of the ^{178}Au^{m} γ-γ coincidence matrix, gated on the indicated γ rays. The 226-keV label in (c) is given in parenthisies due to the weakness of this transition.

Table 6.7: Summary of the transitions observed in the EC/β^+ decay of ^{178}Au^m.

E_γ [keV]	E_i [keV]	J_i^π	E_f [keV]	J_f^π	Intensity
147.5	2344.4	7^+	2196.8	8^+	81(3)
170.1	170.1	2^+	0.0	0^+	1000
232.1	653.0	2^+	420.3	0^+	2.7(13)
240.9	1814.1	7^-	1573.1	5^-	19.0(18)
250.2	420.3	0^+	170.1	2^+	9.3(3)
253.9	2196.8	8^+	1942.8	6^+	25.8(10)
257.1	427.2	4^+	170.1	2^+	840(15)
283.3	2029.6		1746.3		0.23(2)
300.0	2329.6		2029.6		28.7(15)
308.5	2118.1	8^-	1809.6	6^-	4.69(14)
315.1	2344.4	7^+	2029.6		0.33(3)
323.4	2137.5	9^-	1814.1	7^-	30.0(7)
337.6	764.8	6^+	427.4	4^+	604(12)
387.3	2196.8	8^+	1809.6	6^-	84(4)
401.6	2344.4	7^+	1942.8	6^+	35.8(2)
404.9	1058.0	4^+	653.0	2^+	59.4(16)
413.0	1177.9	8^+	764.8	6^+	172.2(9)
418.0	1476.4	6^+	1058.0	4^+	60.7(14)
482.8	653.0	2^+	170.1	2^+	38.5(5)
483.0	1660.9	10^+	1177.9	8^+	3.6(2)
530.3	2344.4	7^+	1814.1	7^-	37.7(2)
534.4	2344.4	7^+	1809.6	6^-	29.4(2)
580.0	1345.3		764.8	6^+	2.0(2)
630.8	1058.0	4^+	427.4	4^+	87.9(6)
636.2	1814.1	7^-	1177.9	8^+	56.2(3)
653.0	653.0	2^+	0	0^+	5.2(7)
684.0	2029.6		1345.3		29.2(7)
711.9	1476.4	6^+	764.8	6^+	96.5(6)
720.4	2196.8	8^+	1476.4	6^+	84(6)
808.3	1573.1	5^-	764.8	6^+	23.5(13)
868.0	2344.4	7^+	1476.4	6^+	72.7(2)
884.6	1942.8	(6^+)	1058.0	4^+	33.4(8)
887.4	1058.0	4^+	170.1	2^+	18.2(4)
907.5	2085.4		1177.9	8^+	10.8(12)
918.0	1345.3		427.2	4^+	42.8(14)
972.7	1982.2		764.8	6^+	3.4(4)
940.2	2118.1	8^-	1177.9	8^+	8.3(5)
1018.0	2196.8	8^+	1177.9	8^+	20.4(14)
1021.5	1191.6		170.1	2^+	11.0(4)
1044.8	1809.6	6^-	764.8	6^+	45.5(4)
1048.9	1476.4	6^+	427.2	4^+	49(7)
1060.0	2237.9		1177.9	8^+	6.5(8)
1069.2	1834.1		764.8	6^+	11.9(3)
1083.7	1253.7		170.1	2^+	26.7(5)
1145.9	1573.1	5^-	427.2	4^+	24.3(3)

E_γ [keV]	E_i [keV]	J_i^π	E_f [keV]	J_f^π	Intensity
1154.5	1581.7		427.2	4^+	11.4(14)
1166.2	2344.4		1177.9	8^+	14.9(14)
1217.4	1982.2		764.8	6^+	26.3(5)
1228.3	1993.1		764.8	6^+	7.4(4)
1263.2	2029.6		764.8	6^+	73.6(7)
1272.5	2037.3		764.8	6^+	2.2(4)
1315.1	2079.9		764.8	6^+	11.0(3)
1319.1	1746.3		427.2	4^+	26.0(11)
1407.0	1834.1		427.2	4^+	6.13(5)
1432.1	2196.8	8^+	764.8	6^+	21.79(6)
1515.3	1942.8	(6^+)	427.2	4^+	18.4(4)
1652.6	2079.9		427.2	4^+	0.52(3)
1658.2	2085.4		427.2	4^+	1.70(3)
1826.1	2590.9		764.8	6^+	0.45(6)
1953.4	2718.2		764.8	6^+	0.42(7)

6.3.3 Experimental Determination $J \to J$ E0-Transition Strengths in ^{178}Pt

E0 transitions are of particular interest as they are sensitive to band mixing and the difference in mean square charge radii between the initial and final states [63, 64]. The strength of the E0 transitions between states of equal angular momentum in two coexisting rotational bands can be calculated by first determining the conversion coefficients. Throughout this discussion, subscripts are used to denote the band a state is in, while J refers to a particular angular momentum and parity, such that $J_2 \to J_1$ refers generally to $0_2^+ \to 0_1^+$, $2_2^+ \to 2_1^+$, $4_2^+ \to 4_1^+$ etc. transitions. Two methods were used to determine the conversion coefficients for such $J_2 \to J_1$ transitions, which are described below. The conversion coefficients produced using both methods are summarised in Table 6.8. The spectra used to produce the values for the 483-keV $2_2^+ \to 2_1^+$ transtion are given in Fig. 6.26 as an example.

Method 1

For the first method, the intensities of the K- and L-CE peaks were directly compared to the intensity of the corresponding γ ray. To reduce the impact of possible background peaks, the CE and γ spectra used were gated on transitions that depopulate the state (J_1) fed by the $J_2 \to J_1$ transition. For example, the gate used for the $2_2^+ \to 2_1^+$ transition was on the 170-keV γ ray ($2_1^+ \to 0_1^+$), while a 257-keV γ gate ($4_1^+ \to 2_1^+$) was used for the $4_2^+ \to 4_1^+$ transition. The γ rays used as gates for this method are shown in green in Fig. 6.25. The K- and L-conversion coefficients were calculated as

$$\alpha_{K,L} = \frac{N_{K,L} \cdot \mathcal{E}_\gamma}{N_\gamma \cdot \mathcal{E}_{K,L}}, \tag{6.10}$$

where $N_{K,L,\gamma}$ is the number of K-, L-CE, or γ rays observed, respectively, and $\mathcal{E}_\gamma$ and $\mathcal{E}_{K,L}$ are the γ-ray- and CE-detection efficiencies at the appropriate energy. To determine the K- and L-conversion coefficients for the 483-keV $2_2^+ \to 2_1^+$ transition, the intensities of the labelled K- and L-CE peaks and the 483-keV γ-ray peak in Figs. 6.26(a,b) were compared. One disadvantage of this method is that for CEs with energies $E_{CE} \gtrsim 300$ keV, the Si-detectors' efficiency drops rapidly - see Fig. 4.13(d). Therefore a second method was also used, which is described below.

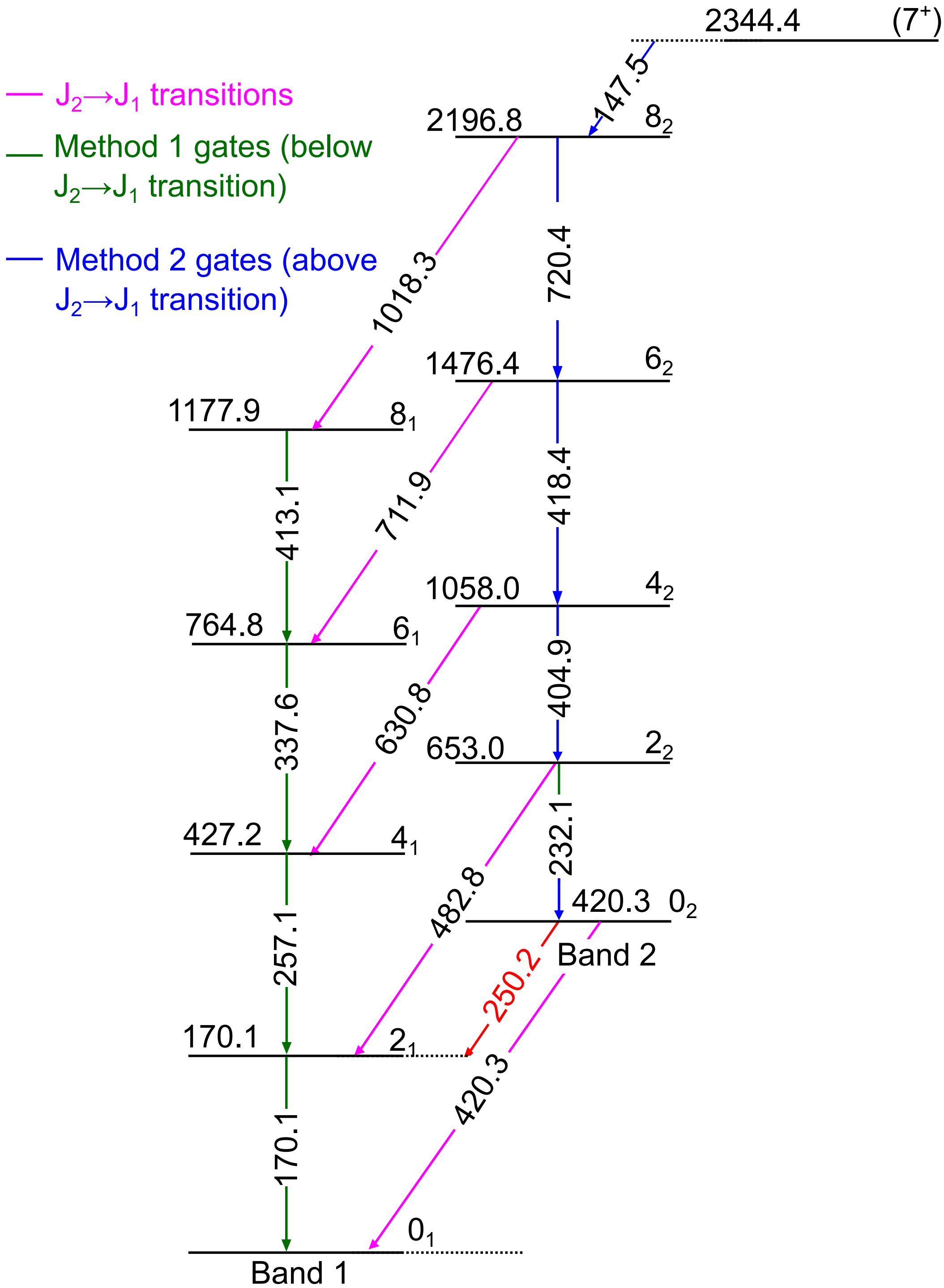

Figure 6.25: Part of the level scheme for ^{178}Pt with transitions colour coded by how they were used in the analysis: Magenta - $J_2 \rightarrow J_1$ transitions whose conversion coefficients are being investigated; Green - transitions used as gates for Method 1; Blue - transitions used as gates for Method 2. The 250.2-keV transition is red to highlight that this provides an indirect path from the $2_2 \rightarrow 2_1$ that was accounted for when using Method 2. This figure is not to scale and excludes most transitions and states shown in the full decay schemes for clarity.

Method 2

The second method uses an intensity-balance argument of transitions seen in the γ-γ matrix, with no reliance on CE data. Here, it is discussed for the specific case of $\alpha_{tot}(2_2^+ \rightarrow 2_1^+)$ to illustrate the principles and procedure, although this method is equally applicable for calculating other $J_2 \rightarrow J_1$ transitions' conversion coefficients.

When a gate is placed on the $4_2^+ \rightarrow 2_2^+$ γ ray, the coincident $2_2^+ \rightarrow 2_1^+$ and $2_1^+ \rightarrow 0_1^+$ transitions must have the same total intensity as each other as they are both in the same $4_2^+ \rightarrow 2_2^+ \rightarrow 2_1 \rightarrow 0_1$ cascade. This is true if side feeding can be accounted for, which can, in the case of ^{178}Pt, be easily done. Since the total intensity is[3]

$$I_{tot,i} \equiv I_{\gamma,i} + I_{CE,i} \equiv I_{\gamma,i}\Big(1 + \alpha_{tot,i}\Big), \tag{6.11}$$

where $i = 170, 483$, it follows that

$$I_{\gamma,170} \cdot \Big(1 + \alpha_{tot,170}\Big) = I_{\gamma,483} \cdot \Big(1 + \alpha_{tot,483}\Big), \tag{6.12}$$

where $\alpha_{tot,i}$ is the total conversion coefficient for transition i, which has an efficiency-corrected γ-ray intensity $I_{\gamma,i}$. This can be rearranged to the form

$$\alpha_{tot,483} = \frac{I_{\gamma,170}}{I_{\gamma,483}} \cdot \Big(1 + \alpha_{tot,170}\Big) - 1. \tag{6.13}$$

The right-hand side of Eq. 6.13 depends only on the efficiency-corrected γ-ray intensities and the conversion coefficient $\alpha_{tot,170}$. Because the 170-keV transition is purely E2, the conversion coefficient $\alpha_{tot,170}$ can be determined using, for example, BrIcc [62].

The same logic can be applied to transitions between higher-spin states in bands 1 and 2. The transitions used as gates for Method 2 are shown in blue in Fig. 6.25. Except for the $8_2^+ \rightarrow 8_1^+$ transition, these gates were placed on the γ-ray transitions within band 2. Because the 10_2^+ state was not seen to be populated in the present data, the 147-keV transition from the 2344-keV state was used instead in this case. The values calculated, along with those determined by Method 1 are summarised in Table 6.8. The spectrum used to obtain this values for the $2_2^+ \rightarrow 2_1^+$ transition is shown in Fig. 6.26(c).

Table 6.8: The total conversion coefficients determined for the $J_2 \rightarrow J_1$ transitions between the second and yrast rotational bands calculated using Methods 1 and 2, as described in the main text. The α_{tot} values reported Davidson *et al.* in Ref. [99] and the E0-transition branching ratio are also given.

		Method 1		Method 2			
E_{trans} [keV]	$J_i^\pi \rightarrow J_f^\pi$	γ gate [keV]	α_{tot}	γ gate [keV]	α_{tot}	α_{tot} Ref. [99]	E0 branch [%]
420.3	$0_2^+ \rightarrow 0_1^+$	-	-	-	-	-	27(2)
482.8	$2_2^+ \rightarrow 2_1^+$	170.1	0.73(8)	404.9	0.76(3)	0.12(1)	41.3(5)
630.8	$4_2^+ \rightarrow 4_1^+$	257.1	0.36(5)	418.4	0.41(2)	<0.09 [4]	27.1(6)
711.9	$6_2^+ \rightarrow 6_1^+$	337.6	-	720.4	0.048(4)	0.020(9)[5]	5.0(8)
1018.3	$8_2^+ \rightarrow 8_1^+$	413.1	-	147.5	0.020(5)	-	4.5(9)

[3]This equation holds so long as the transition energy is below 1.022 MeV. Above this energy, internal pair production can compete with internal conversion so must be accounted for.

[4]Only α_K reported. CE spectrum contaminated by ^{178}Os

[5]Only α_K reported

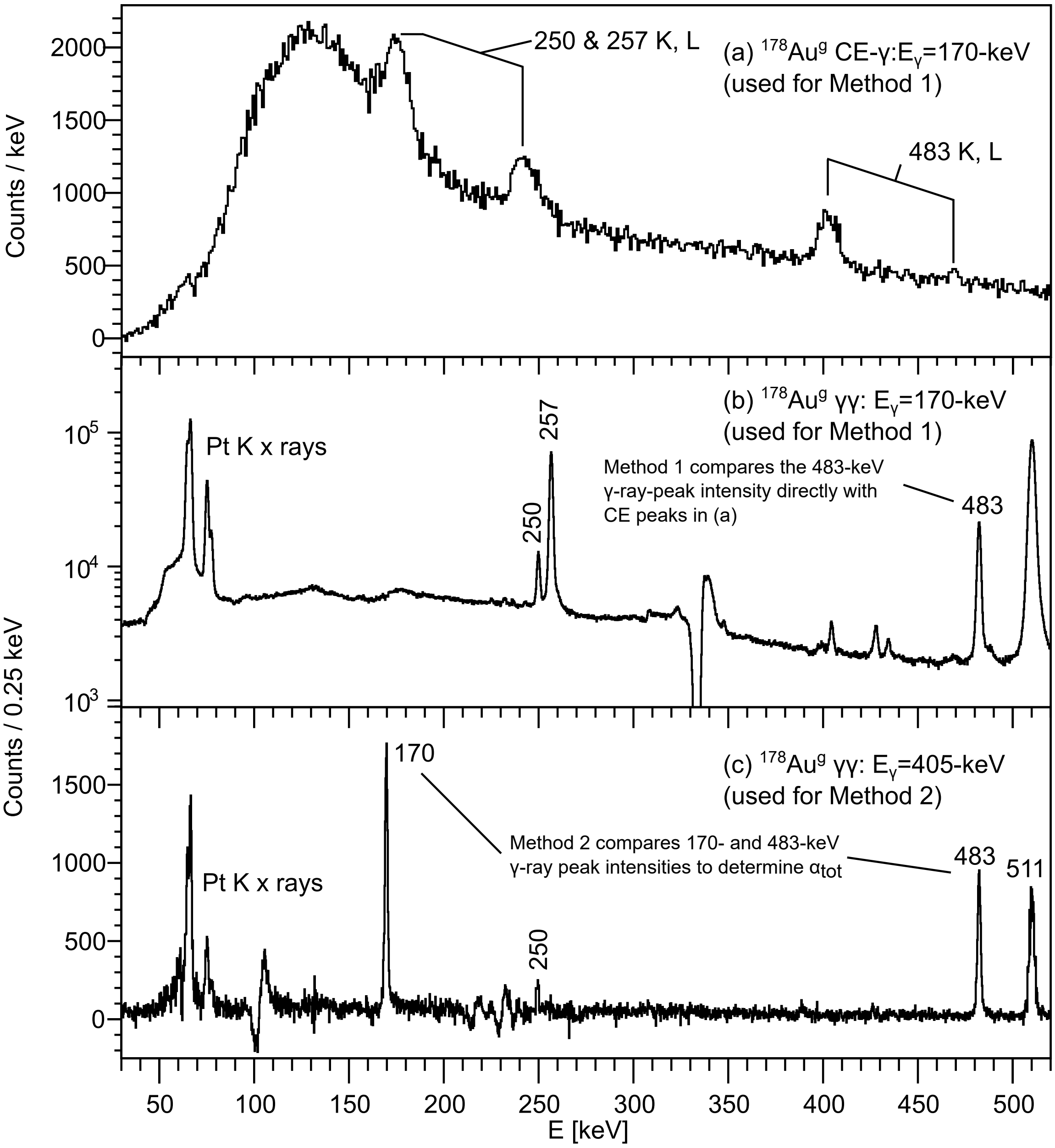

Figure 6.26: (a,b): Projections used to calculate the conversion coefficients for the $2_2^+ \rightarrow 2_1^+$ transition in ^{178}Pt using Method 1. The spectra shown are: (a) the background-subtracted CE spectrum gated on the 170-keV $2_1^+ \rightarrow 0_1^+$ γ-ray; (b) the equivalent background-subtracted γ-γ coincidence matrix projection using the same gate as (a) on the 170-keV transition; (c) the background-subtracted γ-γ coincidence matrix projection gated on the 405-keV $4_2^+ \rightarrow 2_2^+$ transition used for Method 2.

The α_{tot} values calculated using methods 1 and 2 are in good agreement with one another, in cases where both methods can be used. From Table 6.8, it is clear that there are significant differences between the conversion coefficients reported by Davidson *et al.* in Ref. [99] and those calculated for this thesis. The same procedures were used to determine $\alpha_{tot,K}(J_2 \to J_1)$ for ^{174}Os which gave good agreement with the values reported in Ref. [115] - see Table 6.11.

In Davidson's study, α_K and α_L, were determined by comparing the intensities of the peaks in the γ-ray and CE singles spectra, rather than in γ-gated spectra as in Method 1 of the present work. The most signficant issue with this is that they would not have had sufficiently good resolution to distinguish between the 482.8-keV $2_2^+ \to 2_1^+$ and the 483.0-keV $10_1^+ \to 8_1^+$ transitions in ^{178}Pt. Since the latter is a pure E2 transition, it has a significantly lower conversion coefficient than a mixed E0, M1 and E2 transition of the same energy. This is not a problem for the current analysis since γ-ray-gated spectra were used. Also there is no evidence of population of the 8_1^+ state in the ^{178}Au^g data, meaning the $10_1^+ \to 8_1^+$ transition was negligibly weak in the ground-state data - see Figs. 6.18, 6.20(c), and 6.26. Therefore $\alpha_{tot}(2_2^+ \to 2_1^+)$ was determined using the ^{178}Au^g data only. Also, there was no path observed that would allow the 8_1^+ state to feed to the 2_2^+ state meaning that γ-ray energy gates exclude unwanted $10_1^+ \to 8_1^+$ transitions. Because Davidson produced a mixture of ^{178}Au^{g,m} and did not use gated spectra, the conversion coefficients given in Ref. [99] would have been significantly reduced by the similarly energetic pure E2 transition.

How much this impacts Davidson's value of α_{tot} depends on the relative production of ^{178}Au^{g,m} in their experiment, as well as the relative intensities of the 482.8- and 483.0-keV transitions following the EC/β^+ decay of ^{178}Au^{g,m}. There is no evidence of the 413.0-keV $8_1^+ \to 6_1^+$ transition in the present work's isomerically selective ^{178}Au^g data, meaning that there can be no 483.0-keV transitions from $10_1^+ \to 8_1^+$ from the decay of ^{178}Au^g. Thus, all of the $10_1^+ \to 8_1^+$ transitions in Davidson's dataset must follow the EC/β^+ decay of ^{178}Au^m. By comparing the relative intensities of the '483'- and 653.0-keV peaks in the γ-ray singles spectra for ^{178}Au^{g,m}, it was found that the difference between the α_{tot} value calculated for this thesis, and that reported in Ref. [99] can be explained if the earlier experiment produced the two parent states in the ratio $N(^{178}\mathrm{Au}^g)/N(^{178}\mathrm{Au}^m) = 0.97(6)$. This is in excellent agreement with the value of 0.99(3) that was calculated by comparing the relative intensities of the 170.1- and 413.1-keV γ rays ($2_1^+ \to 0_1^+$ and $8_1^+ \to 6_1^+$, respectively) in the ^{178}Au^m data to those reported by Davidson *et al.*

Therefore, the difference in α_{tot} values determined by Davidson *et al.* and those calculated for this thesis can be entirely explained by the contamination from the $10_1^+ \to 8_1^+$ transition. For the other transitions given in Table 6.8, the difference is likely explained by the significant contamination from ^{178}Os that was noted in Ref. [99]. Insufficient information is given in Ref. [99] for a similar comparison to be performed for these states.

The large E0 components of the $J_2 \to J_1$ transitions indicates strong mixing between these bands at low spin ($I = 0, 2, 4$) but weak mixing at $I = 6, 8$. This is in good agreement with the band-mixing calculations presented by Davidson in Table 10 of Ref. [99].

6.3.4 Difference in Mean-Squared Charge Radius Between the 0_2^+ and 0_1^+ States in ^{178}Pt

E0-transition strengths provide a direct way to determine the difference in the mean-square charge radius of the nucleus, $\delta\langle r^2\rangle$, between the initial and final states [63, 64]. To do so, the monopole transition strength squared, ρ^2, must first be calculated [63, 64]

$$\rho^2(\text{E0}) \equiv \alpha^2\beta^2(\delta\langle r^2\rangle)^2\frac{Z^2}{R^4}, \tag{6.14}$$

where α^2 and β^2 are the mixing amplitudes squared between the initial and final states (such that $\alpha^2 + \beta^2 = 1$) and $R = 1.17A^{1/3}$ fm. The values of α and β in Ref. [99] were used, which were found to be consistent with calculations performed by Page [122]. The value of ρ^2 can be determined experimentally using the relative branching of K-conversion components of the E0 and E2 transitions [I_K(E0) and I_K(E2), respectively] depopulating an initial state [63]

$$\rho^2(\text{E0}) = \frac{I_K(\text{E0})}{I_K(\text{E2})} \times \frac{\alpha_K(\text{E2})}{\Omega_K(\text{E0})} \times W_\gamma(\text{E2}), \tag{6.15}$$

where $\Omega_K(E0)$ is the electronic factor for K-shell conversion and $\alpha_K(E2)$ is the K-conversion coefficient for the E2 transition (both of which can be calculated using the BrIcc [62] software), W_γ(E2) is the rate of the E2 transition. Typically, the E2 transition used will be within the same rotational band - e.g. $2_2^+ \rightarrow 0_2^+$ will be used to calculate $\rho^2(E0,\ 2_2^+ \rightarrow 2_1^+)$. For $0^+ \rightarrow 0^+$ transitions, such an E2 transition cannot occur. In such cases, the E2 transition used is typically $0_2^+ \rightarrow 2_1^+$. For ^{178}Pt, the 0_2^+ band head is at 420.3 keV which depopulates to the 170-keV 2^+ yrast state through a 250.2-keV E2 transition or to the ground state of ^{178}Pt through a 420.3-keV internal conversion decay, as shown in Fig. 6.25. Therefore, the difference in mean-square charge radius between the 0_2^+ and 0_1^+ states is

$$\delta\langle r^2\rangle(0_2^+ \rightarrow 0_1^+) = \sqrt{\frac{R^4\rho^2(\text{E0})}{Z^2\alpha^2\beta^2}}, \tag{6.16}$$

where

$$\rho^2(\text{E0}) = \frac{I_K(420.3)}{I_K(250.2)} \times \frac{\alpha_K(250.2)}{\Omega_K(420.3)} \times W_\gamma(250.2). \tag{6.17}$$

Although the lifetimes of the states in the yrast band in ^{178}Pt have been measured in several studies (see e.g. Refs. [123, 124]), the only state in the second rotational band where a life-time measurement has been attempted is the 0_2^+ state where $T_{1/2}$ <700 ps was determined [120]. Using this, an upper bound of $1000{\cdot}\rho^2(0_2^+ \rightarrow 0_1^+)$ >1.4(2) was calculated. This is similar to the value Kibédi *et al.* reported in Ref. [63] of $1000{\cdot}\rho^2$(E0)>2 for the same transition. Using the band-mixing calculations reported in Ref. [99], a limit of $|\delta\langle r^2\rangle|$ >0.045(3) fm^2 was determined using the IDS data.

A follow-up fast-timing study at IDS would be able to measure the lifetimes of these states if they have $T_{1/2} \gtrsim 5$ ps [125]. At this limit for $T_{1/2}$, the corresponding value of $\delta\langle r^2\rangle$ would be approximately 0.5 fm^2. This range (0.045 fm to 0.5 fm) is shown alongside the $\delta\langle r^2\rangle$ values for other platinum, gold, and lead isotopes in Fig. 6.27. Each isotope's chain has been offset such that $\delta\langle r^2\rangle(N = 115) = 0$ for easier visual comparison. If the 0_2^+

state in ^{178}Pt were to have a similar value of $\delta\langle r^2\rangle$ to the ground state of the lead isotone (^{182}Pb), the half life of this state would be approximately 50 ps. Assuming a similar beam production rate to IS665, such lifetime measurements could feasibly be made within a few hours.

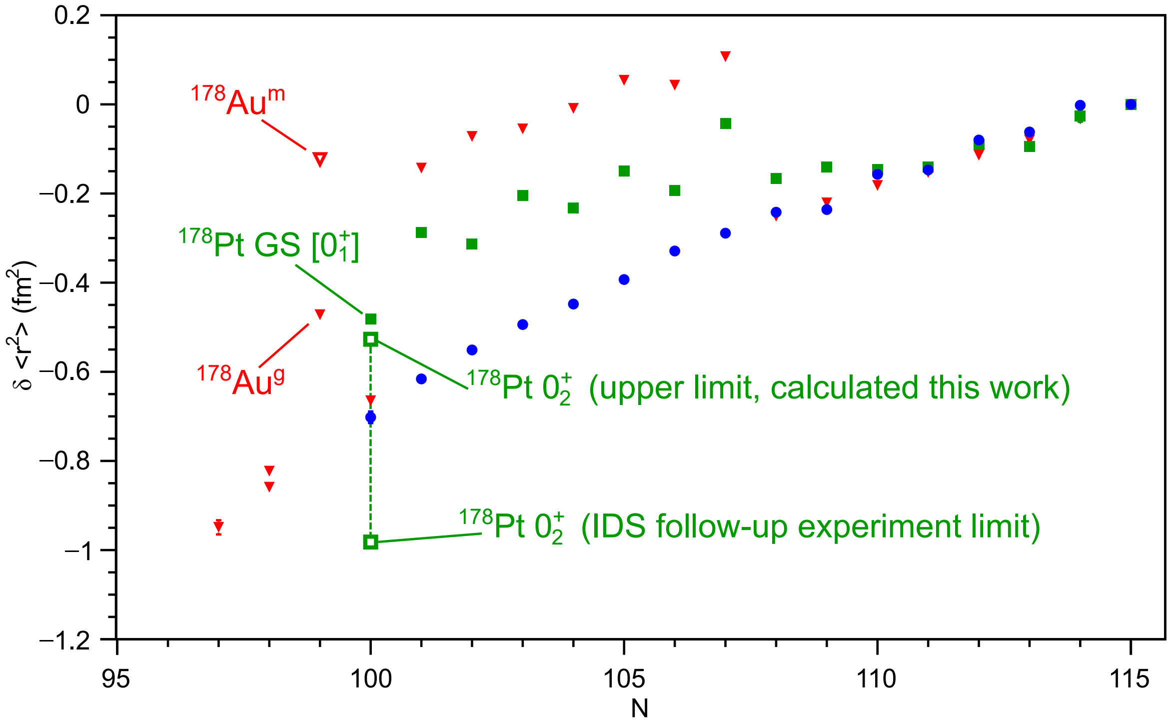

Figure 6.27: Plot of ground-state $\delta\langle r^2\rangle$, for platinum (filled green squares), gold (filled red triangles), and lead (blue circles) as a function of neutron number, N. All three isotopic chains have been offset such that the $\delta\langle r^2\rangle(N = 115) = 0$. The unfilled red triangle shows the value of $\delta\langle r^2\rangle$ for ^{178}Au^{m} and the unfilled green squares show the limit in $\delta\langle r^2\rangle$ for the 420-keV state in ^{178}Pt (upper) and the limit of what could feasibly be measured with a follow-up fast timing experiment at IDS (lower) - see the main text for details. Experimental values of $\delta\langle r^2\rangle$ are taken from Refs. [126–131].

6.3.5 log *ft* Value Calculation for the EC/β^+ decay of ^{178}Au

The first step in determination of the log ft values for the EC/β^+ decay of ^{178}Au^{g,m} was to calculate the total number of decays that occured for each state. This was done by fitting the 5446- and 5291-keV α-decay peaks from ^{178}Pt$\rightarrow^{174}$Os - see Fig. 6.2(a,b). When corrected for the α-decay detection efficiency, $\mathcal{E}_\alpha$ and the α-decay branching ratio, b_α=7.7(3)% [117], this gives the toal number of EC/β^+ decays:

$$N_\beta(^{178}\mathrm{Au}^{g,m}) = \frac{N_\alpha(^{178}\mathrm{Pt})}{\mathcal{E}_\alpha \cdot b_\alpha}. \tag{6.18}$$

The values of $N_\beta(^{178}\mathrm{Au}^{g,m})$ calculated using Eq. 6.18 were within 1σ (or $\sim 6\%$) of the total number of γ-ray/IC transitions to the ground state of ^{178}Pt (via the 170.1-, 420.3-, 653.0- and 855.6-keV transitions) for both datasets. While the total feeding through γ rays and CEs to the ground state of ^{178}Pt could, therefore, give an estimate of N_β, it was decided to use the value calculated using Eq. 6.18 to ensure consistency with the α- and EC/β^+-branching ratio calculation. This also allows the impact of Pandemonium feeding of the ground state to be determined.

The amount of EC/β^+ feeding of the excited state k, $N_{\beta,k}$, was determined by calculating the difference between the efficiency- and internal conversion-corrected number of transitions observed populating and depopulating it

$$N_{\beta,k} = \sum_{i\ \in\ \mathrm{out}} \frac{N_{\gamma,i} \cdot (1+\alpha_{tot,i})}{\mathcal{E}_{\gamma,i}} - \sum_{j\ \in\ \mathrm{in}} \frac{N_{\gamma,j} \cdot (1+\alpha_{tot,j})}{\mathcal{E}_{\gamma,j}}, \tag{6.19}$$

The values of N_γ were determined by fitting each γ-ray peak with a Gaussian function on a linear background. Where possible, this was done using singles spectra, to remove the impact of angular correlations. In a few cases there was a significant overlap between the peak being fitted and some other transition (e.g. the 483.0-keV $10^+_1 \rightarrow 8^+_1$ and 482.8-keV $2^+_2 \rightarrow 2^+_1$ transitions), so $\gamma - \gamma$ coincidence projections were used instead. Whenever the singles-peak intensity was used, the intensity value was within 2σ of that determined with γ-γ coincidence spectra. The 420.3-keV $0^+_2 \rightarrow 0^+_1$ transition is the only case where Eq. 6.19 could not be used, since there is no corresponding γ ray to this pure E0 transition. In this case, the efficiency-corrected number of CEs detected in the Si detectors was used instead.

For the decays from offband states of unknown spin and parity, the α_{tot} was estimated by assuming equal components of M1 and E2 transitions. Most of these offband states populate the yrast band through transitions of $\gtrsim$1 MeV. At such energies, α_{tot} is typically of the order 0.01 for both M1 and E2 transitions, and even lower for E1 decays. The contribution to the overall uncertainty in feeding from incorrect multipolarity assignements of these transitions is therefore small compared to that from the γ-ray detection efficiency or from fitting the peaks.

The log ft values shown in Tables 6.9 and 6.10 were calculated using the LogftCalculator software [132]. The feeding intensities calculated are upper limits because of Pandemonium, meaning that the log ft values determined should be interpreted as a lower limits.

Table 6.9: Table summarising the EC/β^+-decay feeding of and log ft value for each state in ^{178}Pt.

State in ^{178}Pt		Parent-Nucleus State			
		^{178}Au^g		^{178}Au^m	
E [keV]	J$^\pi$	Feeding [%]	log ft	Feeding [%]	log ft
170.1	2_1^+	33(2)	5.40(2)		
420.3	0_2^+	2.57(12)	6.45(3)		
427.2	4_1^+	3.8(2)	6.28(3)		
653.0	2_2^+	9.2(4)	5.85(3)		
764.8	6_1^+	0.69(3)	6.95(3)	5.8(4)	5.94(3)
855.8	(2^+)	6.6(3)	5.95(3)		
1001.2	2^+	5.5(3)	5.99(2)		
1058.0	4_2^+	3.37(15)	6.19(3)		
1177.9	8_1^+			5.0(4)	5.90(3)
1179.6		4.1(2)	6.08(3)		
1212.0		< 0.1			
1253.7		0.12(2)		2.33(16)	6.22(2)
1345.3		0.36(3)		6.75(5)	5.73(17)
1379.6		2.62(14)	6.22(3)		
1392.2		2.07(10)	6.32(3)		
1425.8		6.1(16)	5.84(15)		
1445.0		4.4(2)	5.98(3)		
1472.6		3.9(2)	6.02(3)		
1476.4	6_2^+			11.6(8)	5.45(17)
1481.2		0.33(3)			
1483.9		0.26(2)			
1573.1	5_4^-	0.061(4)	7.86(2)	2.48(17)	6.11(2)
1580.6		3.8(2)	6.01(3)	0.99(7)	6.51(17)
1605.2		2.11(15)	6.26(4)		
1649.1		0.44(6)			
1660.9	10_1^+			0.31(2)	6.49(17)
1716.6		0.27(2)			
1746.3		0.83(6)		7.1(5)	5.62(17)
1809.6	6_3^-			0.94(7)	6.48(16)
1814.1	7_4^-			0.51(4)	6.47(17)
1832.5		0.3(2)			
1834.1				1.59(11)	6.24(17)
1942.8	(6^+)			0.089(6)	
1945.4				0.4(3)	
1982.2				2.30(16)	6.04(18)
1993.1				0.65(5)	6.59(18)
2029.6				6.7(5)	5.57(18)
2037.3				0.089(6)	7.44(2)
2057.4		1.91(10)	6.19(3)		
2079.9				0.96(7)	6.4(18)
2090.9		1.19(6)	6.38(3)		

State in ^{178}Pt		Parent-Nucleus State			
		^{178}Au^{g}		^{178}Au^{m}	
E [keV]	J$^{\pi}$	Feeding [%]	log ft	Feeding [%]	log ft
2095.3		2.05(10)	6.14(3)		
2118.1	8_3^-			0.41(3)	6.76(18)
2137.5	9_4^-			2.61(18)	5.95(18)
2156.7		0.76(6)			
2176.8		0.12(3)			
2184.7		0.18(4)			
2196.8	8_2^+			16.4(11)	5.13(18)
2239.8				0.56(4)	6.59(18)
2329.6				0.023(2)	
2335.5		0.18(4)			
2344.4	7^+			23.7(16)	4.93(18)
2348.8		0.31(5)			
2590.9	7^+			< 0.1	
2718.2	7^+			< 0.1	
4257		0.19(4)			
4312		0.59(5)			
4658		< 0.1			
4934		< 0.1			
5860		< 0.1			
6890		< 0.1			

6.4 Introduction to ^{174}Ir EC/β^+ decay to ^{174}Os

The isomerically pure beams of ^{178}Au^{g,m} provide an opportunity to investigate the EC/β^+ decay of separate samples of ^{174}Ir^{g,m}. As shown in Sec. 6.1, the α decay of each parent, ^{178}Au^{g,m}, populates a single long-lived state in the daughter nucleus (^{174}Ir^{g,m}), either directly or via one or more short-lived excited states. Both of these states are known to undergo α and EC/β^+ decay [2, 116]. While the α-decay branches of isomerically pure ^{174}Ir^{g,m} were studied in Ref. [3], no equivalent investigation has been reported for the EC/β^+ branch as of the time of writing. This investigation was performed using the same γ-γ coincidence technique as for the EC/β^+ decay to ^{178}Pt described in Sec. 6.3. The same γ-γ coincidences matrices and singles spectra were used for this analysis as for that of the EC/β^+ decay of ^{178}Au^{g,m}.

The structure of ^{174}Os has been studied in previous works, including through EC/β^+ with a mixed beam of ^{174}Ir^{g,m} (see e.g. Refs. [2, 115, 116]) which have established two rotational and two vibrational bands. The EC/β^+decay scheme shown in Fig. 6.28 is taken from Ref. [115] is the most extensive from previous works and was used as a starting point for the analysis described below.

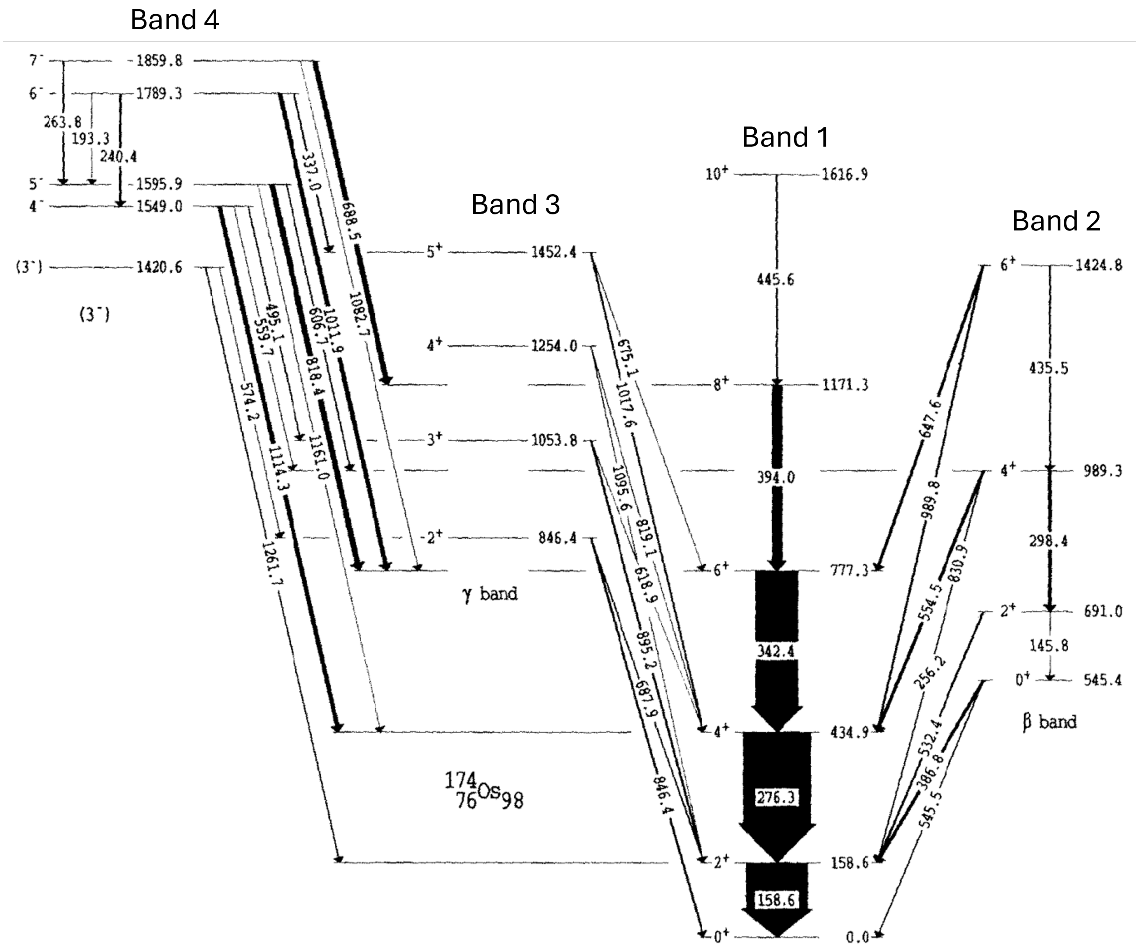

Figure 6.28: The EC/β^+ decay scheme for a mixed source of $^{174}Ir^{g,m} \rightarrow ^{174}Os$ from Ref. [115]. Band numbers used throughout the description of this analysis and in the decay schemes produced for this thesis have been added above each band for easier comparison with the present work's decay schemes.

Most states and transitions observed in the present work were already known from previous studies. As for the other decays discussed thusfar, the analysis details are split between Secs. 6.4.1 and 6.4.2 for data collected with beams of $^{178}Au^{g,m}$, respectively. Throughout this discussion, the band numbers indicated in Figs. 6.30 and 6.32 are used. Key projections of the γ-γ matrices for $^{174}Ir^{g,m}$ are shown in Figs. 6.29 and 6.31, respectively.

Once these decay schemes were constructed, log ft values for the EC/β^+ decay of each parent were calculated in the same way as is outlined in Sec. 6.3.5 - see Table 6.10. The normalisation of EC/β^+-decay feeding was done using the total number of α decays from $^{178}Au^{g,m}$ corrected for the appropriate branching ratios. Significant α-decay feeding from ^{178}Pt to the 2_1^+ state in ^{174}Os was observed in both datasets [see the prominent 5291-keV α-decay peaks in Figs. 6.2(a,b)] which was corrected for when determining the feeding of this state.

6.4.1 EC/β^+ Decay of ^{174}Ir^g $\rightarrow^{174}$Os

Strong direct feeding was observed to the 2_2^+, 2_3^+, and 3_3^+ states in ^{174}Os which together account for just over half of all EC/β^+ decays of ^{174}Ir^g - see Table 6.10. This feeding pattern strongly suggests that $I^\pi(^{174}\text{Ir}) = 2^+$, which is discussed further in Chapter 7. The feeding to bands 2 and 3 is in stark contrast to that of band 1, where all feeding is indirect as it can be accounted for by γ-ray and IC transitions from higher-energy states within ^{174}Os - see Table 6.10. The reason for this difference in feeding to different bands is not clear. There is only a small amount of direct feeding assigned to the 4^+, 5^+, and 6^+ states in these bands which is likely the result of Pandemonium.

Moderate direct feeding of the 3_4^- and 4_4^- states was also observed, which together received $\approx 9\%$ of all EC/β^+ decays. The 5_4^- and 6_4^- states, in contrast, received negligible feeding. This corroborates the $I^\pi(^{174}\text{Ir}^m) = 2^+$ assignment made above, as the 3_4^- and 4_4^- states can be populated through first-forbidden transitions, wheras the 5_4^- and 6_4^- states can only be populated through negligibly weak third-forbidden decays.

Ten offband states were found to be populated by the EC/β^+ decay of ^{174}Ir^g which fed to the yrast band, band 2, or both, as shown in Fig 6.30. These offband states account for $\sim 29\%$ of all feeding collectively, although most of this total ($\sim 21\%$) is from feeding of just the 1622- and 1743-keV states. Given the similarly strong feeding of these two offband states and the $2_{2,3}^+$ states, the 1622- and 1743-keV states liekly have $I^\pi = (1^+, 2^+,$ or $3^+)$.

Strong peaks at E_γ =190.1 and 458.3 keV are present in the spectrm shown in Fig. 6.29(b) but not in Fig. 6.29(a). It was found that these two γ rays were coincident with osmium K x rays, each other and a γ-ray at E_γ =277.3(3) keV. This energy is noticeably different to $E_\gamma(4_1^+ \rightarrow 2_1^+, ^{174}\text{Os}) = 276.3(3)$ keV. These two transitions were also observed in the ^{174}Ir^m data. It is not clear what the origin of these γ rays is, but it is unlikely that they are from transitions with ^{174}Os, so are not included in the decay schems shown in Figs. 6.30 or 6.32.

Table 6.10: Summary of the total EC/β^+-decay feeding and log ft value for ^{174}Ir^{g,m}.

State in ^{174}Os		Parent			
		^{174}Ir^{g}		^{174}Ir^{m}	
E [keV]	J$^{\pi}$	Feeding [%]	log ft	Feeding [%]	log ft
0.0	0_1^+	0.0	-	-	-
158.5	2_1^+	-0.9(6)	-	-	-
434.4	4_1^+	0.44(5)	7.41(8)	0.4(3)	-
545.3	0_2^+	4.73(17)	6.35(4)	-	-
690.9	2_2^+	20.9(9)	5.67(4)	-0.2(6)	-
777.5	6_1^+	-0.1(3)	-	26.6(8)	5.34(3)
846.2	2_3^+	16.6(16)	5.73(6)	-	-
989.4	4_2^+	-0.2(5)	-	0.1(6)	-
1054.0	3_3^+	12.6(5)	5.80(4)	-	-
1171.1	8_1^+	-	-	0.5(4)	-
1254.1	4_3^+	0.71(7)	6.99(6)	4.0(2)	6.0(3)
1406.7	-	0.94(3)	6.83(4)	-	-
1420.1	3_4^-	5.4(2)	6.07(4)	-	-
1424.9	6_2^+	0.70(6)	6.92(5)	18.3(13)	5.33(4)
1452.4	5_3^+	0.022(8)	-	4.1(11)	6.0(2)
1548.1	4_4^-	3.3(3)	6.25(5)	6.5(8)	5.75(8)
1596.0	5_4^-	1.53(6)	6.57(4)	6.0(8)	5.77(8)
1622.3	-	11.8(4)	5.68(4)	-	-
1637.2	-	3.58(13)	6.19(4)	-	-
1678.1	-	2.49(9)	6.34(4)	-	-
1742.8	-	9.0(3)	5.76(4)	-	-
1789.4	6_4^-	-	-	12.7(12)	5.39(5)
1811.1	-	-	-	5.60(3)	5.74(3)
1844.4	-	1.17(4)	6.62(4)	-	-
1855.4	-	0.73(3)	6.82(4)	-	-
1860.2	7_4^-	-	-	6.9(5)	5.63(4)
2075.3	-	-	-	1.4(3)	6.27(12)
2152.1	-	0.20(14)	-	-	-
2271.0	-	0.21(14)	-	-	-
2289.1	-	-	-	1.2(3)	6.26(12)
2294.0	-	-	-	0.48(16)	6.7(2)
2441.9	-	-	-	0.76(6)	6.43(5)
2481.1	-	-	-	0.9(3)	6.35(17)

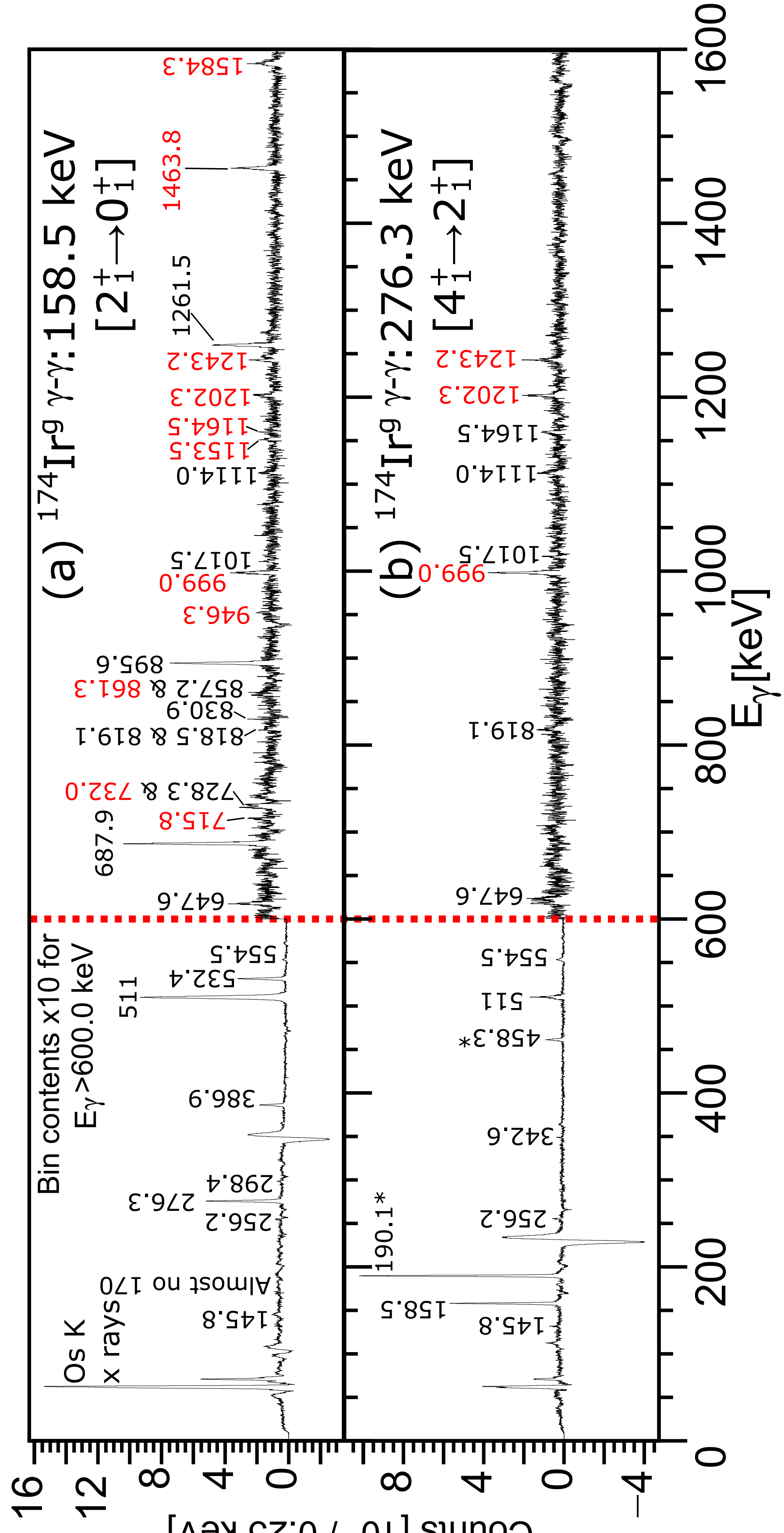

Figure 6.29: The prompt γ-γcoincidence projections on (a) 158.5 keV and (b) 276.3 keV for $^{174}\mathrm{Ir}^{g} \rightarrow {}^{174}\mathrm{Os}$. Peaks at 190.1 and 458.3 keV are marked with an asterix because they are present in (b) but not (a), suggesting these are from a contaminant which has a γ ray at $E \approx 276$ keV - see main text for more details.

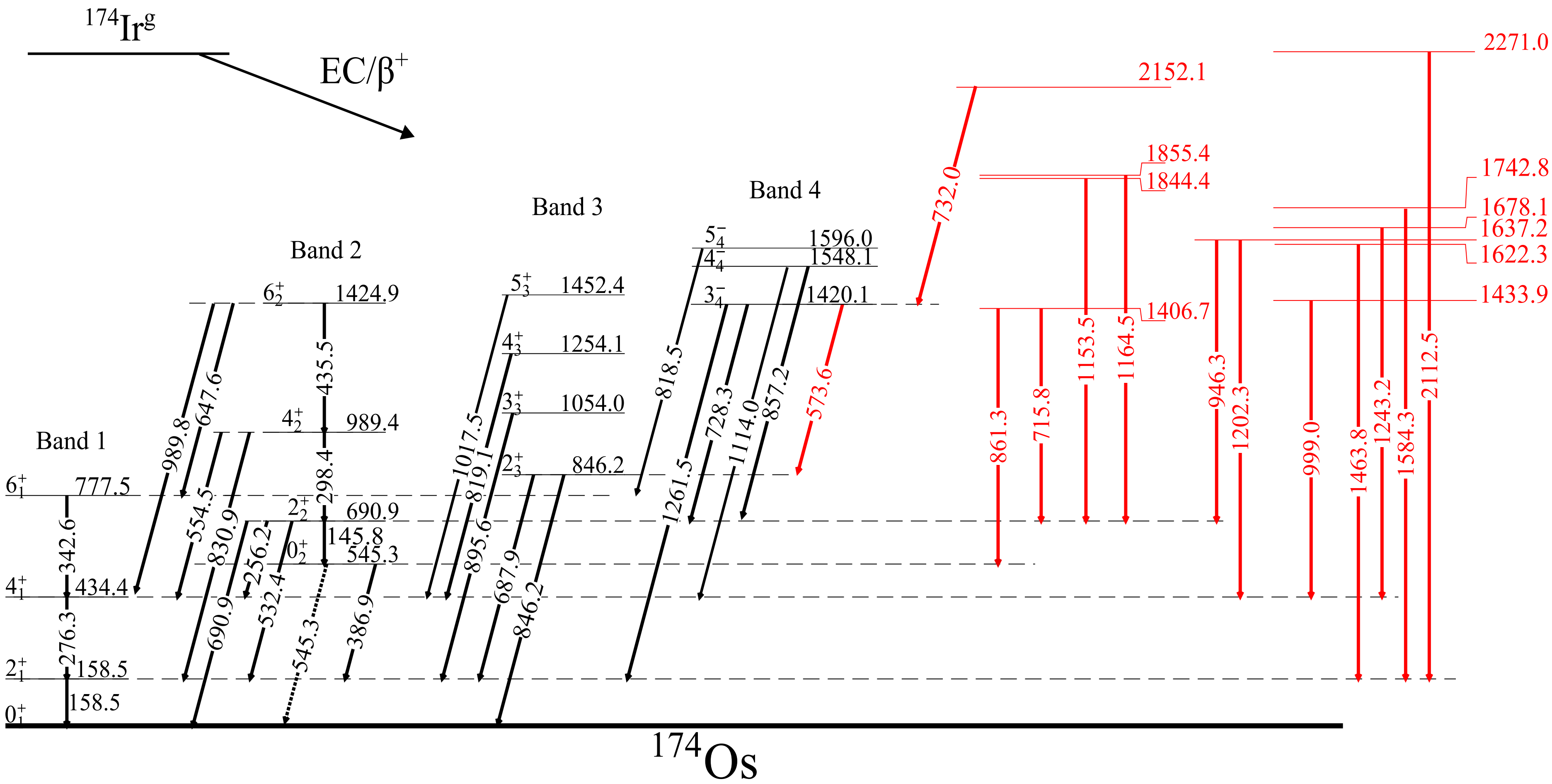

Figure 6.30: Decay scheme for the EC/β^+ decay of ^{174}Ir^g $\rightarrow^{174}$Os following the α decay of ^{178}Au^g. As for previous decay schemes, new states and transitions observed in this study are shown in red, while those reported in any of Refs. [2, 33, 115] are shown in black. Transition line thicknesses are all the same and do not correspond to the relative intensities observed for each transition.

6.4.2 EC/β^+ Decay of ^{174}Ir^m $\rightarrow^{174}$Os

The EC/β^+ decay of ^{174}Ir^m strongly fed the $6^+_{1,2}$ states in ^{174}Os, which together received $\approx$ 45% of all feeding. The $4^+_{1,2}$ and $8^+_{1,2}$ states, in contrast, received essentially no direct feeding, strongly suggesting that $I^\pi(^{174}\text{Ir}^m) = 6^+$.

Moderate feeding was assigned to the 4^+_3 and 5^+_3 states, although most of the former is likely to be from the Pandemonium effect since none was seen to the 4^+ states in bands 1 and 2. If the 6^+ assignment for the parent state is correct, then the 5^+_3 state could be populated through allowed GT decays, while the 4^+_3 state could only be populated through much less probable second-forbidden transitions.

Interestingly, the 6^-_4 state was strongly fed (12.7%) while about half of this feeding was observed to the 5^-_4 and 7^-_4 (6.0% and 6.9%, respectively). If $I^\pi(^{174}\text{Ir}^m) = 6^+$ then direct population of these states would be through first-forbidden transitions. This would mean that there must be significant similarity of proton/neutron states of ^{174}Ir^m and the bandhead of band 4 to allow for the strong feeding to these negative-parity states.

Additionally, six offband states were observed, as shown in the decay scheme given in Fig. 6.32. The feeding of most of these states was small (typically, $\approx$ 1%), except for the 1811-keV which received 5.6% of all feeding.

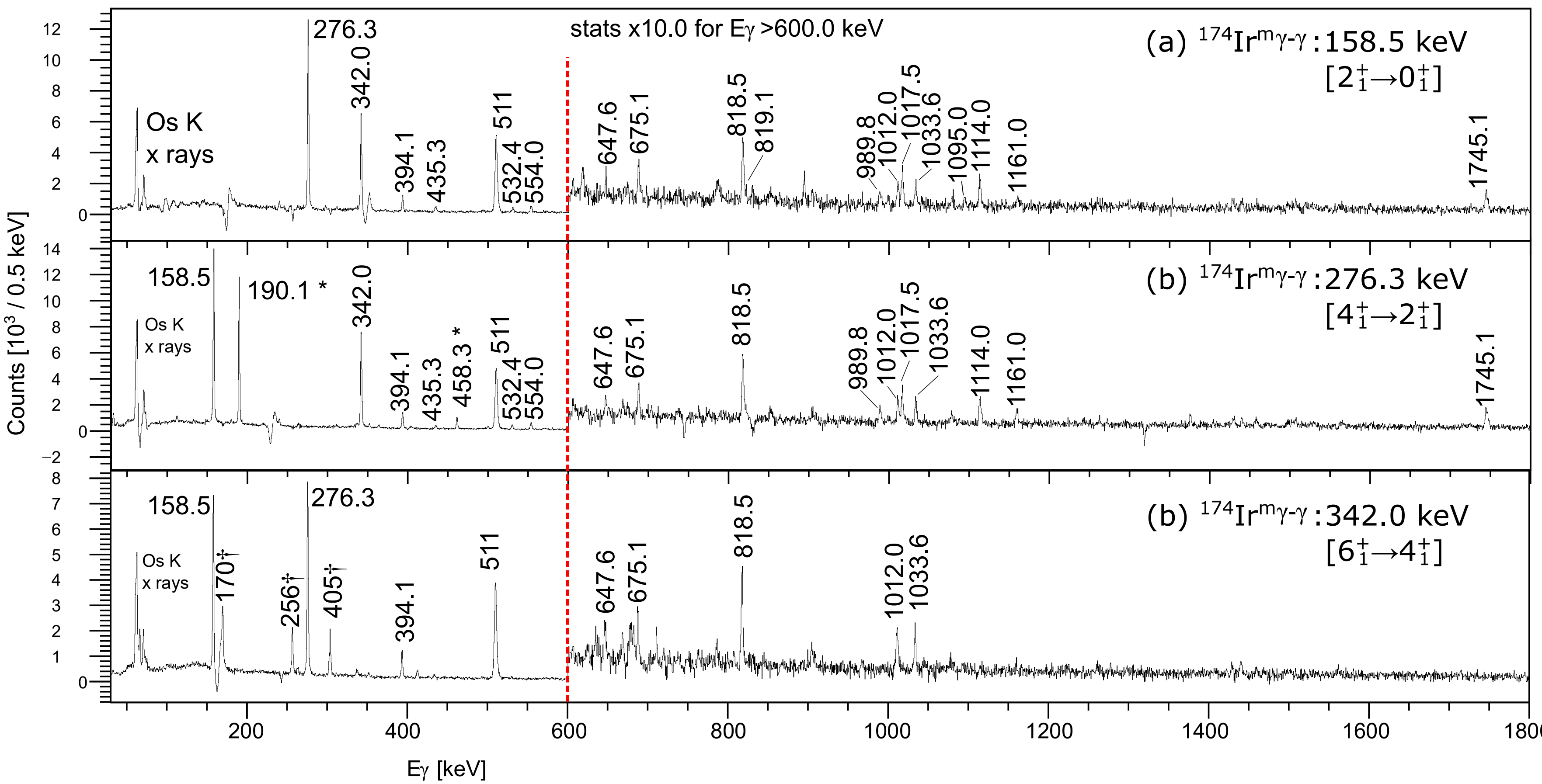

Figure 6.31: The prompt $\gamma - \gamma$-ray coincidence projections on (a) 158.5 keV, (b) 276.3 keV, and (c) 342.0 keV for data collected with the ^{178}Au^m beam. Peaks at 190.1 and 458.3 keV are marked with an asterix because they are present in (b) but not (a), suggesting these are from a contaminant which has a γ ray at $E \approx 276$ keV. Contaminating transitions within ^{178}Pt are marked with an obelus.

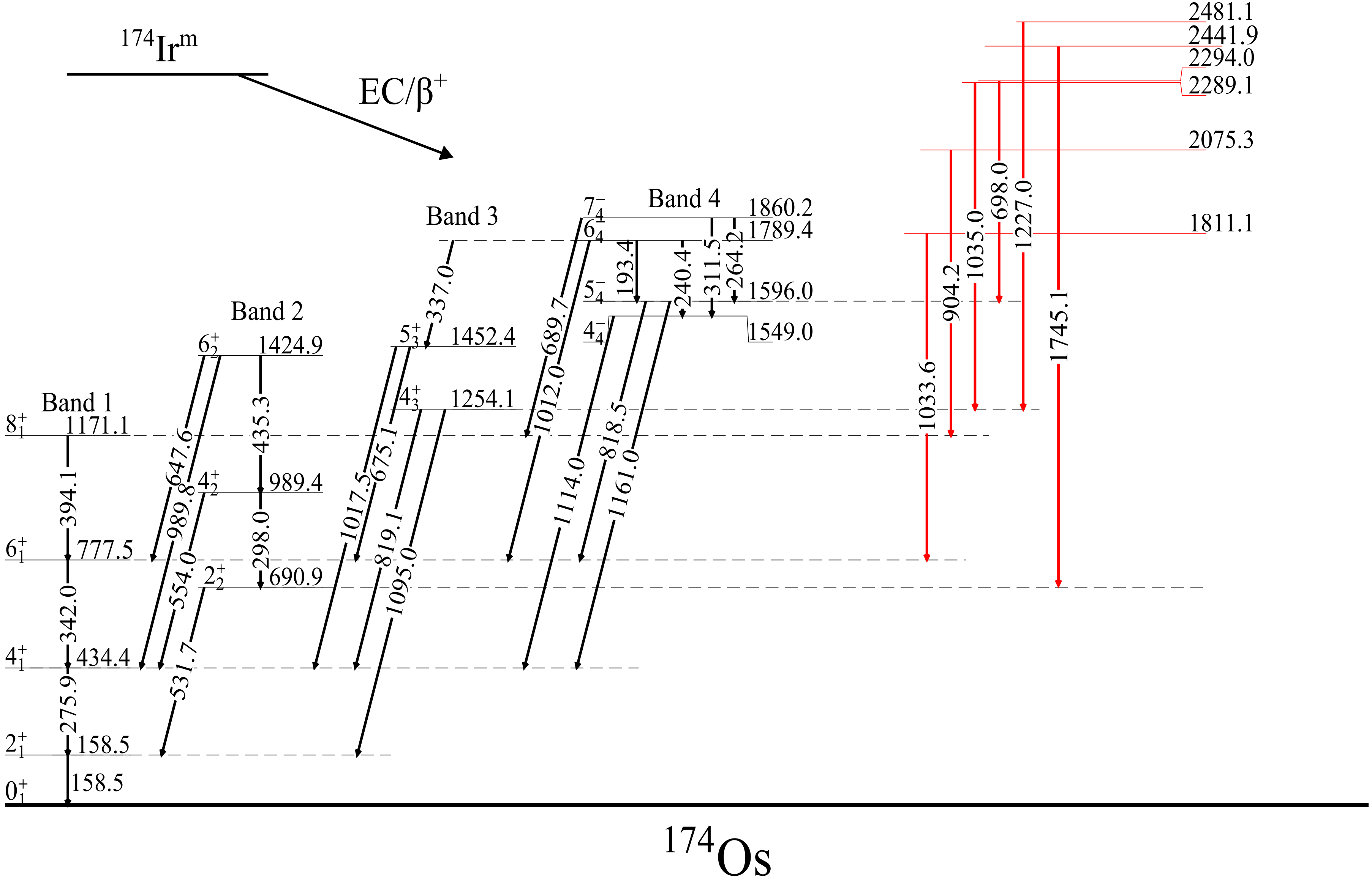

Figure 6.32: Decay scheme for the EC/β^+ decay of ^{174}Ir^{m} $\rightarrow$^{174}Os following the α decay of ^{178}Au^{m}. As for previous decay schemes, new states and transitions observed in this study are shown in red, while those reported in any of Refs. [2, 33, 115] are shown in black. Transition line thicknesses are all the same and do not correspond to the relative intensities observed for each transition.

6.4.3 E0-Transition Strengths in ^{174}Os

The conversion coefficients $\alpha_{tot,K}(J_2 \rightarrow J_1)$ for ^{174}Os were calculated using the methods outlined in Sec. 6.3.3 and are summarised in Table 6.11.

Table 6.11: The K and total conversion coefficients determined for the $J_2 \rightarrow J_1$ transitions between bands 1 and 2 in ^{174}Os - see Figs. 6.30 and 6.32. The conversion coefficients in the $\alpha_{K,1}$ and $\alpha_{tot,2}$ columns were determined using methods 1 and 2, as described in Sec. 6.3.3. The equivalent conversion coefficients reported by Kibédi *et al.* in Ref. [115] are also given.

				This study		Ref. [115]	
E_i [keV]	E_f [keV]	E_{trans} [keV]	J^π	$\alpha_{K,1}$	$\alpha_{tot,2}$	α_K	α_{tot}
690.9	158.5	532.4	2^+	0.10(5)	0.16(4)	0.12(9)	0.146(9)
989.4	434.4	554.5	4^+	-	0.075(3)	0.069(8)	0.083(9)
1424.9	777.5	647.6	6^+	0.050(6)	-	0.044(10)	-

If there were some systematic problem with the methods used, it would likely impact the conversion coefficients determined for ^{174}Os as well as for ^{178}Pt. The good agreement between the conversion coefficients determined in this study with those reported in Ref. [115] in ^{170}Os therefore adds further strength to the arguments made in Sec. 6.3.3 about the conversion coefficients reported by Davidson *et al.* in Ref. [99].

Using the relative intensities of the $0_2^+ \rightarrow 0_1^+$ and $0_2^+ \rightarrow 2_1^+$ transitions (E=545.3 and 386.9 keV, respectively), the values $q_k^2(E0/E2) = 1.8(8)$ and $X(E0/E2) = 0.010(4)$ were determined. The lifetime of the 0_2^+ state is unknown and too short for a meaningful limit to be measured using HPGe detectors, meaning that $\rho^2(E0)$ cannot be calculated. The value of $1000 \cdot \rho^2(E0) \cdot T_{1/2}(0_2^+)$=1.3(7) ns was therefore calculcated. This is similar to the equivalent value for the 420-keV state in ^{178}Pt for which $1000 \cdot \rho^2(E0) \cdot T_{1/2}(0_2^+) =$ 1.00(14) ns. Measuring the lifetime of this state could be done in the same follow-up experiment proposed to measure the lifetimes of states in the second rotational band of ^{178}Pt.

6.4.4 Determination of log ft values for ^{174}Ir

The EC/β^+-decay feeding strength and thus, log ft values were determined using the same method as for the β decay of ^{178}Au^{g,m}. The results obtained are summarised in Table 6.10. The efficiency- and IC-corrected intensity of each γ ray was determined by fitting a Gaussian distribution to each peak in either the singles or a γ-γ matrix projection. The feeding by EC/β^+ decay was determined by finding the difference between the intensity of transitions feeding of a state and those exiting it using Eq. 6.19. The log ft values were calculated using the LogftCalculator [132].

6.5 ^{174}Ir α decay to ^{170}Re

The α decay of $^{174}\mathrm{Ir}^{g,m}$ has been investigated previously by, for example Schmidt-Ott [2] and Al-Monthery [3]. Both studies identified two α-decaying states in the parent and most of the same transitions. Their respective decay schemes are shown in Figs. 6.33(a,b). Al-Monthery added a new 5301-keV α decay requiring a change to the fine structure of ^{170}Re because the 193- and 224-keV γ rays were assigned as transitions from two distinct states, as shown in Fig. 6.33.

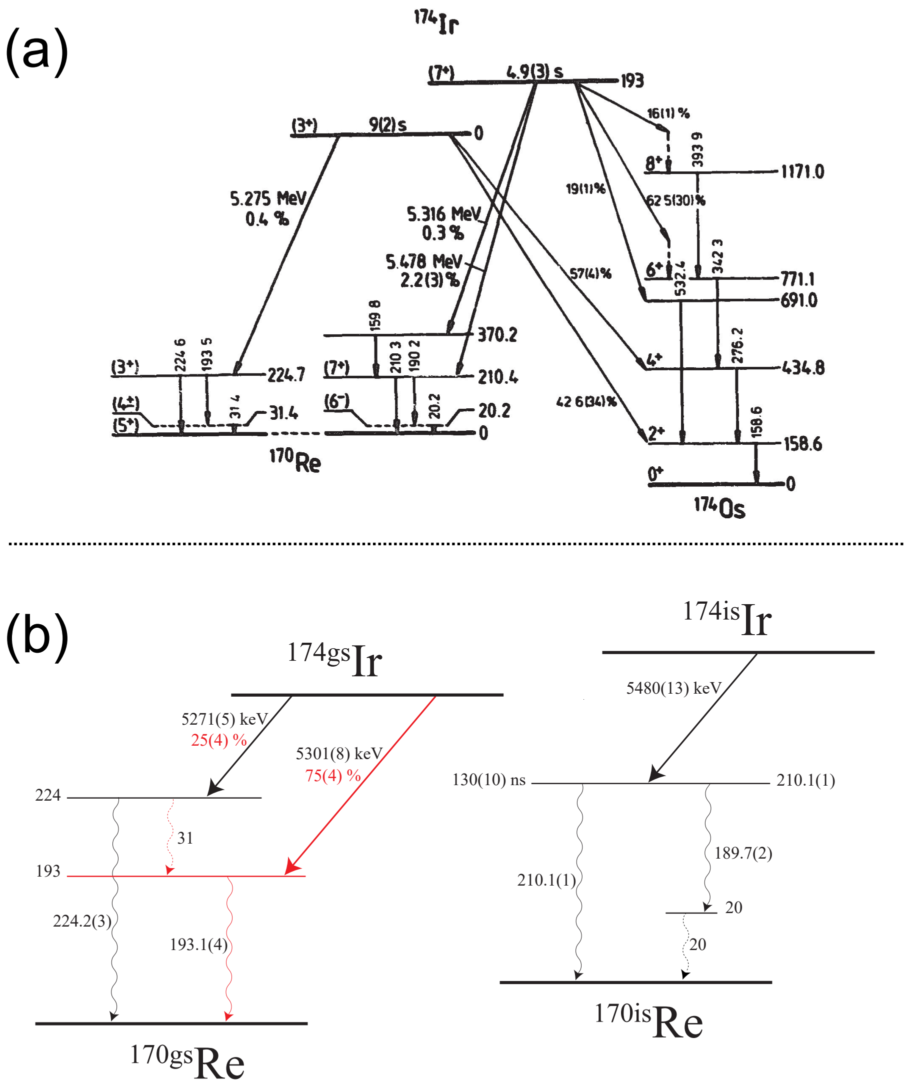

Figure 6.33: The decay schemes deduced for $^{174}\mathrm{Ir}^{g,m}$ in (a) Ref. [2] and (b) Ref. [3].

The α decay of ^{174}Ir^{g,m} was investigated for this thesis using the same α-γ coincidence analysis method described in Sec. 6.1 to produce the decay schemes shown in Figs. 6.35. The relevant part of the α-γ coincidence matrices (produced using the same prompt condition as for the α decay of ^{178}Au^{g,m}, $|\Delta t_{\alpha\gamma}| \leq$150 ns) along with some key projections are shown in Figs. 6.34 and 6.36 for ^{174}Ir^{g,m}, respectively. There is no evidence of any of the α decays or γ rays that were observed from ^{174}Ir^{g} in the ^{174}Ir^{m} data, establishing an absense of internal transitions from ^{174}Ir^{m} $\rightarrow$^{174}Ir^{g} before undergoing α or EC/β^{+} decay.

As will be shown, the α decay of the low-spin ground state of ^{174}Ir populates a low-energy, low-spin isomer in ^{170}Re, which is called ^{170}Re^{ls} in the following discussion. Similarly, the α decay of ^{174}Ir^{m} was found to populate a higher-spin state in ^{170}Re, which is called ^{170}Re^{hs}. It is possible that ^{170}Re^{hs} is the ground state, although this cannot be confirmed by the currently available data.

6.5.1 α Decay of ^{174}Ir^{g} $\rightarrow$^{170}Re^{ls}

All transitions in the α-decay scheme for ^{174}Ir^{g} in Ref. [3] were found in the IDS data - see Fig. 6.34. The 5271(5)-keV α decay reported in that study was found at 5278(5) keV and is coincident with γ rays at 223.9, 192.7, and 31.2 keV. As in Ref. [3], the 223.9- and 31.2-keV transitions are assigned as depopulating a 223.9-keV state, with the latter feeding of a 192.7-keV state - see Fig. 6.35(a). This is, in part, because the 192.7-keV γ is also coincident with a 5308-keV α decay, confirming the modification to Schmidt-Ott's decay scheme suggested by Al-Monthery.

As shown in Fig. 6.34(b), the α-decay peak around 5290 keV is well fit by a function comprising four separate Crystalball peaks. The shaping parameters were set by fitting the 5446-keV peak from ^{178}Pt$\rightarrow$^{174}Os coincident with time-random Compton-scattered γ rays - see Figs. 6.34(b,c). One of the four α decays contributing to this peaks is the 5291-keV α decay to the 2^{+}_{1} state in ^{174}Os while two others are the aforementioned 5278- and 5308-keV transitions. The fourth is a new α decay at E_{α} =5253(7) keV which was in coincidence with the 31.2-, 192.7-, and 223.9-keV transitions, in addition to a new 53.1-keV γ ray. Based on the $Q_{\alpha,tot}$ value, the 53.1-keV transition is assigned as feeding of the 192.7-keV state from a 245.8-keV state. The fact that this α decay is coincident with the 31.2-, and 223.9-keV γ ray requires there to be an additional 21.9(4)-keV transition from the 245.8-keV to the 223.9-keV state. Such a transition would be too low in energy to be observed with the setup used. Therefore, this implied transition is shown with a dashed line in the decay scheme to indicate it was not observed directly.

The 158-keV γ ray from $2_1^+ \rightarrow 0_1^+$ in ^{174}Os is the strongest transition in the spectrum shown in Fig. 6.34(c) due to the strong 5291-keV α-decay from ^{178}Pt overlapping significantly with the gate used. A clean Os K x-ray spectrum was produced using t background-subtracted γ-γ projection on the 132-keV $2_1^+ \rightarrow 0_1^+$ state in ^{178}Os. This was scaled using the intensity of the 158-keV peak, the K conversion coefficient, and the appropriate detection efficiencies, to provide an estimate for the intensities of K x-rays in in Fig. 6.34(c) from the 158-keV transition. This was subtracted from the projection shown, leaving a Re K x-ray spectrum that was used with fits of the 192.7- and 223.9-keV γ-ray peaks to determine R_K. The results, given in Table 6.12, show that both the 192.7- and 223.9-keV transitions must be E1 to explain the small number of Re K x rays in coincidence Fig. 6.34. The 21.9-, 31.2-, and 53.1-keV transitions are not considered because they are not energetic enough to cause K conversion.

Table 6.12: Table showing the ratio R_K values (as defined in Eq. 6.4) determined for combinations of E1, M1, and E2 assignments for the 192.7- and 223.9-keV γ rays.

			192.7		
	Multipolarity		E1	M1	E2
		α_K	5.86E-02	6.67E-01	1.87E-01
	E1	4.02E-02	**120(40)**	950(120)	300(70)
223.9	M1	4.40E-01	510(70)	1300(200)	680(90)
	E2	1.25E-01	200(60)	1040(150)	380(70)

The α-decay branching ratio was determined to be $b_\alpha(^{174}\mathrm{Ir}^g) = 0.38(9)\%$ by comparing the number of α decays from ^{174}Ir^g $\rightarrow ^{170}$Re to the number of α decays from ^{178}Au^g $\rightarrow ^{174}$Ir^g. This is reasonable agreement with the value of 0.3%[6] deduced in Ref. [2]. The δ_α^2 values given in Fig. 6.35(a) were calculated using the same method as described in Sec. 6.2.1.

[6]No uncertainty provided in original publication

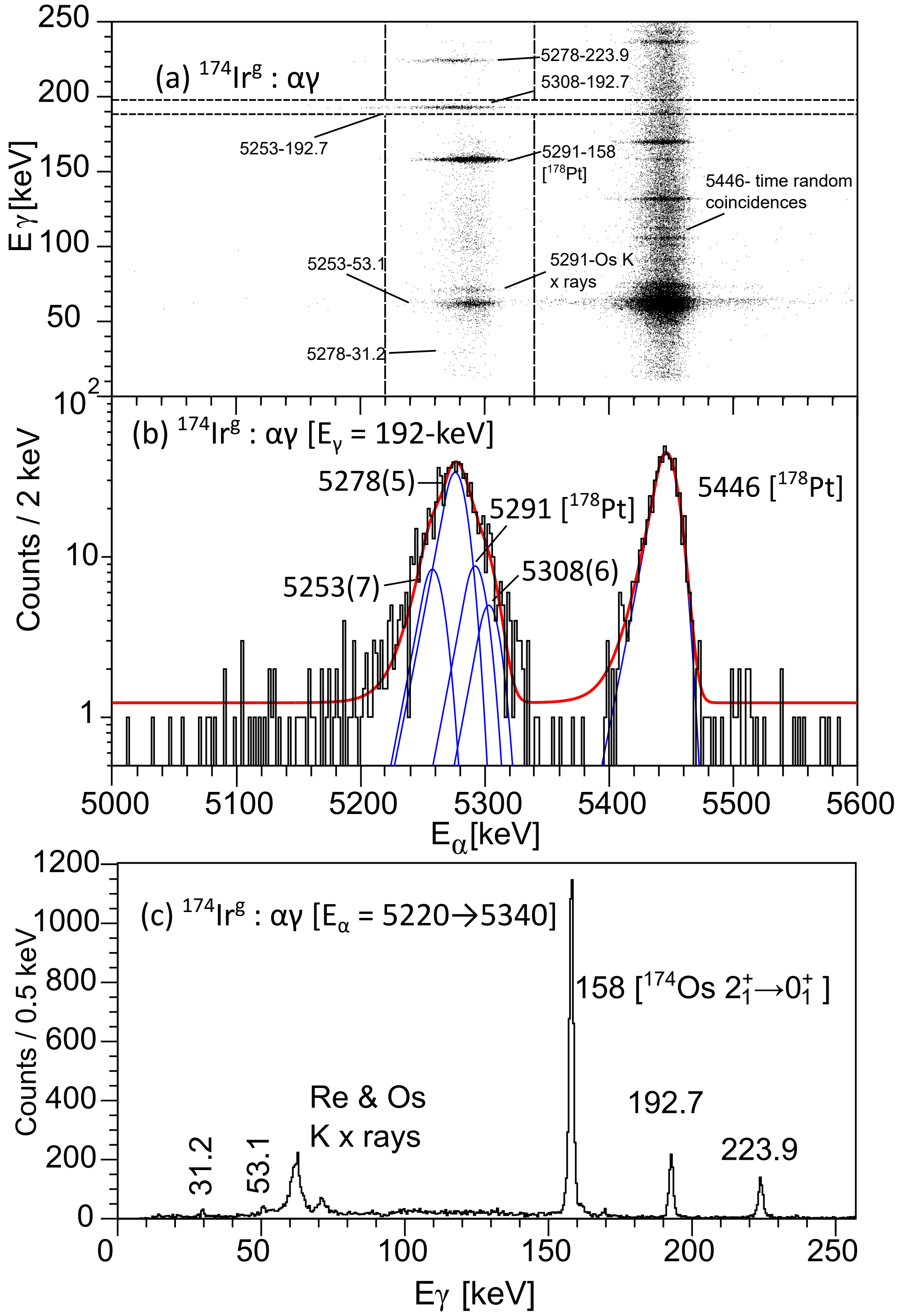

Figure 6.34: ^{174}Ir^{g}: (a) - part of the α-γ coincidence matrix. The gates used in (b,c) are shown with dashed vertical and horizontal lines. (b) the α-decay spectrum produced with a gate on the 192.7-keV γ ray. The data have been fitted with the sum of five Crystalball functions (red) whose shaping parameters were determined by a fit on the 5446-keV α-decay peak. The constituent Crystalball functions are shown in blue. (c) The γ-ray energy spectrum produced with a gate condition that 5220 keV< E_α <5340 keV. The prominent 158-keV peak, corresponding to the $2^+_1 \to 0^+_1$ transition within ^{174}Os, is present due to the 5291-keV α decay from ^{178}Pt.

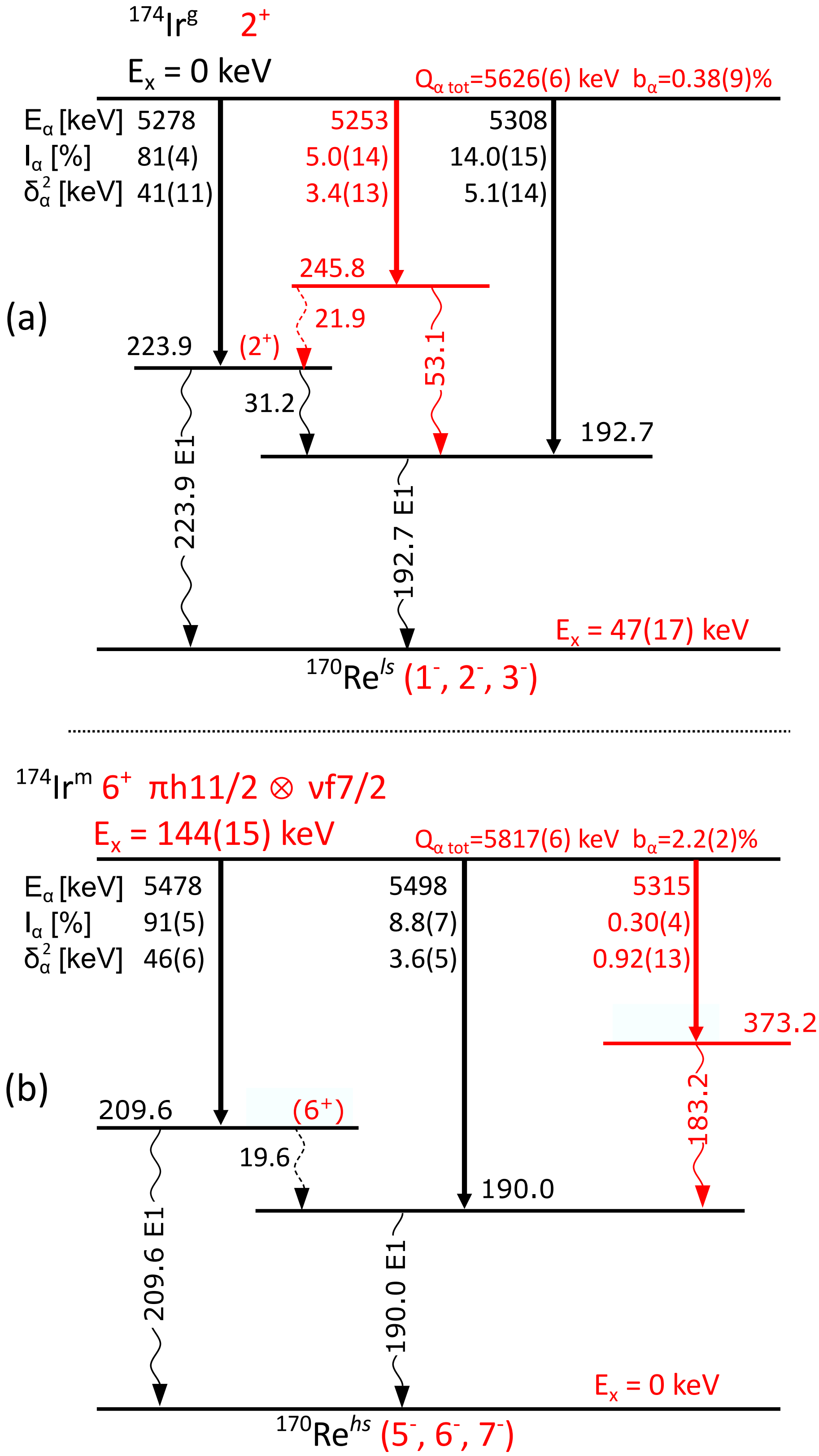

Figure 6.35: The α-decay schemes deduced for (a) $^{174}\mathrm{Ir}^{g}$ and (b) $^{174}\mathrm{Ir}^{m}$. Newly identified transitions and states are shown in red. The 21.9- and 19.6-keV transitions are shown with dashed lines as these transition are implied but too low in energy to have been observed directly.

6.5.2 α Decay of ^{174}Ir^{m} $\rightarrow$^{170}Re^{hs}

The two γ rays reported by Al-Monthery at 210.1 and 189.7 keV following the α decay of ^{174}Ir^{m} were observed in the present work at 209.6(3) and 190.0(3) keV - see Fig. 6.36. Both of these transitions were coincident with the 5478(5)-keV α decay as shown in Fig. 6.36(a). The α-decay peak produced when gating on the 190.0-keV transition has an unusual shape with a high-energy tail (see Fig. 6.36(b)) that can be well explained if there is a separate peak at 5498(6) keV. In principle, this peak shape could alternatively be produced by α-electron summing. This was the reason proposed by Al-Monthery who observed a similar relative intensity of these two peaks. This cannot be the cause, though, as Al-Monthery implanted ^{174}Ir deep into a DSSD, giving high detection efficiency. Therefore, the peak should be much smaller in the present work since the silicon detectors have a solid-angle coverage of less than 4%. This means that an α-electron summing peak should have no more than 4% of the area of the corresponding α-decay peak. The high energy tail is substantially larger than this and, therefore, contrary to Ref. [3], the 190.0-keV γ ray is assigned as feeding directly to a high-spin state of ^{174}Ir. An unseen 19.6-keV transition is required to connect the states fed by the 5478-keV and 5498-keV α decays, which is shown with a dashed line in Fig. 6.35(b).

A new α decay was observed at 5315(7) in coincidence with the 190.0-keV γ ray already discussed [see Fig. 6.36(b)] and a new 183.2(4)-keV transition, which gives $Q_{\alpha,tot}$(5315-183)=5623(7) keV. This is consistent with Q_α(5498 keV) = 5627(6) meaning the 5315-keV α decay is assigned as feeding of a 373.2-keV state which decays to the 190.0-keV state through the emission of a 183.2-keV γ ray. The 5315-keV α-decay peak not being in coincidence with the 209.6-keV γ ray confirms that it is emitted by the deexcitation of a different state to the 190.0-keV γ ray, as suggested above. See Figs 6.36(a,b) and note the relative intensity of the these two γ-ray peaks in (a) and the lack of a 5315-keV α-decay peak when gating on the 209.6-keV γ ray.

The highest-energy decay paths for ^{174}Ir^{g,m} give $Q_{\alpha,tot}$ = 5626(6) and 5816(6) keV, respectively. The latter is 191(8) keV higher than the former but is from an excited state in ^{174}Ir^{m} at 144(15) keV - see Sec. 6.1.2. Therefore, the state eventually fed following the α decay of ^{174}Ir^{m} is 47(17) keV lower than that by ^{174}Ir^{g}. No corresponding γ-ray transition was observed meaning that this is likely isomeric. Assuming that each parent state is similar to the daughter state it feeds, this means that there is an inversion of the state ordering between ^{174}Ir and ^{170}Re since the ground state of the parent feeds to an isomer in the daughter and vice versa.

Values of b_α and δ^2_α for ^{174}Ir^{m} were calculated using the same methods as for ^{174}Ir^{g} - see Sec. 6.5.1. The branching ratio, b_α = 2.2(2)%, was determined by comparing the total area of the α-decay peaks from ^{174}Ir^{m} $\rightarrow$^{170}Re to the number from ^{178}Au^{m} $\rightarrow$^{174}Ir^{m}. This is in good agreement with, but more precise than, the value determined by Schmidt-Ott of b_α = 2.5(3)% [2]. The γ-ray multipolarities were determined by comparing the total number of α decays to the 190.0- and 209.6-keV states to the efficiency- and IC-corrected number of transitions from these states. The unusual shape of the K x-ray region of Fig. 6.36(c) prevented the determination of R_K values for the 190.0- and 209.6-keV γ rays.

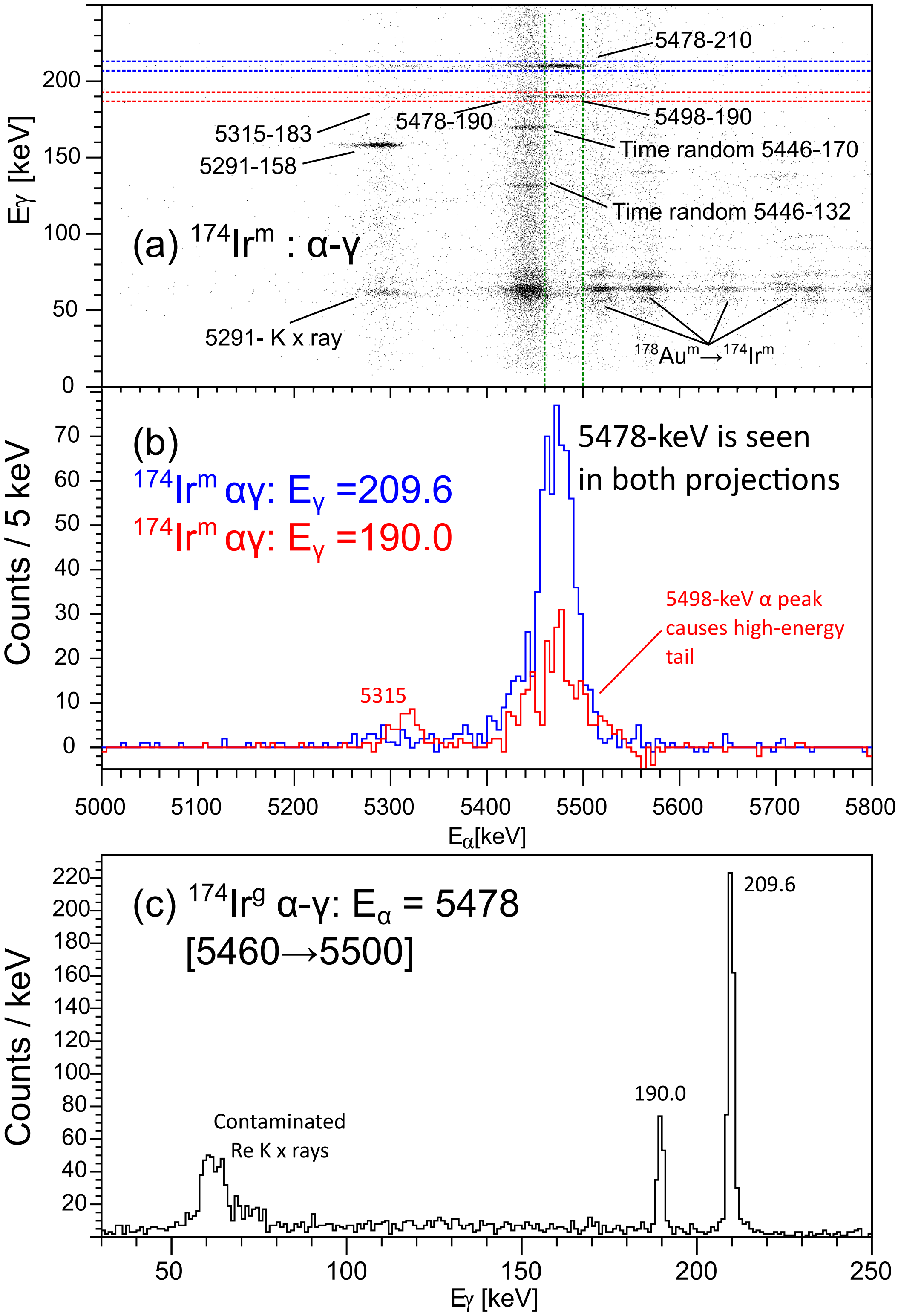

Figure 6.36: ^{174}Ir^{m}: (a) part of the prompt α-γ coincidence matrix. The gates used to produce (b,c) are shown using vertical and horizontal dashed lines. (b) the α-decay spectrum produced with a gate on the 190.0-keV γ ray (red) and the 209.6-keV γ ray (blue). (c) The projection of the prompt α-γ matrix produced with a gate on E_α =5478 keV (5460 keV→5500 keV)

7

Discussion

In this chapter, the α- and EC/β^+-decay feeding patterns are analysed to determine the properties of ^{178}Au^{g,m} and their daughters. The various decay schemes and tables presented in Chapter 6 show a large number of transitions and states. Therefore, to guide the reader through this discussion, simplified versions of the decay schemes are provided in Figs. 7.1 and 7.2 which show only the most important decays and states.

7.1 Interpretation of ^{178}Au^g decay data

7.1.1 EC/β^+ decay of ^{178}Au^g $\rightarrow$^{178}Pt

In Ref. [1], Cubiss *et al.* proposed $I^\pi = 2^+$ or 3^- for ^{178}Au^g, based on the measured HFS - see Table 5.1. The decay study performed for this thesis provides a complementary approach for studying ^{178}Au and its daughters. The EC/β^+ decay of ^{178}Au^g strongly populates the 2^+_1 [33(2)%] and 2^+_2 [9.2(4)%] states in ^{178}Pt - see Fig. 7.1(a). This corresponds to log ft=5.40(2) and 5.85(3), respectively, indicating both states are fed through allowed decay which limits I^π(^{178}Au^g)=1^+, 2^+, or 3^+.

The feeding of the $2^+_{1,2}$ states being so much stronger than that of the $4^+_{1,2}$ states (which received $\sim$ 3%) means that the 3^+ configuration can be rejected. It is assumed that the $\sim$3% feeding assigned to several low-energy states in ^{178}Pt is the result of the Pandemonium effect [59] - see Table 6.9. The total feeding to all excited states in ^{178}Pt determined using γ-ray intensities was 104(5)% of the value expected from the number of ^{178}Pt $\rightarrow$^{174}Os α decays. This is consistent with negligible EC/β^+ feeding directly from ^{178}Au^g to the 0^+_1 ground state of ^{178}Pt. Only weak feeding was assigned to the 0^+_2 state (2.6%) which is likely due to Pandemonium. Both 0^+ states would be expected to receive significantly stronger feeding than observed, if I^π(^{178}Au^g)=1^+. Therefore, the EC/β^+ decay to ^{178}Pt supports a 2^+ assignment for ^{178}Au^g which is consistent with the $\pi 1/2^-[541]_{h9/2} \otimes \nu 5/2^-[512]_{h9/2}$ configuration proposed by Cubiss.

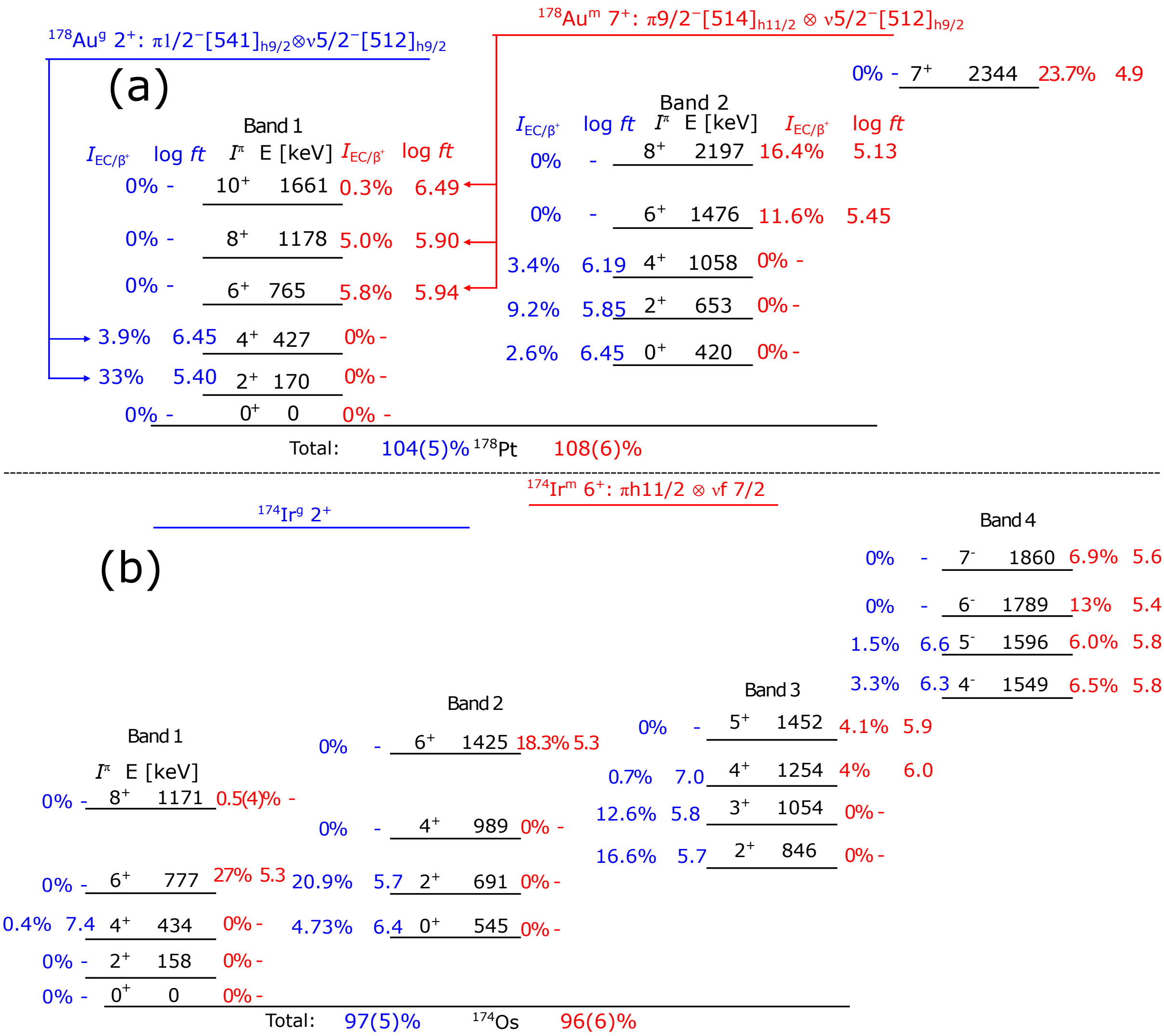

Figure 7.1: Schematic summarising the key aspects of the EC/β^+ feeding from (a) ^{178}Au^{g,m} and (b) ^{174}Ir^{g,m}. The EC/β^+-decay feeding intensities and corresponding log ft values are colour coded with blue and red font used for the decay of the ground states and isomers, respectively. The totals at the bottom of each panel show the sum of the feeding to all states in the daughter nucleus calculated by summing γ-ray and CE intensities divided by the number of EC/β^+ decays expected from the number of α decays of ^{178}Pt and ^{178}Au^{g,m}.

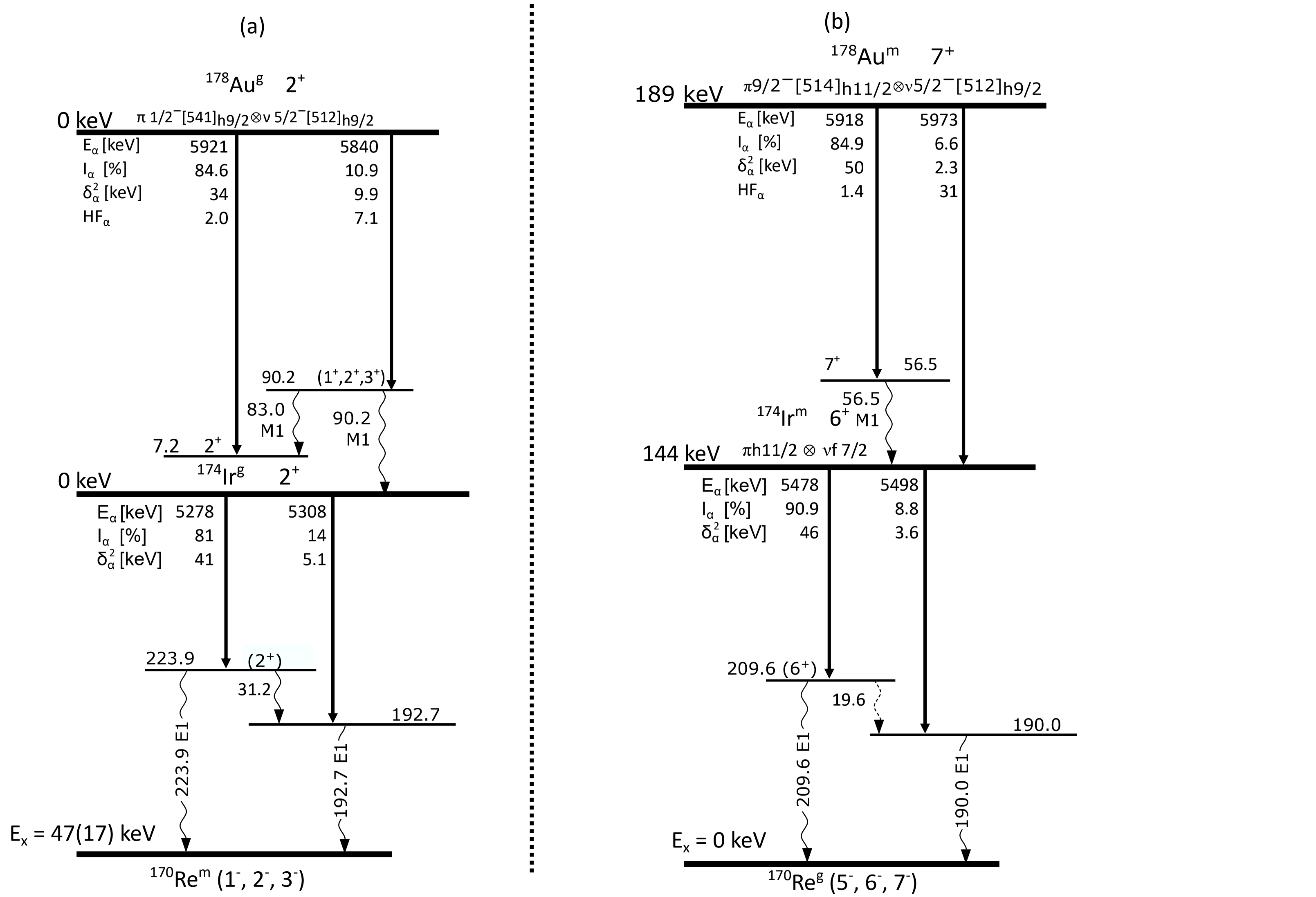

Figure 7.2: Schematics summarising the main α-decay paths from (a) $^{178}\mathrm{Au}^g \rightarrow^{174} \mathrm{Ir}^g \rightarrow^{170} \mathrm{Re}^{hs}$ and (b) $^{178}\mathrm{Au}^m \rightarrow^{174} \mathrm{Ir}^m \rightarrow^{170} \mathrm{Re}^{ls}$, respectively.

7.1.2 α decay of ^{178}Au^{g} $\rightarrow$^{174}Ir^{g}

The most intense α-decay transition from ^{178}Au^{g} has $E_\alpha = 5921$ keV and feeds the 7.2-keV state in ^{174}Ir. This decay has $HF_\alpha = 2.0(3)$, indicating it is unhindered and thus involves no change in angular momentum or parity. Therefore, based on the $I^\pi(^{178}\mathrm{Au}^g) = 2^+$ assignment made in Sec. 7.1.1, the 7.2-keV state is also assigned to have $I^\pi = 2^+$. All γ-ray transitions following the α decay of ^{178}Au^{g} were found to be E0, M1, and/or E2, meaning that all states included in the decay scheme shown in Fig. 6.3(a) have positive parity.

There is no evidence of a significant ground-state-to-ground-state α decay directly from ^{178}Au^{g} $\rightarrow$^{174}Ir^{g}. Given both nuclei are assigned as having $I^\pi = 2^+$ from their respective EC/β^+ decays (see Secs. 7.1.1 and 7.1.3), this suggests that the ground-state structures of ^{178}Au^{g} and ^{174}Ir^{g} are significantly different, with the former being deformed and the latter nearly spherical - see Sec. 7.1.4. The parent and daughter nuclear spins also limit the 90.2-keV state in ^{174}Ir to $I^\pi = 1^+$, 2^+, or 3^+ to explain the moderate hindrance of the 5840-keV α decay of $HF_\alpha = 7.1(9)$.

7.1.3 EC/β^+ decay of ^{174}Ir^{g} $\rightarrow$^{174}Os

As shown in Fig. 7.1(b), the EC/β^+ decay of ^{174}Ir^{g} strongly populates the 2^+_2, 2^+_3, and 3^+_3 states in ^{174}Os, which received just over half of all feeding between them. The log ft values for these decays indicate that they are all allowed EC/β^+, restricting $I^\pi(^{174}\mathrm{Ir}^g) = 2^+$, 3^+. Less than 1% of the EC/β^+ decay of ^{174}Ir^{g} feeds each of the $4^+_{1,2,3}$ states. The lack of significant direct population of any of the 4^+ states in ^{174}Os means that the 3^+ assignment can be excluded, leading to the conclusion that $I^\pi(^{174}\mathrm{Os})$=2^+. The weak feeding to the 4^-_4, and 5^-_4 states is likely a consequence of Pandemonium.

7.1.4 Structure of ^{174}Ir

There is a sudden onset of ground-state deformation in the lead region when moving along isotopic chains away from $N = 126$ towards the $N = 104$ midshell. For example, $^{178-186}$Au$_{100-108}$ are known to have strongly deformed ground states [34, 35, 133–135]. A similar pattern has been observed in the platinum isotopes [136–138] (see Fig. 5.3) and the odd-mass mercury isotopes ^{181,183,185}Hg$_{101,103,105}$ [139–141], as shown in Fig. 1(c) of Ref. [126]. Nuclides outside $100 \lesssim N \lesssim 108$, in contrast, generally have spherical ground states. Using α-decay spectroscopy, Harding *et al.* assigned ^{176}Au$^{m}_{97}$ as having the near-spherical $I^\pi = (7^+, 8^+, 9^+)$ $\pi 11/2^- \otimes \nu 7/2^-$ configuration [11]. Based on the characteristics of these nuclei, it is likely that ^{174}Ir$^{g,m}_{97}$ are also both (nearly) spherical.

In the absence of laser-spectroscopy data for lighest iridium isotopes, the neighbouring odd-mass isotopes of ^{174}Ir, ^{173,175}Ir, have recently been investigated using α-particle and γ-ray spectroscopy [11, 142]. The ground state of ^{175}Ir was assigned a spherical $1/2^+$ configuration, likely originating from a mixed $\pi s_{1/2}$ and $\pi d_{3/2}$ states. Similarly, it has recently been suggested that ^{173}Ir has a spherical $1/2^+$ ground-state configuration and a 226-keV isomer based on the spherical $\pi h_{11/2}$ configuration [143, 144].

The above suggests that ^{174}Ir^{g} is likely nearly spherical, probably based on mixed $\pi s_{1/2}$ and $\pi d_{3/2}$ states, like ^{175}Ir. The near sphericity of ^{174}Ir^{g} would explain the absence of a direct α decay from ^{178}Au^{g} $\rightarrow$^{174}Ir^{g} due to the large structural difference with the deformed parent, ^{178}Au^{g}.

7.1.5 α decay of ^{174}Ir^{g} $\rightarrow$^{170}Re^{ls}

The four $Q_{\alpha,tot}$ values determined for ^{178}Au^{g,m} $\rightarrow$^{174}Ir^{g,m} and ^{174}Ir^{g,m} $\rightarrow$^{170}Re^{ls,hs} in this thesis, combined with the mass measurements of ^{178}Au^{g,m} reported in Ref. [1], show that the α decay of ^{174}Ir^{m} populates a high-spin state, ^{170}Re^{hs}, that is 47 keV below the low-spin state populated by ^{174}Ir^{g}. There was no evidence of the internal transition ^{170}Re^{ls} $\rightarrow$^{170}Re^{hs}, possibly because the EC/β^{+} decay to ^{170}W is significantly faster than the alternative internal transition. In this case, the low-spin state ^{170}Re^{ls} would be a spin-trap isomer. The states ^{174}Ir^{g,m} feeding different states in ^{170}Re is contrary to the decay scheme proposed by Schmidt-Ott *et al.* [2] which assigned all α decays of ^{174}Ir as feeding to the same state.

The value of δ^2_α(5278 keV) = 41 keV indicates that this α decay is unhindered. Therefore, the 223.9-keV state can tentatively be assigned $I^\pi = 2^+$, based on the same assignment being proposed for ^{174}Ir^{g}. The E1 multipolarity assigned to the 223.9-keV transition therefore indicates that the 47-keV state in ^{170}Re^{ls} is $I^\pi = 1^-$, 2^-, or 3^-. Similarly, the E1 designation of the 192.7-keV transition suggests that the state it depopualtes also has positive parity.

7.2 Interpretation of ^{178}Au^{m} decay data

7.2.1 EC/β^{+} decay of ^{178}Au^{m} $\rightarrow$^{178}Pt

Based on the HFS and the α decay of ^{178}Au, Cubiss' preferred configurations for ^{178}Au^{m} gave $I^\pi = 7^+$ or 8^-, although 8^+ was also considered - see Table 5.1. This can be investigated further through the EC/β^{+} decay to ^{178}Pt by considering log ft values which have been determined for the first time in this thesis. The feeding assigned to each daughter-nucleus state is an upper limit due to the Pandemonium effect [59]. Therefore, the log ft values deduced should be considered as lower limits.

The 6^+_1 and 8^+_1 states of ^{178}Au^{m} received 5.8% and 5.0% of the total EC/β^{+} decays of ^{178}Au^{m}, respectively. Stronger direct feeding of the 6^+_2 and 8^+_2 states was observed of 11.6% and 16.4%, respectively. The log ft values for these four decays range between 5 and 6 [see Fig. 7.1(a)], suggesting that these are all allowed transitions. This feeding pattern therefore supports the 7^+ assignment for ^{178}Au^{m} which would enable direct population of these daughter states through allowed EC/β^{+} decays. In contrast, an 8^+ parent would populate 6^+ states through second-forbidden EC/β^{+} decay, which would be negligibly weak.

The feeding of the 7^-_4, 8^-_3, and 9^-_4 states was much weaker, giving log ft values of 6.47(17), 6.76(18), and 5.95(18), respectively. If I^π(^{178}Au^{m}) = 8^-, these states should be strongly fed through allowed EC/β^{+} decay with typical values of log $ft \approx 5.5$. This is not the case and the log ft values assigned to these states suggest they are populated through first-forbidden EC/β^{+} decay, further supporting the $I^\pi = 7^+$ assignment. The Nilsson configuration proposed by Cubiss for I^π(^{178}Au^{m}) = 7^+ is $\pi 9/2^-[514]_{h11/2} \otimes \nu 5/2^-[512]_{h9/2}$ which, based on the EC/β^{+} feeding to ^{178}Pt, is confirmed.

The most strongly fed state from the EC/β^+ decay of ^{178}Au^m is at 2344 keV, despite this being the one of the highest-energy states observed. Through the γ-γ and CE-γ coincidence analysis presented in Sec. 6.3.2, it was shown that this state is likely a two-quasiparticle configuration with $I^\pi(2344 \text{ keV}) = 7^+$. The low log ft value for the 2344-keV state in ^{178}Pt would normally be interpreted as indicating that the EC/β^+ decay feeding it is a spin-flip allowed transition. Based on the $\pi 9/2^-[514]_{h11/2} \otimes \nu 5/2^-[512]_{h9/2}$ assignment of ^{178}Au^m, this would suggest that the 2344-keV state has the $I^\pi = K^\pi = 6^+$, $\nu^2(7/2^-[514]_{h11/2} \otimes 5/2^-[512]_{h9/2})$ configuration. However, the the arguments presented in Sec. 6.3.1 favour a 7^+ spin assignment. It is possible that such a spin-flip transition populates this 6^+ state which could then depopulate to the 2344-keV state through a low-energy, highly converted M1 transition that was not observed. This would artificially inflate the apparent feeding to this state, resulting in the low log ft value observed.

The strong feeding of the 2344-keV $I^\pi = \mathrm{K}^\pi = 7^+$ state could, in part, be a reflection of it being populated through K-unhindered EC/β^+ decay from ^{178}Au^m, which also has $I^\pi = \mathrm{K}^\pi = 7^+$. However, this raises a significant question regarding the feeding of the K=0 $I^\pi = 6^+_{1,2}$, $8^+_{1,2}$ states: if K(^{178}Au^m)=7, then EC/β^+ decay to the $6^+_{1,2}$ and $8^+_{1,2}$ states involve $\Delta K = 7$ and $\Delta I = 1$. This gives reduced hindrance $\nu = \Delta\mathrm{K} - \Delta J = 6$, which should result in negligible direct feeding. However, in total, the $6^+_{1,2}$ and $8^+_{1,2}$ states account for nearly 40% of all EC/β^+ decays of ^{178}Au^m, which is far above the expected limit from Pandemonium.

The same arguments of K hindrance also apply to γ decay and would suggest that the 534-keV γ ray feeding the $K^\pi = 6^-_3$ state should dominate the depopulation of the 2344-keV state. The transitions from the 2344-keV state to bands 1 and 2 should be negligibly weak due to strong K hindrance. This is not the case - see Fig. 7.3. In their recent review article on K-hindered decay [145], Walker and Kondev suggested one mechanism that would allow high-ΔK decays to proceed:

> "the implication for nuclei away from the line of stability, where the decay Q values are large ($Q > 4$ MeV), is clear: it would be unlikely to observe β-decay transitions with large ΔK, unless a specific K-mixing scenario is invoked. For example, even for $\Delta\mathrm{K} = 2$ forbidden decays, one may expect log ft ∼9-10 and therefore the decays would be expected to proceed via non-K-forbidden transitions, by minimizing $\Delta\mathrm{K} = 0, \pm 1$."

While strong mixing was observed between the low-spin $0^+_{1,2}$, and $2^+_{1,2}$ states in ^{178}Pt, the mixing amplitudes determined by Davidson for the $6^+_{1,2}$ and $8^+_{1,2}$ states were found to be small. These were confirmed by further calculations by Page [122], following the methodology of Dracoulis from Ref. [146]. The relative mixing amplitudes calculated for the equal-spin states in bands 1 and 2 are also reflected by the E0-transition strengths determined in Sec. 6.3.3; E0 transitions between the low-spin states are much stronger than between the higher-spin states, due to the difference in state-mixing strengths.

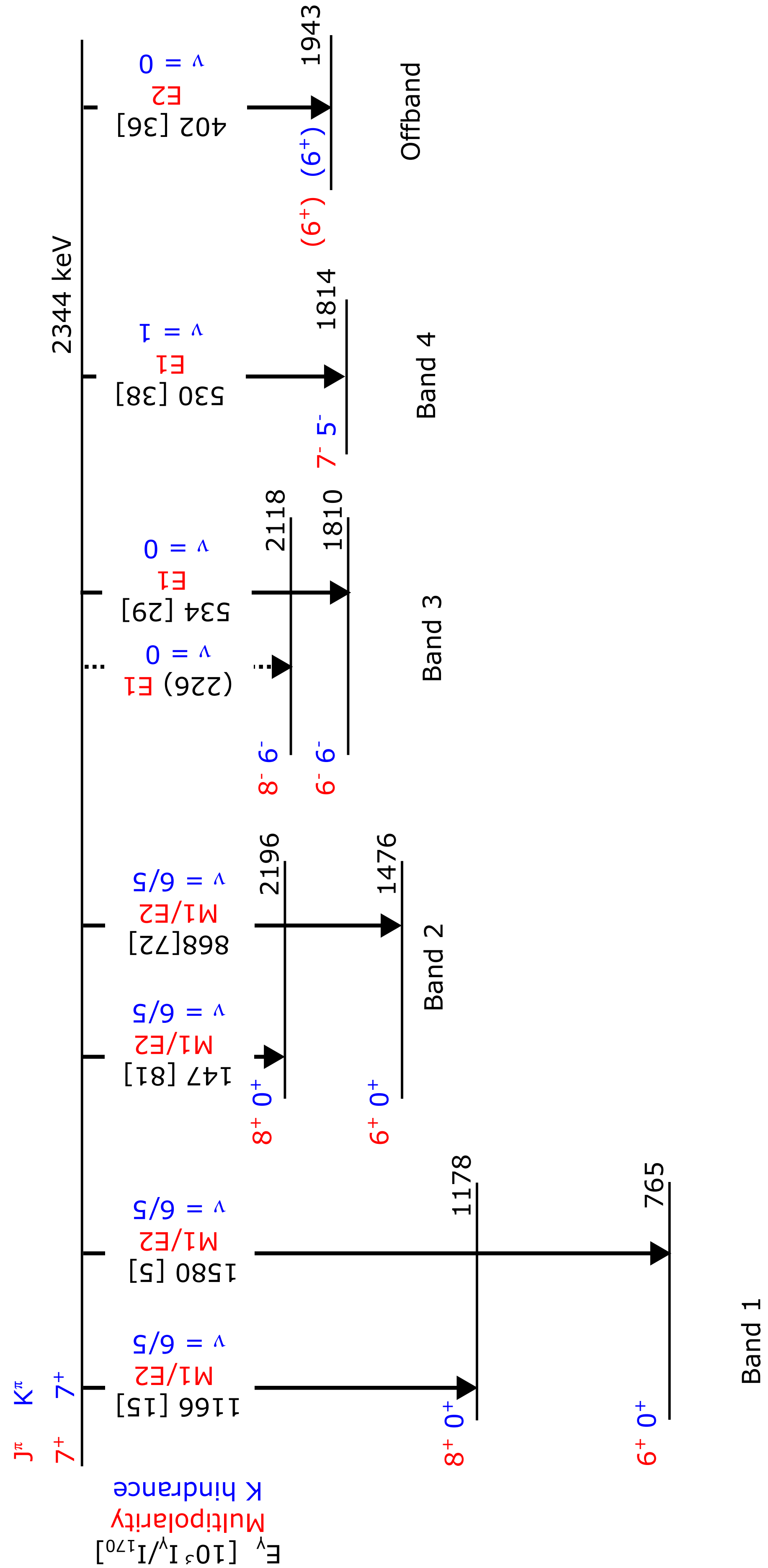

Figure 7.3: Summary of the γ ray transitions observed depopulating the 2344-keV state. Each states' energy is given in black text, with the total angular momentum (J^{π};red), and the expected value of K (blue). Each γ-ray energy, intensity relative to the 170-keV $2_1^+ \rightarrow 0_1^+$ transitions, multipolarity, and expected degree of K hindrance, ν, are given.

An alternative explanation for the apparent lack of K hindrance for EC/β^+ and γ decays feeding the $6^+_{1,2}$ and $8^+_{1,2}$ states is that ^{178}Pt is triaxally deformed. Because K is defined as the projection of the angular-momentum vector onto the axis of symmetry, it is undefined for triaxial nuclei in which no symmetry axis exists [145]. This would mean K is no longer a good quantum number.

In a recent study [147], Balogh *et al.* successfully described the intruder band in ^{179}Au by considering a particle-triaxial rotor model with a ^{178}Pt core. A good agreement between calculations and the experimentally measured structure of ^{179}Au could be achieved only by introducing strong triaxial deformation of $\gamma = 27°$ in the ^{178}Pt core. In this scenario, the absence of K hindrance of the feeding to the $6^+_{1,2}$ and $8^+_{1,2}$ states would be further evidence of strong triaxial deformation in ^{178}Pt. Further calculations [148, 149] also suggest that ^{178}Pt has a triaxially deformed ground state [122]. Triaxial deformation would reduce the impact of K hindrance, possibly enough to explain the observed EC/β^+ and γ-ray feeding patterns.

7.2.2 α decay of ^{178}Au^m →^{174}Ir^m

The most intense α decay from ^{178}Au^m is at $E_\alpha = 5918$ keV [84.9(2) %] which feeds a state 56.5 keV above ^{174}Ir^m. This decay is unhindered with $HF_\alpha = 1.40(2)$, corresponding to a $\Delta l = 0$, $\Delta\pi =$ no transition. Therefore, the assignment $I^\pi(56.5 \text{ keV}) = I^\pi(^{178}\text{Au}^m) = 7^+$ is made. The γ ray from this state to ^{174}Ir^m was found to be a pure M1 transition, restricting $I^\pi(^{174}\text{Ir}^m) = 6^+$, 7^+, or 8^+. This is consistent with the EC/β^+ feeding pattern to ^{174}Os, which is discussed in Sec. 7.2.3. The $HF_\alpha = 31(2)$ of the 5973-keV direct 'isomer-to-isomer' α decay suggests that ^{174}Ir^m and ^{178}Au^m have different proton and/or neutron states - this is discussed further in Sec. 7.2.5.

7.2.3 EC/β^+ decay of ^{174}Ir^m →^{174}Os

As already shown, the α and EC/β^+ decay of ^{178}Au^m suggest that $I^\pi(^{174}\text{Ir}^m) = 6^+$, 7^+, or 8^+. The EC/β^+ decay of ^{174}Ir^m strongly populates the $6^+_{1,2}$ states in ^{174}Os, which together account for approximately 45% of feeding. This corresponds to log $ft \approx 5.3$, indicating that these are allowed transitions. This restricts the possible spin-parity of ^{174}Ir^m to $I^\pi = 5^+, 6^+$, or 7^+. The 5^+ assignment is not consistent with the α- and EC/β^+-decay data from ^{178}Au^m. Furthermore, the absence of direct feeding of the $4^+_{1,2}$ states, which should receive comparable feeding to the 6^+ states from a 5^+ parent, allows this assignment to be firmly rejected. The 7^+ assignment can also be rejected due to the lack of direct feeding of 8^+ states. Thus, 6^+ is the only spin-parity assignment for ^{174}Ir^m that explains its EC/β^+ decay to ^{174}Os and the decay of its parent, ^{178}Au^m.

Direct feeding of the 4^-_4 and 5^-_4 states will therefore proceed through first-forbidden EC/β^+ decays from the 6^+ parent state. The unexpectedly strong feeding to these states may result from the Pandemonium effect or from closely matching parent-daughter configurations.

7.2.4 α decay of ^{174}Ir^{m} $\rightarrow^{170}$Re^{hs}

The relatively large value $\delta_\alpha^2 = 46(6)$ keV for the $E_\alpha = 5478$ keV decay from ^{174}Ir^m likely corresponds to an unhindered α decay, which typically have $\delta_\alpha^2 \approx 50 - 100$ keV in this region - e.g. the 5918 keV α decay from ^{178}Au^m has $\delta_\alpha^2 = 50$ keV and $HF_\alpha = 1.4$. This would mean that $I^\pi(209.6 \text{ keV}) = 6^+$. The 190.0- and 209.6-keV transitions to ^{170}Re^{hs} must both be E1 to explain the low number of K x rays observed in coincidence with 5478-keV α decay - see Fig. 6.36(c). Therefore, the ground state of ^{170}Re can tentatively be assigned to have $I^\pi = 5^-, 6^-$, or 7^-.

7.2.5 Configuration Assignment of ^{174}Ir^{m}

Based on the arguments given in Secs. 7.1.4, 7.2.3, and 7.2.5, the most plausible configuration for ^{174}Ir^m is $\pi h_{11/2} \otimes \nu f_{7/2}$. This combines the proton state assigned to the neighbouring isotope, ^{173}Ir^m [143], with the neutron state of the isotonic ^{176}Au^m and ^{177}Hg [11, 150]. These states would couple to the experimentally measured $I^\pi(^{174}\text{Ir}^m) = 6^+$ assignment, provided that there is an upward Paar's parabola [151].

This configuration would explain the moderate hindrance, $HF_\alpha = 31$, of the direct isomer-to-isomer α decay ^{178}Au^m $\rightarrow^{174}$Ir^m. As discussed in Sec. 7.2.1, the preferred configuration for ^{178}Au^m is $I^\pi = 7^+, \pi 9/2^-[514]_{h_{11/2}} \otimes \nu 5/2^-[512]_{h_{9/2}}$. Therefore, the Nilsson proton state proposed for ^{178}Au^m stems from the same spherical proton state that is assigned to ^{174}Ir^m although the neutron state is entirely different. Changing the neutron configuration and overall nuclear deformation during the α decay could provide the moderate hindrance observed.

8 Conclusions

8.1 Summary of Results

This thesis presents the results of an in-depth decay study of isomerically pure beams of ^{178}Au^{g,m} performed at the ISOLDE Decay Station at CERN. Isomerically selective separation was achieved by exploiting the large hyperfine splitting observed during the in-source laser spectroscopy studies reported by Cubiss *et al.* in Ref. [1]. As summarised in Table 8.1, this analysis identified 119 new γ rays and 70 new states in the daughter and granddaughter nuclei studied.

Table 8.1: Summary of the number of new γ rays and states identified in each daughter nucleus studied in this thesis.

	Newly Identified γ rays				
	^{178}Pt	^{174}Ir	^{174}Os	^{170}Re	Total
Ground-state beam	43	13	13	1	70
Isomeric-state beam	31	11	6	1	49
Total	74	24	19	2	119
	Newly Identified States				
	^{178}Pt	^{174}Ir	^{174}Os	^{170}Re	Total
Ground-state beam	27	7	10	1	45
Isomeric-state beam	12	6	6	1	25
Total	39	13	16	2	70

By determining α-decay hindrance factors, log ft values, and γ-ray multipolarities, the spins and parities of the ^{178}Au^{g,m} were determined to be 2^+ and 7^+, respectively and of ^{174}Ir^{g,m} to be 2^+ and 6^+, respectively. These spin-parity assignments for ^{178}Au^{g,m} determined are consistent with those proposed by Cubiss *et al.* based on the measurement of magnetic moments using in-source laser spectroscopy and correspond to the $\pi 1/2^-[541] \otimes \nu 7/2^+[633]$ and $\pi 9/2^-[514] \otimes \nu 5/2^-[512]$ Nilsson configurations, respectively. The spherical configurations $I^\pi(^{174}\mathrm{Ir}^g) = 2^+$, and $I^\pi(^{174}\mathrm{Ir}^m) = 6^+$ $\pi h11/2 \otimes \nu f7/2$ have also been proposed based on a review of neighbouring nuclides and the α- and EC/β^+-decay investigation performed for this thesis.

A detailed α-decay study was performed in this thesis, with the significantly higher statistics available allowing for a significant expansion of the decay schemes, compared to earlier work [1–3]. The half lives of ^{178}Au^{g,m} were determined, giving values consistent with those reported by Cubiss, but with a lower uncertainty. Using the mass measurements reported by Cubiss and the $Q_{\alpha,tot}$ value determined in this thesis, the excitation energies of isomers in ^{174}Ir and ^{170}Re were determined. This was the first time the relative excitation energies of the high- and low-spin states in ^{170}Re were determined.

The EC/β^+-decay branch ^{178}Au^{g,m} $\rightarrow$^{178}Pt was investigated, resulting in 39 new states and 74 new transitions being identified in ^{178}Pt. The conversion coefficients of the $J_2 \rightarrow J_1$ transitions between the yrast and an excited rotational band were calculated using two methods involving γ-ray and conversion-electron spectroscopy. These were found to be significantly larger than previously reported by Davidson [99].Using the strength of the $0_2^+ \rightarrow 0_1^+$ E0 transition, a lower limit for the difference in the mean-square charge radii of these states was calculated. Remarkably strong EC/β^+-decay feeding to the 2344-keV 7^+ state in ^{178}Pt was observed, indicating this state has a very similar configuration to ^{178}Au^m. The energy and depopulation of this state indicate it is a pure two-quasiparticle state. The spin of this state rules out this feeding proceeding through an allowed spin-flip transition meaning the nature of this state is still unclear.

A similar EC/β^+-decay analysis was also performed for the decay of the α-decay daughters of ^{178}Au^{g,m}, ^{174}Ir^{g,m} to ^{174}Os. The conversion coefficients determined for the $J_2 \rightarrow J_1$ transitions within ^{174}Os agree well with those previously reported by Kibédi *et al.* in Ref. [115].

The α-decay branch from ^{174}Ir^{g,m} $\rightarrow$^{170}Re was also investigated, leading to the addition of a few new transitions and states within ^{170}Re and several modifications of the decay scheme presented in Ref. [3]. The relative energies of two long-lived states (one high spin, one low spin) in ^{170}Re were determined. This showed that, unlike in ^{178}Au^{g,m} and ^{174}Ir^{g,m}, the low-spin isomeric state is at a higher energy than the high-spin state, contrary to the ordering proposed in Ref. [3].

Deformation of the Nuclides Studied

As stated in Chapter 1, nuclear deformation is an important property that influences many other aspects of nuclear structure. Nuclei with $N \approx 104$ and $Z \approx 82$ are well known to be particularly prone to shape coexistence although detailed information on their shape has been experimentally difficult to obtain until recently. As shown in Fig. 6.27, ^{178}Au lies at the edge of a region in which nuclei have strongly deformed ground states which makes them of particular interest for the study of nuclear shape.

The results presented in this thesis provide further detail on the deformation of isotopes in this region. Because the ground state of ^{178}Pt is the bandhead for a rotational band, it has been known for several decades that it is deformed in some way. The lack of K hindrance for the EC/β^+ decay of ^{178}Au^m, in particular, is best explained by a ^{178}Pt being triaxially deformed. This confirms the findings of Ref. [147], in which the structure of ^{179}Au was found to be well explained by assuming a triaxially deformed ^{178}Pt core, through a more direct approach.

Mapping out the boundary between regions of spherical and deformed ground-state configurations provides a key benchmark for nuclear models. The α-decay study of ^{178}Au^{g,m} $\rightarrow$^{174}Ir^{g,m} suggests that both ^{174}Ir^{g,m} are spherical, showing part of the border between regions of strong and weak deformation. A spherical assignment has been proposed for ^{174}Ir^m, which can be investigated further in follow-up studies of nuclear shape. Spherical configurations are also expected for ^{170}Re, although the low α-decay branching ratios to this nuclide prevent a detailed study of its shape to be made using the present data.

8.2 Future Work

The work presented in this thesis provokes several lines of inquiry that could form the basis of future studies. During the analysis performed in this thesis, many new γ rays following the EC/β^+ decays of ^{178}Pt→^{178}Ir and ^{178}Ir→^{178}Os were found but not investigated fully. A future analysis of the same dataset could explore these decays further to understand the structures of nuclei further down the EC/β^+ decay chain.

Although every effort was made to account for the feeding of high-energy γ rays to low-energy states in ^{178}Pt, it is believed that Pandemonium still contributes some feeding. The highest energy γ ray placed in the decay scheme is at 6.72 MeV which is significantly lower than Q_β(^{178}Au)=9670(30) keV [89]. A follow-up study of isomerically pure beams of ^{178}Au^{g,m} using the Total-Absorption γ-ray Spectroscopy setup Lucrecia at ISOLDE [152, 153] would be less susceptible to Pandemonium feeding of low-energy states in ^{178}Pt and allow for more reliable determination of log ft values.

Another follow-up experiment at ISOLDE could be performed at IDS in its fast-timing configuration to determine lifetimes of states in the second rotational band of ^{178}Pt. This would allow the E0-transition strengths for $J_2 \rightarrow J_1$ transitions determined to be used to calculate values of $\delta\langle r^2\rangle$ for these states. Given the expected efficiency of the fast-timing setup, such measurements would only take a few hours, if a similar production rate to the IS665 experiment is achieved. Experiments employing both Lucrecia and IDS have been run numerous times recently, allowing each setup to complement one another. Due to their proximity in the ISOLDE hall, swapping between them is quick and easy, allowing an efficient use of beam time.

Further laser- and decay-spectroscopy studies could provide further insight into the structures of the isotopes in the $N = 104$ lead region. Part of this follow-up work has already been performed through the IS737 laser-spectroscopy experiment of neutron-deficient gold isotopes which was performed at CRIS in the summer of 2024 [154].

Bibliography

[1] J. G. Cubiss *et al.*, Phys. Rev. C **102**, 044332 (2020).

[2] W.-D. Schmidt-Ott *et al.*, Nuclear Physics A **545**, 646 (1992).

[3] M. Al-Monthery, *Decay Studies of 178Au and Its Daughter 174Ir*, Ph.D. thesis, University of York (2019).

[4] L. Gaffney, P. Butler, M. Scheck, *et al.*, Nature **497**, 199 (2013).

[5] P. Möller, A. Sierk, T. Ichikawa, and H. Sagawa, Atomic Data and Nuclear Data Tables **109-110**, 1 (2016).

[6] H. Morinaga, Phys. Rev. **101**, 254 (1956).

[7] D. J. Rowe and J. L. Wood, *Fundamentals of nuclear models: foundational models* (World Scientific, 2010).

[8] D. Tilley, H. Weller, and C. Cheves, Nuclear Physics A **564**, 1 (1993).

[9] K. Heyde and J. L. Wood, Rev. Mod. Phys. **83**, 1467 (2011).

[10] A. Stott, *Studies of excited states in the odd-odd nucleus 178Au*, Phd thesis, University of York (2023).

[11] R. D. Harding *et al.*, Phys. Rev. C **104**, 024326 (2021).

[12] ISOLDE Decay Station Collaboration, Isolde decay station (ids) (2024), [Collaboration website, accessed: 2024-07-25].

[13] B. Andel *et al.*, Laser assisted studies of beta-delayed fission in 178,176au and of the structure of 175au (2020), experiment proposal.

[14] E. Rutherford, The London, Edinburgh, and Dublin Philosophical Magazine and Journal of Science **21**, 669 (1911), https://doi.org/10.1080/14786440508637080 .

[15] J. J. Thomson, Philosophical Magazine **44**, 93 (1897).

[16] J. J. Thomson, Philosophical Magazine **7**, 237 (1904).

[17] G. Gamow and E. Rutherford, Proceedings of the Royal Society of London. Series A, Containing Papers of a Mathematical and Physical Character **126**, 632 (1930), https://royalsocietypublishing.org/doi/pdf/10.1098/rspa.1930.0032 .

[18] J. Chadwick, British Journal of Radiology **6**, 24 (1933).

[19] C. F. v. Weizsäcker, Zeitschrift für Physik **96**, 431 (1935).

[20] R. B. Firestone *et al.*, *Table of Isotopes, CD-ROM Edition, Version 1.0*, version 1.0 ed. (Wiley-Interscience, 1996).

[21] E. Gapon and D. Iwanenko, Naturwissenschaften **20**, 792 (1932).

[22] D. Iwanenko, Nature **129**, 798 (1932).

[23] N. Bohr, The London, Edinburgh, and Dublin Philosophical Magazine and Journal of Science **26**, 1 (1913).

[24] W. Greiner and J. A. Maruhn, *Nuclear Models* (Springer-Verlag, 1996).

[25] K. S. Krane, *Introductory nuclear physics* (John Wiley & Sons, 1991).

[26] O. Haxel, J. H. D. Jensen, and H. E. Suess, Phys. Rev. **75**, 1766 (1949).

[27] M. G. Mayer, Phys. Rev. **75**, 1969 (1949).

[28] S. G. Nilsson, Dan. Mat. Fys. Medd. **29**, 1 (1955).

[29] B. R. Mottelson and S. G. Nilsson, Phys. Rev. **99**, 1615 (1955).

[30] J. M. Blatt and L. C. Biedenharn, Phys. Rev. **86**, 399 (1952).

[31] M. Goldhaber and A. W. Sunyar, Phys. Rev. **83**, 906 (1951).

[32] A. Bohr and B. R. Mottelson, Phys. Rev. **89**, 316 (1953).

[33] M. J. Martin, Nucl. Data Sheets **114 1497** (2023).

[34] K. Heyde *et al.*, Physics Reports **102**, 291 (1983).

[35] J. Wood, K. Heyde, W. Nazarewicz, M. Huyse, and P. van Duppen, Physics Reports **215**, 101 (1992).

[36] S. francaise de physique, ed., *Comptes rendus du Congrès international de physique nucleaire*, Vol. 1 (Éditions du Centre national de la recherche scientifique, 1964).

[37] G. E. Brown and A. M. Green, Nucl. Phys. **85**, 87 (1966).

[38] G. E. Brown and A. M. Green, Nucl. Phys. **75**, 401 (1966).

[39] H. K., Nuclear Physics A **466**, 189 (1987).

[40] K. Heyde, J. Ryckebusch, M. Waroquier, and J. Wood, Nuclear Physics A **484**, 275 (1988).

[41] A. Andreyev, M. Huyse, P. Van Duppen, *et al.*, Nature **405**, 430 (2000).

[42] J. Ojala, J. Pakarinen, P. Papadakis, *et al.*, Communications Physics **5**, 213 (2022).

[43] E. Simpson, Segrè chart, `https://people.physics.anu.edu.au/~ecs103/chart/` (2024), accessed: 2024-09-02.

[44] F. Kondev *et al.*, Chinese Physics C **45**, 030001 (2021).

[45] D. S. Delion and A. Dumitrescu, Phys. Rev. C **103**, 054325 (2021).

[46] D. Delion *et al.*, Physics Reports **424**, 113 (2006).

[47] M. Pfützner *et al.*, Progress in Particle and Nuclear Physics **132**, 104050 (2023).

[48] N. Schunck and L. M. Robledo, Reports on Progress in Physics **79**, 116301 (2016).

[49] J. Sadhukhan, Frontiers in Physics **8**, 567171 (2020).

[50] H. Geiger and J. Nuttall, The London, Edinburgh, and Dublin Philosophical Magazine and Journal of Science **22**, 613 (1911).

[51] C. Qi *et al.*, Physics Letters B **734**, 203 (2014).

[52] A. Beiser, Concepts of modern physics (2003).

[53] G. Gamow, Nature **122**, 805 (1928).

[54] J. O. Rasmussen, Phys. Rev. **113**, 1593 (1959).

[55] P. Van Duppen and M. Huyse, Hyperfine Interactions **129**, 149 (2000).

[56] W. Pauli, Pauli letter collection: letter to lise meitner (1930).

[57] E. Fermi, Ricerca Scientifica **4**, 491 (1933).

[58] F. Reines, Nature **178**, 446 (1956).

[59] J. Hardy, L. Carraz, B. Jonson, and P. Hansen, Physics Letters B **71**, 307 (1977).

[60] C. Walz, H. Scheit, N. Pietralla, *et al.*, Nature **526**, 406 (2015), issue Date: 15 October 2015.

[61] D. Freire-Fernández *et al.*, Phys. Rev. Lett. **133**, 022502 (2024).

[62] T. Kibédi *et al.*, Nuclear Instruments and Methods in Physics Research Section A: Accelerators, Spectrometers, Detectors and Associated Equipment **589**, 202 (2008).

[63] T. Kibédi, A. Garnsworthy, and J. Wood, Progress in Particle and Nuclear Physics **123**, 103930 (2022).

[64] J. Wood *et al.*, Nuclear Physics A **651**, 323 (1999).

[65] F. Flakus, IAEA bulletin **23**, 31 (1982).

[66] H. R. Bilger, Phys. Rev. **163**, 238 (1967).

[67] G. F. Knoll, *Radiation detection and measurement* (John Wiley & Sons, 2010).

[68] Canberra Industries, Inc., *HPGe Clover Detector Manual*, Meriden, CT (2003).

[69] M. Technologies, *Clover HPGe Detector Spec Sheet*, Mirion Technologies (2022).

[70] J. Palms, P. V. Rao, and R. Wood, Nuclear Instruments and Methods **76**, 59 (1969).

[71] *Xia LLC Pixie-16 User Manual* (2019).

[72] M. Borge, Nuclear Instruments and Methods in Physics Research Section B: Beam Interactions with Materials and Atoms **376**, 408 (2016), proceedings of the XVIIth International Conference on Electromagnetic Isotope Separators and Related Topics (EMIS2015), Grand Rapids, MI, U.S.A., 11-15 May 2015.

[73] M. Borge and K. Riisager, Eur. Phys. J. A **52**, 334 (2016).

[74] E. Kugler, Hyperfine interactions **129**, 23 (2000).

[75] R. Catherall, W. Andreazza, M. Breitenfeldt, A. Dorsival, G. Focker, T. Gharsa, T. Giles, J. Grenard, F. Locci, P. Martins, *et al.*, Journal of Physics G: Nuclear and Particle Physics **44**, 094002 (2017).

[76] CERN, The cern accelerator complex, layout in 2022, CERN Website (2022).

[77] J. Ballof *et al.*, Nuclear Instruments and Methods in Physics Research Section B: Beam Interactions with Materials and Atoms **463**, 211 (2020).

[78] J. Lettry *et al.*, Review of Scientific Instruments **69**, 761 (1998), https://pubs.aip.org/aip/rsi/article-pdf/69/2/761/19172359/761_1_online.pdf .

[79] K. Chrysalidis, *Improving the Spectral Coverage and Resolution of the ISOLDE RILIS*, Ph.D. thesis, Dissertation, Mainz, Johannes Gutenberg-Universität, 2019 (2019).

[80] B. Marsh *et al.*, Nuclear Instruments and Methods in Physics Research Section B: Beam Interactions with Materials and Atoms **317**, 550 (2013), xVIth International Conference on ElectroMagnetic Isotope Separators and Techniques Related to their Applications, December 2–7, 2012 at Matsue, Japan.

[81] T. D. Goodacre, *Developments of the ISOLDE RILIS for radioactive ion beam production and the results of their application in the study of exotic mercury isotopes* (The University of Manchester (United Kingdom), 2017).

[82] R. Catherall, V. Fedosseev, U. Köster, J. Lettry, G. Suberlucq, B. Marsh, E. Tengborn, I. Collaboration, *et al.*, Review of scientific instruments **75**, 1614 (2004).

[83] T. A. Berry *et al.*, Phys. Rev. C **101**, 054311 (2020).

[84] T. Berry, Physics Letters B **793**, 271 (2019).

[85] R. Lica *et al.*, Journal of Physics G **44**, 054002 (2017).

[86] I. A. Alnour *et al.*, in *AIP Conference Proceedings*, Vol. 1584 (American Institute of Physics, 2014) pp. 38–44.

[87] Xia, (2022), private communications with Xia LLC representatives.

[88] M. J. Oreglia, Ph.D. Thesis, SLAC-R-236 (1980).

[89] A. Rytz, Atomic Data and Nuclear Data Tables **47**, 205 (1991).

[90] Z. Kalaninová and others., Phys. Rev. C **89**, 054312 (2014).

[91] G. Bastin, C. Leang, and R. Walen, Journal de Physique Colloques **29**, C1 (1968).

[92] A. Siivola, Nuclear Physics A **109**, 231 (1968).

[93] A. N. Andreyev *et al.*, Phys. Rev. C **80**, 024302 (2009).

[94] T. a. Enqvist, Zeitschrift für Physik A Hadrons and Nuclei **354**, 1 (1996).

[95] K. Santhosh and B. Priyanka, The European Physical Journal A **49**, 150 (2013).

[96] J. Keller *et al.*, Nuclear Physics A **452**, 173 (1986).

[97] R. D. Page *et al.*, Physical Review C **53**, 660 (1996).

[98] J. G. Cubiss, *In-source laser spectroscopy of At isotopes and decay studies of 178Au*, Ph.D. thesis, University of York (2017).

[99] P. Davidson *et al.*, Nuclear Physics A **657**, 219 (1999).

[100] R. Wolf *et al.*, International Journal of Mass Spectrometry **349-350**, 123 (2013), 100 years of Mass Spectrometry.

[101] J. L. Wood, C. E. Bemis, and H. K. Carter, in *Nuclear Science Research Conference Series*, Vol. 3 (Harwood, New York, 1982) p. 481.

[102] F. G. Kondev *et al.*, Phys. Rev. C **61**, 044323 (2000).

[103] P. E. Garrett *et al.*, Progress in Particle and Nuclear Physics **124**, 103931 (2022).

[104] K. Thayer, Physics division argonne national laboratory description of the programs and facilities. (1999).

[105] Argonne National Laboratory, (2024).

[106] C. Davids *et al.*, Nuclear Instruments and Methods in Physics Research Section B: Beam Interactions with Materials and Atoms **70**, 358 (1992).

[107] M. H. AL-Monthery, *Decay Studies of 178Au and Its Daughter 174Ir*, Phd thesis, University of York (2019).

[108] J. Pakarinen, J. Ojala, P. Ruotsalainen, *et al.*, The European Physical Journal A **56**, 149 (2020).

[109] M. Leino, Nuclear Instruments and Methods in Physics Research Section B: Beam Interactions with Materials and Atoms **204**, 129 (2003), 14th International Conference on Electromagnetic Isotope Separators and Techniques Related to their Applications.

[110] R. D. Page *et al.*, Nuclear Instruments and Methods in Physics Research Section B: Beam Interactions with Materials and Atoms **204**, 634 (2003), 14th International Conference on Electromagnetic Isotope Separators and Techniques Related to their Applications.

[111] F. Meissner *et al.*, Phys. Rev. C **48**, 2089 (1993).

[112] C. R. Bingham *et al.*, Phys. Rev. C **51**, 125 (1995).

[113] J. Keller, K.-H. Schmidt, F. Hessberger, G. Münzenberg, W. Reisdorf, H.-G. Clerc, and C.-C. Sahm, Nuclear Physics A **452**, 173 (1986).

[114] G. Audi *et al.*, Nuclear Physics A **729**, 3 (2003), the 2003 NUBASE and Atomic Mass Evaluations.

[115] T. Kibédi *et al.*, Nuclear Physics A **567**, 183 (1994).

[116] A. Bouldjedri *et al.*, Springer Nature **342**, 267 (1992).

[117] B. E., Nuclear Data Sheets **72**, 221 (1994).

[118] N. Bijnens *et al.*, Physica Scripta **1995**, 110 (1995).

[119] P. Hansen *et al.*, Nuclear Physics A **148**, 249 (1970).

[120] J. Wauters *et al.*, Zeitschrift fur Physik A Hadrons and Nuclei **345**, 21 (1993).

[121] G. Igo, Phys. Rev. **115**, 1665 (1959).

[122] R. D. Page, Private communication (2025).

[123] J. Heery *et al.*, Nature (2021).

[124] C. B. Li *et al.*, Physical Review C **90**, 047302 (2014).

[125] L. Fraile, Journal of Physics G: Nuclear and Particle Physics **44**, 094004 (2017).

[126] J. G. Cubiss *et al.*, Phys. Rev. Lett. **131**, 202501 (2023).

[127] J. Sauvage, N. Boos, L. Cabaret, *et al.*, Hyperfine Interactions **129**, 303 (2000).

[128] I. Angeli and K. Marinova, Atomic Data and Nuclear Data Tables **99**, 69 (2013).

[129] J. Sauvage, N. Boos, L. Cabaret, *et al.*, Hyperfine Interactions **127**, 71 (2000).

[130] H. De Witte *et al.*, Phys. Rev. Lett. **98**, 112502 (2007).

[131] M. Seliverstov *et al.*, Eur. Phys. J. A **41**, 315 (2009).

[132] J. Chen, Logftcalculator (2024), accessed: June 5, 2024.

[133] K. Wallmeroth, Nuclear Physics A **493**, 224 (1989).

[134] K. Wallmeroth *et al.*, Phys. Rev. Lett. **58**, 1516 (1987).

[135] G. Savard *et al.*, Nuclear Physics A **512**, 241 (1990).

[136] T. Hilberath and et al., Z. Physik A - Hadrons and Nuclei **342**, 1 (1992).

[137] F. Le Blanc, Hyperfine Interactions **127**, 71 (2000).

[138] J. Sauvage and et al., Hyperfine Interactions **129**, 303 (2000).

[139] J. B. others, Physics Letters B **38**, 308 (1972).

[140] S. Sels *et al.*, Phys. Rev. C **99**, 044306 (2019).

[141] G. Ulm *et al.*, Z. Physik A - Atomic Nuclei **325**, 247 (1986).

[142] S. A. Gillespie *et al.*, Phys. Rev. C **99**, 064310 (2019).

[143] A. N. Andreyev *et al.*, Phys. Rev. C **80**, 024302 (2009).

[144] J. Cubiss *et al.*, Physics Letters B **786**, 355 (2018).

[145] P. M. Walker and F. G. Kondev, The European Physical Journal Special Topics **233**, 983 (2024).

[146] G. D. Dracoulis, Phys. Rev. C **49**, 3324 (1994).

[147] M. Balogh *et al.*, Phys. Rev. C **106**, 064324 (2022).

[148] A. Sánchez-Fernández, S. Bara, W. Ryssens, and S. Goriely (2025), in preparation.

[149] G. Grams, W. Ryssens, G. Scamps, *et al.*, Eur. Phys. J. A **59**, 270 (2023).

[150] A. Melarangi *et al.*, Phys. Rev. C **68**, 041301 (2003).

[151] V. Paar, Nuclear Physics A **331**, 16 (1979).

[152] ISOLDE Collaboration, (2024), tAS Lucrecia Experiment at ISOLDE, CERN.

[153] A. Algora *et al.*, European Physical Journal A **57**, 85 (2021).

[154] X. Yang *et al.*, High-resolution laser spectroscopy of light gold isotopes: investigation of “island of deformation” and shape coexistence (2023), experiment proposal.